An Experimental and CFD Based Analysis on Industrial Biomass Drying Production

By

Marcia Jo Pryce

This thesis is submitted for the degree of Masters of Research in Chemical Engineering at Lancaster University, United Kingdom.

Engineering, Faculty of Science and Technology

May 2021

In collaboration with

Bowland Bioenergy

Academic First Supervisor: Dr David Cheneler

Academic Second Supervisor: Dr Farid Aiouache

Industrial First Supervisor: Mike Ingoldby
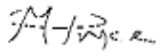
Industrial Second Supervisor: Anne Seed

Declaration

I, Marcia Pryce, declare that this Thesis titled 'An Experimental and CFD Based Analysis on Industrial Biomass Drying Production' is my own work, and has not been submitted in substantially the same form for the award of a higher degree elsewhere.

Date: 15th May 2021

Signature:

Abstract

This thesis presents an investigation on the drying processes of woodchip, by means of convective drying and infrared, drying. Two processes are considered, woodchip- bed drying (based on industrial site Bowland Bioenergy) and the drying of a singular woodchip, with additional analysis of the dust released during the drying process.

The core objectives were to investigate parameters influencing drying rate and to characterise dust produced during drying. Parameters considered surrounding woodchip drying were infrared radiation, temperature, air flow rate, bed depth, drier floor speed, and covering the drier. Primarily developing an understanding of the drying mechanism within wood and seeking to alter these parameters for a desired yield. Drying of woodchip is characterised by means of mathematical models and Computational Fluid Dynamics (CFD) simulations which are validated by experimental analyses and show qualitative agreement.

Comparatively to the experimental results there was a correlation between temperature and airflow increase and drying rate in both experimental and simulation results. Woodchip bed results suggested that increasing bed-depth from 24.5 cm to 34 cm will dry the woodchip effectively whilst increasing woodchip production by 39 %, covering the drier increased to moisture loss by ~15 %, and increasing the time in the drier decreased the final moisture content, the influence of time on moisture content decreases as the curves show a falling rate period. Single chip results showed temperature and airflow impacted the drying rate. Characterisation of the wood dust showed the surface area results ranged from 0.429 to 0.825 $m^2.g^{-1}$, average density of 502 $kg.m^{-3}$ and dust load of 2 $g.m^{-3}$. Particle size results aided the proposed design of a dust removal system to mitigate the risks of wood dust using a cyclone filter.

Acknowledgements

I would like to extend my thanks to Dr David Cheneler and Dr Farid Aiouache for supervision and support throughout this project. For helping me adapt to these trying times immediately providing me with the tools I needed to conduct this research. With thanks to the Centre for Global Eco Innovation, ERDF and my Industrial sponsors Bowland Bioenergy.

I express my gratitude to Dr John Crosse and Jessica Fisher for giving me the opportunity to use their laboratory equipment. The technicians Andrew Verden, Dr James Dickinson and Malcolm Weightman for assisting with experimental setup. My colleagues and friends that I have made this year at Lancaster University, particularly Andrew, Michael and Oliver with whom I had the longest tea breaks in my life. My biggest thanks to my family for all the support you have shown me through this research.

This thesis is in memory of my Nana Mary Cook and Cousin Jennifer Bill who supported me from the beginning of this work.

Publication

This work has been in part submitted and confirmed for publication, has been published and is to be submitted for publication as part of the following papers:

Published

Title: Mathematical Model Analysis for Mass and Rates of Woodchip IR Drying

Journal: Proceedings of the 6th World Congresson Mechanical, Chemical, and Material Engineering (MCM'20), 2020

Authors: Pryce M.J., Cheneler D., Martin A. and Aiouache F

DOI: 10.11159/htff20.177

Title: A Comparative Study of Diffusion Coefficients from Convective and IR Drying of Woodchip

Authors: Pryce M.J., Cheneler D., Martin A. and Aiouache F

Contents

List of Figures

List of Tables

Nomenclature

Symbol	Unit	Description	Symbol	Unit	Description
a	-	Coefficient	py	Pa	Pressure in the y Direction
$\dfrac{A_e}{A_i}$	-	Characteristic Ratio- Inlet Cross Section Area to Outlet Cross Section Area	q	$W.m^{-2}$	Rate of Heat Transfer
A_f	m^2	Area of Friction of Particles on The Cyclone Sides	Q	$W.m^{-3}$	Heat Source
a_w	-	Water activity	$q_{diffusion}$	$W.m^{-2}$	Diffusive Heat Flux
A	m^2	Cross sectional Area	$\dot{Q}_{evap}$	W	Energy Transferred To Evaporate Water
b	-	Coefficient	$\dot{Q}_{in}$	W	Energy In the Airflow Into the System
Bc	m	Cyclone Inlet Width	$\dot{Q}_{out}$	W	Energy In the Airflow out of the System
BD	m	Bed Depth	$\dot{Q}_s$	W	Energy Transferred Into the Solid
c	$mol.m^{-3}$	concentration	$\dot{Q}_{tran}$	W	Energy Transferred Into the System
$C_{p,s}$	$J.kg^{-1}.K^{-1}$	Specific Heat Capacity Solid	q_0	$W.m^{-2}$	Inward Heat Capacity

Symbol	Unit	Description
$C_{p,w}$	J.kg⁻¹.K⁻¹	Specific Heat Capacity Liquid Water
$C_{p,v}$	J.kg⁻¹.K⁻¹	Specific Heat Capacity Water Vapour
c_p	J.kg⁻¹.K⁻¹	Heat Capacity
$c_{v,sat}$	mol.m⁻³	Saturation vapour concentration
C_e	-	Frictional Coefficient
C_f	-	Frictional Coefficient
c_i	kg.m³	Concentration
$c_{l,sat}$	mol.m⁻³	Liquid Saturation Concentration
C_p	-	Design Constant
d_{50}	μm	Cyclone Cut off Diameter
D_{cap}	m².s⁻¹	Capillary diffusivity
D_i	m².s⁻¹	Diffusion Coefficient
D_i^*	m².s⁻¹	Effective Diffusivity
D_{Ld}	m²s⁻¹	Grouped Liquid Diffusivity
$D_{mixture}$	m².s⁻¹	Diffusion Coefficient
D_{va}	m².s⁻¹	Air-vapour Diffusivity
D_{vd}	m².s⁻¹	Grouped Vapour Diffusivity
d_z	m	Thickness of The Domain in The out of Plane Direction
Dc	m	Cyclone Body Diameter
Di	m	Cyclone Overflow Diameter
D_L	m².s⁻¹	Liquid diffusivity
d_{pi}	μm	Particle Diameter
Q_m	kg.m⁻³.s⁻¹	Mass Source
Q_p	W.m⁻³	Pressure Work,
Q_{vd}	W.m⁻³	Viscous Dissipation
Q_g	kg.s⁻¹	Gas Volumetric Flow
q	W.m⁻²	Conductive Heat Flux
$\dfrac{R_i}{r_e}$	-	Characteristic Ratio-Radius of Outlet to Average Radius of Vortex
Re_g	-	Reynolds Number
$R_{m/T}$	MPa	Tensile Strength at Temperature T
$R_{p1.0/T}$	MPa	1% Proof Strength at Temperature T
R_{const}	J.K⁻¹.mol⁻¹	Ideal Gas Constant
R_i	mol.m⁻³.s⁻¹	Reaction Rate per Unit Volume
RH	%	Relative Humidity
S	-	Saturation
S_0	m².m⁻³	Specific Surface Area Per Unit Volume
S_i	-	Saturation
S_{I0}	-	Initial water saturation
S_{il}	-	Irreducible liquid phase saturation
Sc	m	Cyclone Discharge Duct Length
S_l	-	Liquid Saturation
S_{ma}	-	Vapour Saturation
S_w	$\dfrac{m^2}{M_{woodchip}}$	Specific Surface Area Woodchip
t	s	Drying Time

Symbol	Unit	Description	Symbol	Unit	Description
D_S	m	Cyclone Base Diameter	T	K	Temperature
e	mm	Thickness	T_∞	K	Temperature of the Surrounding Air
eps	-	Floating Point Relative Accuracy for Double Floating Point Numbers/ Machine Epsilon	T_i	K	Initial Temperature
$\vec{F}$	N	External Forces Vector	t_I	s	Constant Rate Period Drying Time
F_{cent}	kg.m.s^{-2}	Centrifugal Force	t_{II}	s	Falling Rate Period Drying Time
$\mathbf{f_d}$	MPa	Design Stress	T_s	K	Solid Temperature Residence Time
F_{drag}	kg.m.s^{-2}	Drag Force	Δt	s	
FI	min	Top Floor Interval Time	T_0	K	Initial Temperature
h	W.m^{-3}.K^{-1}	Convective Heat Transfer Coefficient	t_h	m	Thickness
Hc	m	Cyclone Inlet Height	T_s	K	Temperature of the Solid
H_{evap}	J.kg^{-1}	Enthalpy of Vaporisation	u	m.s^{-1}	Velocity
il	-	Unit Matrix	u_{in}	m.s^{-1}	Velocity of Air Into the System
J_i	kg.m^2.s^{-1}	Diffusive Mass Flux	u_L	m.s^{-1}	Darcy velocity of liquid phase (x-component)
k	W.m^{-1}.K^{-1}	Conductive Heat Transfer Coefficient	u_{Lx}	m.s^{-1}	Liquid Velocity Field in x Direction
k_{evap}	s^{-1}	Evaporation rate constant	u_{Ly}	m.s^{-1}	Liquid Velocity Field in y Direction
K_H	-	Henrys Constant	u_{mean}	m.s^{-1}	Mean velocity for heat transfer equation – In the x direction
k_{Kozeny}	-	Kozeny Coefficient	u_{mean}	m.s^{-1}	Mean velocity for heat transfer equation
k_{Kozeny}	-	Kozeny Coefficient	$u_{mixture}$	m.s^{-1}	Velocity Field
k_{tot}	W.m^{-1}K^{-1}	Combined thermal conductivity of moist air and liquid phase	$\mathbf{u_x}$	m.s^{-1}	Fluid Velocity Vector In the x Direction
$\mathbf{K_B}$	-	Cyclone Standard Geometry Ratio	$\mathbf{u_y}$	m.s^{-1}	Fluid Velocity Vector In the y Direction

Symbol	Unit	Description	Symbol	Unit	Description
$\mathbf{K_D}$	-	Cyclone Standard Geometry Ratio	$\mathbf{u}$	m.s^{-1}	Fluid Velocity Vector
$\mathbf{K_H}$	-	Cyclone Standard Geometry Ratio	V	m^3	Volume
$\mathbf{K_i}$	-	Cyclone Standard Geometry Ratio	$\vec{V}$	m.s^{-1}	Directional Velocity Vector
$\mathbf{K_L}$	-	Cyclone Standard Geometry Ratio	$v_{c\theta i}$	m.s^{-1}	Characteristic Velocity
$\mathbf{K_S}$	-	Cyclone Standard Geometry Ratio	v_{in}	m.s^{-1}	Inlet Gas Velocity
$\mathbf{K_Z}$	-	Cyclone Standard Geometry Ratio	v_L	m.s^{-1}	Darcy velocity of liquid phase (y-component)
L_{entr}	m	Inlet Length Scale	v_{mean}	m.s^{-1}	Mean velocity for heat transfer equation – In the y direction
Lc	m	Cyclone Body Height	v_{out}	m.s^{-1}	Outlet Gas Velocity
M	kg	Mass	v_{tr}	m.s^{-1}	Terminal Velocity in The Radial Direction
$\dot{m}_1^s$	kg.s^{-1}	Cyclone Overflow Stream	v_{walls}	m.s^{-1}	Velocity at Centrifuge Walls
$\dot{m}_2^s$	kg.s^{-1}	Cyclone Base Stream	W	m	Inlet Width
$\dot{m}_{a,in}$	kg.s^{-1}	Mass Flow Rate of Air Into the System	$W_{D,I}$	kg.m^{-2}.s^{-1}	Drying Rate During Constant Rate Period
$\dot{m}_{a,out}$	kg.s^{-1}	Mass Flow Rate of Air Out of the System	$W_{D,II}$	kg.m^{-2}.s^{-1}	Drying Rate During Falling Rate Period
$\dot{m}_f^s$	kg.s^{-1}	Cyclone Feed Mass Flow	W_D	kg.m^{-2}.s^{-1}	Drying Rate
$\dot{m}_{w,evap}$	kg.s^{-1}	Mass Flow Rate of Water Evaporated	W_D	kg.m^{-2}.s^{-1}	Drying Rate
m_{evap}	mol.m^{-3}s^{-1}	Moles of evaporation	x	-	Directional Vector
m_i	-	Mass Fraction of Particles with Diameter i	X_a	%	Mass Fraction of Air
Mn	g.mol^{-1}	Molecular Mass	$X_{in(WB)}$	%	Input Moisture Content – Wet Basis
Mn_L	g.mol^{-1}	Molecular Mass of Water	$X_{loss}(DB)$	%	Moisture lost Dry Basis
M_0	kg	Initial Mass	$X_{loss}(WB)$	%	Moisture lost Wet Basis
M_e	kg	Equilibrium/Dry Mass	$X_{m(wb)}$	g·g^{-1}	Moisture content on wet basis
MR	-	Moisture Ratio	X_{mil}	g·g^{-1}	Irreducible moisture

Symbol	Unit	Description	Symbol	Unit	Description
					content dry basis
M_t	kg	Mass at Time t	$X_{out(WB)}$	%	Desired output Moisture Content – Wet Basis
n	kg.m^{-2}.s^{-1}	Component flux	$X_{present}(DB)$	%	Moisture Content at Time t Dry Basis
N_e	-	Number of Effective Turns	$X_{present}(WB)$	%	Moisture Content at Time t Wet Basis
η_i	-	Collection Efficiency	X_v	%	Mass Fraction of Vapour
n	-	Normal Vector Toward Exterior	X_1	%	Initial Moisture Content
P	Pa	Pressure	X_2	%	Moisture Content at the End of the Constant Drying Rate Period
$\hat{p}_0$	Pa	Predicted Pressure	X_{CR}	%	Critical Moisture Content
$(\rho c_p)_{eff}$	J.m^{-3}.K^{-1}	Effective Volumetric Heat Capacity	X_{EQ}	%	Equilibrium Moisture Content on a Dry Basis
p	atm	Pressure	X_m	%	Moisture Content Dry Basis
p_{entr}	Pa	Input Pressure	$X(DB)$	%	Moisture Content Dry Basis
P_i	Pa	Internal Design Pressure	$X(WB)$	%	Moisture Content Wet Basis
P_{max}	Pa	Maximum Design Pressure	y	-	Directional Vector
p_{sat}	Pa	Vapour saturation pressure	Zc	m	Cyclone Base Height
px	Pa	Pressure in the x Direction	z	-	Joint Coefficient

Greek Symbols

Symbol	Unit	Description	Symbol	Unit	Description
β_F	kg.m^{-4}	Forchheimer coefficient	σ_{hoop}	MPa	Hoop Stress
β, α, γ	-	Coefficients	$\sigma_{longitudinal}$	MPa	Longitudinal Stress
ξ_{ce}	-	Drop Coefficient of the Inlet and Inside of the Cyclone	σ	W/m^{2}K^{-4}	Boltzmann constant
ξ_{ci}	-	Pressure Drop Coefficient For The	φ	-	Porosity

xviii

Symbol	Unit	Description	Symbol	Unit	Description
		Outlet of the Cyclone	Φ		Relative humidity
ϵ	-	Surface emissivity			
ΔH_0	J.kg^{-1}	Latent Heat of Vaporisation of Water	ϕ	-	Coefficient for moist air viscosity and conductivity
κ	-	Permeability	ρ	kg.m^{-3}	Density
κ_i	-	Intrinsic Permeability	$\rho_{v\infty}$	kg.m^{-3}	Density of Surrounding Air
κ_r	-	Relative Permeability	$\rho_{v\infty}$	kg.m^{-3}	Density of the Surrounding Air
κ_{rg}^{L}	-	Relative Longitudinal Permeability of Gas	ρ_{vs}	kg.m^{-3}	The Density of the Volatiles In The Solid
κ_{rg}^{T}	-	Relative Tangential Permeability of Gas	ρ_v	kg.m^{-3}	Vapour density
κ_{rl}^{L}	-	Relative Longitudinal Permeability of Liquid	ΔP_c	Pa	Pressure Drop Cyclone
κ_{rl}^{T}	-	Relative Tangential Permeability of Liquid	μ	Pa.s	Viscosity

Chapter 1

Introduction

Drying is necessary for a wide range of industries from food and pharmaceuticals to textiles and ceramics. One of the most common drying industries, and the subject of this research is wood biomass, where biomass is defined here as plant material that is used for energy production. With biomass processing, it is necessary to lower moisture content to increase the calorific value of the wood, progressively so in the UK for woodchip manufacturers as from February 2021 sales of 'wet wood' smaller than 2 m^3 is to be phased out by the government (Government, 2020). In this case, less than 20 % moisture content is classed as dry and over this value as wet. Dry wood is more beneficial as it reduces pollutants, for example drier wood produces less smoke and soot, whilst reducing the chances of microbial growth during storage (Aguilar and Publications, 2019). Presently, Bowland Bioenergy produces woodchip from wood sourced from four local sites within Lancashire, that is compliant with BSI 17225-1 (Institute, 2014b) and BSI 17225-4 (Institute, 2014a), and currently supplies moisture contents of 20.1 % - 25 %, 25.1 % - 30 %, 30.1 % - 35 % and 35 %+ on a dry basis. The chipped wood consists of small roundwood of a variety of species, namely Sitka and Norway Spruce (*Picea sitchensis, Picea abies*) Larch (*Larix spp.*) and Scots pine (*Pinus sylvestris*), in standard lengths of 2.5 m with diameters ranging from 7cm to 40cm overbark with a variety of water contents. The biomass drying procedure can be broken into sections, as shown in Figure 1. This drying procedure is the focus of this thesis.
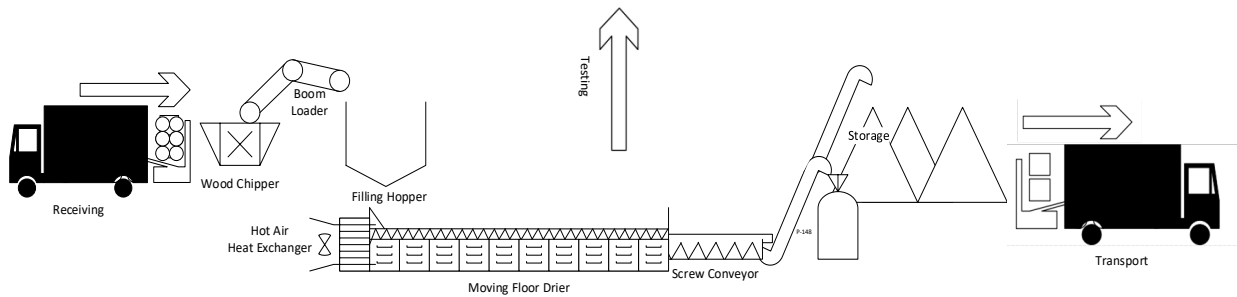
Figure 1 Process Overview

Though drying occurs in many ways, the idea in principle is to remove moisture from a material. Moisture removal means drying is often the most energy intensive operation within process industries, due to the latent heat required to separate the liquid from the solid in the form of vapour known as enthalpy of vaporisation. A lower moisture content is achieved by using an air-water system. This system consists of passing hot air over wet chips to remove the water by increasing the temperature of the chips.

Open air driers are often used in warm climates due to their low operational and capital costs, however when forced convection using hot air is introduced as a factor, the majority of the new heat introduced will rise to the materials surroundings rather than effectively dry the material. Figure 2 shows the heat loss from the Bowland Bioenergy open air dryer. Hot air is used as it can effectively cover the surface area of the material, achieve a larger moisture loss than cold air and is readily available from powered heat exchangers. Air flow from the top of an open bed drier is similar to the moisture removed by airflow in a cooling tower, known as drift. The air streams from drying are possible hazards to health. Some of these hazards are due

to the dust produced in the woodchip drying process, prompting further research into the dust produced onsite.
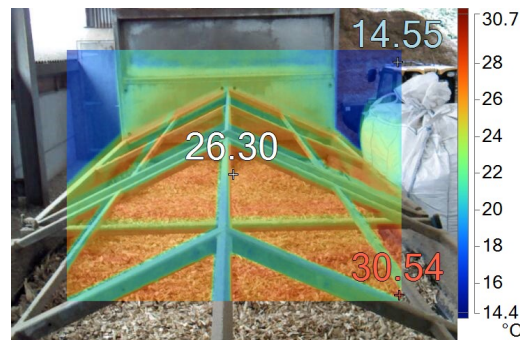
Figure 2 Infrared Image of Bowland Bioenergy's drier

1.1 Problem Definition and Aims

Settings of the drier at Bowland Bioenergy are based on experience from the operator. In general, these are kept the same with a set bed depth and moving floor settings. Because of this, these settings may not be the optimal settings to run the drier. Several parameters were investigated with the aim of to reduce the total tonnes of carbon emissions (tCO_2e) per tonne of woodchip through the drier, therefore, improving efficiency and reducing production costs per tonne.

When the drier is in operation, the dust is visible in the airflow around the drier and the drying space. The characteristics and impact of this dust is evaluated, and dust removal systems are designed, aiming to improving the working conditions.

1.2 Objectives

Drying rates are dependent on the nature of the solid dried and the method of drying. As woodchip with specified moisture content is the manufacturers product, the effect of the dryer parameters on the drying performance are investigated here. In addition, a common issue in the wood drying industry is the bi-product wood dust and the health and safety implications thereof. The thesis objectives are to quantify and characterise the following aspects:

1. Develop a testing strategy for convective woodchip drying.

2. Develop a testing strategy for infrared woodchip drying.

3. Assess the influence of temperature, airflow, bed depth, moving floor speed, and covering the drier on heat transfer and final moisture content.

4. Characterise the wood dust produced during the drying procedure.

5. Quantify and determine the health and safety implications of wood dust.

6. Investigate the methods of removing wood dust from the air in the woodchip drying room.

For the first three of these objectives, drying rates were determined through differentiating curve fits to existing models from literature that characterise a drying rate curve. All curve fits are obtained using results collected in this work based on the convective and infrared drying of a single woodchip or woodchip packed bed. Investigating the influence of temperature, airflow, bed depth and moving floor speed will be achieved through development of a computational fluid dynamics model and incorporate results from experimentation.

1.3 Research Outcome

From these results, improved efficiency will aid with reduction of the tonnes of carbon emitted (tCO_2e) per tonne of woodchip through the drier. A baseline tCO_2e assessment shows that onsite, the drier produces 22.13 tCO_2e per annum (see Appendix A), which is approximately 30% of the emissions on site. Research surrounding the dust on site will provide an understanding for the workers of the conditions on site and if recommendations are followed, the air quality on site can be improved and therefore reaching sustainable working conditions.

1.4 Existing Related Work

Drying is a common operation within chemical engineering applicable in the food, textile, paper, wood, pharmaceutical and biotechnological industries. With an increasing awareness of environmental impact, designs are changing with sustainability in mind. To develop

foundations to improve design, an understanding of the design of existing infrastructure is required. Within the design, process control, and optimisation of experimental and numerical methods are used to improve the process. The developed numerical simulations which cover basic mass and energy balances, dryer design, or cost estimation. The use of Computational Fluid Dynamics (CFD) is well known in many industries but are not used as widely for modelling drying.

Simplified drying models which consider the moisture ratio over time have been widely used and fitted to drying kinetics of various materials. The best fit of these computational models differs between material, drier style, temperature, air flow and sample size.

Drying involves multiphase transport which can be difficult to simulate in some software packages, the complexity is also increased when modelling inside a porous media (Ingham and Pop, 2005). An in-depth knowledge of material properties is required to effectively model drying, the process of collecting information on these requires specialist equipment and can be time consuming. Researchers have developed different versions of drying models, drying various products and have been using different mechanisms (Sapto et al., 2016, Gianfrancesco et al., 2010, AktaE et al., 2017). Drying equipment is common with very different designs with differing complexities (Towler and Sinnott, 2012). The drying of wood has been previously modelled as wooden plaques using the CFD package COMSOL. One such study emphasised on the fact that some of the model parameters are not well known (Hervé, 2010). The drying of woodchip has also previously been simulated using Discrete Element Modelling (DEM), in three dimensions within a rotary drum (Scherer et al., 2016) applied to the specific case, but has shown that coupled DEM and CFD can reduce the computational time, which can be very significant for models of drying of compact, but discrete media.

The research presented here is specific to the drier in operation at Bowland Bioenergy, which considers both experimental work coupled with simulation. A similar study to that considered here is the convective drying of Longan berries (Phupaichitkun et al., 2013), which has been carried out using ANSYS FLUENT, a CFD package, with some comparison to thermal images of the drier and utilising previous studies on the same material. This study assumed that the woodchip bed is a porous domain and with a flow of hot air at 6 m.s^{-1}. Longan berries have a lower permeability than wood and the study considered the evaporation of water using a thin layer-drying model with a lumped diffusive term. This study on Longan berries had a greater emphasis on air and heat transfer, rather than evaporation and moisture content.

1.5 Chapter Summary

This chapter shows industrial and academic relevance of this research, covering the research objectives and outlining the scope of this thesis. The process at Bowland Bioenergy consists of 6 primary steps, loading, wood chipping, drying, testing, sorting and distributing. Drying is situationally dependent on setup and materials, with existing works describing systems differing from that at Bowland Bioenergy. An introduction to previous work is outlined and will be used within the thesis to provide a basic understanding of models and theory going forward.

Chapter 2

Literature Review: Convective Drying, Infrared Drying and CFD

This chapter comprises of a literature review outlining drying principles, heat and mass transfer, profiles during drying and existing models. As simulation can be used to investigate the effect of parameters, this section also discusses the simulation software and provides an outline of CFD.

2.1 Drying Principles

Within a simple batch drier simultaneous mass and energy transfer occur (Chandra, 2010). The humidity of the air stream increases as the moisture content of the solid decreases. The driving forces for this energy and mass transfer include a temperature gradient, pressure gradient and a concentration gradient (Plawsky, 2014). During the drying process, the air stream increases in humidity (vapour concentration) and the temperature decreases as energy is transferred to the solid and volatile liquid reducing the driving force. To establish a dying time, a drying curve can be evaluated which shows distinct drying regimes. From this, the time to reach the critical, equilibrium and other desired moisture contents can be extrapolated (Daïan et al, 2014)

2.1.1 Mass and Energy Balances

During the drying process, the moisture from the woodchip becomes entrained in the air, increasing the moisture content of the air over time. As volatile liquids evaporate into the air, the mass of the chip changes. This mass change shows that the moisture content of the chip has changed. A mass balance over the system can be performed to establish the fundamental consequences of properties on the system (Morris et al, 2011). The mass of air entering the system over time $\dot{m}_{a,in}$ (kg.s^{-1}) is dependent on the velocity of air u_{in} (m.s^{-1}), the density of the surrounding air $\rho_{v\infty}$ (kg.m^{-3}), and the cross-sectional area A (m^2).

$$\dot{m}_{a,in} = \rho_{v\infty} u_{in} A \tag{1}$$

Energy transfer to the solid $\dot{Q}_{tran}$ (in Watts) is dependent on temperature T and the mass of air entering the system $\dot{m}_{in}$ as outlined in Figure 3. As mentioned previously, the driving force for energy transfer is the temperature difference between the surrounding air and the solid, $(T_s - T_\infty)$. The concentration difference in vapour can be described by the density of air, as the more vapour in the air the denser it will be. Thus, this is the driving force for mass transfer $(\rho_{vs} - \rho_{v\infty})$. The temperature and density affect the vapour pressure which produces internal moisture transport, in turn affected by structure and capillary effects.

$$\dot{m}_{a,out}$$
$$\dot{Q}_{tran}$$
$$\dot{m}_{a,in}, T_\infty, \rho_{v\infty}$$
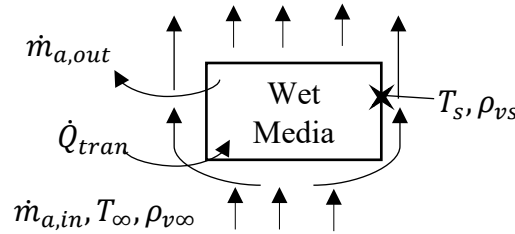
Figure 3 Mass and Energy Balance Drying

Figure 3 shows the mass of air entering the system over time $\dot{m}_{a,in}$ (kg.s^{-1}), the density of the surrounding air $\rho_{v\infty}$ (kg.m^{-3}) and the density of the volatiles in the solid ρ_{vs} (kg.m^{-3}), the energy transferred to the porous media and water $\dot{Q}_{tran}$, the temperature of the surrounding air T_∞ (K) and the solid T_s (K). The moisture content of the air can be established with the wet and dry bulb temperature using the Mollier diagram (Wernecke et al, 2014). The effective moisture content of the air exiting the drier was established and the effect of covering the drier was investigated using the saturation of the surrounding air.

Mass Balances

Air carries the water vapour away from the solid (output term), which is the output, as described by the mass balance Equation 2.

$$Output = Input - Accumulation \tag{2}$$

Initially the airflow is dry and as mass is lost, the accumulation is a negative value making the output mass larger than the input mass shown in Equation 3.

$$\dot{m}_{a,out} = \dot{m}_{a,in} + \dot{m}_{w,evap} \tag{3}$$

Where $\dot{m}_{a,out}$ is the mass flow rate of air out of the system (kg.s^{-1}), $\dot{m}_{a,in}$ is the mass flow rate of air into the system (kg.s^{-1}), and $\dot{m}_{w,evap}$ is the mass flow rate of water evaporated (kg.s^{-1}). This assumes that the airflow only contains water vapour and air, meaning no dust or dry matter is removed from the woodchip. In the simulations this simplified approach is used, as the main area of interest is the moisture content and any mass loss from woodchip carried in the air stream is assumed to have the same moisture content of the woodchip surface, which is minimal when dust is produced.

To determine the moisture content in the woodchip on a wet or dry basis X(DB) or X(WB) (%), the final "equilibrium mass" or "dry mass" M_e (kg), and the initial mass M_0 (kg) are required (Bajpai, 2018). This final mass was used to calculate moisture content on a wet basis or dry basis.

$$X(DB) = \frac{M_0 - M_e}{M_e} \quad X(WB) = \frac{M_0 - M_e}{M_0} \tag{4}$$

As the mass, M (kg), is conserved during the drying process the moisture content of the woodchip at a point in time can be calculated with regards to the mass of water still present in the woodchip or the mass lost from the chip. For all cases, the equilibrium mass is needed, which represents the dry solid.

$$X_{present}(DB) = \frac{M_t - M_e}{M_e} \quad X_{present}(WB) = \frac{M_t - M_e}{M_0} \tag{5} \tag{6}$$

$$MR = \frac{M_t - M_e}{M_0 - M_e} \tag{7}$$

$$X_{loss}(DB) = \frac{M_0 - M_t}{M_e} \quad X_{loss}(WB) = \frac{M_0 - M_t}{M_0} \tag{8}\tag{9}$$

Where $X_{present}(DB)$ and $X_{present}(WB)$ are the percentage moisture content on a wet or dry basis at time t (%), M_t is the mass at time t (kg), MR is moisture ratio and $X_{loss}(DB)$ and

X_{loss}(WB) are the moisture lost on a wet and dry basis (%). During the drying process plotting Equations 5, 6 and 7 against time produce curves of moisture content which decrease over time and Equations 8 and 9 for moisture loss which increases over time.

Energy Balances

To evaporate water, energy transfer is required. In a similar fashion to mass transfer, energy transfer can be described using energy balances. Energy comes in different forms, mechanical, thermal, electrical, nuclear, chemical and electromagnetic. The energy considered in this case is thermal which is removed from the system to convert liquid water into water vapour. In addition to this mechanical energy plays a role in airflow and is described in Chapter 5 using the Navier-Stokes Model (Temam, R et al, 1995).

The energy transferred into the system ($\dot{Q}_{tran}$(W)) heats the solid material ($\dot{Q}_s$ (W)) and evaporates water ($\dot{Q}_{evap}$(W)) shown by Equation 10.

$$\dot{Q}_{tran} = \dot{Q}_s + \dot{Q}_{evap} \tag{10}$$

where,

$$\dot{Q}_s = M_e(C_{p,s} + X(DB)_{in}C_{p,w})(T_s - T_i) \tag{11}$$

$$\dot{Q}_{evap} = M_e(X(DB)_{in} - X(DB)_{out})(\Delta H_0 - (C_{p,w} - C_{p,v})T_s) \tag{12}$$

Where M_e is the dry mass of the solid (kg), $C_{p,s}$, $C_{p,w}$, and $C_{p,v}$ are the specific heat of solid, liquid water and water vapour (J.kg^{-1}K^{-1}), T_s, and T_i are the final temperature and initial temperature of the solid (K). $X(DB)_{in}$, and $X(DB)_{out}$ are the initial and final moisture content of the solid (%), and ΔH_0 is the latent heat of vaporisation of water (J.kg^{-1}).

Equations 11 and 12 describe the energy transferred to the solid and water to form water vapour, however, not all of the energy from the hot air is transferred. Heat transfer requires a

temperature gradient, as the air surrounding the solid decreases in temperature, leading to a decrease of temperature gradient, thus reducing the heat transfer. The surrounding air cannot transfer all of its energy to the solid and will therefore hold some energy in the form of heat.

$$\dot{Q}_{tran} = \dot{Q}_{in} - \dot{Q}_{out} \qquad (13)$$

Where $\dot{Q}_{tran}$ is energy transferred (W), $\dot{Q}_{in}$ is the energy of the airflow into the system (W) $\dot{Q}_{out}$ is the energy of the airflow out of the system (W).

2.1.2 Profiles During the Drying Process

In addition to the moisture content, over time and depth, temperature, velocity and concentrations change during the drying. As mentioned in the mass and energy balances energy is taken by the wet media to evaporate liquid and heat the water and solid, changing temperature profiles as energy in the form of heat is adsorbed and passed over the porous media. The porous media hinders the inlet air stream velocity but gas and liquid can travel through the pores diffusively, as the moisture content decreases the hindrance from water decreases allowing more air to pass through. Finally, concentration profiles change through the solid as more water evaporates over time.

2.1.3 Transport Mechanisms

Free Moisture

Within the porous structure there are voids. Water found in these spaces is free water, which moves more freely than bound moisture but is harder to remove than surface moisture which is exposed to the air. Mainly, this moisture is transported through capillaries. How difficult this moisture is to remove depends on the activation energy required to break bonds and overcome physical forces(Zhou et al, 2020).

Bound Moisture

In contrast to free moisture, bound moisture is held on or within the porous structure, this moisture can be chemically bonded and/or physical bonded. Some chemically bonded moisture cannot be removed by drying alone this is known as the irreducible moisture (Wang et al, 2011). To remove this moisture the energy of the bonds needs to be overcome. This energy is the activation energy as for all bonds energy is required to break them and for stronger bonds this energy is larger (Fiorentini et al., 2015). Physical-chemical bonds include structural (from collisions between particles themselves, and between the structures walls and particles), absorptive and osmotic. Weaker physical bonds include capillary and those that effect free water in and between pores.

These bonding characteristics lead to two forms of internal transport through the solid, capillary and diffusion (Li et al, 2003). Capillary moisture transport forces liquid to the solid surface where it can evaporate and diffusive transport allows vapour to diffuse through the solid to the surface. Capillary applies to both liquid water and water vapour in air. Diffusive transport is faster and is applied to vapour. High volumes of liquid mean that more energy is required to produce a phase change. Liquid transport is dominant in saturated solids and as the saturation decreases, vapour transport has a greater impact on drying rate than liquid transport.

Chapters 4 and 5 cover in detail the equations used to describe heat and mass transfer through the woodchip.

2.1.4 Kinetics

Drying regimes can be interpreted due to the change in rate of drying (gradient). During the drying, liquid is transported from the interior of the solid to the surface. The surface liquid is then evaporated and the vapour transported. Typical drying curves can be interpreted in three stages, 1) heating of the material to an equilibrium temperature, 2) the constant drying rate

period with a constant gradient and 3) the falling rate period where the rate of drying decreases over time (Yiotis, et al, 2006).

For drying curves, experimental time and mass measurements over the drying period are required. The sampling, transporting, taking measurements and disposal need to be established in parallel with an overall experimental procedure.

Drying Rate

The moisture loss over time in a material is defined as the drying rate (Gavhane 2014):

$$W_D = \frac{-dM}{Adt} = \frac{-M_e dX(DB)}{Adt} \tag{14}$$

Where W_D is the drying rate ($kg.m^{-2}.s^{-1}$), M is mass (kg), A is the cross sectional area (m^2), t is time (s), M_e is the equilibrium mass (kg) and X(DB) is the moisture content on a dry basis (%).

$$X(DB) = \frac{M_0 - M_t}{M_e} \tag{15}$$

Like most rates of chemical reactions, drying rate depends on concentration, dispersion and temperature.

Constant Drying Rate Period

During the constant rate drying period, where the drying rate is constant ($W_{D,I}$ ($kg.m^{-2}.s^{-1}$))and the drying curve (mass (M (kg)) vs time (t (s))) has a linear slope (Yiotis, et al, 2006). Integrating between X_1 and X_2 which are the initial moisture content and the moisture content at the end of drying on a dry basis (%).

$$\int_0^{t_I} dt = \int_{x_1}^{x_2} -\frac{M_e dX}{W_{D,I}A} \rightarrow t_I = -\frac{M_e}{A} \int_{x_1}^{x_2} \frac{1}{W_{D,I}} dX \tag{16}$$

$$t_I = -\frac{M_e}{A} \int_{x_1}^{x_2} \frac{1}{W_{D,I}} dX = -\frac{M_e}{AW_{D,I}}(X_2 - X_1) \tag{17}$$

However, plotting drying rate vs moisture content can show the falling drying rate period and the constant drying rate period, meaning that X_2 is not reached in the constant drying rate period. Splitting the overall time for these two sections eases the process of integration. After the critical moisture content is reached, the drying rate is constant:

$$t = t_I + t_{II} \qquad (18)$$

Where t is the overall drying time, t_I is the time required to dry solid from X_1 to X_{CR} (the constant drying rate period), t_{II} is the time required to dry solids from X_{CR} to X_2 (the falling rate period), and X_{CR} is the critical moisture content on a dry basis (%) . As $W_{D,I} = \text{Constant}$ and if X_2 is replaced with X_{CR}:

$$t_I = -\frac{M_e}{AW_{D,I}}(X_{CR} - X_1) \qquad (19)$$

where X_{CR} is the moisture content at the end of the constant drying rate period, known as the critical moisture content.

Falling Drying Rate Period

In the falling rate period, the rate of mass loss decreases with time (Yiotis, et al, 2006). This is believed to occur due to a moving moisture front (Mikhailov, 1975). This is where the diffusive rates become more dominant as the capillary flow is less than the moisture flow removed from the surface, creating a greater gradient in moisture content between the external layers of the woodchip and the centre. The drying time for the falling rate period can be written as:

When the final moisture content X_2 is less than the critical moisture content X_{CR}

$$t_{II} = -\frac{M_e}{A} \int_{X_{CR}}^{X_2} \frac{1}{W_{D,II}} dX \qquad W_{D,II} = f(X) \qquad (20)$$

where, X_2-final moisture content (%) and M_e-mass of dry solid (kg)

As the drying rate is a function of moisture content X, it cannot be eliminated from the integral. To predict the rate, "scenarios" can be formed:

If the plot $W_{D,II}=f(X)$ is known, then the integral value can be determined by a graphical method e.g. If period II is the falling rate period and is not linear.

The auxiliary graph $1/W_{D,II}=f(X)$ should be constructed and the area beneath the curve calculated for the desired range (Between X_{CR} and X_2). Substituting the values of the integral from Equation 20, the drying time of the falling rate period can be obtained.

If $f(X)$ is Linear

$$t_{II} = -\frac{M_e}{A} \int_{X_{CR}}^{X_2} \frac{1}{W_{D,II}} dX \tag{21}$$

$$t_{II} = -\frac{M_e}{A} \int_{X_{CR}}^{X_2} \frac{1}{aX+b} dX \tag{22}$$

$$t_{II} = -\frac{M_e}{A}\frac{1}{a} [\ln(aX + b)]_{X_{CR}}^{X_2} \tag{23}$$

$$t_{II} = -\frac{M_e}{A}\frac{1}{a}\ln\left(\frac{aX_2+b}{aX_{CR}+b}\right) \tag{24}$$

By using the logarithmic and quotient rule Equation 21 becomes Equation 24, where a can be obtained as follows.

For linear falling rate regime at 2 points X_{CR} and X_2 (final moisture content)

$$W_{D,I} = aX_{CR} + b(1) \tag{25}$$

$$W_{D,II} = aX_2 + b(2) \tag{26}$$

From Equations 25 and 26:

$$W_{D,II} - W_{D,I} = aX_2 - aX_{CR} = a(X_2 - X_{CR}) \tag{27}$$

$$a = \frac{(W_{D,II}-W_{D,I})}{X_2-X_{CR}} \tag{28}$$

Replace "a" in Equation 24 then sub into t_{II}

$$t_{II} = -\frac{M_e}{A}\frac{1}{a}\ln\left(\frac{aX_2+b}{aX_{CR}+b}\right) = -\frac{M_e}{A}\frac{1}{\frac{W_{D,II}-W_{D,I}}{X_2-X_{CR}}}\ln\left(\frac{W_{D,II}}{W_{D,I}}\right) \tag{29}$$

$$t_{II} = -\frac{M_e}{A}\frac{1}{a}\ln\left(\frac{aX_2+b}{aX_{CR}+b}\right) = -\frac{M_e}{A}\frac{(X_2-X_{CR})}{W_{D,I}\left(\frac{W_{D,II}}{W_{D,I}}-1\right)}\ln\left(\frac{W_{D,II}}{W_{D,I}}\right) \tag{30}$$

If the moisture content at the end of the drying time is larger than the equilibrium moisture content X_{eq} (%), it is then possible to find $\frac{W_{D,II}}{W_{D,I}}$ from plots of drying rate vs moisture content, shown in Figure 4, using similar gradient/triangles;

$$\frac{W_{DI}}{X_{CR}-X_{EQ}} = \frac{W_{D,II}}{X_2 - X_{EQ}} \tag{31}$$

$$\frac{W_{D,II}}{W_{D,I}} = \frac{X_2 - X_{EQ}}{X_{CR}-X_{EQ}} \tag{32}$$
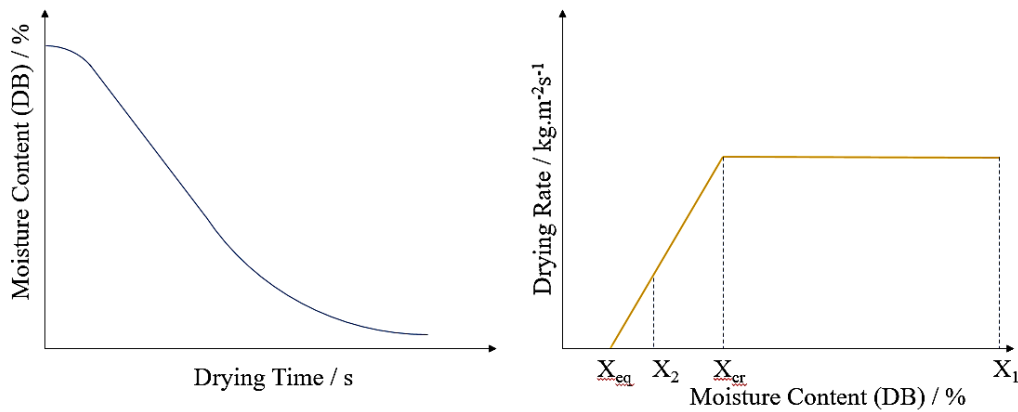
Figure 4 Drying Curve and Drying Rate vs Moisture Content Plot

Other Descriptions of Rate

Due to the variations in capillary and diffusive flow, through the porous media the drying rate is dependent on structure, concentration, the vapours driven off and environment (Shokri et al, 2009). To describe the drying rate, different models exist, including those which consider a falling and constant drying rate periods. Mass transfer is often described by a two-term model, examples are shown in Table 1.

Table 1 Thin Layer Drying Models MR=f(t)

Model Name	Expression MR(t)		Model Name	Expression MR(t)	
Lewis/Newton Model	e^{-at}	(Lewis, 1921)	Page	e^{-aX^b}	(Heldman, 2003)
Henderson and Pablis	ae^{-bX}	(Henderson, 1961)	Silva	$e^{-aX-b\sqrt{X}}$	(Silva et al., 2013)
Logorithmic	$ae^{-kt} + c$	(Henderson, (1961))	Diffusion	$ae^{-bX} + (1-a)e^{-bX}$	(Kassem, 1998)
Wang and Singh	$1 + aX + bX^2$	(Wang and Singh, 1978)	Verma	$ae^{-bX} + (1-a)e^{-cX}$	(Verma et al., 1985)
Peleg	$1 - \left(\dfrac{X}{a+bX}\right)$	(Peleg, 1988)	Two Term Exponential	$ae^{-bX} + (1-a)e^{-baX}$	(Henderson, 1974)

Diffusion is slower in solids compared to liquids and gasses as it is impacted by the path by which the vapour must travel to exit the structure. Within woodchip vapours can follow grain boundaries and fill voids. The activation energy required for vapours to diffuse through a porous material differs between solids, hence the coefficients of the equations in Table 1 are situationally dependent.

These models are largely empirical, in this study Fick's 2nd law of diffusion is implemented in the simulation in Section 5, where the diffusive coefficient is typically determined empirically.

Fick's 1st and 2nd Law

The driving force for diffusion is concentration, Fick's first law describes steady state systems where concentration is constant with time (Theodore et al, 2010).

$$J_i = -D_i \frac{\partial c}{\partial x} \tag{33}$$

Increasing the surface area per unit volume means that a greater number of molecules can diffuse out of the material per unit time, effectively increasing $\frac{\partial c}{\partial x}$. Fick's second law of diffusion takes into consideration concentration changes with time. For continuity:

$$\frac{\partial c}{\partial t} = -\frac{\partial J_i}{\partial x} \tag{34}$$

$$\frac{\partial c}{\partial t} = \frac{\partial}{\partial x_i}\left(D_i \frac{\partial c}{\partial x}\right) \tag{35}$$

If the Diffusion coefficient D_i is independent of c:

$$\frac{\partial}{\partial x_i}\left(D_i \frac{\partial c}{\partial x}\right) = D_i \frac{\partial^2 c}{\partial x^2} \tag{36}$$

2.2 Drying Methods

The evaporation process occurs when the latent heat of vaporisation is achieved or passed (Scherer, 1990). The temperature (and therefore energy) required for a liquid to reach this point changes with pressure. The methods of drying can be described using a phase diagram. Figure 5 shows the temperatures and pressure paths of different drying methods. Under atmospheric pressure, the most common methods of drying woodchip are convective and radiative drying, through more complex methods exist and include the freeze drying and the vacuum drying process.
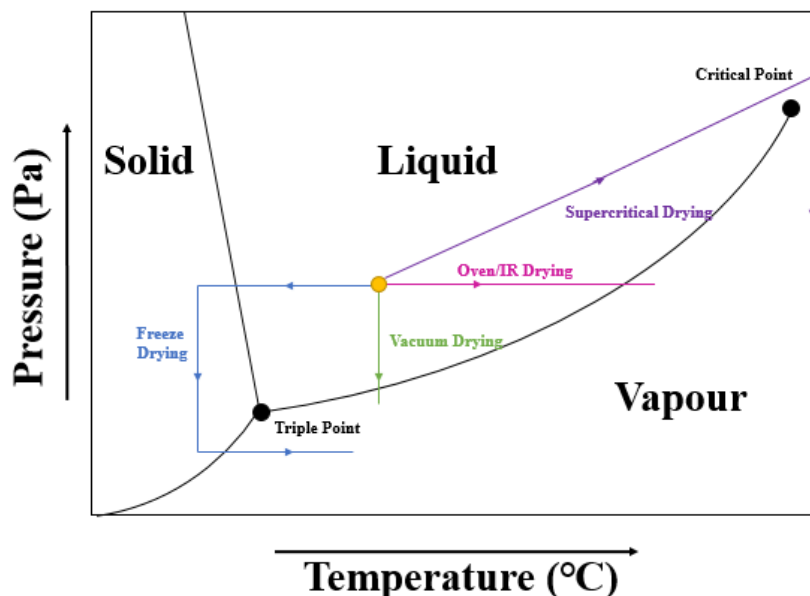
Figure 5 Phase Diagram with Drying Methods (adapted from (Bisht and Iqbal, 2018))

Heating can be achieved through a direct contact with a heated gas or radiation, or indirectly by separating the heating medium from the product. This heating can be carried out in a co-current or counter current manner. Counter current heating often achieves a greater heat

transfer, as shown in the example in Figure 6, which shows the temperature profiles of a counter current (left-hand plot) and co-current (right-hand plot) heating process. In the drier in operation at Bowland Bioenergy the airflow is in the same direction as the woodchip, with air flow crossing through the chip as it passes through a grating.
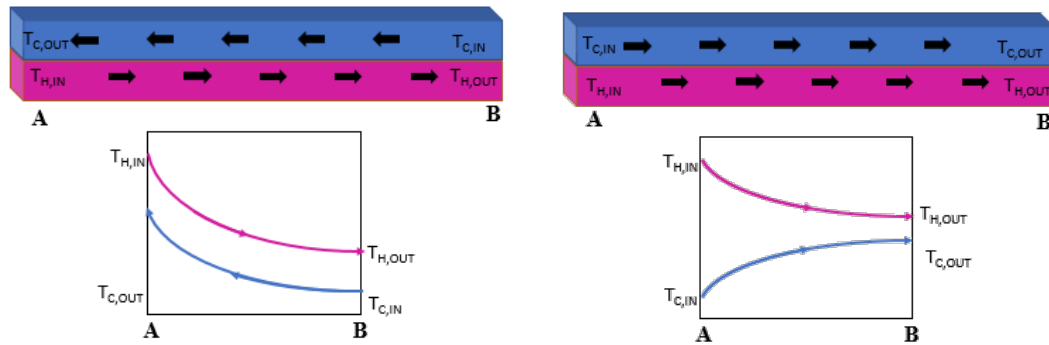
Figure 6 Temperature Profiles in Counter Current and Co-Current Heating (adapted from (Schlunder, 1983))

2.2.1 Convective Drying

In the convective drying, the air must first be heated (by a heating source) before it can heat the product. The heat transfer through conduction can be described by Fourier's law (Equation 37) of conduction and convective heat transfer is described using Newton's Law of Cooling (Equation 38) (Theodore et al, 2010).

$$q = -\frac{k(T_s - T_\infty)}{t_h} \tag{37}$$

$$q = -h(T_s - T_\infty) \tag{38}$$

Where q is the rate of heat transfer (W.m^{-2}), k is a conductive heat transfer coefficient (W.m^{-1}K^{-1}), h is the convective heat transfer coefficient (W.m^{-2}.K^{-1}), t_h is the thickness (m), T_s is the solid surface temperature (K) and T_∞ is the ambient temperature (K). This heat transfer impacts the mass transfer as water is evaporated from the external surface and within pores, diffusing out. Coupling between heat and mass transfer is important due to the influence mass diffusivity

in the gaseous phase can have on thermal conductivity (Wang et al, 2020). In both convective and infrared drying the mass transport principles in Section 2.1 are applicable.

2.2.2 Infrared Drying

In contrast to convective drying, radiative drying is more efficient with studies showing above 50% efficiency for the IR drying and for the convective drying around 10% efficiency (El-Mesery and Mwithiga, 2015). In a study by Hebbar et al (Hebbar et al., 2004) evaporation of water took ~50% less time and ~60% less energy using a combined convective and IR rather than convective alone in vegetables. This is because the IR drying, being through radiation which interacts directly with water, as opposed to the convective heat transfer to the air and then to the product. Of this radiation, specific wavelengths are adsorbed, some are reflected, and some are transmitted through the material (Jun and Irudayaraj, 2008). Energy transfer through the IR drying is also dependent on temperature to the fourth power shown by Stefan-Boltzmann's law of radiation (Equation 39) (Saunders, 2007).

$$q = -\epsilon\sigma(T_s^4 - T_\infty^4) \qquad (39)$$

Where ϵ is surface emissivity and σ is the Stefan-Boltzmann constant (W/m^{2}K^{-4}).

Despite this higher efficiency, IR drying cannot be effectively achieved without convection as moisture needs to be carried away from the dried product. The heating ability of IR drying is also limited by distance through the material due to attenuation of the radiation.

2.2.3 Other Drying Methods

Drying on site is achieved by the convective drying at atmospheric conditions and temperatures of less than 60 °C. Moisture content testing on site at Bowland Bioenergy is carried out using convective drying at 105 °C and IR drying at 105 °C. In addition to convective and IR drying other alternative methods include freeze drying, high temperature, steam drying, fluidized bed drying, and vacuum drying. The drying process can occur using convective, conductive,

radiative, and dielectric modes of heat transfer individually or in combination (Mujumdar, 2006).

2.3 The Structure of Wood

The structure of wood impacts the fluid and heat transport mechanisms present (Tsotsas et al, 2014). Longitudinal, radial, and tangential directions are used to describe wood. Considering a cylindrical tree longitudinal along the axis, radial runs on a horizontal plane from the centre to the external of the tree and tangential follows the circumference of the tree, as shown in Figure 7. Cutting along these planes can be used to the show features of wood (Clair et al., 2013).
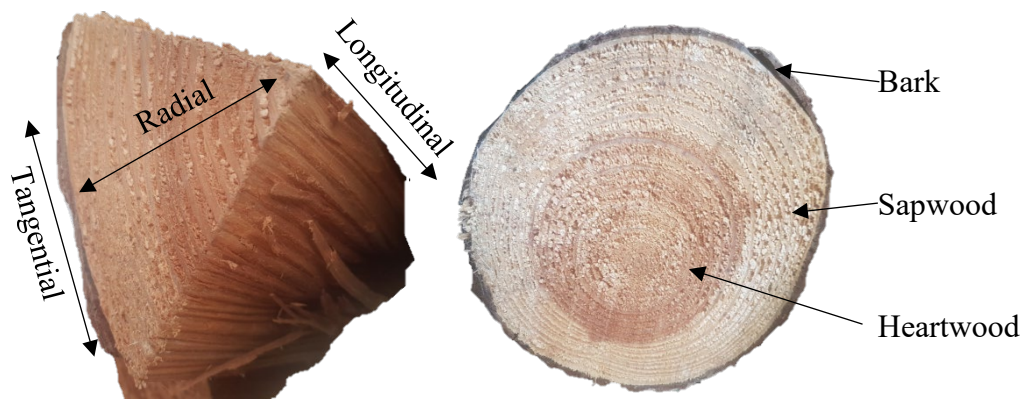
Figure 7 Structure of Wood - Direction and Features

Closer to the centre of the tree the wood is known as heartwood, towards the edge of the tree is sapwood and bark on the outer of the tree, which has an outer and inner layer. Trees grow by forming layers of wood in the shape of 'rings', discolouration in rings usually depicts the time of year when these are formed and these differ between trees and species. Figure 7 shows a cross section of a trunk with discolouration, this non-uniformity shows there will be varying vapour-diffusion transport, due to differences between different trees and indeed within a single tree itself, and therefore the difficulty of accurately operating driers of woodchips.

Softwood

Characteristically, the softwood is lighter in colour and mass, lasts a shorter length of time, is not as weather resistant and is faster growing by comparison to the hardwood. With a tubular

structure, the permeability is higher for softwood and their structure lends softwood to weathering and absorbing water, increasing the moisture content. Some cells within softwood structure are tracheids, which are empty dead cells with lignin walls and large cavities. In softwoods tracheids are 3mm long and 20-30μm in diameter, in addition there are structures called rays less than 1mm long made from smaller cells, examples of cells in soft and hard woods can be seen in Figure 8 (Rowell, 2012).
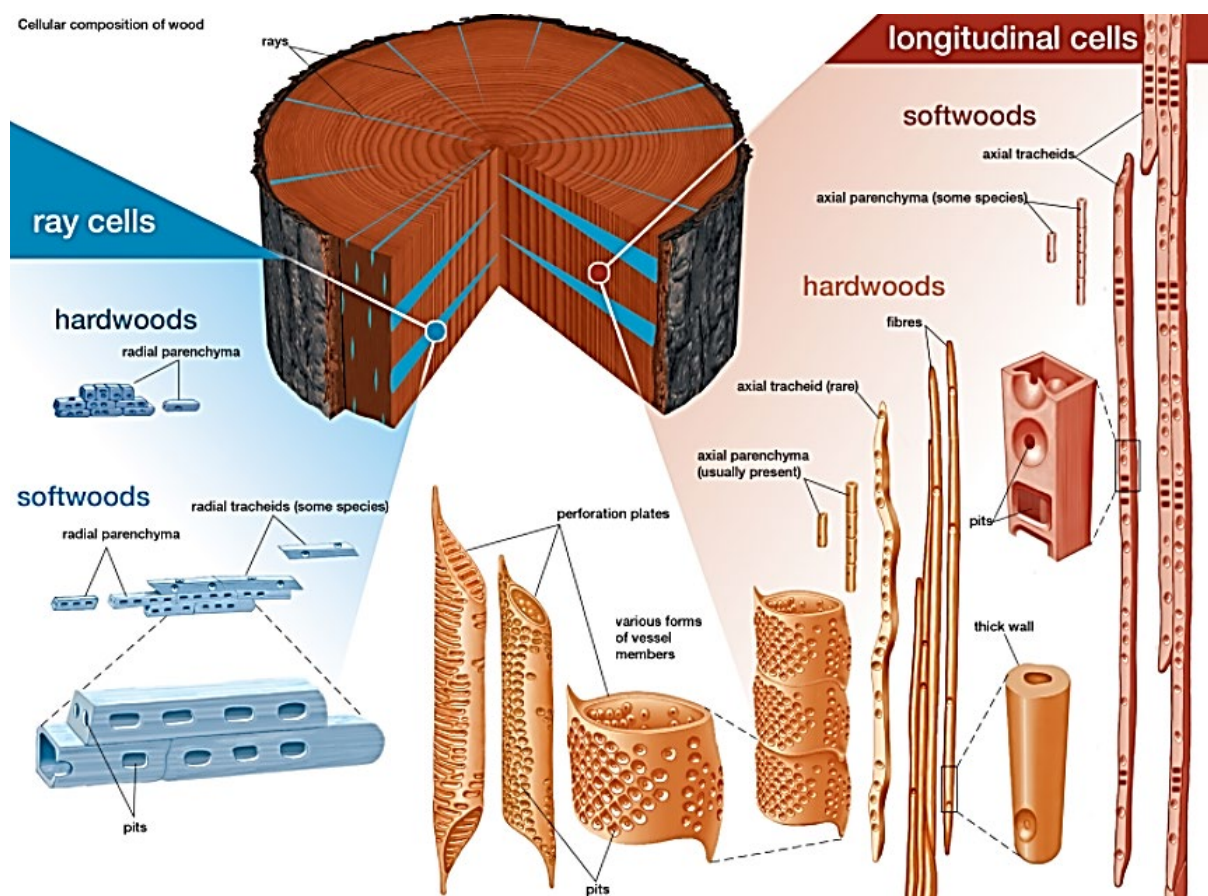
Figure 8 Cellular Composition of Wood (Tsoumis, 2000)

Hardwood

Hardwood does not weather as easily due to the cellular structure which contains vessels and tubular structures. Tubular structures in hardwoods are usually referred to as fibres. Vessels are cylindrical and tubular structures made of cells and forming longer structures by connecting

pores and plates, wider than tracheids with flat ends rather than tapered. Fibres in hardwood are shorter and thinner than tracheids in softwood at 1mm long (Rowell, 2012).

Knots

A large proportion of the wood used in woodchip production is unsuitable for use within furniture due to structural weaknesses (Foley, 2003) and aesthetic blemishes which can naturally occur from knots in the woods grain. Knots deviate from the grain pattern in wood, which is often the path of least resistance for vapour and liquid movement, therefore also impacting the drying. Typically for pine and spruce 8 % and 21 % of logs by volume can contain knots (Sandberg and Holmberg, 1996).As the basis of this work is for woodchip, the impact on knots within drying is reduced as breaks in wood usually occur along the grain and wood chipping often causes knots to segregate and break into smaller pieces.

Chemical Composition

The most common components associated with wood are cellulose and lignin. Cellulose forms cell walls and is a complex carbohydrate, whereas lignin is a component of secondary cell walls forming fibres and vessels and is a complex non-carbohydrate aromatic polymer (Belgacem, et al, 2016). These both have monomers which form polymers, cellulose forms straight chain and lignin's irregular. The chemical composition of the wood differs between species and location on the tree that it originated from, much like cell dimensions. Chemical composition varies over the body of the tree and can be generalised statistically based on volume of sapwood, heartwood, bark etc. to the overall tree and the appropriate sampling (Rowell, 2005). In addition to lignin and cellulose other components found in woodchip can be seen in Table 2.

Table 2 Main Constituents of Soft and Hard Wood Based on Average Values from Common Pulpwood Species (Sjöström and Raimo, 2013)

Constituent	Soft Wood	Constituent	Hardwood
Cellulose	37-43%	Cellulose	39-45%
Lignin	25-33%	Lignin	20-25%
Galactoglucomannans	15-20%	Glucuronoxylan	15-30%
Arbinoglucuronoxylan	5-10%	Glucomannan	2-5%
Exctractives	2-5%	Exctractives	2-4%

2.4 Porous Media

The porous medium contains voids in the form of pores within the material or spaces between the packed material. When considering woodchip, each chip is a porous medium and on a macro-level due to the structure of wood and the drier, the bed can also be considered a porous medium. For this study, these pores are considered as filled with air or water and the loss of other chemicals in the composition (shown in Table 2) is negligible, with these chemicals staying within the porous media due to their lower volatility and the temperature used of up to 105 °C (Institute, 2017b). The porosity is often used to characterise a porous medium. The porosity or void fraction is a measure of the space in a material and is the ratio of the empty volume and solid material volume, varying between 0 and 1 or as a percentage between 0 % and 100 %. Other important characteristics that are used to describe the drying of porous media include permeability, diffusivity of liquids and vapours through the medium and capillary diffusivity, which are described in Chapter 4.

2.5 Computational Fluid Dynamics

To numerically model the drying of wood, the development of a simulation model with a porous medium is required. The basis of this is a solid matrix with a mixture of air, liquid water and water vapour. The porous characteristics of the woodchip are represented as continuous medium with a volume average of porosity 0.556 (Chapter 4) the wood is treated as inert (the porous matrix does not react), isotropic (properties are independent of direction) and non-hygroscopic (the matrix does not take up/retain moisture). Water is instead held within the pores within the matrix defined by the porosity (Chapter 4). Heat and energy transport through

the material is simplified by assuming there is thermal equilibrium between the solid, liquid and gas phases locally. Energy transport can be characterised by the conservation of energy equation (Equation 107). The thermal equilibrium means that the vapour pressure of water vapour in contact with liquid water can be calculated as a function of temperature and saturation (Table 18). On a mass basis, the moisture content is used to describe the amount of water in an entire woodchip or at a point in space.

Prior to creating the above model, the solver or simulation software needs to be selected (a review of solvers is detailed below). The choice of solver is important as simulations should be a time effective and accurate (Tu et al, 2012). To describe pressure, concentration, and temperature profiles within woodchip before, during and after drying modelling, a simulation was carried out through application of Finite Volume Analysis (FVA), using commercial COMSOL Multiphysics 5.4. For the description of airflow across the drier and below the drier bed, commercial ANSYS-Fluent was used.

2.5.1 Review of Prediction Methods

Finite Element Method (FEM)

FEM is a computational model that discretises a CAD model into smaller sized elements of simpler geometry, collated these make up a finite-element mesh. In FEM, partial differential equations (PDE's), which describe the physics, are solved across the boundary of the simpler geometry. Cham: Springer International Publishing.). Approximating the fields in the PDEs, as a simpler function with a finite number of degrees of freedom (DOF's), means that at each boundary a local description of the physics from these simpler functions can be solved with each boundary. A contributing element to the overall mesh and matrix of equations can then be solved. Primarily used in structural analysis, this method has been developed for use for problems with multi-physics (Zimmerman, 2006). This method is commonly used for

structural analysis, chemical reactions, heat transfer, electromagnetics, multi-physics and CFD, through porous materials heat and mass transfer is regularly modelled using FEM (Datta, 2007).

Finite Volume Method (FVM)

Similar to the finite element method, a mesh of finite-sized contiguous control volumes is required. This however does not concentrate the boundaries of each simple geometry shape instead the volume as a whole. Considering the laws of conservation, what goes into each shape must come out or accumulate in this volume. There are existing FEM drying models for porous media, however fluid-flow is frequently modelled in CFD using FVM (Norton et al., 2013) as this is more stable and computationally efficient. This method works well for CFD, heat transfer and chemical reactions.

Finite Difference Method (FDM)

This method is also similar to FEM, as the finite difference method requires a mesh, in the case of FDM ODEs are solved at the nodes where each simple geometry shape is connected (Andreassen et al., 1992). At this point in space, discrete equations are solved; this method is more suited for regular geometries. This method is used in a wide range of applications in civil, mechanical and aeronautical engineering. (Zhu, 2018).

Lattice Boltzmann Method (LBM)

This simulation method is a relatively new technique for simulation, midway between microscopic (Hamilton's equation) and macroscopic (Navier-Stokes) using mesoscopic kinetic equations. Collectively considering particles using a distribution function from the lattice Boltzmann equation. In addition to considering velocity and pressure like Navier-Stokes, lattice Boltzmann considers momentum applicable to the distribution functions. The movement and collisions of particles whilst considering them on a cubic grid with eight possible directions of

movement (diagonal and straight). Though this method is useful when simulating flow through complex geometries and porous media, the grids must have to be regular and square, there are only a few commercial software's available and numerically this method is unstable for small viscosities (Karniadakis et al., 2006).

Conclusion

The aforementioned methods present some similarities, however, they differ in ease of implementation, FDM is easiest to implement and FEM the most difficult of the element methods. LBM is considered the easiest method; however, this method is relatively new and there is limited software available. FEM generally requires more sophisticated mathematics and therefore more computational power. In multi-physics cases FEM is often used and is critical to some cases, particularly increasing accuracy with smaller geometry is required, making the mesh denser or changing the element order which is the uniformity between the smaller geometry within the mesh. Of greatest importance to the model is the ability to combine different kinds of function by approximating the solution, i.e. coupling heat transfer and phase changes. To simulate drying in porous media, both FEM and FVM are required, ideally solved in parallel in a computationally efficient way. The finite-volume method is required as this one only requires flux evaluation over cell boundaries, making it suitable for nonlinear conservation laws that occur in transport problems. All of these factors should be considered when choosing a software to simulate the drying of woodchip (Anderson and Wendt, 1995).

2.5.2 Review of Available Software

FASTEST3D

FASTEST3D (Flow Analysis by Solving Transport Equations Simulating Turbulence) is a 3D flow prediction code that solves flow equations using FVM (Chandra Mohan and Talukdar, 2010). The generation of the geometric file and mesh requires a second package, such as the

commercially available ANSYS ICEM CFD. In addition to the fluid flow model, an additional heat and mass transfer model through porous medium is required. This additional requirement means that using this method would require a lot of time and computational power to complete as well as a second simulation software or method to provide an overall model for simultaneous moisture and heat transfer.

PoreFlow

This CFD software tool aids in finite volume methods to simulate flow behind a moving boundary. With the ability to simulate flow through a porous media and heat transfer similar to MATLAB, however this software requires editing a command file and the geometry requires an existing HEX file, so depending on the scenario post- and pre-processing using different software may be required (Hua Tan et al., 2011).

SolidWorks Simulation

With a user-friendly interface and ease of use, SolidWorks simulation allows for fast simulation for linear models with common boundary conditions. The software however does not allow for easily scripting user defined functions, somewhat decreasing the precision and control in comparison to many purpose-built flow simulation programmes (Lombard, 2018).

MATLAB

Using PDE solver toolbox or linked to opensource software such as Openfoam, flow through porous medium can be simulated. Simulation in MATLAB is achieved solely using the command window, making it difficult to link with complex CAD designs, and alterations require a greater amount of effort to locate and implement for optimisation (Elman et al, 2005).

ANSYS Fluent

ANSYS Fluent is one of few software packages available that offer the ability to model porous material and fluid-flow. This commercially available software is widely used in CFD drying,

particularly ANSYS Fluent and ANSYS CFX. With most software unable to solve transport in both domains, air and porous media, coupling ANSYS FLUENT is simpler to setup and the software is intuitive with freely available tutorials and advice online. Amongst the wide range of CFD-based commercial software, COMSOL Multiphysics and ANSYS FLUENT are the most widely implemented by researches in order to effectively simulate the drying process.

COMSOL 5.4

COMSOL (formerly FEMLAB) is very user-friendly and is designed to simulate physics-based problems (Karim and Law, 2017). The Multiphysics environment allows for fluid-flow, heat transfer and chemical phase change to be coupled and used within a single model. User defined functions can be easily implemented into independent variables and the material properties change with temperature can be effectively modelled.

Conclusion

Of the software reviewed, COMSOL was selected as the main programme for all pre- solving and post-processing. This software is widely used amongst academics and has been validated with many similar works, for instance (Chai et al., 2018), where COMSOL was used to study the drying rate of a moist-porous media under a forced convective flow. Multiphysics flows can be readily incorporated (for fluid flow through porous media, heat transfer and phase changes) and is commercially available.

2.6 Relevant Previous Drying Studies

Table 3 Summary of Relevant Previous Drying Studies

Study	Porous Material	Drying Method	Dimension(s)	Simulation CFD	Fluid Modelling
(ElGamal et al, 2013)	Grain	Convective	3	COMSOL	Navier- Stokes
(Babu et al, 2020)	Leaves	Convective	2	ANSYS FLUENT	Navier- Stokes
(Chilka et al, 2019)	Almond	Convective	3	ANSYS FLUENT	Boundary Layer
(Antony et al, 2016)	Sand	Fluidised Bed	3	ANSYS FLUENT	Eulerian- Eulerian
(Ljung, 2008)	Iron Ore	Convective	2	ANSYS CFX	Navier-Stokes
(Onwude et al, 2019)	Sweet Potato	IR and Convective	2	COMSOL	Navier-Stokes

(Terzi et al, 2016)	Capillary	Convective	2	SIMPLE	Boundary Layer
(Kurnia et al, 2013)	Potato Slice	Convective	2	ANSYS FLUENT	Navier-Stokes
(Mahapatra et al, 2018)	Carrot	Solar	2	COMSOL	Navier-Stokes

Table 3, above, details related literature. The core principals used in Chapter 4 and 5 are described within (Datta, 2007a) and (Datta, 2007b) covering the fundamental mechanisms within the model, and implementation of these models within COMSOL covered in (COMSOL, 2007). Sources that have been used to derive, determine or source the various parameters used in the porous bed and woodchip drying CFD-based simulation models in this research are described in Chapter 4. The recently published work of (Selimefendigil, 2020) was also very relevant to this research and considered drying of a porous medium by forced natural convection. The paper utilises many of the components, equations and methods used in this study and reinforce the methodology applied.

The first of these core references (Datta, 2007a) characterises porous media into four categories; large pores with applied pressure, small pores with pressure mostly from internal evaporation, small pores with capillary pressure only (no significant internal evaporation), and small pores with capillary plus other models with some evaporation. Covering the fundamental conservation laws governing evaporation such as Darcy's law for mass transport.

The relationship between properties such as porosity, thermal, permeability, and diffusion are further covered within (Datta, 2007b). This paper provides a comprehensive overview of a fundamental based multiphase porous media model, with distributed evaporation, and the broad range of input parameters required.

For defining explicit functions in COMSOL and to gain understanding of the software's functions (COMSOL, 2007) provides details for using COMSOL's GUI with inbuilt and user defined parameters, studies and functions.

Other studies include (Dietl et al., 1995), (Tsilingiris, 2008) and (Abaci et al., 1992) which use similar equations to (Datta, 2007a) and (Datta, 2007b), equations in spherical coordinates that can also be used for other geometries.

(Dietl et al., 1995) contains a simulation model produced for steady and time dependent drying conditions which are with experimental data in this literature. Demonstrating moisture and temperature distributions for the drying of concrete and pine.

From a wide literature review the transport properties in air are covered in (Tsilingiris, 2008), defining properties of water vapour and air mixtures as well as dry air. Showing the dependency of properties on temperature and humidity and comparing expressions to existing experimental data.

(Abaci et al., 1992) Discusses the relative permeability of two phase mixtures and their dependency on saturation. With important governing properties of multiphase flow through porous media.

2.7 Chapter Summary

The overview of drying in this chapter indicates the complexity of drying through porous media with simultaneous heat and mass transfer, as well as, vapour pressure and concentration dictating the drying rate. It was shown that drying rate can be described by a constant drying rate where the surface moisture loss is supplemented by capillary moisture transport, and a falling drying rate where the evaporative water front progresses into the solid and surface evaporation decreases. The wood structure, heat energy supplied, concentration gradients and are flow impact the drying process. The CFD simulation software COMSOL was selected to simulate drying and ANYS FLUENT was chosen to simulate the air flow through the drier, with different software and predictive methods reviewed.

Chapter 3

Experimental Methods

To evaluate whether the conceptual system effectively represents the physical system, data was collected on-site for multiple situations, which depend upon several independent variables. The first measurable dependent variable was the moisture content of woodchip. As the measurement method for this on-site was by drying in batches, the method used to collect this data differed between the on-site bed drying, in the laboratory convective drying and in the laboratory IR drying. Therefore the two experimental methods are detailed separately herein, Section 3.1 for on site drying and Section 3.2 for Laboratory- based drying

3.1 Laboratory Convective Drying

3.1.1 Preliminary Setup

Initially, convective experiments were conducted in a closed oven and measured every 5 minutes using a mass balance (method detailed in Appendix B). The results from this method are plotted in Figure 9 and show that the oven temperature fluctuated significantly over time. In addition, this initial method was prone to human error as material handling was involved every 5 minutes.
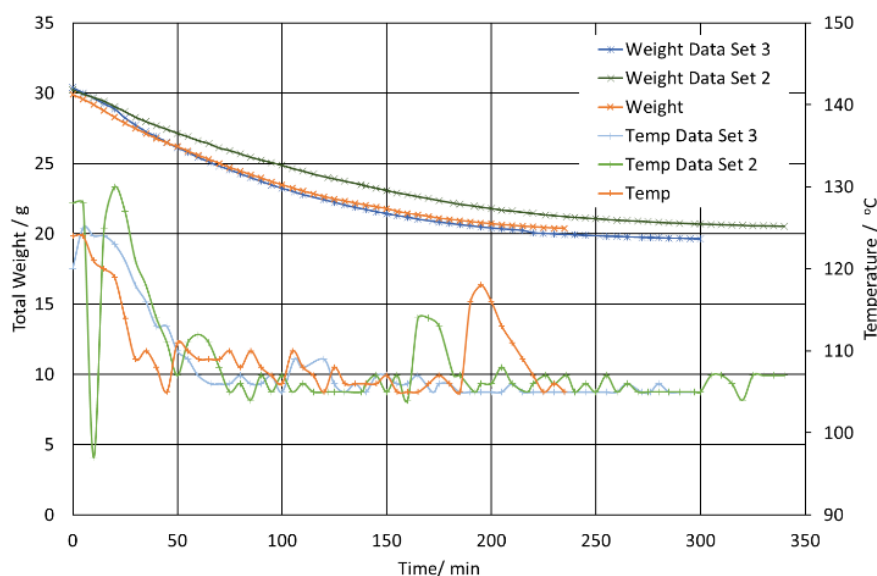
Figure 9 Convective Experiment Results Initial Method

Though relatively linear, this method took 5 hours to complete with a low air flow and fluctuating temperature. The temperature used in Figure 9 was set to 105 °C which was

approximately 50 °C higher than the temperature used at Bowland Bioenergy, while using lower temperatures in theory increases drying time. Hence for this method, the drying time would be much longer than 5 hours for temperatures closer to the values used on site.

3.1.2 Convective Laboratory Drying Set Up

Due to the handling required and temperature fluctuations in the initial method for conducting convective drying experiments, the drying method was altered. The scales were connected to a computer and automatically logged mass data and the air flow temperature and flow rate were controlled using a heat gun. This method produces a more constant and measurable flow rate and temperature as well as live data, significantly reducing the handling during operation and saving project time.

Adjacent to a set of scales, with an accuracy of ±0.0005 g, a variable temperature heat gun was mounted (shown in Figure 10) which passes air at a minimum speed of 1.6 m.s^{-1} over a sample tray. The mass on this tray was recorded every 5 seconds, with the heat gun causing an initial constant fluctuation in the mass and variations around this caused by changes in the air flow. The temperature of the air was measured 4 cm from the outlet of the heat gun and 5 cm from the centre of the 10 cm ø sample tray. This temperature stayed at the set temperature ±5 °C and an on/off controller was constructed and set to turn off +6 °C from the set point which turns the heat source off until the temperature drops below this value. The ambient temperature of the room was 22 °C at the start of every experiment and the equipment was uncovered, increasing this ambient temperature close to the sample over time.
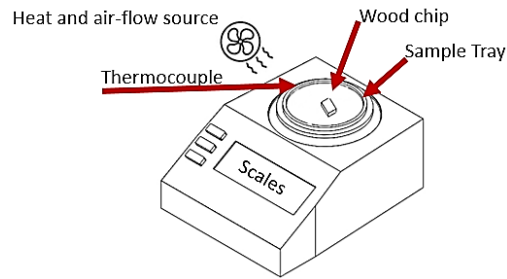
Figure 10 Experimental Setup - Convective

3.1.3 On/Off Heat Gun Controller

An On/Off electrical controller was constructed, seen in Figure 11.

Figure 11 On/Off Controller

Temperature readings from the green thermistor are sent to the controller which plugs into a electrical socket and controls the electrical supply to the extension cord. During the experiments the heat gun is plugged in to the extension cord. Coupled with the temperature settings on the heat gun itself this allowed for tighter control of the temperature.

3.1.4 Experimental Laboratory Convective Drying Conditions

As not all of the settings can be easily altered on the on site drier, to investigate the influence of temperature and air flow rate on convective drying within the laboratory the following experiments were conducted.

Temperature

Laboratory and on-site tests were conducted to evaluate the fidelity of the simulated results. Similar principles were applied to the on-site and the lab tests, with:

1. A heat source of a known temperature and airflow.

2. Mass (and herein the moisture content) of woodchip measured over time.

The laboratory tests of moisture content over time were recorded using a balance connected to a computer so logging the mass in increments of 5 seconds, the parameters during these experiments can be seen in Table 4.

Table 4 Parameters - Variable Temperature

	55 °C	65 °C	75 °C	85 °C
Temperature Heat Source	55 °C	65 °C	75 °C	85 °C
Velocity of Air	1.6 m.s^{-1}	1.6 m.s^{-1}	1.6 m.s^{-1}	1.6 m.s^{-1}
External Temperature	21°C	21°C	21°C	21°C

Air Flow Rate

Although the air flow rate was not variable on the drier bed, laboratory tests for air flow were conducted to investigate the effect of air flow rate on drying rate. For these tests a temperature controller was constructed and set to 65 °C, as at this setpoint the temperature measured by the thermistor fluctuated least and the experiment could be conducted in the time available. The experiments are similar to that used for the temperature experiments with the conditions shown in Table 5.

Table 5 Parameters - Variable Air Flow Rate

	1.6m.s^{-1}	2.3 m.s^{-1}	3 m.s^{-1}
Temperature Heat Source	65°C	65°C	65°C
Velocity of Air	1.6m.s^{-1}	2.3 m.s^{-1}	3 m.s^{-1}
External Temperature	21°C	21°C	21°C

3.2 Laboratory Infrared (IR)

Onsite IR drying is used during daily operation at Bowland Bioenergy for testing the moisture content of woodchip. For the on site drying this method is used to measure moisture content,

within the laboratory this is used to find the dry mass and in a separate set of experiments IR drying is used to record the mass over time of infrared drying at different temperatures.

3.2.1 Laboratory Infrared (IR) Setup

During IR drying mass data over time under set conditions can be logged. Like the convective drying method mass is recorded over time until the mass loss is decreased. IR drying at 105 °C was used to collect the dry mass of the samples for the convective drying samples, woodchip samples collected from the drier and IR drying samples.

The halogen drier had a mass accuracy of ±0.0005 g, and was set to stop when a change of 0.001g per 99 seconds was reached and the total mass was recorded every 10 seconds. The moisture balance was set to rapid heat to the desired temperatures, which resulted in some overshoots in temperature control by a few degrees in the first minute and then remained at the set drying temperature ±1 °C. Though it has a maximum capacity of 50 g, a single woodchip was used on the 100 mm ø pan. The ambient temperature of the room where the experiments were conducted was in the range of 19 °C to 21 °C, though this was found to have no discernible effect on the results of IR drying due to the enclosed chamber of the dryer. The drying temperatures were set to 55,65,75 and 85 °C. The halogen heater had a heat duty of 400W and logged the data via a bi-directional RS-232 cable that was connected to a laptop with appropriate data logging software logging the mass every 5 seconds.

M_t, was recorded after the original session stopped and saved to a file, the first mass recorded in this session was M_0. So as to obtain the equilibrium value (M_e) the balance was kept at the same settings, with the exception that the temperature which was set to 105 °C. The final mass value from this new setting was M_e relating to the previous saved session.

Once M_e was obtained the tested sample was then soaked in deionised water, by using a mesh bag, for 12 hours and drained for 5 minutes to reach the mass $M_0 \pm 0.5$ g after draining. The

drying procedure for the next set temperature was then repeated to obtain M_t and M_e data for each set temperature.

3.2.2 Experimental Laboratory IR Drying Conditions
IR Drying

Laboratory experiments conducted with Infrared woodchip drying were carried out under the conditions outlined in Table 6. Similar to the convective experiments in the laboratory, the same single woodchip soaked over 12hours is used and the mass is measured every 5 seconds. Infrared drying from experience is faster than convective drying and is expected to have a faster rate of mass loss than convective drying. The ambient external temperature was found to have no discernible effect on the results of IR drying due to the enclosed chamber of the dryer, and airflow over the chip was considered as negligible.

Table 6 Parameters – IR Drying

	55 °C	65 °C	75 °C	85 °C
Temperature Heat Source	55 °C	65 °C	75 °C	85 °C

3.3 On Site Drying
In order to integrate the theoretical and simulation perspectives of this work an on site study was conducted to establish an understanding of the existing processing abilities, limitations and variable aspects of existing infrastructure.

3.3.1 On Site Dryer Setup
The setup used on site is altered during production based on experience using the floor speed of the drier, with other settings unaltered. The onsite team change the floor speed from 2 minute intervals to 7 minute intervals based on conditions, for noticeably 'wet' input samples this setting is usually adjusted to a longer interval speed. The sample moisture content is not measured prior to drying and this is based on the experience of the operator.

Bed Depth

The feed hopper of the drier bed has a guillotine style plate, shown as the blue panel in Figure 12, which is adjusted in the vertical direction to allow woodchip to pass through at the height which the plate has been set to. Under normal operation the bed depth is not adjusted and is set to 24.5cm.
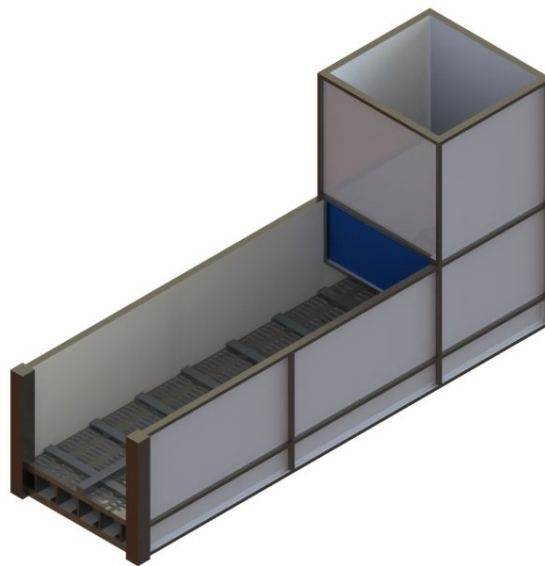
Figure 12 Diagram Illustrating The Panel Which Determines Bed Height- Not to Scale

Floor Speed

The 'Floor' section of the drier which moves is a ladder system over a fixed bed, shown in Figure 13. The blue ladder aspect of Figure 13 moves parallel to the slotted plate cover floor in a forwards and backwards motion at a set interval time. The moving floor moves after the interval time has passed. Once the floor has moved to the far end of the drier, 6m from the opening of the feed hopper, it moves back into the starting position. The interval time between movement is changed using an electronic interface.
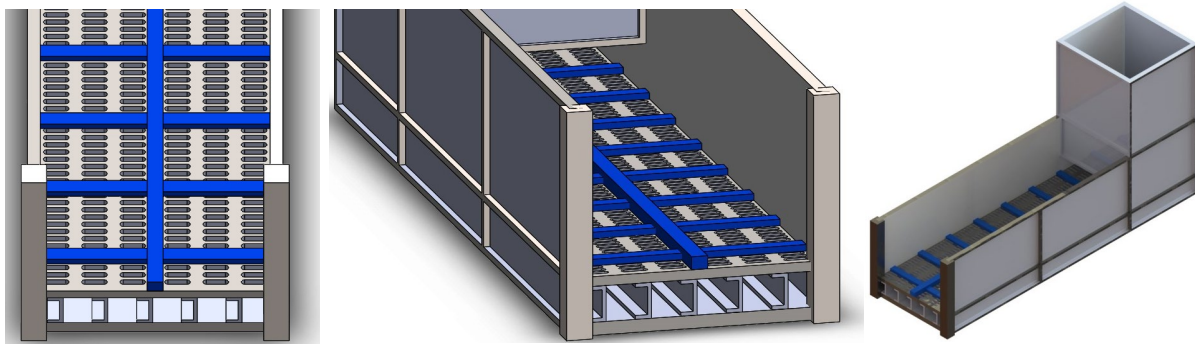
Figure 13 Diagram Illustrating The Moving Ladder Floor- Not to Scale

Covering The Drier

Over the open bed section of the drier the evaporated water is carried away in the airflow from the base, with this airflow heat is also lost and the air may not be fully saturated. To investigate the impact of covering the drier on moisture content the open bed moving floor section of the drier was covered over with felt 2 mm thick on the existing framework. Over the end 3 m the felt was doubled over to cover any holes in the material.

Figure 14 Drier Before and After Covering

Limitations of Current Equipment

Under the current setup the heat exchanger temperature, boiler temperature and the airflow through the drier are not adjusted. These could in future be adapted for adjusting, however for the purpose of this study the impact of varying temperature and air flow will be investigated on a smaller scale with a woodchip.

3.3.2 Sampling

To establish moisture content at different points in time and location samples were taken from four locations (detailed below) and a fifth location when the drier was covered.
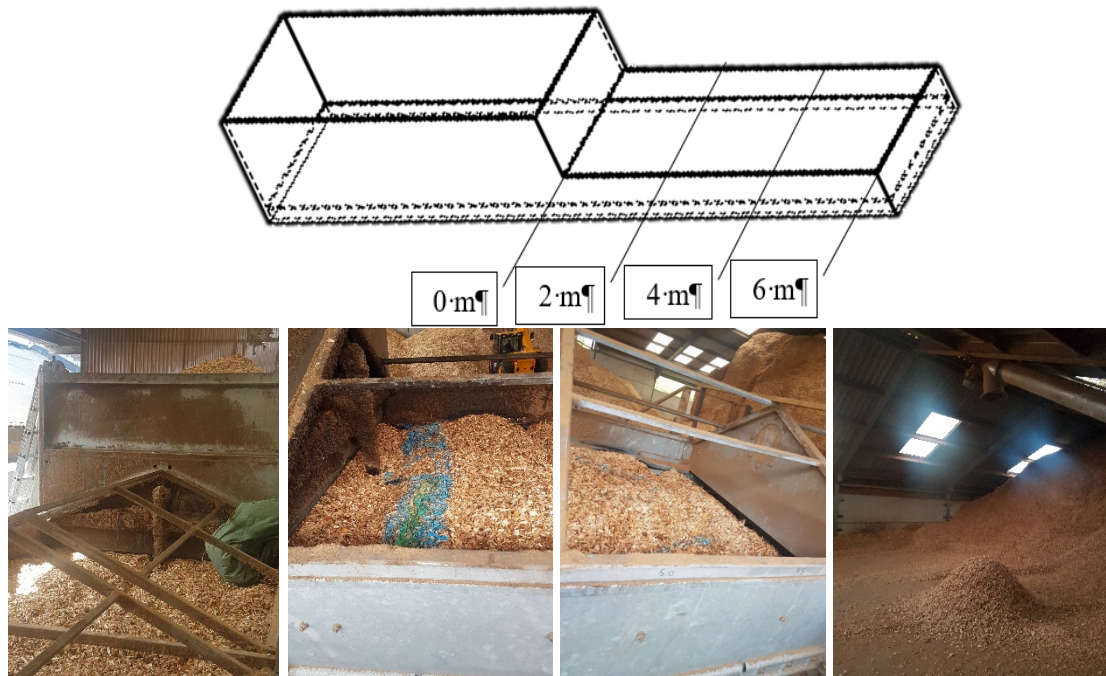
Figure 15 Images of the Drier Bin, Open Drier Bed 0m and 6m points, and the Auger Outlet

The sampling procedure is as follows:

1. Firstly, the initial moisture content was measured from a sample taken from the top of the chip in the feed hopper to the drier.

2. The second sample was taken from the start of the bed (reference point of 0 m, Figure 15) 30 minutes after the first sample, when this sample is taken a painted line along the drier bed shows the location where this sample was taken from.

3. A sample was then taken from the middle of the drier bed when the woodchip chip at the start of the bed (visible by a painted line when the second sample was taken) reaches the 3 m point.

4. A sample was taken when the woodchip reached the end of the bed, the 6 m point.

5. In addition to these samples, a sample was taken for the covered situation at the product pile every hour to monitor the effects of the cover.

The moisture content of the woodchip within each sample was measured 5 times to evaluate repeatability of measurement of woodchip from the same sample.

Additionally, the humidity and temperature were recorded in two places, over the bed and outside the bed to act as an environment reference. Infrared drying, temperature and airflow cannot be practicably altered on the on-site drier, therefore these experiments were carried out in the laboratory. Differing to the on-site tests, samples which were taken in batches from the drier as the chip was difficult to trace as it goes through the drier and moisture content measurements on site requires the dry mass of the chip.

3.3.3 Experimental on Site Drying Conditions

Bed Depth
The variables from Table 7 are used on-site and the samples taken at different points along the bed from behind the reference line. The time at which these samples were taken was recorded and used to compare the simulation to the on-site results.

Table 7 Parameters - Variable Bed Depth

	43cm	34cm	24.5cm
Temperature Air	SET-54°C/51	SET-55°C	SET-53°C
Temperature Boiler	SET-82°C	SET-86°C	SET-82°C
Velocity of Air	SET-0.14 m.s^{-1}	SET-0.14 m.s^{-1}	SET-0.14 m.s^{-1}
Top Floor Interval	5 min	5 min	5 min
Bed Depth	43cm	34cm	24.5cm
Cover	No	No	No
Average External Temperature	15°C	16°C	15°C
X_m0 (WB)	1.256	0.879	0.475
K_evap	0.07	0.07	0.07

Top Floor Speed

The floor speed can be altered from a minimum interval between floor movements of 3 minutes to a maximum of 12 minutes, if the speed was lower than 3 minutes the discharge auger does not synchronise properly causing it to stop. Industrial experience has found that running for longer than 12 minutes results in the woodchip to become very dry, making it more difficult to

blend and to sell, Table 8 describes the conditions set for the experimentation to determine the influence time in the drier has on the moisture content, the time in the open bed of the drier is also shown as this influences the run time of the simulation.

Table 8 Parameters - Variable Top Floor Speed, Interval Time

	5 min	Maximum 12 min	Minimum 3min
Temperature Air	SET-51°C /54	SET-50°C	SET-52°C
Temperature Boiler	SET-86°C	SET-85°C	SET-85°C
Velocity of Air	SET-0.14	SET-0.14	SET-0.14
Top Floor Interval	5 min	Maximum 12 min	Minimum 3min
Bed Depth	24.5cm	24.5cm	24.5cm
Cover	No	No	No
Time in Open Bed*	2 hours	4 hours 48 minutes	1 hour 12 minutes
X_m0 (DB)	0.475	0.782	1.01
Average External Temperature	15°C	13°C	14°C

*Approximate dependent on where the moving floor starts

Covering the Drier

The open area of the drier was covered with felted fabric and the end 3 m of the material was doubled over to cover any holes in the material, the conditions of these two experiments is shown in Table 9. Covering the drier could conserve heat in the system and reduce the dust emitted from the drier. The limitation of this however is that the fabric may let water drip back into the woodchip bed, or allow the water vapour to circulate increasing the humidity and decreasing the rate of drying.

Table 9 Parameters - Covering Drier Bed

	Uncovered	Covered
Temperature Air	SET-53°C	SET-54°C
Temperature Boiler	SET-86°C	SET-87°C
Velocity of Air	SET-0.14 m.s^{-1}	SET-0.14 m.s^{-1}
Top Floor Interval	5 min	5 min
Bed Depth	24.5cm	24.5cm
Cover	No	Yes
Average External Temperature	15°C	18°C

To simulate this would require altering the geometry, removing the airflow over the woodchip bed and adding an upper region which would as a second porous membrane, in this case the properties would need to be altered for properties of felted material.

3.3.4 Relative Humidity

Several data logging humidity sensors were placed on-site at Bowland Bioenergy to measure the external humidity as well as the humidity above the drier bed. Measuring the wet and dry bulb temperature of the surrounding air, the percentage humidity was calculated by the sensory device using the logged data.

Chapter Summary

This Chapter has detailed the experimental methods and procedures that are used to measure the moisture contents and drying rates of both packed woodchip bed (onsite) and singular woodchips (laboratory). Due to limitations of existing equipment, as some parameters currently cannot be altered on site without effecting production, laboratory experiments were conducted. External conditions such as floor speed, bed depth and covering the drier on the onsite dryer, temperature and flowrate for single woodchip laboratory scale tests and IR drying are then altered to determine their effect on the drying rates and moisture contents. These results of these experiments are presented in Chapter 6.

Chapter 4

Parameter Derivation - Experimental Methodology and Results

To simulate the drying of woodchip there are some parameters required beforehand which are set by the environment and process materials. In this section these parameters are determined for a given situation either through experimentation or taken/derived from literature. In addition, other commonly used property values such as density, viscosity, molecular mass and specific heat capacities pre-defined within the CFD software are shown in Table 14 to Table 17.

4.1 Air, Liquid Water and Water Vapour Properties

The properties of air were found through a review of literature, as the properties of air have been widely studied and used within research.

4.1.1 Heat Capacity

The heat capacity of the medium used to dry the woodchip impacts the energy available from the air per unit mass and temperature, for the same temperature and mass the higher the heat capacity the greater the energy available for heating. From (Dietl et al., 1995), which contains the development models of heterogenous diffusion in capillary porous materials considering and not considering heat conduction, the heat capacities used has a small dependency on temperature:

$$c_{p,a} \ (\text{J.kg}^{-1}\text{K}^{-1}) = 1.006\times10^3\times(1+5\times10^{-7}(T_{in}-273.15)^2) \tag{40}$$

$$c_{p,v} \ (\text{J.kg}^{-1}\text{K}^{-1}) = 1.88\times10^3 \ (1+2.2\times10^{-4}(T0-273.15)) \tag{41}$$

$$c_{p,l} \ (\text{J.kg}^{-1}\text{K}^{-1}) = 4.178\times10^3+(9\times10^{-3})(T0-308.15)^2 \tag{42}$$

These equations can also be found in numerous studies including (Bejan et al., 2013).

4.1.2 Thermal Conductivity

Thermal conductivity influences the heat energy conducted over time through a unit cross section of material when there is a temperature gradient, similarly to the heat capacity the thermal conductivity used in the simulation is dependent on the air temperature, for air and water the equations from (Bejan et al., 2013) were used which contains fluid properties for numerical calculations of drying porous media, the conductivity of water used from (Mohindroo, 1997) :

$$k_a(\text{W.m}^{-1}\text{K}^{-1}) = 0.02454\left(\frac{T_{in}}{273.15\text{K}}\right)^{0.83} \tag{43}$$

$$k_v(\text{W.m}^{-1}\text{K}^{-1}) = 0.0182\left(\frac{T0}{273.15}\right)^{0.87+0.001(T0-273.15)} \tag{44}$$

$$k_l(\text{W.m}^{-1}\text{K}^{-1}) = 0.59 \tag{45}$$

4.1.3 Molecular mass

The molecular mass of air and water is determined from the periodic table and typical air composition as 28.95 and 18.05 g.mol-1 respectively for air and water. Molecular mass plays an important role in determining the material properties of moist air, which are derived using the properties of air and water vapour. It is also known that water vapour in the air reduces the total density of the mixture, aiding dispersion of water vapour due to buoyancy.

4.1.4 Viscosity

The viscosity of air, water vapour and liquid water are 1.81×10^{-5}, 1.7×10^{-5} and 1.01×10^{-3} kg.m^{-1}s^{-1}, respectively, from (Kuo, 2018) and (Warhaft, 1997) which cover fundamentals of Environmental Engineering and Thermal-Fluid Engineering.

4.1.5 Density

The density of air used in all simulations is 1.205 kg.m^{-3} and similarly liquid water density is 998.2 kg.m^{-3} from (Ababou, 2019) covering flow through different porous media based on Dary's law.

4.1.6 Latent heat of evaporation

The input energy required to change a liquid, in this instance water, to water vapor at a constant temperature is known as the latent heat of evaporation, given by H$_{evap}$ (Dietl et al., 1995).

$$H_{evap} = 2.51 \times 10^6 - (c_{p,l} - c_{p,v})(T0 - 273.15) \tag{46}$$

4.2 Porous Matrix Properties

The properties of the porous media domain are defined using experimental methods and literature. These properties are dependent on the material and due to the non-uniformity of pores the porous properties vary with samples. Therefore, to determine a sufficiently accurate measure of the properties, several samples were considered giving a representative average.

4.2.1 Heat Capacity

The heat capacity of the porous matrix was taken from literature and is dependent on temperature of the sample. As the water content in the pores changes the overall heat capacity of the domain changes and this heat capacity represents the heat capacity of the porous media dry. Taken from (Mehrabian et al., 2012) where a one dimensional model for the combustion of woody biomass is developed.

$$cp_p = 1500 + T0 \tag{47}$$

4.2.2 Thermal Conductivity

Similar to the heat capacity of the dried porous media, the thermal conductivity is found from literature and is dependent on temperature (Lu, 2006) which also investigates modelling of wood-based biomass combustion.

$$k_p = 0.056 + 2.6 \times 10^{-4} T0 \qquad (48)$$

4.2.3 Permeability

Permeability is a property that defines the ability of a fluid to flow in a porous medium or membrane. Permeability is unique for each saturating fluid, due to interactions between fluids altering fluid flow and therefore the permeability. This was why relative permeability was considered. Relative permeability was with reference to 100% fluid saturation as absolute permeability and 0% as a minimum fluid saturation. The fluid saturation was described as S_i. For this two-phase system, the sum of both the saturation of liquid and vapour in the woodchip was equal to 1. The permeability of multiphase flow within porous media, κ, can be described using the relative permeability of the gas or liquid phase, κ_r, and the intrinsic permeability, κ_i, which is the permeability of the liquid or gas at 100% saturation:

$$\kappa = \kappa_i \kappa_r \qquad (49)$$

In order to describe the relative and intrinsic permeability, properties of both vapour and liquid water was used.

Due to the nature of woodchip drying species movement along the grain was different to that against the grain, which has more resistance, hence a radial and longitudinal equations of liquid and gas permeability were considered. From literature, previously proposed equations for softwoods define the relationship between the liquid saturation S_l and relative permeability of liquid and gas, as given by (Perre and Keey, 2014):

$$\kappa_{rg}^T = 1 + (2S_l - 3)S_l^2 \qquad (50)$$

$$\kappa_{rl}^T = S^3 \qquad (51)$$

$$\kappa_{rg}^L = 1 + (4S_l - 5)S_l^4 \qquad (52)$$

$$\kappa_{rl}^L = S^8 \qquad (53)$$

where, κ^T is the tangential permeability, κ^L is the longitudinal permeability, and the subscript rg is relative for gas and rl is relative for liquid, liquid saturation S_{lq} is described in section 4.3.6. As there is irreducible liquid in the woodchip S_{lq} is the ratio of liquid saturation in the mobile phases:

$$S = \frac{S_l - S_{il}}{1 - S_{il}} \tag{54}$$

For the woodchip bed an average of longitude and radial relative permeability were used, assuming that there was a statistically even distribution of woodchip resulting in a 50:50 split of directional flow through and along the grain.

$$\kappa_{rg} = \frac{(2 + (2S_l - 3)S_l^2 + (4S_l - 5)S_l^4)}{2} \tag{55}$$

$$\kappa_{rl} = \frac{S^3 + S^8}{2} \tag{56}$$

The overall intrinsic permeability was dependent on the distribution of pores. The most common approach to describe the permeability of a material based on porosity was using the Kozeny-Carman equation (Shamey and Zhao, 2014), containing the Kozeny Carman Coefficient k_{Kozeny}, specific surface area per unit volume S_0 and the porosity φ. This equation simplifies the requirement of pore dimensions to the porosity, as exact pore dimensions are difficult to achieve due to the overall volume of chip being much greater than the volume of pores. For a woodchip bed permeability the expected value from this method was of the order of magnitude $\kappa \sim 10^{-8}$ (Alaqqad et al., (2012)) and variations for the Kozeny-Carman coefficient in Table 10 were plotted in Figure 16.

$$\kappa = \frac{1}{k_{Kozeny} S_0^2} \frac{\varphi^3}{(1 - \varphi)^2} \tag{57}$$

Table 10 Formulas for the Kozeny Carman Coefficient

k_{Kozeny}	Porosity Range	#	Reference

5.55	0.4-0.8	1	(Singh, 2007)
$\dfrac{4\varphi^3[1+56(1-\varphi)^3]}{(1-\varphi)^{0.5}}$	0.7-0.994	2	(Singh, 2007)
$\dfrac{3.5\varphi^3[1+57(1-\varphi)^3]}{(1-\varphi)^{0.5}}$	0.6-0.99	3	(Singh, 2007)
$5.0+e^{(14(\varphi-0.8))}$	0.68-0.96	4	(Singh, 2007)
$4.7+e^{(14(\varphi-0.8))}$	0.4-0.99	5	(Singh, 2007)
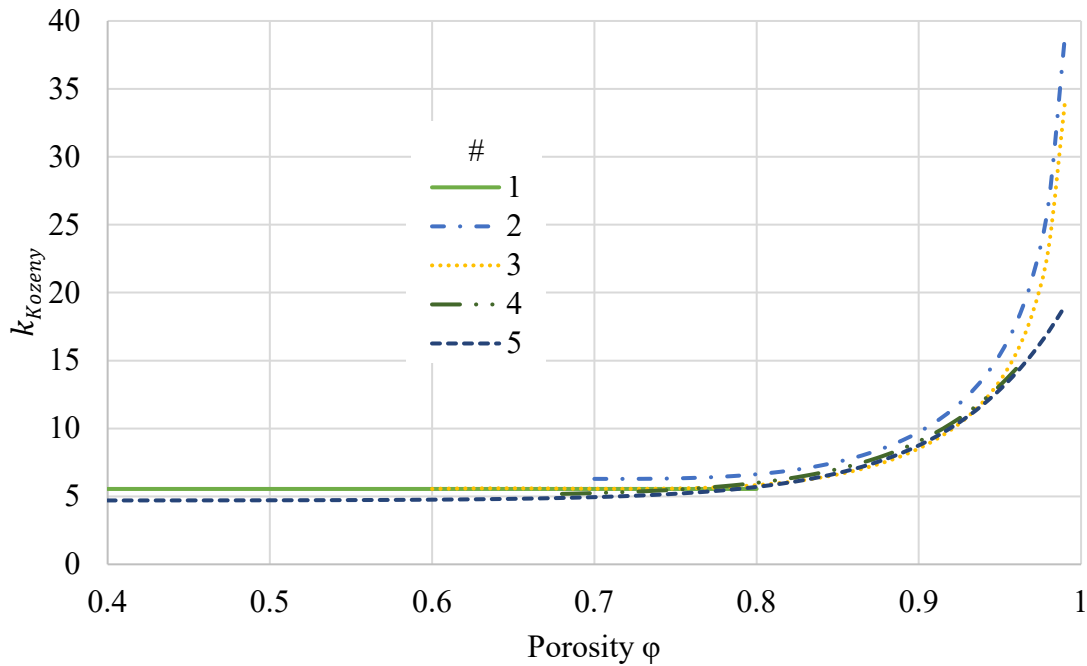
Figure 16 Kozeny constant Plots

As porosity increases above 0.8 the Kozeny constant approaches infinity, below this value the Kozeny constant was relatively fixed, as shown by the 5th and first function in Table 10 on Figure 16. As Equations 1 and 3 from Table 10 are midrange and superimposed in Figure 16 between porosity values of 0.6 and 0.8, for porosity <0.6 the value of 0.55 was to be used and for porosity values ≥0.6 Equation 3 from Table 10 was used.

To calculate the permeability from the Kozeny-Carman equation, the surface area per unit volume of chip, S_0, is required.

Surface Area Per Unit Volume

To determine the surface area of the woodchip a relationship between the thickness, density and specific surface area can be derived (Lunguleasa et al., 2009):

$$M_{woodchip} = V_{woodchip} \rho_{woodchip} = \frac{S_w t_h}{2} \rho_{woodchip} \tag{58}$$

$$S_w = \frac{2M_{woodchip}}{\rho_{woodchip} t_h} \tag{59}$$

Where S_w has the units $\left(\frac{m^2}{M_{woodchip}}\right)$, M is the mass (kg), V the volume (m³), t_h the thickness (m), and ρ the density (kg.m⁻³). For the specific surface area per unit volume:

$$S_0 = \frac{S_w}{v_f} = S_w \rho_{woodchip} = \frac{2M_{woodchip}}{t_h} \tag{60}$$

Where v_f is the specific volume $\left(\frac{m^3}{kg}\right)$. Hence for 1kg of woodchip with an average thickness to the nearest mm of 5mm.

$$S_0 = \frac{2}{5 \times 10^{-3}} = 400 m^{-1}$$

With 5 mm thickness from testing 100 pieces of woodchip from a random sample which provided a mean thickness of 4.81mm.

By comparison for a randomly selected woodchip 19.95 mm ×26.77 mm ×5.30 mm.

$$\frac{SA}{V} =$$

$$\frac{(5.3 \times 10^{-3} \times 26.77 \times 10^{-3}) \times 2 + (19.95 \times 10^{-3} \times 26.77 \times 10^{-3}) \times 2 + (5.3 \times 10^{-3} \times 19.95 \times 10^{-3}) \times 2}{19.95 \times 10^{-3} \times 26.77 \times 10^{-3} \times 5.3 \times 10^{-3}}$$

$$= \frac{1.56 \times 10^{-3}}{2.83 \times 10^{-6}} = 551 m^2 kg^{-1} \tag{61}$$

4.2.4 Porosity

The porosity of the woodchip used at Bowland Bioenergy was also determined using experimental methods. Several methods were proposed to measure porosity, with pros and cons of each discussed below:

- Volumetric- the initial volume of the bulk material is compared to the crushed volume of the material.

- Photographic-The solid external area is compared to the area of the voids.

- Density-The mass of dry material is compared to the mass of a fully wetted material, determining the difference in density. Comparatively the density of the pure solid material can be compared to the bulk material.

- Mercury-The volume of mercury a material can hold is measured.

- Gas Injection-The volume of an inert gas that a material holds at specific pressure is measured.

- Radiative methods- The intensity of Gamma or X-Rays passing through the bulk material can be compared to the intensity of those passing through a pure solid of the same material.

Crushing the chip would prove difficult as wood dust (analysed in Chapter 8) contains pores and this would affect the accuracy of the results. Thus, the material would need to be in highly compressed state, which would deform the ligands inside of wood, altering the density and volume. The photographic method would require rigorous analysis of the surface area of the chip and due to the irregularity of pores, the area of voids would prove difficult to measure. Woodchip as a material has natural pores, meaning a pure solid version of the material cannot be obtained. Mercury adsorption would provide a measurement of porosity, however mercury requires a lot of safety precautions as it is a toxic material with many exposure risks. Gas injection using the apparatus available (used in Chapter 8) would achieve a measurement of

pore volume, however these apparatus require a sample to be contained within a flask that has a thin neck which can only fit small chips. These small chips may have a different porosity to the bulk volume of chips. Radiative methods require expensive equipment and extensive safety precautions in addition to the fact that solid wood is also porous. Therefore, in this research, density is determined by measuring the dry and fully wetted mass of the chip.

Determining Porosity Using Density

The method detailed herein was used for the moving woodchip bed as well as for singular woodchip. Firstly, the woodchip/s were dried at 105 °C until a constant mass was achieved. This mass was recorded, and then the chip/s were soaked in deionised water for 15hours, subsequently wetted mass of the chip was measured and recorded. The woodchip is then soaked for a further two hours and the new mass recorded, until the mass no longer changes. The difference between the dry and the wet mass was the quantity of water which fills the pores of the wood, dividing this by the density of deionised water gives the volume filled by pores. To get the volume of the woodchip a pycnometer was used, weighing this full of water, the chip separately and the pycnometer with the wet woodchip/s and the water. The difference in mass divided by the density of water gives the overall volume of the chip, Table 11 shows the resulting porosity values.

Pore Volume:

$$V_{pores} = \frac{M_{wet-woodchip} - M_{woodchip}}{\rho_{deionised-water}} \tag{62}$$

$$V_{pores} = \frac{0.783 - 0.428g}{0.997g.\,cm^{-3}} = 0.356cm^3$$

The woodchip volume:

$$V_{woodchip} = \frac{M_{pycometer-water} - (M_{pycometer-water-woodchip} - M_{wet-woodchip})}{\rho_{deionised-water}} \tag{63}$$

$$= \frac{141.244\text{g} - (141.216\text{g} - 0.783\text{g})}{0.997\text{g. cm}^{-3}} = 0.813\text{cm}^3$$

$$\varphi = \frac{V_{\text{pores}}}{V_{\text{woodchip}}} = \frac{0.356\text{cm}^3}{0.813\text{cm}^3} = 0.438 \tag{64}$$

Table 11 Porosity Measurements Woodchip

	W_{woodchip}	$W_{\text{wet-woodchip}}$	$W_{\text{pycometer-water-woodchip}}$	$W_{\text{pycometer-water}}$	φ
1	0.09	0.299	141.215	141.257	0.612
2	0.083	0.193	141.227	141.27	0.466
3	0.189	0.497	141.194	141.246	0.561
4	0.167	0.415	141.244	141.281	0.548
5	0.12	0.291	141.254	141.251	0.593
6	0.184	0.407	141.228	141.244	0.527
7	0.241	0.568	141.238	141.233	0.580
8	0.348	0.839	141.25	141.251	0.584
9	0.147	0.386	141.244	141.228	0.645
10	0.428	0.783	141.216	141.244	0.437
			Average		0.556

For the chip bed a similar methodology was employed, where instead using a pycnometer, multiple layers of chip within a cubic box were used. This could then be used to give the effective porosity of the drier bed. The dry mass of the chip was measured, the chip was then soaked and weighed. The wet chip was then placed randomly into the box and shook. Deionised water was then added to a set level and the mass of the water and chip measured, the chip was then removed, and deionised water was added to the same level.

Volume of woodchip:

$$V_{\text{woodchip}} = \frac{W_{\text{box-water}} - (W_{\text{box-woodchip-water}} - W_{\text{woodchip}})}{\rho_{\text{deionised water}}} = \frac{200.997\text{g} - (179.656\text{g} - 48.084\text{g})}{0.997\text{g.cm}^{-3}} =$$

$$69.6\text{cm}^3 \tag{65}$$

Volume of available space:

$$V_{\text{Space Available}} = \frac{W_{\text{box-water}} - W_{\text{box}}}{\rho_{\text{deionised water}}} = \frac{200.997\text{g} - 9.479\text{g}}{0.997\text{g.cm}^{-3}} = 192.09\text{cm}^3 \tag{66}$$

Volume of Free Space:

$$V_{\text{Free Space}} = V_{\text{Space available}} - V_{\text{woodchip}} = 122.46\text{cm}^3 \qquad (67)$$

where H_{set} was the height set, W_{Box} the width and L_{box} length of the box. Within the woodchip bed

$$\varphi_{\text{bed}} = \frac{V_{\text{Free Space}}}{V_{\text{space available}}} = 0.637 \qquad (68)$$

$$\varphi = \frac{V_{\text{pores}} + V_{\text{Free Space}}}{V_{\text{Space Available}}} = (1 - \varphi_{\text{bed}})\varphi_{\text{chip}} + \varphi_{\text{bed}} = 0.839 \qquad (69)$$

4.2.5 Density

To measure the density of a single woodchip, a liquid pycnometer was used (with experimental method detailed in Appendix B). From these measurements the woodchip volume can be determined, as follows:

The woodchip volume V (m³):

$$V_{\text{woodchip}} = \frac{M_{\text{pycometer-water}} - (M_{\text{pycometer-water-woodchip}} - M_{\text{wet-woodchip}})}{\rho_{\text{deionised-water}}} =$$

$$\frac{141.244\text{g} - (141.216\text{g} - 0.783\text{g})}{0.997\text{g.cm}^{-3}} = 0.813\text{cm}^3 \qquad (70)$$

The density of the woodchip ρ (kg.m⁻³):

$$\rho_{\text{woodchip}} = \frac{M_{\text{woodchip}}}{V_{\text{woodchip}}} = \frac{0.428\text{g}}{0.813\text{cm}^3} = 0.526\text{g. cm}^{-3} \qquad (71)$$

The estimated density of the chip includes the pores, to exclude the pore volume:

$$\rho_{\text{woodchip-pores removed}} = \frac{M_{\text{woodchip}}}{V_{\text{woodchip}}(1-\varphi)} = \frac{1.244\text{g}}{4.83\text{cm}^3(1-0.358)} = 0.936\text{g. cm}^{-3} \qquad (72)$$

Where φ is the porosity from Section 4.2.4.

Appendix C, Table 39 shows the resulting density readings for 10 pieces of woodchip using Equations 37 and 38, these results had an average density of woodchip and density of woodchip with pores removed of 0.394±0.05 g.cm^{-3} and 0.894±0.08 g.cm^{-3} respectively. The density of water and air are set to 998.2 kg.m^{-3} and 1.205 kg.m^{-3} respectfully. Note this relationship with porosity and density is not applicable to the bed volume and is for the woodchip itself.

4.2.6 Initial water saturation

Saturation is described as the volume of water per pore volume within the woodchip. The concentration of liquid is dependent on saturation, S_L:

$$c_l = \frac{S_L \varphi \rho_L}{Mn_L} \tag{73}$$

When the pores are completely saturated the liquid concentration becomes $c_{l,sat}$ (mol.m^{-3}):

$$c_{l,sat} = \frac{\varphi \rho_L}{Mn_L} \tag{74}$$

The moisture content on a dry basis is dependent on the concentration of liquid, c_l:

$$X_m = \frac{c_l Mn_L}{(1-\varphi)\rho_p} = \frac{S_L \varphi \rho_L}{(1-\varphi)\rho_p} \tag{75}$$

At complete saturation $S_L = 1$:

$$X_{msat} = \frac{\varphi \rho_L}{(1-\varphi)\rho_p} \tag{76}$$

As the porosity is based off volume of water adsorbed the value of X_m at time zero can be used to calculate the initial liquid saturation of the material S_{L0}:

$$S_{L0} = \frac{X_{m0}(1-\varphi)\rho_p}{\varphi \rho_L} \tag{77}$$

where X_{m0} differs between cases.

4.2.7 Irreducible liquid phase saturation

In the form of S_{il}, the irreducible saturation the liquid that is bound within the woodchip by Van der Waals is described, the irreducible liquid phase is described at different temperatures from a moisture content on a dry basis:

$$S_{il} = \frac{X_{il}(1-\varphi)\rho_p}{\varphi\rho_L} \tag{78}$$

4.3 Additional Properties

4.3.1 Ambient Pressure

The experiments were conducted at atmospheric pressure, hence the pressure used within the simulations is 1atm.

4.3.2 Ambient Temperature

The temperature of the environment surrounding the drier was logged for 14 days at a time, during which the experiments occurred, this was repeated twice. The temperature recorded during experimentation ranged from 14 °C to 20 °C, a large variation that was highly dependent on the local weather conditions.

4.3.3 Inlet Air Temperature

On site at Bowland Bioenergy, the air flow in the drier was heated by a plate style hot water to air heat exchanger. The hot water temperature was controlled by an on/off boiler which burnt woodchip for a heat source, the temperature of the air was measured with a thermocouple and displayed on the heat exchanger; this recorded air temperature was shown for each of the on-site test to the nearest integer (°C). To alter the air temperature in the lab, a heat gun was used with the setup in Figure 17, which shows the laboratory setup for the convective-air drying experiments over a single woodchip.
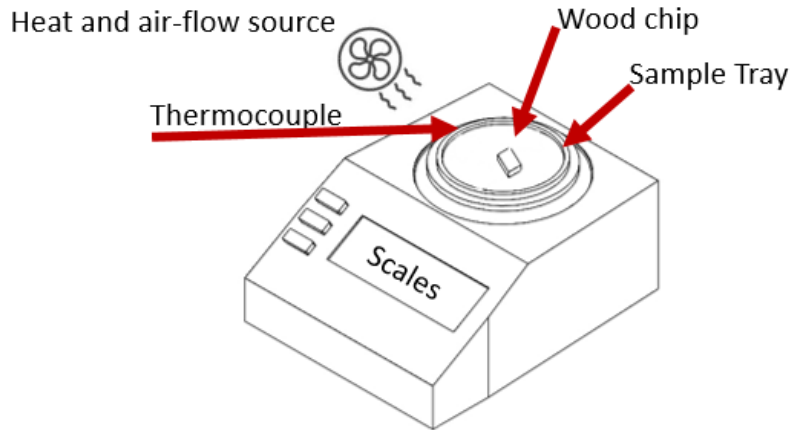
Figure 17 Laboratory Setup of Convective Experiment

4.3.4 Freestream velocity

From specification the maximum flowrate from the heat exchanger is 4 m^3s^{-1}. The area of the covered and uncovered drier sections are 14.2 m^2 and 14.1 m^2, respectively. As the flow covered the entire drier bed, it was assumed that over the area of 28.3 m^2, the volumetric flow was evenly distributed, resulting in an air flowrate through the bed of ~ 0.14 $m.s^{-1}$.

4.3.5 Saturation vapour concentration

The saturation vapour concentration is the concentration within the pores at which the liquid and vapour are at equilibrium at a given temperature. At this vapour concentration the vapour concentration in a closed system cannot increase and in turn the water concentration can't decrease, temperature influences this equilibrium point. The initial saturation vapour concentration cv_{sat0} (Dietl et al., 1995) is defined as:

$$cv_{sat0} = \frac{610.7Pa \times 10^{\frac{7.5(T0-273.15K)}{T0-35.85K}}}{R_{const}T0} \tag{79}$$

4.3.6 Liquid Saturation

Gas saturation is the volume of gas per volume of pores, in this case the gas is moist air, at any point the pores are full of liquid, moist air or a mixture of the two meaning:

$$S_{ma} = 1 - S_L \tag{80}$$

If these values reach more than one or less than zero an error will occur in the simulation as more than 100% and less than 0% saturation is not possible, hence the built in "eps" constant is utilised for this reason which is the smallest real number in COMSOL above zero.

$$S_{ma} = \max(1 - S_L, eps) \tag{81}$$

$$S_L = \min\left(\left(\frac{c_L Mn_L}{\varphi \rho_L}\right), 1 - eps\right) \tag{82}$$

Liquid saturation is the mass of water per mass of porous media, shown in Equation 82 this value is inclusively between 1 and 0.

4.3.7 Vapour saturation pressure

The saturation pressure influences the point at which the equilibrium moisture content is reached, this is because this defines the maximum pressure that is excreted by water vapour at a given temperature, the higher the saturation pressure the greater the force driving diffusive transport. Initially:

$$P_{sat} = 610.7 Pa \times 10^{\frac{7.5(T0 - 273.15K)}{T0 - 35.85K}} \tag{83}$$

4.3.8 Air-vapour diffusivity

Applying Fick's Law, the diffusivity relates to the diffusive mass flux $J_i (kg.m^2.s^{-1})$:

$$J_i = -D_i \nabla c_i \tag{84}$$

where D_i ($m^2.s^{-1}$) is a diffusion coefficient and c_i is the concentration ($kg.m^{-3}$). Equation 84 can be changed to be pressure dependent, if necessary.

The diffusion coefficient D_i through a porous medium is altered slightly to the effective diffusivity D_i^* ($m^2.s^{-1}$), which has a dependency on the porosity φ and saturation S_i (Ho and Webb, 2006). Where the subscript, p, denotes the porous zone.

$$D_p^* = \varphi^{\frac{4}{3}} S_g^{\frac{10}{3}} D_p \tag{85}$$

As both liquid water and water vapour diffuse through the porous medium (Ho and Webb, 2006), this term was split into the diffusion of vapour (vd) and liquid (Ld):

$$D_p^* = \varphi^{\frac{4}{3}} \left(S_g^{\frac{10}{3}} D_{va} + S_L^{\frac{10}{3}} D_L / K_H \right) = D_{vd} + D_{Ld} \tag{86}$$

$$D_{vd} = \varphi^{\frac{4}{3}} \left(S_g^{\frac{10}{3}} D_{va} \right) \qquad D_{Ld} = \varphi^{\frac{4}{3}} \left(S_L^{\frac{10}{3}} D_L / K_H \right) \tag{87}$$

Where K_H is Henry's Constant, D_{va} ($m^2 s^{-1}$) is the vapour air diffusivity and D_L ($m^2 s^{-1}$) is the liquid diffusivity. As the coefficients in this form for liquid diffusion through wood are difficult to obtain, an alternative equation for D_{Ld} is used which describes capillary diffusion D_{cap} (Kurjatko and KC:dela, 1998);

$$D_{Ld} = D_{cap} = 7 \times 10^{-6} e^{-\frac{38500 - 29000 X_{mwb}}{R_{const} T0}} \tag{88}$$

The vapour also diffuses in the air both in and out of the woodchip cells by Fick's law with a defined diffusion coefficient as shown in Table 21. In addition to diffusion, there is also movement of vapour by convection through the porous medium. This movement of vapour has a velocity field as defined in Table 20.

4.3.9 Evaporation rate Constant

The moles evaporated over time (m_{evap}($mol.m^{-3}s^{-1}$)) is based on the water activity (a_w) within the porous medium, the evaporation rate constant k_{evap}, the vapour saturation ($c_{v,sat}$ ($mol.m^{-3}$)) and the concentration of vapour present (c_v ($mol.m^{-3}$)), and is given by:

$$m_{evap} = k_{evap} \left(a_w \times c_{v,sat} - c_v \right) \tag{89}$$

Where

$$a_w = e^{\left(-\frac{0.0267}{X_m^{1.656}}\right)} (p_{sat})^{0.0107 \, e^{(-1.287 \, X_m)}\left(X_m^{1.513}\right)} \tag{90}$$

$$c_{v,sat} = \frac{610.7 \text{Pa} \times 10^{\frac{7.5(T0-273.15K)}{T0-35.85K}}}{R_{const}T0} \tag{91}$$

With the saturation pressure of water (p_{sat}(Pa)), the moisture content on a dry basis X_m (%), and the initial temperature T_0 (K), this can be expressed in terms of relative humidity RH (%):

$$RH = \frac{cv}{cv_{sat}} \tag{92}$$

$$\frac{m_{evap}}{c_{v,sat}} = k_{evap}(a_w \times 1 - RH) \tag{93}$$

$$m_{evap} = c_{v,sat}k_{evap}(a_w \times 1 - RH) \tag{94}$$

The concentration of vapour refers to the concentration within the pores and therefore using humidity from the top of the chip will not effectively show this concentration and the effect of the evaporated water on the surrounding environment is minimal due to the small mass evaporated. Assuming the concentration of vapour in the pores is zero which it initially is within the simulation, and that for the water activity is effectively 1, an initial guess of the value for k_{evap} can be established using Equation 95.

$$m_{evap} = k_{evap}c_{v,sat} \tag{95}$$

Many models exist for establishing moisture ratio as a function of time, MR(t), differentiating moisture ratio with respect to time and multiplying by $M_0 - M_e$ (which is the initial mass of water within the woodchip) to find $m_{evap}VMn_L$ as the units of m_{evap} are mol.m^{3}s^{-1}. An example of such equation is Equation 98, which can be fitted to experimental data and a plot of m_{evap} found shown in Figure 18 and Figure 19.

$$MR = \alpha e^{-\beta t} + (1-\alpha)e^{-\beta \gamma t} \tag{96}$$

$$\frac{dMR}{dt} = -\beta\alpha e^{-\beta t} - \beta\gamma(1-\alpha)e^{-\beta\gamma t} \tag{97}$$

$$m_{evap}VMn_L = \frac{dMR}{dt}(M_0 - M_e) \tag{98}$$

where β, α, γ are coefficients which depend on temperature, Mn_L is the molecular mass of water ($g.mol^{-1}$).

Many variations of Equation 96 exist. As part of this work these were fitted to the convective drying data of a single chip and a 10g sample of woodchip (Pryce et al., 2020), for different temperatures of convective and IR drying. The volume of the single woodchip used in these experiments was approximately measured as 6.13 mm×29.87 mm×25.61 mm, for a volume of $4.69\times10^{-6}\,m^3$.
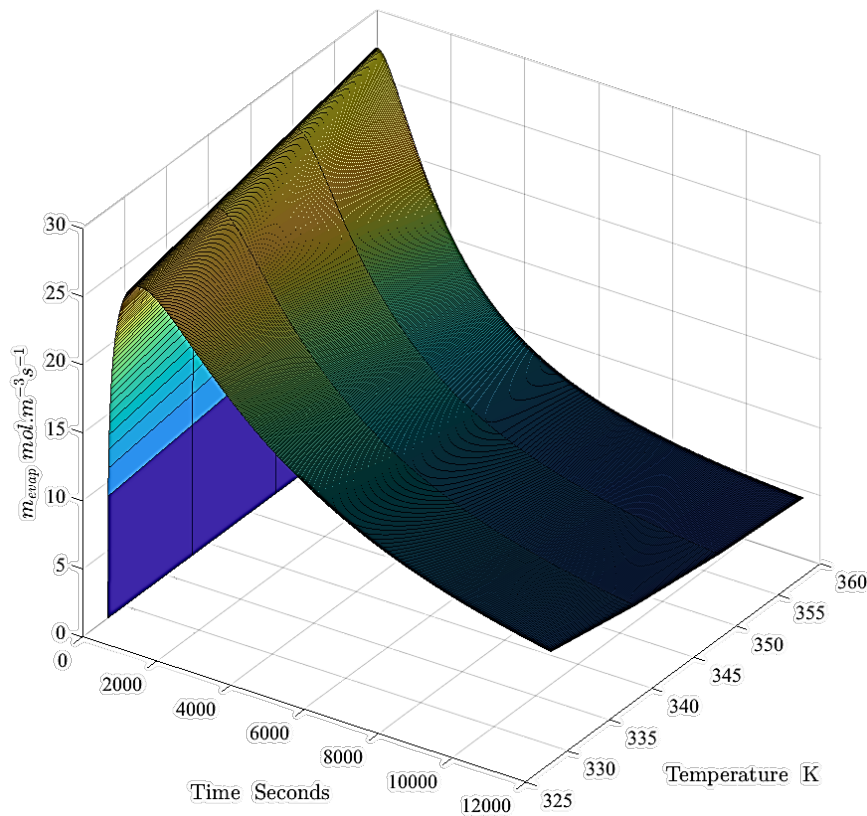
Figure 18 m_{evap} vs Temperature for Convective Drying
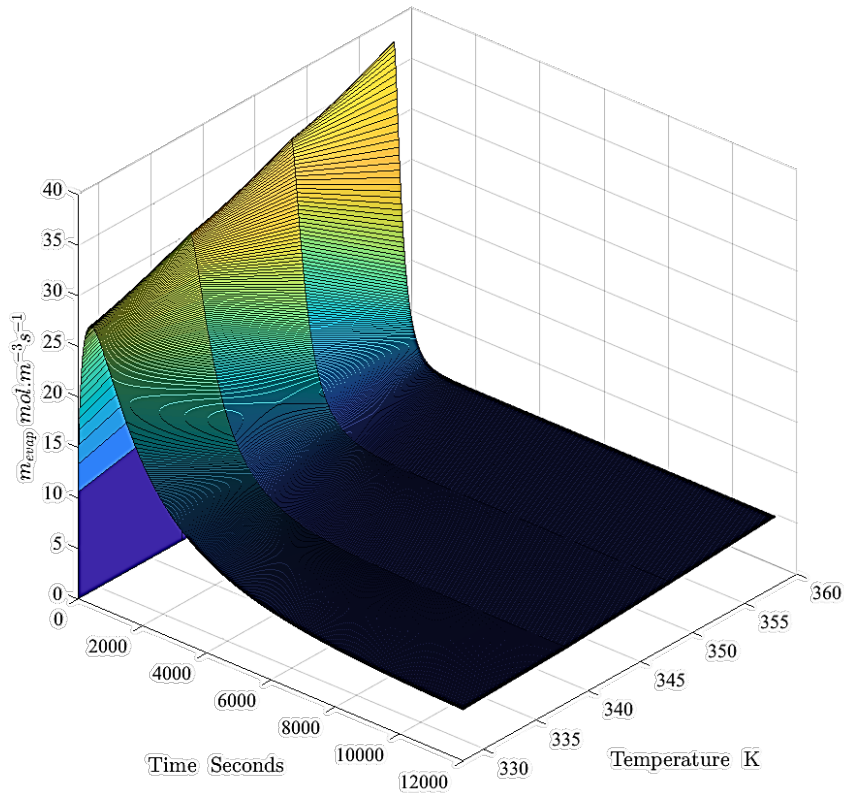
Figure 19 m_{evap} vs Temperature for IR drying

This assumption provided an initial guess for the model. 8.5s^{-1} and 11 s^{-1} was used as initial guess values for the drying rate constant for the convective drying laboratory model and for the IR drying model respectively. For the on-site drying tests, an initial value of 0.1 s^{-1} was used.
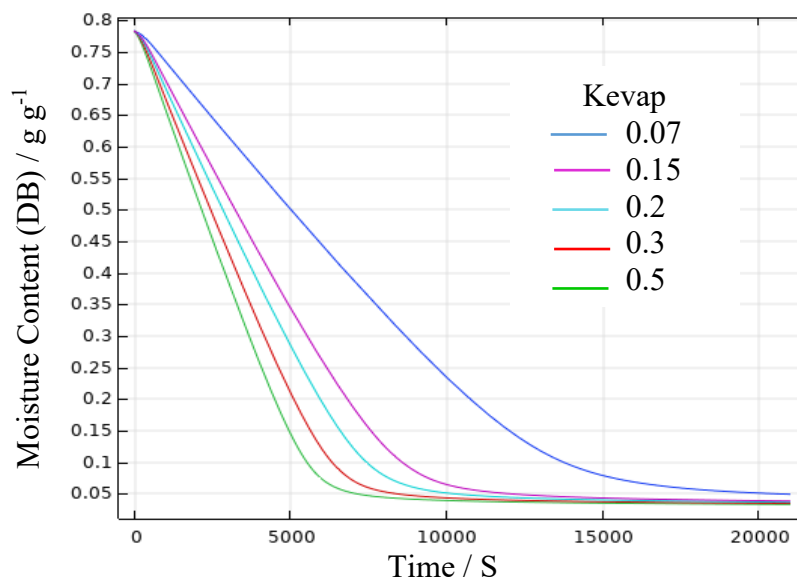
Figure 20 Impact of k_{evap} on Drying

The impact of k_{evap}, shown by Figure 20, is substantial on increasing and decreasing steepness of the drying kinetics curve.

As the diffusive and capillary transport of water vapour and liquid are material dependent k_{evap} was further altered in the simulation to reflect the porous media used. The initial rate is dependent on k_{evap} capillary diffusivity, D_{cap} and air-vapour diffusivity D_{vd}. The ratio of the two is altered by changing the coefficients in D_{cap} and the overall value is increased by increasing k_{evap}.

4.3.10 Initial moisture content on dry basis

The moisture content of the woodchip was measured on a wet basis using am A&D ML-50 apparatus (Appendix B). The samples taken from the drier bed had a moisture content that ranged from 51.9 %DB to 31.4 %DB, whereas the majority of the samples dried in the lab had a starting moisture content of 56 %DB to 58 %DB for the same single chip used. For the simulations, the initial moisture content value was set on a case-by-case basis and was reported before each simulation. An average value of moisture content from the start of the open drier bed was given in each case.

4.3.11 Irreducible moisture content dry basis

From preliminary experimental data, for a single chip dried until equilibrium moisture content (a steady mass was reached at 300 minutes) the moisture ratio MR is 0.05 for results at 45, 55, 65, 75 and 85 °C:

$$MR = 0.05\%$$

$$X_{il} = 0.07\%(DB)$$

4.4 Dimensions

The dimensions of the on site drier and the single woodchip used in experiments was measured and are detailed in the following sub sections:

4.4.1 Woodchip Bed Dimensions

The drier has set dimensions in length and width as shown by the dashed line in Figure 21, which shows a schematic layout of the drier at Bowland Bioenergy. The bed depth can be altered. The external open bed dimensions and the bed depths used in the simulations (Chapters 5 and 6) were measured with an accuracy of ± 1cm.
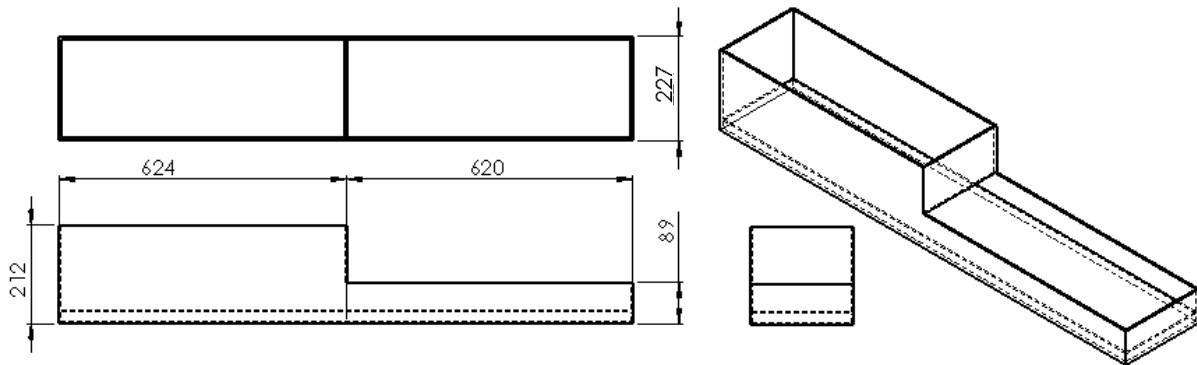
Figure 21 Drier Dimensions (cm)

4.4.2 Drier Bed Woodchip Size Distribution

To evaluate the distribution of chip size, five samples of the chipped product produced at Bowland Bioenergy were randomly selected. These samples were passed through 7 sieves in series by a tap sieve which moves in a circular motion, and vertical motion is generated by impulses. The vertical motion allowed for smaller particles to change their orientation. The sieves used had circular holes sized 100, 63, 45, 31.5, 16, 8 and 3.15 mm.

Woodchip size standards BSI 17225-1 (Institute, 2014b) and BSI 17225– 4 (Institute, 2014a) outline the suitable percentage mass of woodchip above the size 150mm, between 31.5mm and 16mm, 16mm and 3.15mm and less than 31.5mm. In each of these categories, the percentage mass for each sample is calculated by accumulating the masses within the relative sized sieves as shown in Table 12.

Table 12 Size Distribution Woodchip

Size	Sample 1	Sample 2	Sample 3	Sample 4	Sample 5
150mm ≤	100%	100%	100%	100%	100%
31.5mm ≤	4%	1%	1%	4%	4%
16 mm ≤ - < 31.5mm	29%	16%	14%	8%	24%
3.15mm ≤ - <16 mm	67%	80%	79%	87%	69%
< 3.15mm	2%	3%	6%	1%	3%

In Table 12, it is shown that the majority of woodchip is within the rage of 3.15 mm - 16 mm along the smallest length.

4.2.3 Single Woodchip Dimensions

The chip used in the single chip experiment had measured dimensions of 6.13 mm $\times$29.87 mm $\times$25.61 mm. The temperature of the air was measured 4 cm from the outlet of the heat gun and 5 cm from the centre of the 10 cm ø sample tray.

Chapter Summary

This chapter covered the derivation of input parameters required for the simulation further described for the different scenarios in Table 15 to Table 18, through experimentation and the literature survey. Literature review was used to derive the liquid water, water vapour and air properties, whilst a combination of experimental and literature review was used to find the properties of the woodchip. Experimental methods, for instance by use of a pycnometer, have been used to determine the woodchip densities and size, as well as predict the packed bed density for the onsite drier at Bowland Bio Energy. The calculated densities in Table 39 are comparable with those given in literature. Similarly, all other calculated variables given in this section were found to be in good agreement with literature sources.

Chapter 5

Simulation Setup

This chapter covers the simulation setup within ANSYS Fluent and COMSOL Multiphysics, describing in depth the setup required and explaining the equations used.

5.1 Air flow simulation by ANSYS Fluent

A 2D model for airflow through the entire drier was simulated in the commercially available CFD software ANSYS Fluent 19.3. The model is representative of the entire drier domain, as shown in Figure 22, which detailed the various zones and boundary conditions of the simulation. The simulation was used to assess the airflow in the drier and through the porous 'woodchip' zone. No evaporation was considered. The details of the simulation are given in Table 13 and cover modelling methods, the boundary conditions, which relate to Figure 22 and the simulation setup.
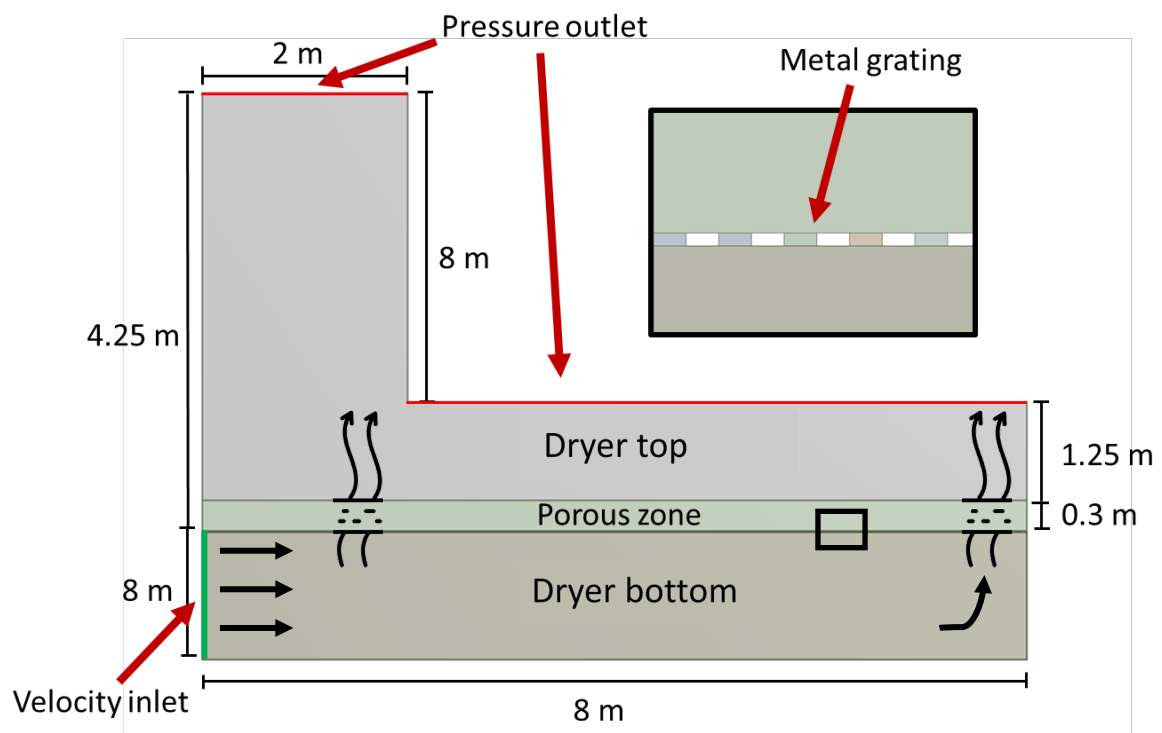
Figure 22 Computational Domain of Drier (2 Dimensional)

The computational domain shown in Figure 22 consists of the dryer bottom, porous 'woodchip' zone, the dryer top and a metal grating. The holes in the metal grating are reminiscent of the physical model and allow air flow through the gaps to the woodchip. The top faces of the 2D domain are set to allow the air-flow to escape and are described as pressure outlets at atmospheric pressure (101325 Pa), or 0 Pa differential gauge as prescribed in Table 13. The domain extents are given in metres in Figure 22. The domain was meshed using ANSYS built-in meshing, using hexahedral elements with a minimum of 10 cells across a gap (i.e across the metal grating).

Table 13 ANSYS FLUENT Solver Settings and Boundary Conditions

Simulation Details		Boundary conditions	
Software	ANSYS Fluent 19.3	Velocity inlet	1 m.s^{-1}
Turbulence model	Laminar	Porous zone:	
Multi-phase model	Eulerian 3 - phases	Porosity	0.319
Fluid	Air and Water	Permeability	
Solution methods	PV coupled	Pressure outlet	0 Pa
State	Unsteady		
Time step Temporal discretisation	0.5 seconds 2nd Order accurate	Walls	No slip
Spatial Discretisation	2nd Order accurate		

A laminar flow model was used to simplify the problem. The PV (Pressure velocity) coupled scheme was employed due to low speed flow (Mach<< 1) and the higher solution accuracy and simulation robustness obtained when using the coupled method, as reported in ANSYS Fluent User Guide (Ansys-Inc., 2015). In the coupled method, the software uses coupled equations to solve pressure and velocity simultaneously. Water was 'patched' into the simulation model in the woodchip zone, with a volume fraction of 0.4. Air was pumped into the domain, as in the physical drier at the bottom of the bed, through the velocity inlet, with an approximate air speed of 1 m/s. The simulation can then be used to analyse how the airflow reacts through the woodchip bed drier.

The time step size was set to 0.5 seconds, with 30 iterations per time step, thereby ensuring a reduction in the residuals (a measure of convergence) of at least 3 orders of magnitude. A mesh/time dependence study was not conducted due to high computational cost of running the simulation. Numerical validation was solely based on residual reduction and checking mass conservation of the simulation.

5.2 2D Model by COMSOL Multiphysics

5.2.1 Environmental Set-up

The simulation was based on 2D coordinates. To run the simulation, several physics-based modules are selected, these include: laminar flow, transport of dilute species, and heat transfer. Both Stationary and Time Dependent simulations were considered, as the heat was transferred and there are phase changes over time.

5.2.2 Laminar Flow

With a Reynolds number less than 2000 (Widden, 1996), the flow is said to be Laminar. The Laminar Flow interface within COMSOL allows for velocity and pressure fields to be calculated for single-phase fluid flow in the laminar regime. This interface supports incompressible, compressible and non-Newtonian fluid flow. This interface solves the Navier-Stokes (Temam, R et al, 1995) conservation of momentum and conservation of mass equations, these equations are the base of fluid flow modelling, solving them for specific boundary conditions and geometry.

Navier-Stokes Equation

The Navier-Stokes equation describes the behavioural flow of fluids, in the case of compressible fluids:

$$\rho \left(\frac{\partial \vec{V}}{\partial t} + \vec{V}.\nabla \vec{V} \right) = -\nabla P + \vec{F} + \mu \nabla^2 \vec{V} \qquad (99)$$

For incompressible fluids:

$$\rho \frac{(\partial \vec{V})}{\partial t} = -\nabla P + \vec{F} + \mu \nabla^2 \vec{V} \tag{100}$$

Where ρ is density (kg.m^{-3}), P is pressure (Pa), t is time (s), $\vec{V}$ is the directional velocity vector (m.s^{-1}), $\vec{F}$ is the vector of the external forces acting on the fluid (N), μ the viscosity (Pa.s) and ∇ is the directional vector differential operator. This equation is valid for cases where the mean free path of a molecule is less than a tenth of the overall scale length described by the Knudsen number, due to the scale of the domains these equations are valid for this case.

Conservation of Mass

Mass, momentum nor energy can be created or destroyed, instead it is conserved and, in some cases, converted into other forms. Within the system any mass is either conserved or can exit the system into the larger system which it is contained within through a 'sink' and enter a system through a 'source'.

$$\frac{\partial \rho_{wv}}{\partial t} + \nabla \cdot (-D_{mixture} \nabla c_{wv}) + u_{mixture} \rho_{cw} = 0 \tag{101}$$

$$\frac{\partial \rho_a}{\partial t} + \nabla \cdot (-D_{mixture} \nabla c_a) + u_{mixture} \rho_a = 0 \tag{102}$$

Where ρ is density(kg.m^{-3}), $D_{mixture}$ is a diffusion coefficient (m^2.s^{-1}), c is the concentration (mol.m^{-3}), $u_{mixture}$ is the velocity field (m.s^{-1}), the subscript wv denotes water vapour and a denotes air.

Conservation of Momentum

$$\rho_{mixture} \frac{\partial u_{mixture}}{\partial t} + \rho_{mixture} (u_{mixture} \cdot \nabla) u_{mixture} = -\nabla p + \mu \nabla^2 u_{mixture} \tag{103}$$

$$\frac{\partial \rho_{mixture}}{\partial t} + \nabla \cdot (\rho_{mixture} u_{mixture}) = 0 \tag{104}$$

5.2.3 Transport of Diluted Species

Within the 'Chemical Species Transport' options, the transport of diluted species was selected. This feature contains the terms required to model the mass transport of a species within multiple species systems, in this case a multiphase system of solid, liquid and gas based upon species concentration. This also applies to mixtures and solutions, for cases where there was a concentration gradient between the species transported and the carrier species. This selection allows convective fluid flow and Fick's law to be applied for diffusion. In this case, the water vapour will be the species transported through the solid medium.

5.2.4 Heat Transfer in Fluids

The heat transfer in fluids interfaces within COMSOL include transfer by conduction, convection and radiation. For this simulation, heat is transferred diffusively though conduction. Like the equations for mass and momentum, energy cannot be created or destroyed so the conservation of energy equation is applicable for heat transfer as heat is converted into energy to cause phase changes as the liquid water is converted into vapour.

Fourier's law defines diffusive heat flux ($q_{diffusion}$), for this a temperature gradient is the driving force:

$$q_{diffusion} = -k_{mixture}\nabla T \tag{105}$$

In addition to this, there is existing energy from each component in the system:

$$q_{system} = \textstyle\sum_i c_{p,i} J_i T \tag{106}$$

Conservation of Energy:

$$\left[c_{p,a}(\rho_a u_{mixture} - D_{mixture}\nabla c_a) + c_{p,v}(\rho_{wv}u_{mixture} - D_{mixture}\nabla c_{wv})\right].\nabla T$$

$$+(\rho_a c_{p,a}\rho_{wv}c_{p,wv})\frac{\partial T}{\partial t} += \nabla.(k_{effective}\nabla T) \tag{107}$$

$$k_{effective} = \frac{\rho_a k_a + \rho_{wv} k_{wv}}{\rho_a + \rho_v} \qquad (108)$$

5.2.5 Geometry Development Single Woodchip Model

Two different geometries were considered for the COMSOL based flow and heat analyses, 1. Flow over a single chip (Figure 23) and 2. Flow through a porous woodchip bed (Figure 24). For the case of a single chip, the geometry differs slightly to the drier bed, in both cases the woodchip and woodchip layers were modelled as a rectangular shape. In both cases, this was surrounded by a larger rectangular domain, which provided boundaries for the walls, heat sources and heat sinks as well as acting as the surrounding environment.

In the single chip model 'Rectangle 1 (r1)' was the air surrounding the porous media zone. For a single woodchip, r1 has the same width as the diameter of the sample tray and height of the heat gun outlet.

'Rectangle 2 (r2)' was the porous media zone representing the chip or the bed of woodchip. r2 has the width and diameter of the test chip for the woodchip and for the drier bed height represents the bed depth and the width was 0.03 m less than the drier bed.

To prevent discontinuities at the sharp edges, a 'Fillet 1 (fil1)' was added to the geometry. This was implemented onto the top two corners of r2. The radius of 2×10^{-3} m for the single chip case was used.

These geometries were merged into a single geometry through 'Form Union (fin)', making any geometry that overlaps into a single object with differing physical properties. This occurs due to a Boolean union of the two geometries.
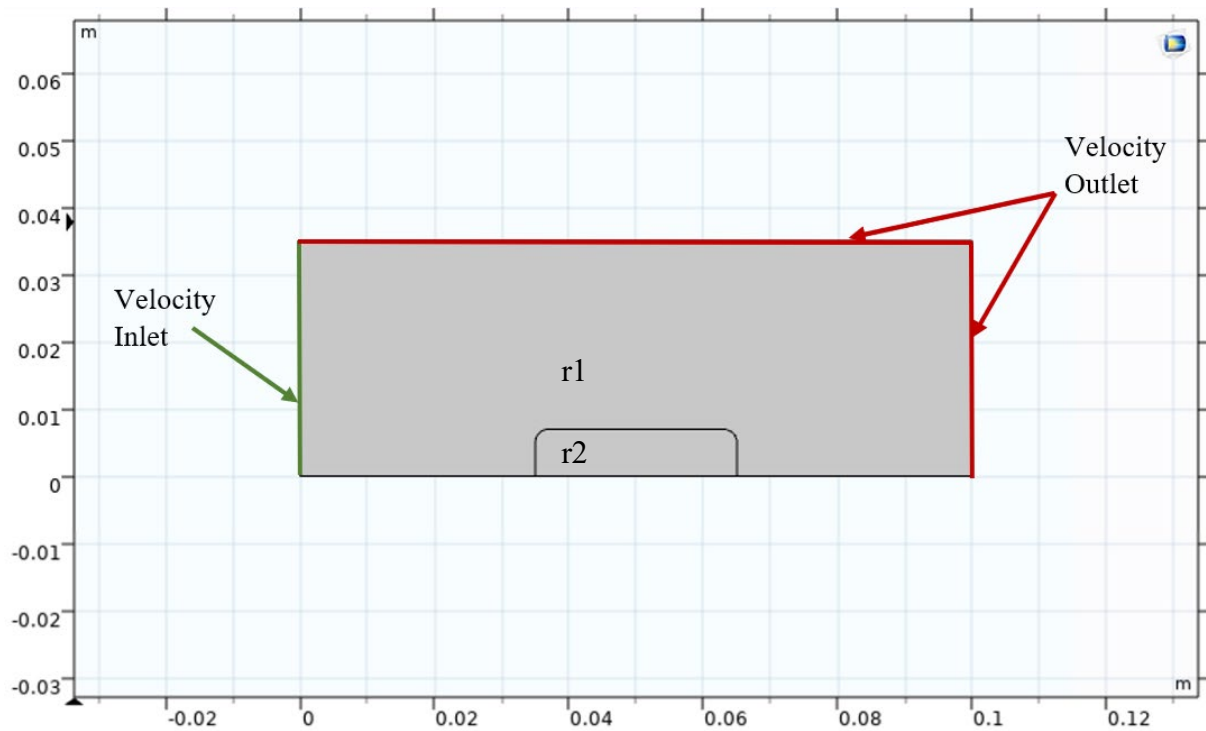
Figure 23 COMSOL Geometry for a Single Woodchip

5.2.6 Geometry Development Woodchip Bed Model

The woodchip bed model differed slightly, 'Rectangle 1 (r1)' was the air within the drier surrounding the porous media zone, with the width of r1 equal to the width of the drier and the height of the drier walls.

'Rectangle 2 (r2)' was the porous media zone representing the chip or the bed of woodchip. The height of r2 represents the bed depth and the width was 0.03 m less than the measured width of the drier bed.

'Rectangle 3 (r3)' in the case of the drier bed represents the natural airflow over the drier.

To prevent discontinuities at the sharp edges, a 'Fillet 1 (fil1)' was added to the geometry. For the case of the woodchip bed this affects all four corners of r2 and for the single chip, it affects the top two corners. The radius of 2×10^{-2} m for the bed and 2×10^{-3} m for the single chip case were allocated.
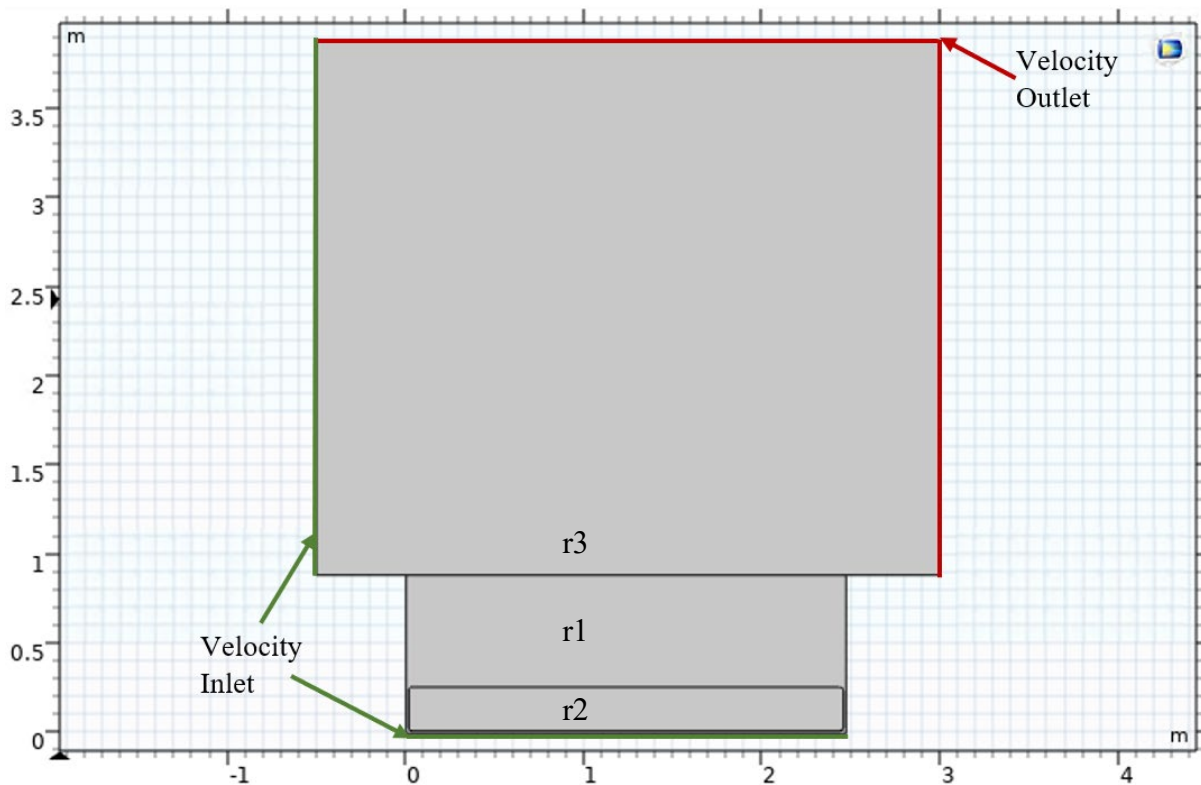
Figure 24 COMSOL Geometry for the Bed of Woodchip

5.3 COMSOL Material Property Specification

There are four materials in the system, air, liquid water, water vapour and the porous matrix which represents the woodchip or woodchip bed. Air and water vapour are combined producing moist air in a binary mixture.

5.3.1 Input Parameters Single Woodchip Model

The four materials necessitate that various properties to be defined, either as fixed values or determined through equation models. In the following tables, these properties are outlined. Some are fixed by the physical system in place pre-defined by the environment and materials, these values are constant throughout the simulation and are defined by the initial conditions. Table 14 to Table 21 are defined under the 'Global Definitions' tab. In the case of a single woodchip, Table 14 to Table 21 are applied, to consider the drier bed the changes in Table 22 are applied.

<p align="center">Table 14 Air Properties</p>

Nomenclature		Value	Unit	Description	Ref
COMSOL	Equations				
cp_a	$c_{p,a}$	$1.006\times10^3\times(1+5\times10^{-7}(T_{in}-273.15)^2)$	$J.kg^{-1}K^{-1}$	Heat Capacity at 293.15K and 1 atm	(Dietl et al., 1995)
k_a	k_a	$0.02454\left(\frac{T_{in}}{273.15K}\right)^{0.83}$	$W.m^{-1}K^{-1}$	Thermal Conductivity at 293.15K and 1 atm	(Bejan et al., 2013)
Mn_a	Mn_a	0.028	$kg.mol^{-1}$	Molecular mass of Air	
mu_a	μ_a	1.81×10^{-5}	$kg.m^{-1}s^{-1}$	Air viscosity at 293.15K and 1 atm	(Kuo, 2018)
rho_a	ρ_a	1.205	$kg.m^{-3}$	Air density at 293.15K and 1 atm	(Ababou, 2019)

<p align="center">Table 15 Liquid Water Properties</p>

Nomenclature		Value	Unit	Description	Ref
COMSOL	Equations				
cp_l	$c_{p,l}$	$4.178\times10^3+(9\times10^{-3})(T0-308.15)^2$	$J.kg^{-1}K^{-1}$	Heat Capacity	(Dietl et al., 1995)
k_l	k_l	0.59	$W.m^{-1}K^{-1}$	Thermal Conductivity	(Mohindroo, 1997)
Mn_l	Mn_l	0.018	$kg.mol^{-1}$	Molecular Mass	
mu_l	μ_l	1.01×10^{-3}	$kg.m^{-1}s^{-1}$	Viscosity	(Kuo, 2018)
rho_l	ρ_l	998.2	$kg.m^{-3}$	Density	(Ababou, 2019)

<p align="center">Table 16 Water Vapour Properties</p>

Nomenclature		Value	Unit	Description	Ref
COMSOL	Equations				
cp_v	$c_{p,v}$	$1.88\times10^3(1+2.2\times10^{-4}(T0-273.15))$	$J.kg^{-1}K^{-1}$	Heat Capacity	(Dietl et al., 1995)
k_v	k_v	$0.0182\left(\frac{T0}{273.15}\right)^{0.87+0.001(T0-273.15)}$	$W.m^{-1}K^{-1}$	Thermal Conductivity	(Bejan et al., 2013)
mu_v	μ_v	1.7×10^{-5}	$kg.m^{-1}s^{-1}$	Viscosity	(Warhaft, 1997)
H_evap	H_{evap}	$2.51\times10^6-(c_{p,l}-c_{p,v})(T0-273.15)$	$J.kg^{-1}$	Latent heat of evaporation	(Dietl et al., 1995)

<p style="text-align:center">Table 17 Porous Matrix Properties</p>

Nomenclature		Value	Unit	Description	Ref
COMSOL	Equations				
cp_p	cp_p	1500+T0	$J.kg^{-1}K^{-1}$	Heat Capacity	(Mehrabian et al., 2012)
k_p	k_p	$0.056+2.6\times10^{-4}$T0	$W.m^{-1}K^{-1}$	Thermal Conductivity	(Lu, 2006)
kappa	κ	$2\times10^{-25}T^2 - 9\times10^{-23}T + 1\times10^{-20}$	m^2	Permeability	(Palin and Petty, 1983)
por	φ	0.785		Porosity	Section 4.2.4
rho_p	ρ_p	527	$kg.m^{-3}$	Density	(Plötze and Niemz, 2011)
S_il	S_{il}	$\dfrac{X_{mil}(1-\varphi)\rho_p}{\varphi\rho_L}$		Irreducible liquid phase saturation	Section 4.2.6
S_I_0	S_{I0}	$\dfrac{X_{m0}(1-\varphi)\rho_p}{\varphi\rho_L}$		Initial water saturation	Section 4.2.7

Table 18 Miscellaneous Properties

Nomenclature		Value	Unit	Description	Ref
COMSOL	Equations				
p0	p_0	1	atm	Ambient Pressure	Atmospheric
T0	T_0	293.15 Case Dependent	K	Ambient Temperature	Measured
T_in	T_{in}	342 Case Dependent	K	Inlet Air Temperature	Measured
u0	u_0	0.14 Case Dependent	m.s^{-1}	Freestream velocity	Measured
cv_sat_0	cv_{sat0}	$\dfrac{610.7\text{Pa} \times 10^{\frac{7.5(T0-273.15K)}{T0-35.85K}}}{R_{const}T0}$	mol.m^{-3}	Saturation vapour concentration at ambient temperature	(Dietl et al., 1995)
P_sat	P_{sat}	$610.7\text{Pa} \times 10^{\frac{7.5(T0-273.15K)}{T0-35.85K}}$		Vapour saturation pressure at ambient temperature	(Dietl et al., 1995)
D_va	D_{va}	2.51×10^{-5}	m^2.s^{-1}	Air-vapour diffusivity at 298K and 1 atm	(Denny and Meeting, 1993)
K_evap	K_{evap}	15000	s^{-1}	Evaporation rate Constant	Section 4.3.9
X_m0	X_{m0}	Initially set to 1.4 X_{m0} Case Dependent		Initial moisture content on dry basis	Measured
X_mil	X_{mil}	0.05		Irreducible moisture content dry basis	Section 4.3.11

In addition to the 'Global Definitions', a large proportion of user defined variables in the simulation are detailed in the 'Component Definitions'.

Table 19 Moist Air Material Properties

Nomenclature		Value	Unit	Description	Ref
COMSOL	Equations				
Mn_ma	Mn_{ma}	$X_v Mn_L + X_a Mn_a$	$kg.mol^{-1}$	Molecular Mass of moist air	(Tsilingiris, 2008)
rho_ma	ρ_{ma}	$\dfrac{(p + p_0)(Mn_l X_v + Mn_a X_a)}{R_{const} T}$	$kg.m^{-3}$	Density of moist air (ideal gas)	(Tsilingiris, 2008)
cp_ma	$c_{p,ma}$	$\dfrac{Mn_L X_v c_{p,v} + Mn_a X_a c_{p,a}}{Mn_{ma}}$	$J.kg^{-1}K^{-1}$	Heat capacity of moist air	(Tsilingiris, 2008)
mu_ma	μ_{ma}	$\dfrac{X_a \mu_a}{X_v \phi_{av} + X_a \phi_{aa}} + \dfrac{X_v \mu_v}{X_v \phi_{vv} + X_a \phi_{va}}$	$kg.m^{-1}s^{-1}$	Viscosity of moist air	(Tsilingiris, 2008)
k_ma	k_{ma}	$\dfrac{X_a k_a}{X_v \phi_{av} + X_a \phi_{aa}} + \dfrac{X_v k_v}{X_v \phi_{vv} + X_a \phi_{va}}$	$W.m^{-1}K^{-1}$	Conductivity of moist air	(Tsilingiris, 2008)
phi_aa	ϕ_{aa}	1		Coefficient for moist air viscosity and conductivity	(Tsilingiris, 2008)
phi_vv	ϕ_{vv}	1		Coefficient for moist air viscosity and conductivity	(Tsilingiris, 2008)
phi_av	ϕ_{av}	$\dfrac{\left(1 + \left(\frac{\mu_a}{\mu_v}\right)^{0.5}\left(\frac{Mn_L}{Mn_a}\right)^{0.25}\right)}{\left(8\left(1 + \frac{Mn_a}{Mn_L}\right)\right)^{0.5}}$		Coefficient for moist air viscosity and conductivity	(Tsilingiris, 2008)
phi_va	ϕ_{va}	$\dfrac{\left(1 + \left(\frac{\mu_v}{\mu_a}\right)^{0.5}\left(\frac{Mn_a}{Mn_L}\right)^{0.25}\right)}{\left(8\left(1 + \frac{Mn_L}{Mn_a}\right)\right)^{0.5}}$		Coefficient for moist air viscosity and conductivity	(Tsilingiris, 2008)
rho_tot	ρ_{tot}	$S_{ma}\rho_{ma} + S_L \rho_L$	$kg.m^{-3}$	Combined density of moist air and liquid phase	(COMSOL, 1998–2017)

Nomenclature		Value	Unit	Description	Ref
COMSOL	Equations				
cp_tot	$c_{p,tot}$	$\dfrac{\left(S_{ma}\rho_{ma}c_{p,ma} + S_L\rho_L c_{p,L}\right)}{\rho_{tot}}$	$J.kg^{-1}K^{-1}$	Combined heat capacity of moist air and liquid phase	(COMSOL, 1998–2017)
k_tot	k_{tot}	$S_{ma}k_{ma} + S_L k_L$	$W.m^{-1}K^{-1}$	Combined thermal conductivity of moist air and liquid phase	(COMSOL, 1998–2017)

Table 20 Porous Medium Velocity Variables

Nomenclature COMSOL	Nomenclature Equations	Value	Unit	Description	Ref
kappa_l	κ_L	$\kappa \times \kappa_{rl}$ where $\kappa_{rl} = f(S_L)$	m^2	Permeability liquid phase	(Abaci et al., 1992)
kappa_ma	κ_{ma}	$\kappa \times \kappa_{rma}$ where $\kappa_{rma} = f(S_L)$	m^2	Permeability moist air	(Abaci et al., 1992)
u_l	u_L	$-\dfrac{\kappa_L px}{\mu_L}$	$m.s^{-1}$	Darcy velocity of liquid phase (x-component)	(Abaci et al., 1992)
v_l	v_L	$-\dfrac{\kappa_L py}{\mu_L}$	$m.s^{-1}$	Darcy velocity of liquid phase (y-component)	(Abaci et al., 1992)
n_l_x	$n_{L,x}$	$\rho_L u_L - D_{cap}\nabla(c_L, x)Mn_L$	$kg.m^{-2}s^{-1}$	Liquid flux (x-component)	(Datta, 2007)
n_l_y	$n_{L,y}$	$\rho_L v_L - D_{cap}\nabla(c_L, y)Mn_L$	$kg.m^{-2}s^{-1}$	Liquid flux (y-component)	(Datta, 2007)
n_a_x	$n_{a,x}$	$\rho_a u - \rho_{ma}D_{eff}\nabla\left(\dfrac{\rho_a}{\rho_{ma}}, x\right)$	$kg.m^{-2}s^{-1}$	Dry air flux (x-component)	(Datta, 2007)
n_a_y	$n_{a,y}$	$\rho_a v - \rho_{ma}D_{eff}\nabla\left(\dfrac{\rho_a}{\rho_{ma}}, y\right)$	$kg.m^{-2}s^{-1}$	Dry air flux (y-component)	(Datta, 2007)
n_v_x	$n_{v,x}$	$\rho_v u - \rho_{ma}D_{eff}\nabla\left(\dfrac{\rho_v}{\rho_{ma}}, x\right)$	$kg.m^{-2}s^{-1}$	Water vapor flux (x-component)	(Datta, 2007)
n_v_y	$n_{v,y}$	$\rho_v v - \rho_{ma}D_{eff}\nabla(\dfrac{\rho_v}{\rho_{ma}}, y)$	$kg.m^{-2}s^{-1}$	Water vapor flux (y-component)	(Datta, 2007)
u_mean	u_{mean}	$\dfrac{(c_{p,a}n_{a,x} + c_{p,v}n_{v,x} + c_{p,L}n_{L,x})}{\rho_{tot}c_{p,tot}}$	$m.s^{-1}$	Mean velocity for heat transfer equation	(Datta, 2007)
v_mean	v_{mean}	$\dfrac{(c_{p,a}n_{a,y} + c_{p,v}n_{v,y} + c_{p,L}n_{L,y})}{\rho_{tot}c_{p,tot}}$	$m.s^{-1}$	Mean velocity for heat transfer equation	(Datta, 2007)

Table 21 Miscellaneous Variables

Nomenclature		Value	Unit	Description	Ref
COMSOL	Equations				
X_m	X_m	$$\frac{(abs(cl) + abs(cv))Mn_L}{(1 - \varphi)(\rho_p)}$$	$g.g^{-1}$	Moisture content on dry basis, mass of water per mass of solid	(Prakash and Kumar, 2017)
X_mwb	$X_{m(wb)}$	$$\frac{100X_{m(db)}}{100 + 100X_{m(db)}}$$		Moisture content on wet basis	
X_v	X_v	$$\frac{R_{const}Tcv}{(p + p_0)}$$		Molar fraction of vapour	(Tyagi, 2009)
D_cap	D_{cap}	$$7 \times 10^{-6}e^{-\frac{38500-29000X_{mwb}}{R_{const}T0}}$$	m^2s^{-1}	Capillary diffusivity	(Kurjatko and KC:dela, 1998)
X_a	X_a	$1 - X_v$		Molar fraction of air	(Halder, 2014)
cv_sat	$c_{v,sat}$	$$\frac{610.7Pa \times 10^{\frac{7.5(T-273.15K)}{T-35.85K}}}{R_{const}T0}$$	mol. m^{-3}	Saturation vapour concentration	(Bejan et al., 2013)
phi	Φ	$$\frac{cv}{cv_{sat}}$$		Relative humidity	(Chen and Putranto, 2013)
rho_v	ρ_v	$$\frac{cv \times Mn_L}{\varphi \times S_{ma}}$$	kg.m^{-3}	Vapour density (Derived as mass of vapour per pore volume)	
D_vd	D_{vd}	$$D_{va}\varphi^{\frac{4}{3}}S_{ma}^{\frac{10}{3}}$$	m^2s^{-1}	Effective vapour diffusivity	(Ho and Webb, 2006)
aw	aw	$$e^{\left(-\frac{0.0267}{X_m^{1.656}}\right)}(pv_{sat})^{0.0107}e^{(-1.287\,X_m)(X_m^{1.51}}$$		Water activity	(Datta, 2007b)
m_evap	m_{evap}	$k_{evap}(a_w \times c_{v,sat} - c_v)$	mol. $m^{-3}s^{-1}$	Mass of evaporation	(Fernando, 2012)
S_ma	S_{ma}	$max(1 - S_L, eps)$		Gas phase saturation	Section 4.3.5
S_l	S_L	$$min\left(\left(\frac{c_LMn_L}{\varphi\rho_L}\right), 1 - eps\right)$$		Liquid water saturation	Section 4.3.6

5.3.2 Input Parameters Woodchip Bed Model

Table 22 Changes for Woodchip Bed Simulation

Nomenclature COMSOL	Nomenclature Equations	Value	Unit	Description	Ref
por_bed	φ_{bed}	0.637		Porosity of woodchip bed	Section 4.2.4
por_chip	φ_{chip}	0.556		Porosity of woodchip bed	Section 4.2.4
por	φ	$(1 - \varphi_{bed})\varphi_{chip} + \varphi_{bed}$		Overall porosity woodchip bed	Section 4.2.4
kappa	κ	$\dfrac{1}{k_{Kozeny}400^2}\dfrac{\varphi^3}{(1-\varphi)^2}$	m^2	Permeability	(Alaqqad et al., (2012))
	k_{Kozeny}	$\dfrac{3.5\varphi^3[1 + 57(1-\varphi)^3]}{(1-\varphi)^{0.5}}$			
K_evap	K_{evap}	3	s^{-1}	Evaporation rate Constant	Section 4.3.9
D_cap	D_{cap}	$7 \times 10^{-6}e^{-\frac{38500-29000X_{mwb}}{R_{const}T0}}$	m^2s^{-1}	Capillary diffusivity	(Kurjatko and KC:dela, 1998)

5.4 COMSOL Numerical Setup

To describe the phenomena in the system, boundary conditions need to be set within the physics of the system. For example, at the walls there is no flow, there is an inlet heat source and an outlet to the system, these conditions are further described in each of the physics section.

5.4.1 Laminar Flow Model

A velocity field is created to simulate the flow of air across the woodchip.

$$\rho(\mathbf{u}.\nabla)\mathbf{u} = \nabla.[-p\mathbf{I} + \mathbf{K}] + \mathbf{F} \tag{109}$$

$$\nabla.(\rho\mathbf{u}) = 0 \tag{110}$$

$$\mathbf{K} = \mu(\nabla\mathbf{u} + (\nabla\mathbf{u})^T) - \frac{2}{3}\mu(\nabla.\mathbf{u})\mathbf{I} \tag{111}$$

Where:

- ρ is density in kg.m^{-3}

- **u** is the fluid velocity vector in m.s^{-1}

- p is the pressure in Pa

- **I** is the unit matrix

- **K** Contains the Lagrange multipliers that are used to implement the boundary conditions.

- **F** is the volume force vector in N.m^{-3}

- μ is the dynamic viscosity Pa.s

Note: In this case T is transpose rather than to the power of temperature.

The physical mode is set to compressible flow, enabling the porous media domains with a reference pressure p$_{ref}$ as 1 atm, and reference temperature user defined, $T_{ref} = 293.15K$.

There is no turbulence model within this simulation because laminar flow is assumed.

The discretization of the fluids is set to P1+P1 which is a piecewise linear interpolation for velocity and pressure and suitable for most flow problems (COMSOL, 1998–2018). Dependent variables include the velocity field, **u**, velocity components, u, v and w, and pressure p.

Fluid Properties

The fluid properties are described by the properties of moist air (Tsilingiris, 2008), while pressure p was set as gauge pressure and thus above the atmospheric value.

$$\rho = \rho_{ma} = \frac{(p+p_0)(Mn_l X_v + Mn_a X_a)}{R_{const} T} \qquad (112)$$

$$\mu = \mu_{ma} = \frac{X_a \mu_a}{X_v \phi_{av} + X_a \phi_{aa}} + \frac{X_v \mu_v}{X_v \phi_{vv} + X_a \phi_{va}} \qquad (113)$$

$$\phi_{aa} \text{ and } \phi_{vv} = 1 \tag{114}$$

Where X_v is the mass fraction of water vapour, X_a is the mass fraction of air and ϕ is the coefficient for moist air viscosity and conductivity.

Note: The molecular mass of liquid water is the same as that of water vapour.

Initial Values

The initial velocity fields and pressure is set to zero for all regions.

Walls

Left and right walls of the outer rectangle have no laminar flow or wall movement

$$u = 0 \tag{115}$$

The wall condition is set to no slip as an assumption.

Fluid and Matrix Properties

The fluid flow within the central rectangle has laminar fluid flow:

$$\frac{1}{\phi}\rho(\mathbf{u}.\nabla)\mathbf{u}\frac{1}{\phi} = \nabla.[-p\mathbf{l} + \mathbf{K}] - \left(\mu\kappa^{-1} + \beta_F|\mathbf{u}| + \frac{Q_m}{\phi^2}\right)\mathbf{u} + \mathbf{F} \tag{116}$$

$$\nabla.(\rho\mathbf{u}) = Q_m \tag{117}$$

$$\mathbf{K} = \mu\frac{1}{\phi}(\nabla\mathbf{u} + (\nabla\mathbf{u})^T) - \frac{2}{3}\mu\frac{1}{\phi^2}(\nabla.\mathbf{u})\mathbf{l} \tag{118}$$

Where **l is** the unit matrix, β_F is the Forchheimer drag (proportional to the square of the fluid velocity) (kg.m^{-4}), **u** is the Fluid Velocity Vector (m.s^{-1}), κ is the permeability of the porous medium(m^2), Q_m is the mass source (kg.m^{-3}.s^{-1}), and **F** is the volume force (N.m^{-3}).

The temperature is set to user defined 293.15K for the model input.

Within fluid properties, the fluid material is set to domain material. The density, ρ, dynamic viscosity, μ, porosity, φ_p, and permeability κ are user defined. With the extended equations described within definitions (Tsilingiris, 2008):

$$\rho = \rho_{ma} = \frac{(p+p_0)(Mn_l X_v + Mn_a X_a)}{R_{const} T} \tag{119}$$

$$\mu = \mu_{ma} = \frac{X_a \mu_a}{X_v \phi_{av} + X_a \phi_{aa}} + \frac{X_v \mu_v}{X_v \phi_{vv} + X_a \phi_{va}} \tag{120}$$

$$\varphi_p = \varphi S_{ma} \tag{121}$$

$$\kappa = \kappa_{ma} = \kappa_p \times \kappa_{rma} \tag{122}$$

Where:

$$S_{ma} = \max(1 - S_L, eps) \tag{123}$$

$$S_L = \min\left(\left(\frac{c_L Mn_L}{\varphi \rho_L}\right), 1 - eps\right) \tag{124}$$

For the permeability, the relative permeability of moist air, κ_{rma} (m^2) is defined in a piecewise function:

$$\kappa_{rg}^{T} = 1 + (2S_L - 3)S_L^2 \tag{125}$$

$$\kappa_{rg}^{L} = 1 + (4S_L - 5_L)S_L^4 \tag{126}$$

The permeability of the porous matrix, κ_p (m^2) is defined in the porous matrix properties:

$$\kappa_p = \frac{1}{k_{Kozeny} 400^2} \frac{\varphi^3}{(1-\varphi)^2} \tag{127}$$

Inlet

The base of the outer region is the selected inlet boundary as in practice the air flow comes from the base of the bed.

$$L_{entr}\nabla_t \cdot \left[-p\mathbf{l} + \mu(\nabla_t\mathbf{u} + (\nabla_t\mathbf{u})^T) - \frac{2}{3}\mu(\nabla.\mathbf{u})\mathbf{l}\right] = -p_{entr}n \qquad (128)$$

Where L_{entr} is the inlet length scale (m) and p_{entr} is the input pressure (Pa).

Outlet

$$[-p\mathbf{l} + k]n = -\hat{p}_0 n \qquad (129)$$

$$\hat{p}_0 \leq p_0 \qquad (130)$$

Where p_0 is the reference pressure (Pa) and $\hat{p}_0$ is the predicted pressure (Pa).

5.4.2 Transport of Diluted Species: Liquid Water

Assuming water is only present in the vapour form within the air and is present as both liquid and vapour within the woodchip, species transport for liquid water is applicable to geometrical region r2. The equations for species transport describe the movement of water, water vapour and air through the porous medium, accounting for saturation. The hydrodynamic dispersion consists of mechanical and diffusive movement:

$$\nabla.J_i + u.\nabla c_i = R_i \qquad (131)$$

$$J = -D_i\nabla c_i \qquad (132)$$

The first term in Equation (131) describes the diffusive transport through the porous medium, the second term describes the convective movement of liquid due to the velocity field u (m.s^{-1}), and R_i is the reactive term which in this situation describes the mass evaporated.

The convective transport mechanism is selected as an additional mechanism in the 'Transport Mechanisms' tab. Discretization concentration is set to Linear and within dependent variables, the number of species is set to 1 and the concentration of liquid, c_L, is added.

$$c_i = c_L \qquad (133)$$

Transport

The same governing equations apply to defining the transport properties of liquid water:

$$\nabla . J + u . \nabla c_L = R_L \tag{134}$$

$$J = -D_L \nabla c_L \tag{135}$$

The input temperature is set to 293.15 K, coordinate system set to global and convective velocity field set to user defined.

The velocity field of water in the x direction u_{Lx} (m.s^{-1}) (COMSOL, 2007):

$$u_{Lx} = -px \times \frac{k_L}{S_L \times \varphi \times \mu_L} \tag{136}$$

Where px is the pressure in the x direction (Pa), k_L permeability liquid water in porous medium, S_L is the liquid water saturation, ϕ is porosity and μ_L is the viscosity (Pa.s).

The velocity field of water in the y direction u_{Ly} (m.s^{-1}) (COMSOL, 2007):

$$u_{Ly} = -py \times \frac{k_L}{S_L \times \varphi \times \mu_L} \tag{137}$$

The Diffusive Transport Isotropic diffusive coefficient is added as a user defined term (Kurjatko and KC:dela, 1998);

$$D_L = D_{cap} = 7 \times 10^{-6} e^{-\frac{38500 - 29000 X_{mwb}}{R_{const} T0}} \tag{138}$$

Where x_m is the moisture content on a dry basis.

No Flux

Boundaries of Central Rectangle

$$-n . J_L = 0 \tag{139}$$

Initial concentration (COMSOL, 2007):

$$c_L = S_{L0} \times \varphi \times Mn_L \qquad (140)$$

c_L is the concentration, S_L is the liquid water saturation, φ is porosity and Mn_L is the molar mass of water.

Reactions

The rate of mass evaporated is defined by (COMSOL, 2007):

$$\nabla.J + u.\nabla c_L = R_L + S_L \qquad (141)$$

$$R_L = -m_{evap} \qquad (142)$$

Where m_{evap} is moles evaporated described by a_w the activation of water, c_v the concentration of vapour and $c_{v,sat}$ the saturation concentration of vapour (COMSOL, 2007):

$$m_{evap} = k_{evap}(a_w \times c_{v,sat} - c_v) \qquad (143)$$

$$a_w = e^{\left(-\frac{0.0267}{x_m^{1.656}}\right)}(pv_{sat})^{0.0107\, e^{(-1.287\, x_m)}(x_m^{1.513})} \qquad (144)$$

x_m is the moisture content of the chip on a dry basis.

Note the negative sign is present as the mass of liquid water decreases and as it becomes a vapour.

5.4.3 Transport of Diluted Species 2: Water Vapour

Applicable to the whole of the geometry, the governing equations within the section are set to study controlled and 'Study 1, stationary':

$$\nabla.J_i + u.\nabla c_i = R_i \qquad (145)$$

$$J = -D_i \nabla c_i \qquad (146)$$

Where R_i is the reaction rate per unit volume (mol.m^{-3}s^{-1}). Convection is selected as an additional transport mechanism in the 'Transport Mechanisms' tab. In the case of water vapour the 'reaction' is an increase in water vapour as liquid water is evaporated changing from liquid to gas phase. Discretization concentration is set to Linear and within dependent variables, the number of species is set to 1 and the concentration of vapour, cv, is added.

$$c_i = c_v \qquad (147)$$

Transport

For the area surrounding the wood water vapour, transport has the same governing equation as above.

$$\nabla \cdot J_{va} + u \cdot \nabla c_v = R_{va} \qquad (148)$$

$$J_v = -D_{cv} \nabla c_v \qquad (149)$$

293.15[K] is the user defined temperature, T, in the 'Model Input' tab. The coordinate system is set to global. The convective velocity field, **u**, is set to velocity field (spf).

The variables within the governing equation are altered in the 'Diffusion' tab with D_{cv} (m.s^{-1}) set to user defined and isotropic.

$$D_{cv} = D_{va} \qquad (150)$$

No Flux

The side walls of the outer region do not allow water vapour to pass through:

$$-nJ_i = 0 \qquad (151)$$

Initial Values

For the outer region, 1, the concentration of water vapour c_v (mol.m^{-3}) is initially set:

$$c_v = 0 \qquad (152)$$

Transport Porous Medium

The central region, 2, is set to simulate the woodchip as a porous medium. Water vapour is set to move through the chip. For this, the following governing equation is applied:

$$\nabla . J_i + u. \nabla c_i = R_i \qquad (153)$$

$$J_i = -D_i \nabla c_i \qquad (154)$$

The model input temperature is set to 293.15 K and coordinate system set to global.

The convective velocity field is defined in both the x and the y directions.

The velocity field of water in the x direction:

$$u_{va,x} = \frac{u}{\varphi \times S_{ma}} - Mn_a \times D_{eff} \times \rho_{ma} \times \frac{d\left(\frac{Mn_{ma}}{\rho_{ma,x}}\right)}{Mn_{ma}^2} \qquad (155)$$

The velocity field of water in the y direction:

$$u_{va,y} = \frac{v}{\varphi \times S_{ma}} - Mn_a \times D_{eff} \times \rho_{ma} \times \frac{d\left(\frac{Mn_{ma}}{\rho_{ma,x}}\right)}{Mn_{ma}^2} \qquad (156)$$

For diffusive Transport, the isotropic diffusive coefficient within the porous zone:

$$D_{cv,por} = \frac{D_{vd} Mn_a}{Mn_{ma}} \qquad (157)$$

Where D_{vd} is the effective vapour diffusivity and is dependent on the porous medias structure and flow. The saturation of the porous media affects these terms as the higher the saturation, the greater the free flow of a species, in this case water vapour.

Initial values

$$c_v = c_{v,sat,0} \qquad (158)$$

Reactions

The mass evaporated is defined by

$$\nabla . J + u . \nabla c_{va} = R_{va} + S_{va} \qquad (159)$$

$$R_{va} = m_{evap} \qquad (160)$$

Where m_{evap} is rate of mass evaporated described by the a_w the activation of water, c_v the concentration of vapour and $c_{v,sat}$ the saturation concentration of vapour. Note that there is no negative sign as the amount of vapour increases as the amount of liquid water decreases.

$$m_{evap} = k_{evap}\left(a_w \times c_{v,sat} - c_v\right) \qquad (161)$$

$$a_w = e^{\left(-\frac{0.0267}{x_m^{1.656}}\right)}\left(pv_{sat}\right)^{0.0107 \, e^{(-1.287 \, x_m)}\left(x_m^{1.513}\right)} \qquad (162)$$

Outflow

The top of the outer rectangle, edge, is set as the outflow region with the equation:

$$\mathbf{n} . D_i \nabla c_i = 0 \qquad (163)$$

Where $\mathbf{n}$ is the normal vector toward exterior.

5.4.4 Heat Transfer in Fluids

$$d_z \rho c_p \frac{\partial T}{\partial t} + d_z \rho c_p \mathbf{u} . \nabla T + \nabla . \mathbf{q} = d_z Q + q_0 + d_z Q_p + d_z Q_{vd} \qquad (164)$$

Where:
- d_z is the thickness of the domain in the out of plane direction, m
- $\left(\rho c_p\right)_{eff}$ is the effective volumetric heat capacity at constant pressure, J.m^{-3}K^{-1}
- $\frac{\partial T}{\partial t}$ is the change in temperature per unit time, K.s^{-1}
- c_p is the heat capacity at constant pressure, J.m^{-3}K^{-1}

- ρ is the density, kg.m⁻³
- **u** the fluid velocity vector, m.s⁻¹
- T is the temperature K
- **q** is the conductive heat flux, W.m⁻²
- Q is the heat source, W.m⁻³
- q_0 is the inward heat flux, W.m⁻²
- Q_p is the pressure work, W.m⁻³
- Q_{vd} is the viscous dissipation, W.m⁻³

$$\mathbf{q} = -d_z k \nabla T \tag{165}$$

Where k is the thermal conductivity of the selected region.

Fluid

Applicable to region 1, which is an air water vapour mixture:

$$d_z \rho_{ma} c_{p,ma} \frac{\partial T}{\partial t} + d_z \rho_{ma} c_{p,ma} \mathbf{u}.\nabla T + \nabla.\mathbf{q} = d_z Q + q_0 + d_z Q_p + d_z Q_{vd} \tag{166}$$

$$\mathbf{q} = -d_z k_{ma} \nabla T \tag{167}$$

Using the standard heat transfer equations requires inputting the following terms:

Velocity **u** as the velocity field (spf) and absolute pressure p_A as the absolute pressure (spf)

The coordinate system selected is the global coordinate system.

The heat conduction of the fluid is changed to user defined and shown in the equation for **q** above, k becomes the thermal conductivity of moist air, k_{ma} (Tsilingiris, 2008) (W.m⁻¹K⁻¹), which is isotropic. k_{ma} is defined in material property variables as:

$$k_{ma} = \frac{X_a k_a}{X_v \phi_{av} + X_a \phi_{aa}} + \frac{X_v k_v}{X_v \phi_{vv} + X_a \phi_{va}} \tag{168}$$

For the thermodynamics of the fluid, the fluid type is gas/liquid and the density, ρ (kg.m⁻³), heat capacity (Tsilingiris, 2008), c_p (J.kg⁻¹K), and ratio of specific heats, γ (dimensionless), are user defined.

$$\rho = \rho_{ma} = \frac{(p+p_0)(Mn_L X_v + Mn_a X_a)}{R_{const} T} \qquad (169)$$

$$c_p = c_{p,ma} = \frac{Mn_L X_v c_{p,v} + Mn_a X_a c_{p,a}}{Mn_{ma}} \qquad (170)$$

Where (Tsilingiris, 2008):

$$Mn_{ma} = X_v Mn_L + X_a Mn_a \qquad (171)$$

Note: The molecular mass of water vapour is equal to the molecular mass of liquid water, hence the liquid subscript multiplied with a mass fraction of vapour.

$$\gamma = 1 \qquad (172)$$

Initial Values

For regions 1 and 2, the initial temperature T is set to user defined T_0.

Thermal Insulation

This is applicable to the left and right walls on the external rectangle, in this region there is no heat flux:

$$-\mathbf{n}.\mathbf{q} = 0 \qquad (173)$$

In this equation **n** is the normal vector toward the exterior of the region.

Porous medium

The base standard heat transfer equation alters slightly for a porous medium using an effective heat capacity, which changes depending on the voidage of the material:

$$d_z \left(\rho c_p\right)_{eff} \frac{\partial T}{\partial t} + d_z \rho c_p \mathbf{u}. \nabla T + \nabla. q = d_z Q + q_0 + d_z Q_p + d_z Q_{vd} \qquad (174)$$

The effective volumetric heat capacity at constant pressure $(\rho c_p)_{eff}$ J.m^{-3}K^{-1} can be described by the specific heat capacity of the porous media, moist air and liquid phase, their densities ρ and the volume fraction θ_p(Datta, 2007b).

$$(\rho c_p)_{eff} = \theta_p \rho_p c_p + (1 - \theta_p)\rho_{tot}c_p \tag{175}$$

$$q = -d_z k_{eff}\nabla T \tag{176}$$

Where k_{eff} is the effective thermal conductivity, W.m^{-1}K^{-1}, described by the component thermal conductivity and volume fraction θ_p(Datta, 2007b).

$$k_{eff} = \theta_p k_p + (1 - \theta_p)k_{tot} + k_{disp} \tag{177}$$

k_{disp} is the dispersive thermal conductivity tensor, k_p is the thermal capacity of the solid material in the porous media and k_{tot} is the total thermal capacity for moist air, where the units are W.m^{-1}K^{-1}. Equations 161 to 164 are predefined in COMSOL, via setting the 'Effective Thermal Conductivity' tab to volume average.

Inputs into the model include velocity in x (m.s^{-1}), velocity in y (m.s^{-1}) and absolute pressure (Pa), these are all set to user defined:

$$\mathbf{u}_x = u_{mean} \tag{178}$$

$$\mathbf{u}_y = v_{mean} \tag{179}$$

$$u_{mean} = \frac{(c_{p,a}n_{a,x} + c_{p,v}n_{v,x} + c_{p,L}n_{L,x})}{\rho_{tot}c_{p,tot}} \tag{180}$$

$$v_{mean} = \frac{(c_{p,a}n_{a,y} + c_{p,v}n_{v,y} + c_{p,L}n_{L,y})}{\rho_{tot}c_{p,tot}} \tag{181}$$

Where:

$$n_{a,x} = \rho_a u - \rho_{ma} D_{eff} \nabla \left(\frac{\rho_a}{\rho_{ma}}, x \right) \tag{182}$$

$$n_{a,y} = \rho_a v - \rho_{ma} D_{eff} \nabla \left(\frac{\rho_a}{\rho_{ma}}, y \right) \tag{183}$$

$$n_{v,x} = \rho_v u - \rho_{ma} D_{eff} \nabla \left(\frac{\rho_v}{\rho_{ma}}, x \right) \tag{184}$$

$$n_{v,y} = \rho_v v - \rho_{ma} D_{eff} \nabla \left(\frac{\rho_v}{\rho_{ma}}, y \right) \tag{185}$$

$$n_{L,x} = \rho_L u_L - D_{cap} \nabla (c_L, x) M n_L \tag{186}$$

$$n_{L,y} = \rho_L v_L - D_{cap} \nabla (c_L, y) M n_L \tag{187}$$

$$p_A = 1 \text{ atm} \tag{188}$$

The coordinate system selected is 'Global coordinate system' and the fluid material 'Domain material'.

The thermal conductivity, within the 'Heat Conduction, Fluid' tab, is set to user defined and isotropic:

$$k = k_{tot} \tag{189}$$

$$k_{tot} = S_{ma} k_{ma} + S_L k_L \tag{190}$$

Within the 'Thermodynamics, Fluid' tab the fluid type is set to gas/liquid and the density, ρ (kg.m^{-3}), heat capacity, c_p (J.kg^{-1}.K), and ratio of specific heats, γ (dimensionless), are user defined.

$$\rho = \rho_{tot} \tag{191}$$

$$\rho_{tot} = S_{ma} \rho_{ma} + S_L \rho_L \tag{192}$$

$$c_p = c_{p,tot} \tag{193}$$

$$c_{p,tot} = \frac{(S_{ma}\rho_{ma}c_{p,ma} + S_L\rho_L c_{p,L})}{\rho_{tot}} \tag{194}$$

$$\gamma = 1 \tag{195}$$

In the porous medium, there is immobile solid (the dry woodchip itself). The solid material is set as Domain material with the volume fraction θ_p user defined:

$$\theta_p = 1 - \varphi \tag{196}$$

The porous matrix also has an independent thermal conductivity, k_p, density, ρ_p, and specific heat, $c_{p,p}$ all defined in porous matrix properties.

Heat Source

The governing equation for this section is Q=Q₀.

Material type is set to solid, the heat source selected as general, and user defined (COMSOL, 2007):

$$Q_0 = -H_{evap}Mn_L m_{evap} \tag{197}$$

Where H_{evap} is the Enthalpy of Vaporisation (J.kg⁻¹).

Temperature

For this section temperature T is user defined:

$$T = T_0 = T_{in} \tag{198}$$

Outflow

As for insulating material the equation applicable to this section is:

$$-\mathbf{n}.\mathbf{q} = 0 \tag{199}$$

5.5 Creating the Mesh

After setting up the environment, creating the geometry, specifying the material and input parameters and defining boundary conditions, the last step before computation is creating the mesh. Meshing divides the overall geometry into discrete components. In general, the denser the mesh the more computational power required and the greater the time to run a simulation, due to the increased degrees of freedom. The finer the mesh the greater the accuracy as equations are solved over smaller discretised boundaries.

In addition to the mesh density, mesh can be structured or unstructured. Structured mesh is advantageous when mass and energy is transported as conservation of mass, energy and momentum is generally more successful with a structured mesh. Structured mesh however increases the degrees of freedom per element.

Since this case has two rectangular regions, a structured mesh can be easily implemented. In this case, user-controlled mesh must be defined as an equation-based approach.

5.6 Computing the Simulation

To produce results from the properties, and meshing Studies are added.

Global Evaluation

From the results toolbar, Global Evaluation two expressions are added, describing the concentration of liquid and vapour across the geometry:

timeint(0,t,intopOutlet(tds2.ntflux_cv))+ intopFree(cv)+intopPorous(cv+cl)

at(0,intopFree(cv))+at(0,intopPorous(cv+cl))

Stationary

The stationary solver is set to compute for the 'Laminar Flow' physics interface. This computes initial input variables for the pressure fields.

Time Dependent

The time dependent solver computes for both 'Transport of Dilute Species' physics interfaces and the 'Heat Transfer' module. This study is added as field variables are changing over time including, pressure, chemical composition, and temperature profile.

5.7 Post processing the Results

To compare moisture content data from the field and the laboratory an average value of moisture content over the area is required. Within the 'Derived Values' tab in COMSOL 'Surface Average' can calculate the average of the moisture content over the selected geometry and time scale.

To analyse the velocity, pressure, concentration, temperature and humidity profiles '2D Plot Groups' were set up in the results tab. These plots aid the understanding of the behaviours of properties over time, showing a trace of each property and are an indicator if the simulation is following the expected physics.

5.8 Situational Simulation Setup

Temperature

Air flow temperature impacts drying efficiency as drying rate has a dependency on temperature. Increasing temperature however, increases utility costs from the heating, subsequently, the gain from increasing efficiency in drying through temperature diminishes the cost effectiveness of the process. To determine the trade off point for optimisation against cost and product moisture content, it is important to understand the impact of temperature on final moisture content and fuel cost, therefore temperature was selected as a key variable for experiments and simulations.

Altering T_0 in the heat transfer heat source tab for the heat source is the model equivalent of changing the inlet air temperature.

Table 23 Parameters - Variable Temperature

	55 °C	65 °C	75 °C	85 °C
Temperature Heat Source	55 °C	65 °C	75 °C	85 °C
Velocity of Air	1.6 m.s^{-1}	1.6 m.s^{-1}	1.6 m.s^{-1}	1.6 m.s^{-1}
External Temperature	21°C	21°C	21°C	21°C

Air Flow Rate

Air flow rate can also impact on drying rates and to replicate experiments, whereby flow was controlled by altering the fan speed, the air flow rate in the simulations can be increased or decreased. Air flow is required to carry vapour away from the woodchip and for convective drying to transfer heat, a flow rate too high and less energy is transferred from the airflow to the woodchip, too low and the velocity is not great enough to drive moisture from the woodchip surface.

To change the air flow rate within COMSOL u_0 can be altered, the variables from Table 24 are used. A 'Parameter Sweep' is used to altering these values in a single simulation.

Table 24 Parameters - Variable Air Flow Rate

	1.6 m.s^{-1}	2.3 m.s^{-1}	2.7 m.s^{-1}	3 m.s^{-1}
Temperature Heat Source	65 °C	65 °C	65 °C	65 °C
Velocity of Air	1.6 m.s^{-1}	2.3 m.s^{-1}	2.7 m.s^{-1}	3 m.s^{-1}
External Temperature	21 °C	21 °C	22 °C	21 °C

Bed Depth

The depth of the bed effects the airflow through the bed and the path of exiting moist air. The bed depth at Bowland Bioenergy can be altered from 23 cm to 43 cm on the current drier and is used at the bed depth of 23 cm under normal operation, increasing this bed depth could increase throughput.

When changing the bed depth, the height of the woodchip changes, within the model the height can also be altered to mimic this effect. For this, the geometry of r2 is altered increasing and decreasing the size of the porous matrix. Setting the height as a parameter, this height and other variables, shown in Table 25, can be altered using a 'Parametric Sweep'.

Table 25 Parameters - Variable Bed Depth

	43 cm	34 cm	24.5 cm
Temperature Air	SET-54 °C	SET-55 °C	SET-53 °C
Temperature Boiler	SET-82 °C	SET-86 °C	SET-82 °C
Velocity of Air	SET-0.14 m.s^{-1}	SET-0.14 m.s^{-1}	SET-0.14 m.s^{-1}
Top Floor Interval	5 min	5 min	5 min
Bed Depth	43 cm	34 cm	24.5 cm
Cover	No	No	No
Average External Temperature	15 °C	16 °C	15 °C
X_m0 (WB)	1.256	0.879	0.475
K_evap	0.07	0.07	0.07

Top Floor Speed

The interval between the top floor moving at Bowland Bioenergy can be altered, this changes the time the chip is in the drier, therefore affecting the final moisture content. This frequency of the chip discharge are set on the dryer control panel. At the end of each discharging operation the ladder floor stops moving, at the start of the next unloading, this frequently results in the ladder moving away from the auger to start a new discharge stroke. Predicting the interval time based on moisture content would help achieve target moisture contents more effectively. Altering the floor speed alters the overall time available for drying, in the base 2D model this is achieved by altering the overall running time of the simulation shown in row 8 of Table 26.

Table 26 Parameters - Variable Top Floor Speed, Interval Time

	5 min	Maximum 12 min	Minimum 3min
Temperature Air	SET-53 °C	SET-50°C	SET-52°C
Temperature Boiler	SET-86 °C	SET-85°C	SET-85°C
Velocity of Air	SET-0.14	SET-0.14	SET-0.14
Top Floor Interval	5 min	Maximum 12 min	Minimum 3min
Bed Depth	24.5 cm	24.5cm	24.5cm
Cover	No	No	No
Time in Open Bed*	2 hours	4 hours 48 minutes	1 hour 12 minutes
X_m0 (DB)	0.475	0.782	1.01
Average External Temperature	15°C	13°C	14°C

*Approximate dependent on where the moving floor starts

5.9 Chapter Summary

This section shows the implementation of the experimental and literature values found in Chapter 3, with an extensive outline of the model setup. The boundary conditions, initial conditions and governing equations for the simulation models have been introduced and their implantation outlined within the numerical CFD code. The 3 simulation types have also been detailed, one for an air-flow case in Ansys Fluent, and two based in COMSOL, which consider evaporation of wetted wood chip in a packed bed and from a single wood chip by means of hot air. In ANSYS a porous zone was used to investigate airflow, with water hold up and evaporation difficult to achieve within the porous media the porosity of the bed was used. In COMSOL the 'Laminar Flow', 'Transport of Dilute Species' and 'Heat Transfer in Fluids' modules are used to describe the system.

Chapter 6

Drying Experimental and Simulation Results

This chapter covers results from simulated and experimental drying discussing the effect of each parameter and the modelled results. To validate the model, a comparison to physical experiments has been performed. The validated model will aid prediction of future experiments.

6.1 ANSYS Fluent – Airflow Through the Drier

The main results of the ANSYS simulation, described in Chapter 5, are reported in Figure 27 to Figure 25. All figures are based on the results obtained with final time step of the simulation. In Figure 27, a contour plot of the air-velocity magnitude is presented. The air velocity plot shows that the flow is stagnating and recirculating at the far side (away from the velocity inlet) in the bottom drier. This would suggest that the amount of hot air distributed to the woodchip bed may not be even. Close inspection of the changing velocity shows that less airflow passes through the grating at the far side of the drier.

In Figure 26, the static pressure contours in the drier are presented. In Figure 26 the profiles show that the pressure drop over the woodchip porous zone is fairly even and in-line with literature.

The Figure 25 shows the volume fraction of water in the woodchip porous zone. This has been fixed in place, by prescribing a maximum water negative 'y' velocity of 0 m/s (i.e. to prevent water simple falling out of the porous zone due to gravity). Future work could include an evaporation model that results in a phase change of the water to water vapour. This was beyond the scope of this work.
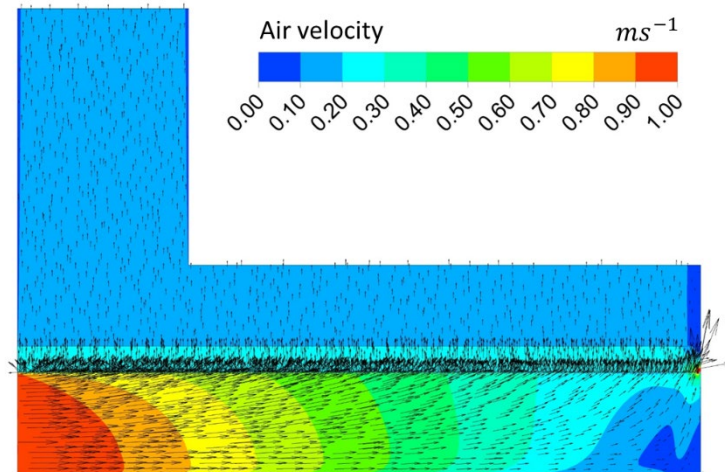
Figure 25 Velocity Magnitude Contours Through The Drier conditions in Table 13
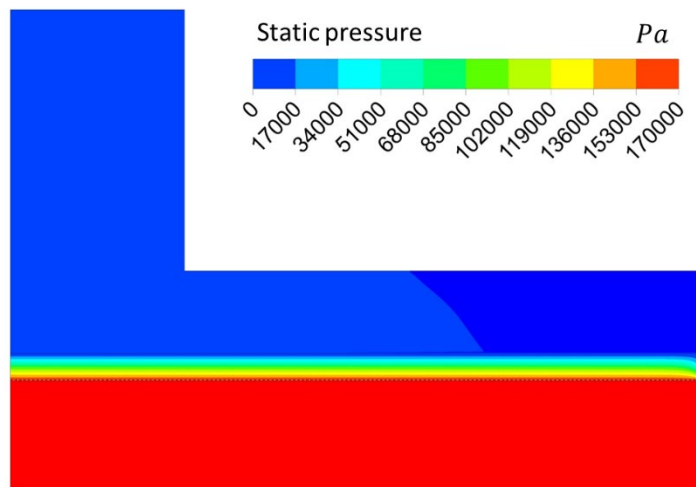
Figure 26 Static Pressure Contours Through The Drier conditions in Table 13
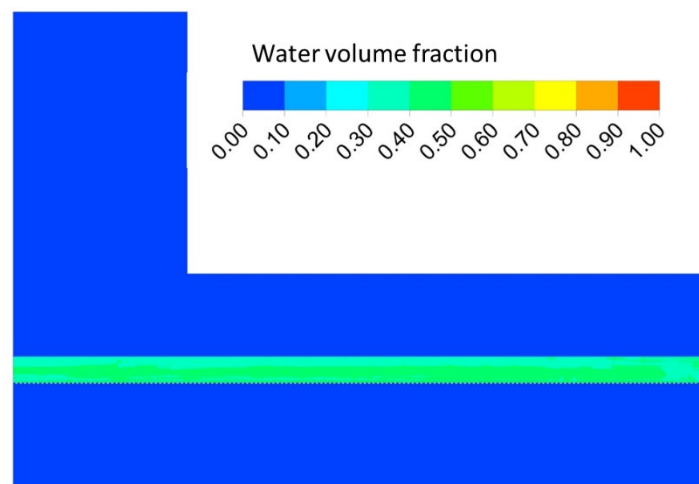
Figure 27 Water Fraction Profile of The Drier conditions in Table 13

6.2 2D Model by COMSOL Multiphysics

From the setup described in Chapter 5 for each simulation and parameters found in Chapter 4 the following results were gathered.

6.2.1 Investigating the Effect of Temperature

This section shows changes made within the model regarding temperature effects. In addition, to validate the numerical simulation, the results are compared to experimental data obtained for a single chip on laboratory scale at different temperatures, Figure 28.

Table 27 shows the settings relating to Figure 28.

Table 27 Parameters - Variable Temperature				
	55 °C	65 °C	75 °C	85 °C
Temperature Heat Source	55 °C	65 °C	75 °C	85 °C
Velocity of Air	1.6 m.s^{-1}	1.6 m.s^{-1}	1.6 m.s^{-1}	1.6 m.s^{-1}
External Temperature	21 °C	21 °C	21 °C	21 °C
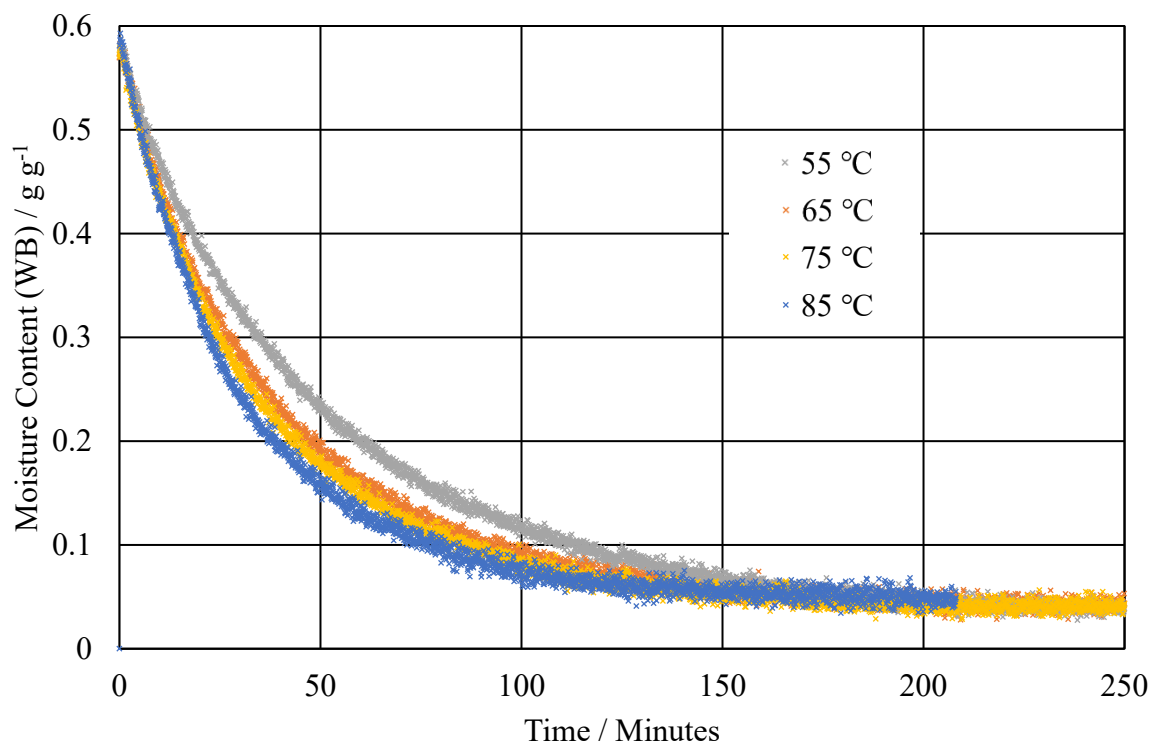
Figure 28 Experimental Results Varying Temperature Single Woodchip

The laboratory results show a slight increase in rate with temperature, as the curves in Figure 28 are steeper at 85 °C than any other temperature. These results have some noise due to differences in force from the airflow over the scales, however the general drying trend can still be seen.
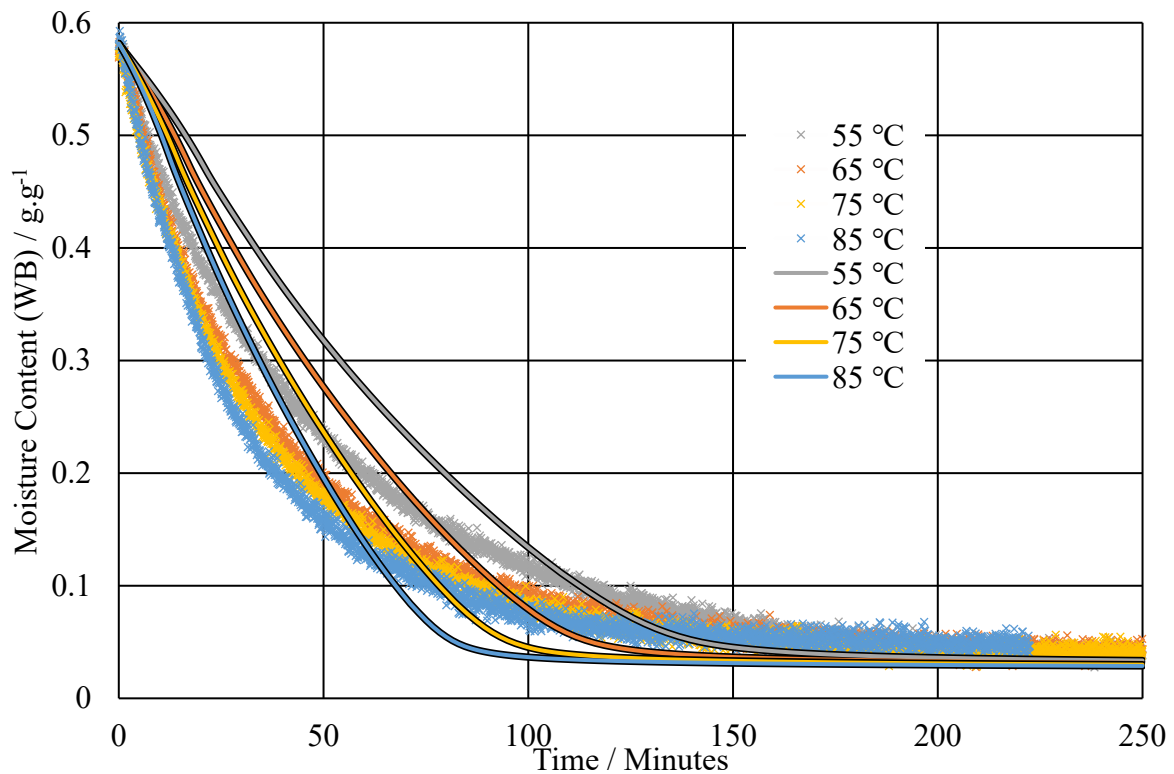
Figure 29 Measured and Simulated Data Varying Temperature Single Woodchip

Figure 29 contains the simulation and experimental results, both show that the increase in temperature increased the drying rate. The initial falling rate period of the experimental results is likely steeper due to non-uniformities in the porous medium and surface water, whereas within the simulation the water is uniformly distributed in a uniformly porous zone. In addition, as noted in the literature review, water nearest the surface requires the least activation energy and this will result in a greater initial drop in the moisture content. Both the experiments and simulations show this; however, it is more prominent in the experiments. The reason for this is that due to the time dependency of the simulations it takes several time steps to develop the correct initial conditions. One can see that once the initial conditions have properly developed there is a significant drop in the moisture content recorded. The spread of results shows that the impact on drying rate of the temperature was slightly more significant within the simulation by comparison to the experimental results, this is likely because of non-uniformity in the air

flow from the heat gun in practice causing greater mixing with the 21 °C air from the environment and less heat transfer to the woodchip.

6.2.2 Investigating the Effect of Air Flow Rate

Table 28 Parameters - Variable Air Flow Rate			
	1.6 m.s^{-1}	2.3 m.s^{-1}	3 m.s^{-1}
Temperature Heat Source	65 °C	65 °C	65 °C
Velocity of Air	1.6 m.s^{-1}	2.3 m.s^{-1}	3 m.s^{-1}
External Temperature	21 °C	21 °C	21 °C
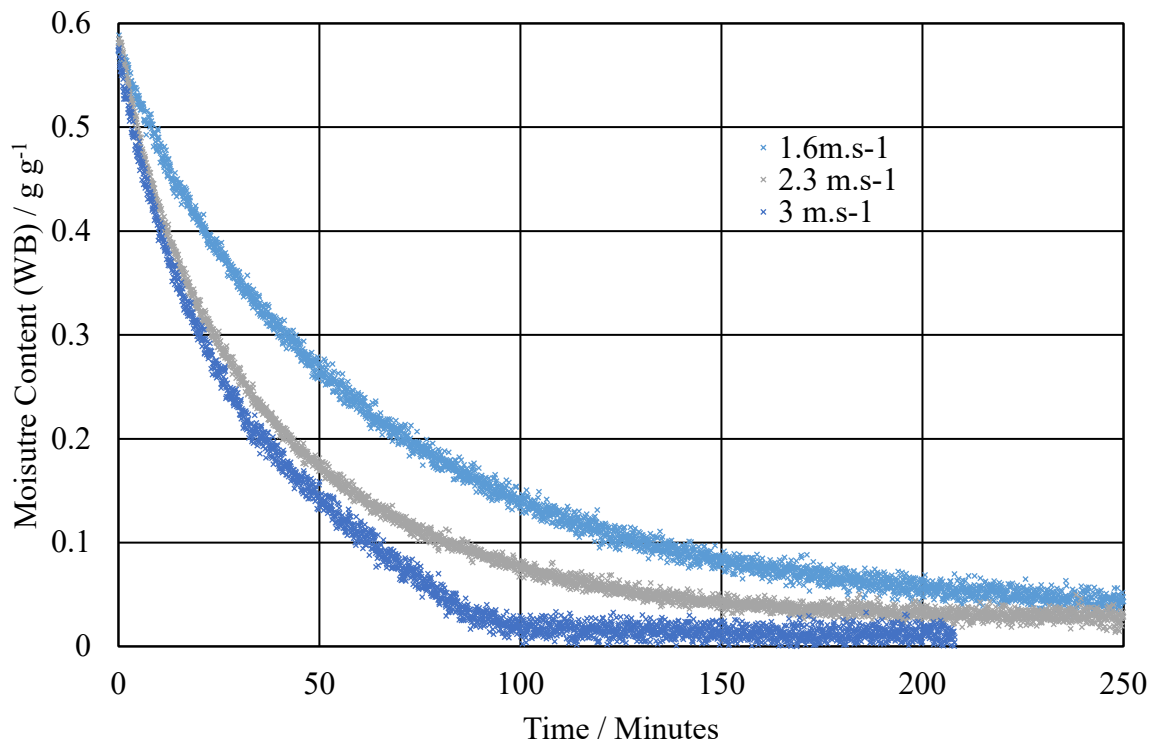
Figure 30 Experimental Results for Drying of Single Woodchip at 65 °C at Different air Flow Rates
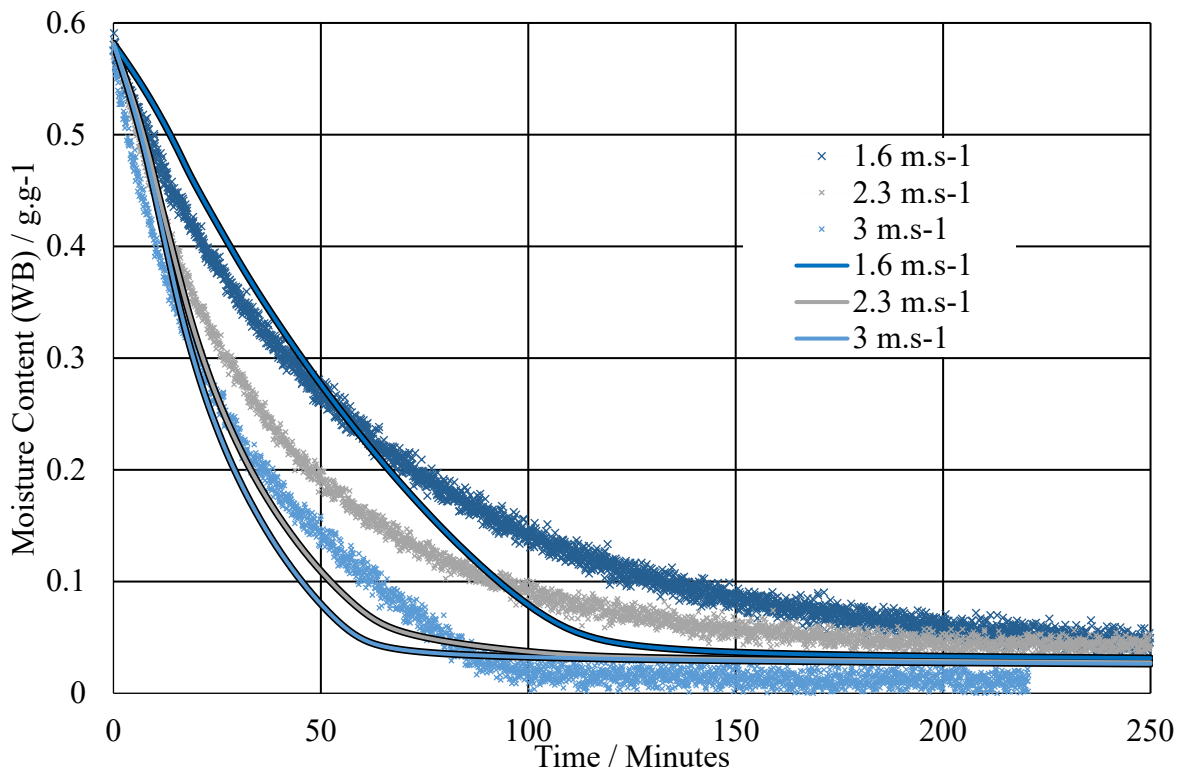
Figure 31 Measured and Simulated Data Varying Air Flow Rates Single Woodchip

Flow rate impacted the rate of mass loss of water shown in Figure 30 and Figure 31. The impact of flow rate has a similar range to the experimental results however the distribution of the curves is not evenly spread. Within the simulations a, higher air flow lead to a greater loss in moisture content, though there is a point of trade off where the increased airflow does not significantly impact flow rate as once a certain air flow is achieved, heat transfer is limited by transfer through the woodchip from the surface of the woodchip. In practice, an increase in air flowrate had a clear impact on the drying rate of the woodchip at all of the flow rates measured, this may be due to the non-uniformity of the woodchip surface, meaning the point at which the air flow has a lesser impact is greater than the airflows used. The dispersion of the air flow over the woodchip may also have led to a more significant effect of airflow on drying rate than the uniform source of laminar flow within the simulation.

6.2.3 IR Drying

Table 29 Parameters – IR Drying

	55 °C	65 °C	75 °C	85 °C
Temperature Heat Source	55 °C	65 °C	75 °C	85 °C
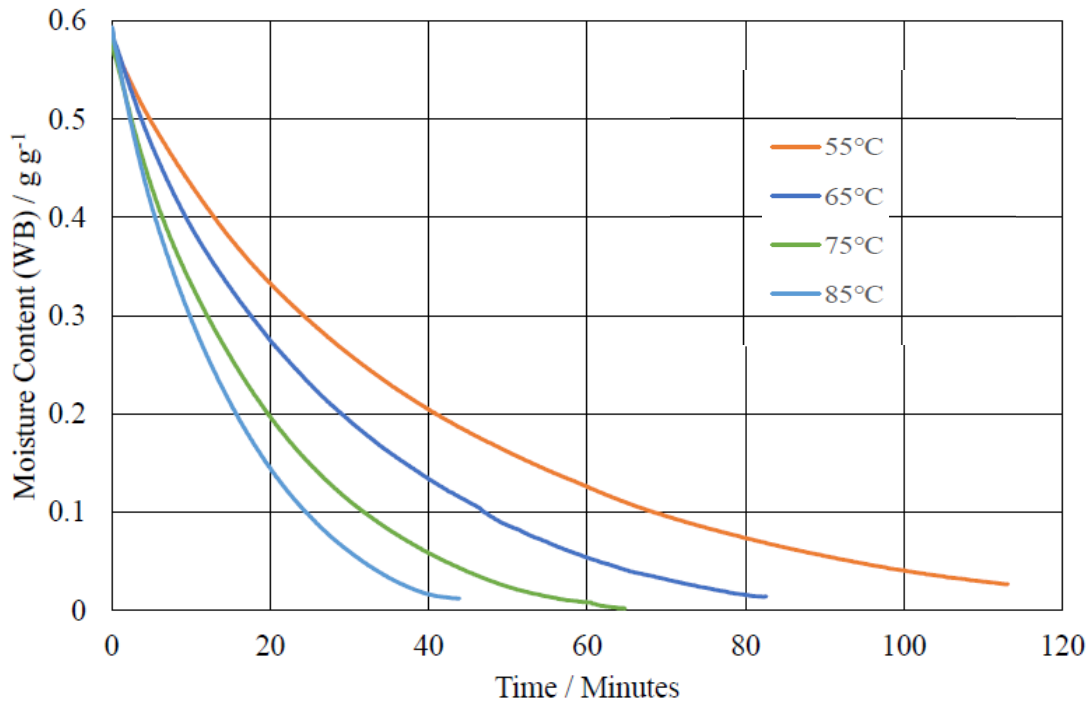
Figure 32 IR Drying Experimental Results

The distribution of results for IR drying is wider than that of convective (Figure 32 and Figure 28), due to the heat transfer mechanisms within IR drying. Lower temperatures increased drying time for both convective and IR drying, with convective drying taking up to 5 times longer than IR. The measurements from this method had less noise with respect to the mass due to the low air flow rate over the scales.

6.2.4 Investigating the Effect of the Bed Depth

Three tests were conducted on site with three different depths of bed, testing the impact of the bed depth on the final moisture content of the woodchip. For the on-site testing at Bowland Bioenergy experiments, the humidity and temperature were logged as the drier is open and could be affected by external conditions. The moisture content of woodchip is then used for

comparison with the COMSOL model results. The bed was set at three heights under the conditions shown in Figure 37.

Table 30 Parameters - Variable Bed Depth

	43 cm	34 cm	24.5 cm
Temperature Air	SET-54 °C	SET-55 °C	SET-53 °C
Temperature Boiler	SET-82 °C	SET-86 °C	SET-82 °C
Velocity of Air	SET-0.14 m.s^{-1}	SET-0.14 m.s^{-1}	SET-0.14 m.s^{-1}
Top Floor Interval	5 min	5 min	5 min
Bed Depth	43 cm	34 cm	24.5 cm
Cover	No	No	No
Average External Temperature	15 °C	16 °C	15 °C
X_m0 (WB)	1.256	0.879	0.475
K_evap	0.07	0.07	0.07

Samples were taken from the high inlet section, the start of the open bed section, end of the open bed section and product pile. For each of these samples the moisture content was taken 5 times, as shown in Table 31.

Table 31 Moisture Content Readings - Variable Bed Depth

	43 cm		34c m		24.5 cm	
	Start Mass	Moisture %	Start Mass	Moisture %	Start Mass	Moisture %
MC In	5.57±0.26	50.81±6.38	5.28±0.18	53.59±6.66	5.42±0.13	34.80±3.02
MC Start of Bed	5.58±0.26	55.67±5.24	5.35±0.25	46.79±4.13	5.17±0.20	32.20±3.03
MC Middle of Bed	5.40±0.22	55.23±3.79	5.13±0.06	27.02±2.90	5.34±0.16	17.30±0.48
MC End of Bed	5.28±0.26	47.19±2.82	5.25±0.16	14.57±0.82	5.02±0.04	10.57±0.41

For comparison of the dependency of bed depth on moisture content at locations along the drier, the results were plotted with 1,2,3 and 4 referencing each location. The analysis considers the same batch of woodchip, following the batch from the hopper to the end of drier.

In Figure 33 to Figure 35, the temperature readings above the drier bed are reported for each of the 3 bed-depth experiments. The temperature readings are given over time and refer to several locations along and above the drier bed. The Figure 33 to Figure 35 show that there is no significant variation in the temperature caused either by the ambient environment temperature or the due to the bed depth.

Similarly, in Figure 36 to Figure 38, the humidity readings above the drier bed are reported for each of the 3 bed-depth experiments. The humidity above the drier is reported over time (x-axis). The different curves in the Figures refer to the different points along the drier bed. These graphs show that there is large fluctuation in humidity during the day. However, the ambient humidity shows no significant variation when comparing the different bed depth experiments, the exception being Figure 36, where at the start of the test (0 hrs), the ambient humidity is higher – circa 70 %. This ambient humidity however, likely has little effect considering the measured values, as the humidity values above the drier bed are generally higher than this in all cases and across all locations.
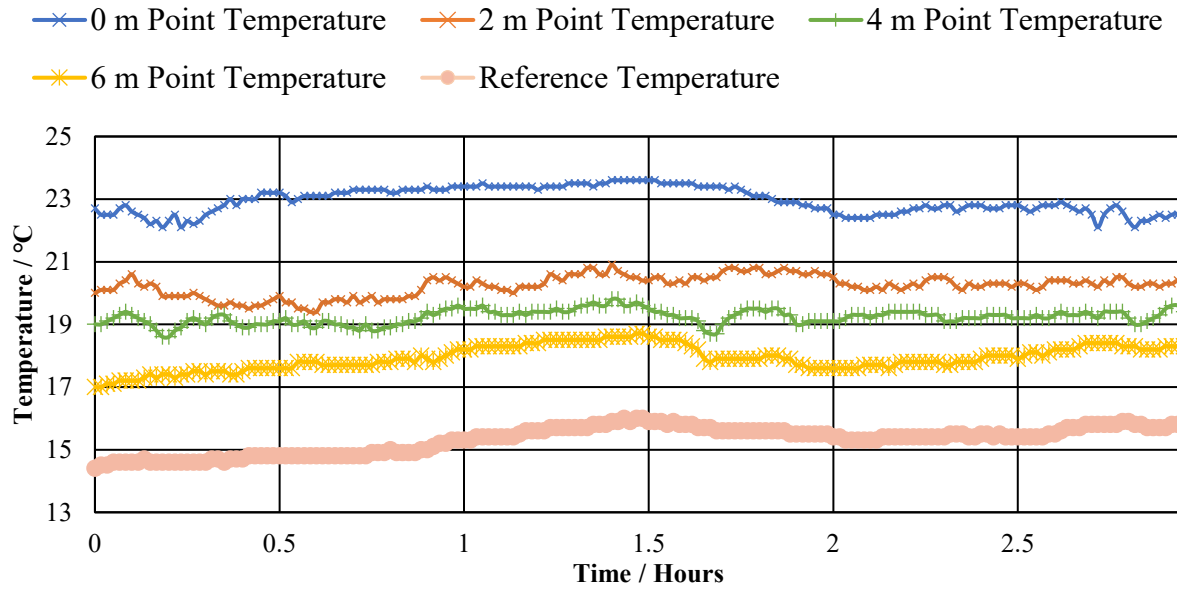
Figure 33 Temperature Profile for Bed Depth of 34 cm
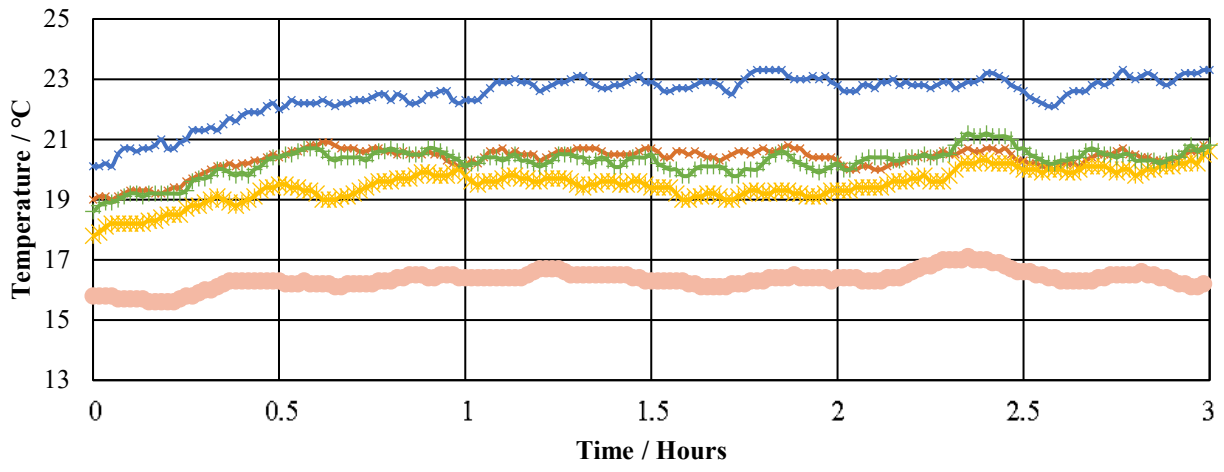
Figure 34 Temperature Profile for Bed Depth of 43 cm
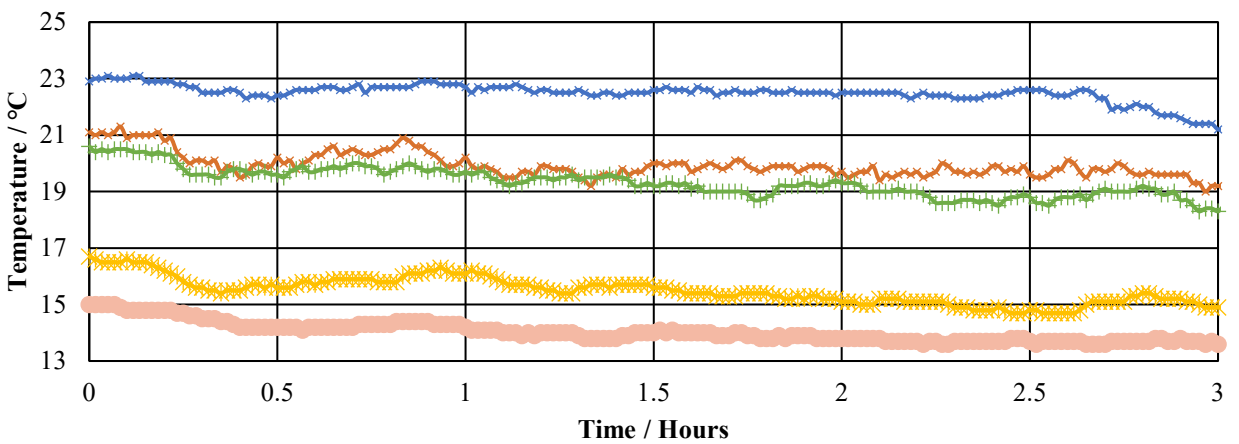
Figure 35 Temperature Profile for Bed Depth of 24.5 cm
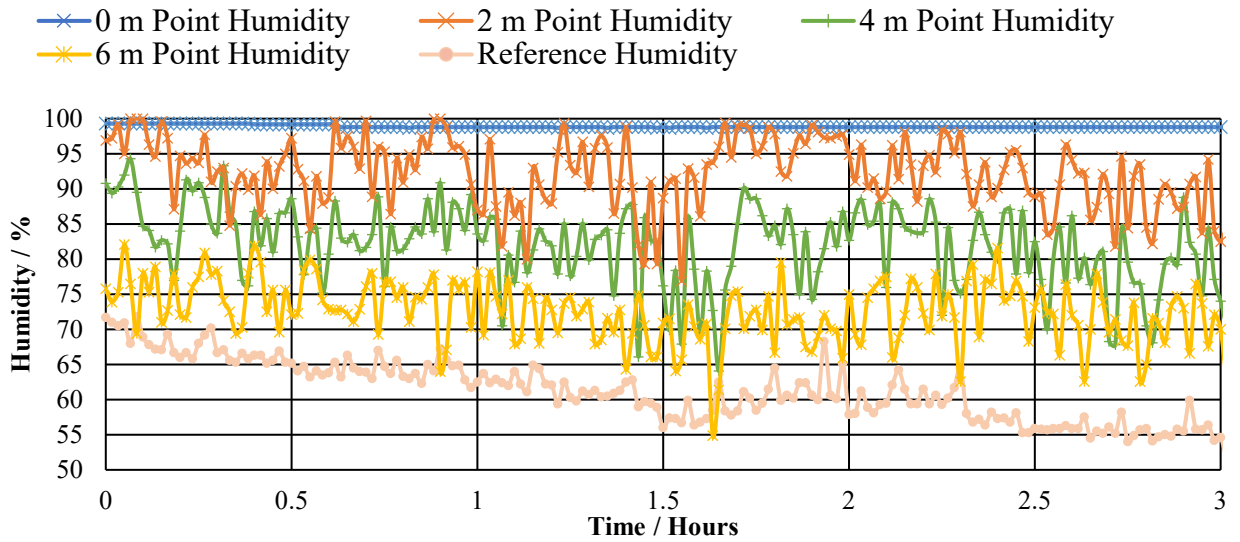
Figure 36 Humidity Profile for Bed Depth of 34 cm
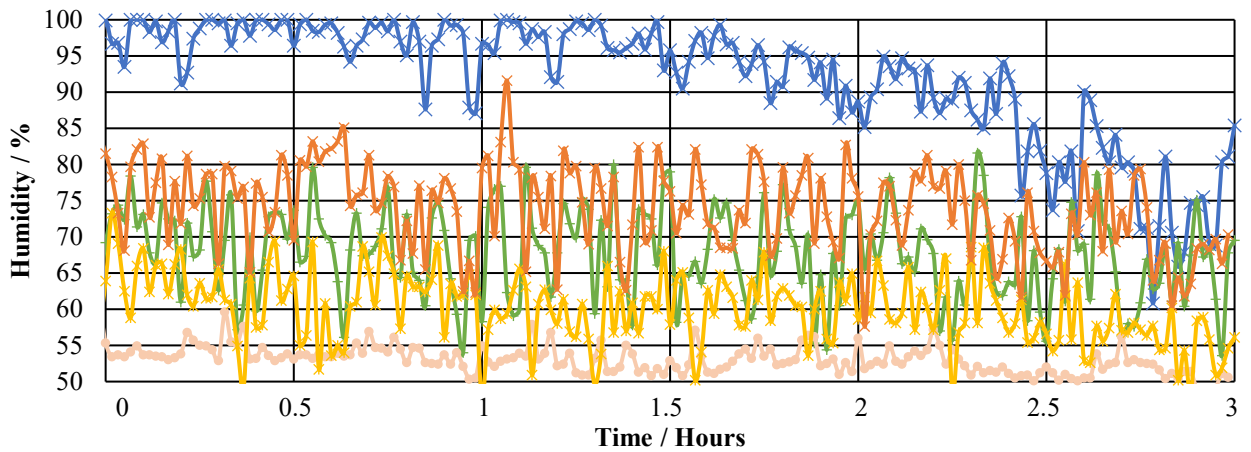
Figure 37 Humidity Profile for Bed Depth of 43 cm
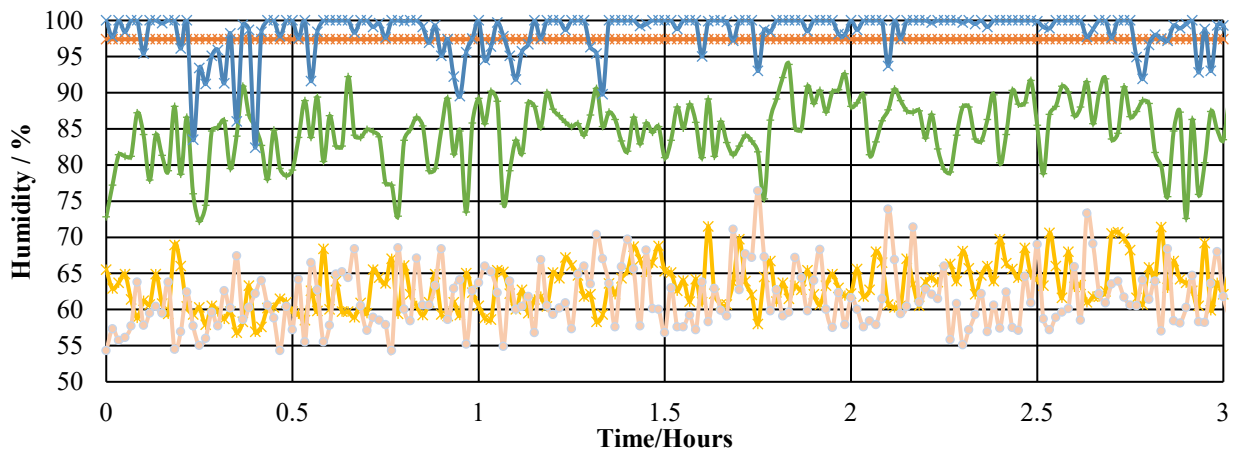
Figure 38 Humidity Profile for Bed Depth of 24.5 cm
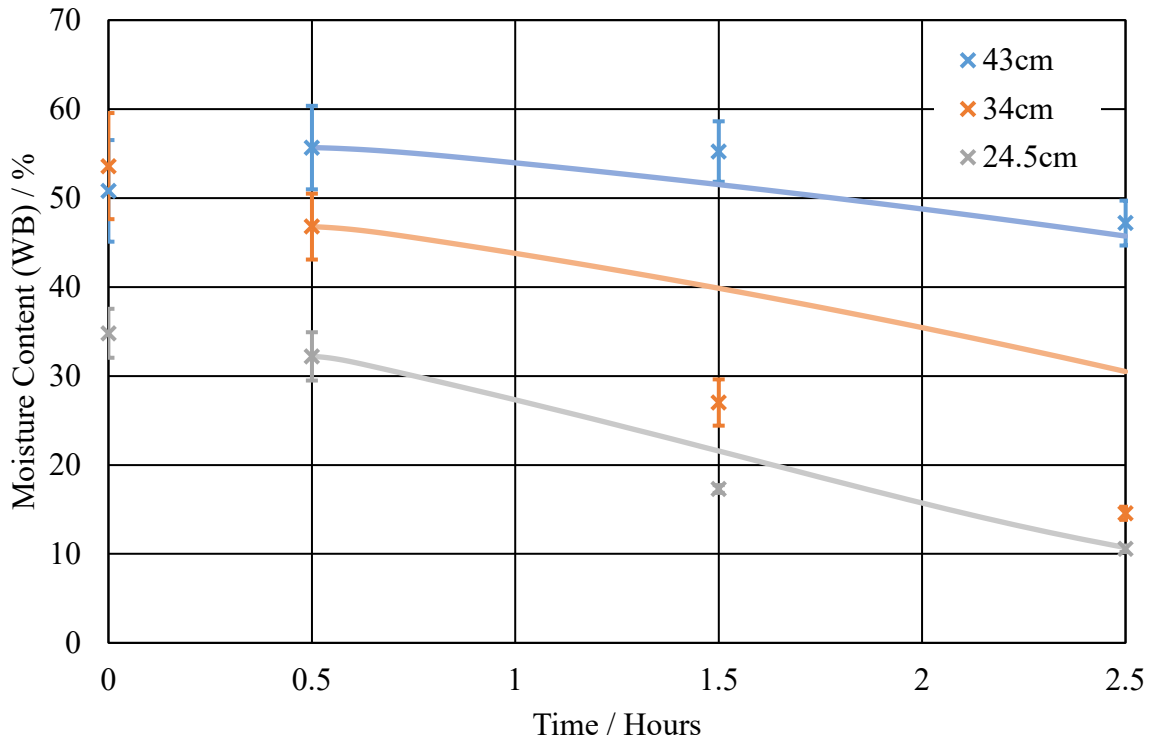
Figure 39 Experimental and Simulated Results for Moisture content Over Time at Different Bed Depths (k_{evap} = 0.065 s^{-1})
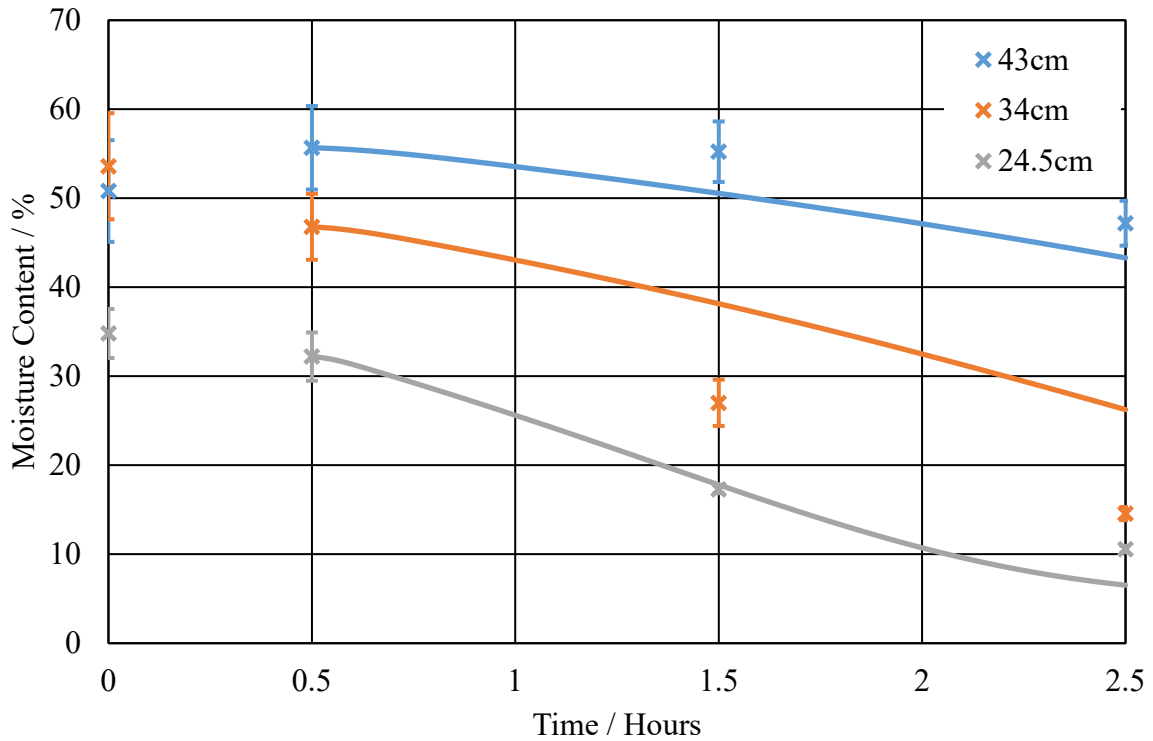
Figure 40 Experimental and Simulated Results for Moisture content Over Time at Different Bed Depths (k_{evap} = 0.1 s^{-1})

Figure 39 and Figure 40 shows the moisture content of woodchip as it dries over time and considers both experimental results (scatter plots) and numerically obtained results (line plots). The three different bed head depths are reported, as denoted by the legend. The X-scatter plots are based on the experimentally measured values of MC, as presented in Table 31. The centre of the plot denotes the average of the 5 MC values sampled, and associated error bars. The results of the CFD simulations are presented in the figure by the solid lines. For the experimental values, in Figure 39, the x-axis denotes the time taken for the woodchip to traverse the drier, at time 0, the chip is in the hopper and at 2.5 hours, the batch of chipped product is at the end of drier. The CFD simulations also report the drop in MC over time and start at time = 1 hour. Results within Figure 39 and Figure 40 show that the shallower the bed depth, the lower the final woodchip moisture content, though all of these experiments had different starting moisture conditions and so a more valid comparison is the difference in moisture content from the initial to the final measures. It can be seen that the moisture content for the deepest bed depth, 43cm, increases from the value for the inlet hopper woodchip. This increase in moisture may be due to lower layers of chip, loosing moisture and this moisture condensing on colder chip above. Notably, the chip in the drier for the largest bed depth was cold to the touch on the top layer of the woodchip bed. The highest bed depth had the smallest change in moisture content of approximately 8.5 %, the medium bed depth had ~32 % change and the lowest bed depth had a change of ~22 %. The lowest bed depth reached a significantly lower moisture content and though the change is less than that of the median bed depth this is believed to be due to the lower moisture content reached and therefore a lower rate of mass loss, supported by the curvature of the simulation plot for 24.5 cm shown in Figure 40.

Temperature

The temperature results from the simulation through the woodchip bed shown in Figure 41 to Figure 43. These show that the greater the bed depth the greater the temperature loss over the

woodchip bed as there is more water evaporated. The shallower the bed depth the greater the difference between the temperature profile at 0 m, 3 m and 6 m across the woodchip bed.
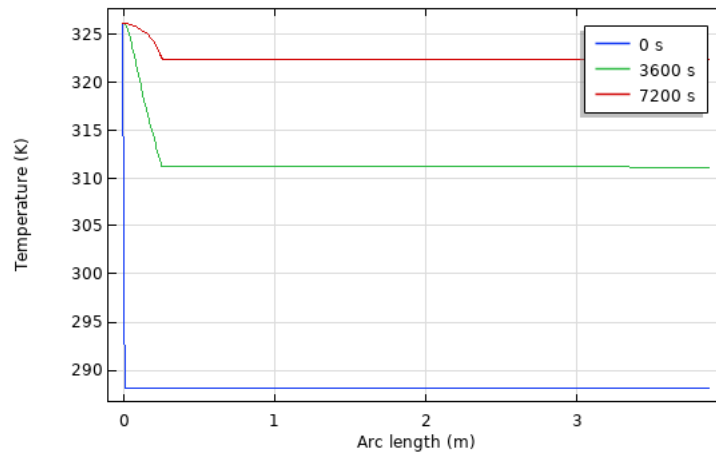
Figure 41 Temperature Profile Across the Woodchip Bed - Simulation 24.5 cm Bed Depth

In Figure 41 the lower temperature drop between the profile at 3600 s and 7200 s shows that the woodchip has lost moisture and the rate of drying is becoming closer to equilibrium.
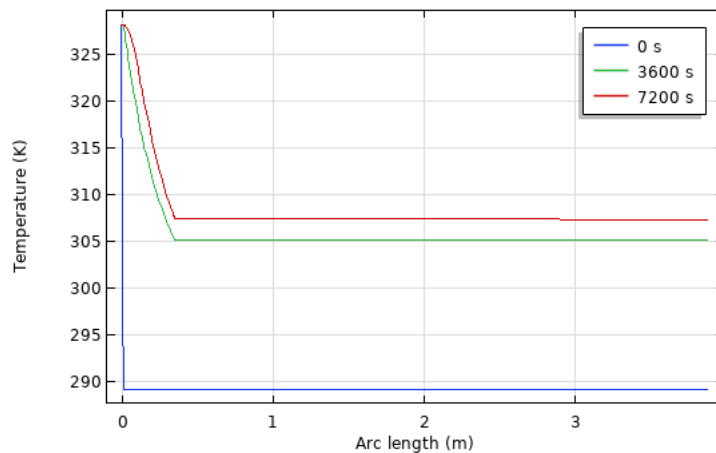
Figure 42 Temperature Profile Across the Woodchip Bed - Simulation 34 cm Bed Depth

The smaller temperature difference between 3600 and 7200 s in Figure 42 shows that the woodchip has decreased slightly in moisture content, but is not as close to equilibrium as the 24.5 cm bed depth simulation results.
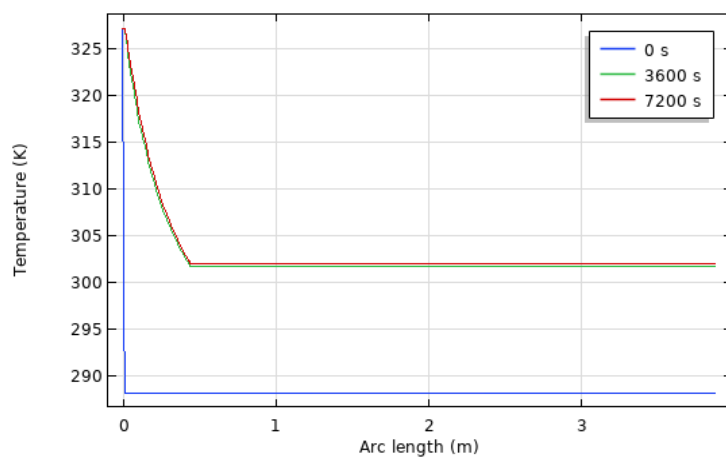
Figure 43 Temperature Profile Across the Woodchip Bed - Simulation 43 cm Bed Depth

The temperature profiles in Figure 43 for 3600 s and 7200 s are very similar showing that the enthalpy of evaporation is similar at the 0 m and 3 m points in the woodchip bed when the bed depth is 43cm.

6.2.5 Investigating the Top Floor Speed

The bed depth is altered in simulation which replicates the experimental setup. Moisture content, humidity and temperature data was recorded on site.

Table 32 Parameters - Variable Top Floor Speed, Interval Time

	5 min	Maximum 12 min	Minimum 3min
Temperature Air	SET-53 °C	SET-50 °C	SET-52 °C
Temperature Boiler	SET-86 °C	SET-85 °C	SET-85 °C
Velocity of Air	SET-0.14 m.s^{-1}	SET-0.14 m.s^{-1}	SET-0.14 m.s^{-1}
Top Floor Interval	5 min	Maximum 12 min	Minimum 3min
Bed Depth	24.5 cm	24.5 cm	24.5 cm
Cover	No	No	No
Time in Open Bed*	2 hours	4 hours 48 minutes	1 hour 12 minutes
X_m0 (DB)	0.475	0.782	1.01
Average External Temperature	15°C	13°C	14°C

*Approximate dependent on where the moving floor starts

Table 33 Average Moisture Content Readings - Variable Top Floor Speed

	5 min		Maximum 12 min		Minimum 3min	
	Start Mass	Moisture %	Start Mass	Moisture %	Start Mass	Moisture %
MC In	5.42±0.13	34.80±3.02	5.38±0.2	42.41±3.48	5.54±0.32	50.65±3.31
MC Start of Bed	5.17±0.20	32.20±3.03	5.42±0.24	43.88±4.78	5.47±0.21	50.36±5.46
MC Middle of Bed	5.34±0.16	17.30±0.48	5.47±0.17	13.58±0.83	5.42±0.17	42.14±7.91
MC End of Bed	5.02±0.04	10.57±0.41	5.24±0.10	4.68±0.22	5.17±0.17	25.99±3.23

Moisture Content

To evaluate the effect of the top floor interval on moisture content at locations along the drier, the results were plotted with 1, 2, 3 and 4 referencing each location. To compare the physical experimental results to numerical-simulated theoretical the results, physical and theoretical, were plotted against time. For the theoretical and physical data, the dependency of overall moisture content change on the interval time was evaluated.

In Figure 44 to Figure 46, the humidity readings of the drier bed are reported, pertaining to the experiments carried out on the effect of moving bed speed. The humidity change is reported over time. As with the previous analyses it is shown that there is large fluctuation in humidity during the day. Foremost in Figure 46 it is evident that the humidity above the drier at the end of the bed is very low. This is expected due to the very dry material produced at this setting. The humdity profile for the 12 minute floor speed run (Figure 46) is more evenly distributed along the bed, this is because at each point along the bed less water is evaporated from the chip as metioned previously. The fastest run (3 minute floor speed Figure 44) has a high humidity value from the start to the four meter point of the bed, this suggests that after this point there is a decrease in evaporation rate. This decrease in rate can be seen clearer on the 12 minute and 5 minute runs (Figure 47) as the moisture content value taken at the centre of the bed is lower than the predicted value, suggesting a steeper initial rate than the simulation and a greater change in rate as the moisture content lowers.
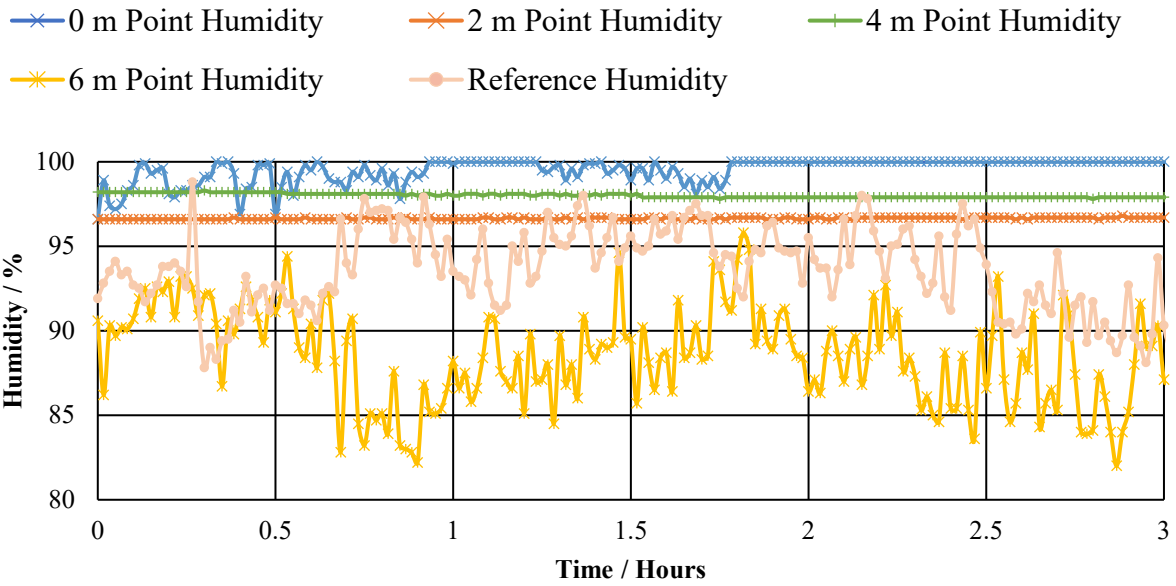
Figure 44 Humidity Profile for Top Floor Speed of 3 minutes
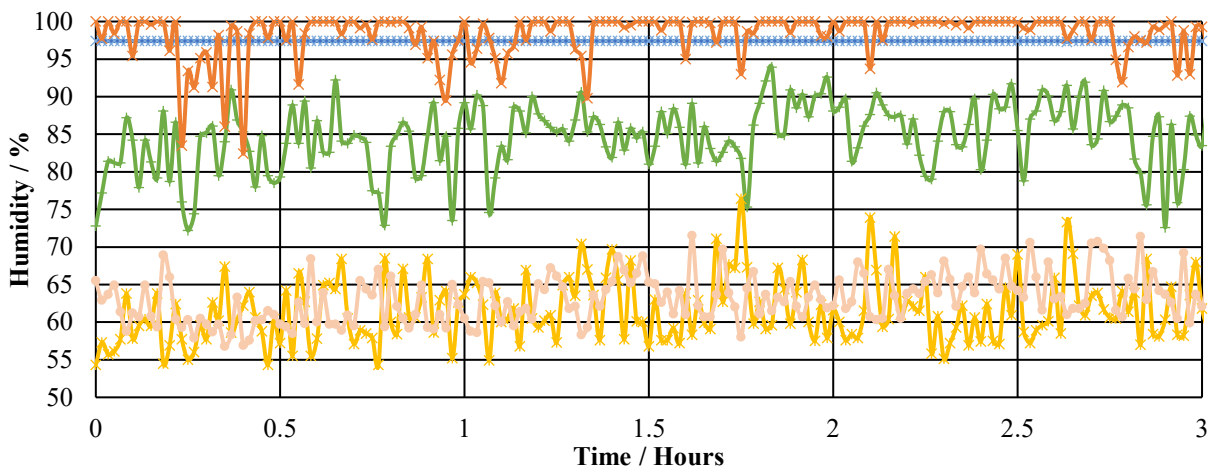
Figure 45 Humidity Profile for Top Floor Speed of 5 minutes
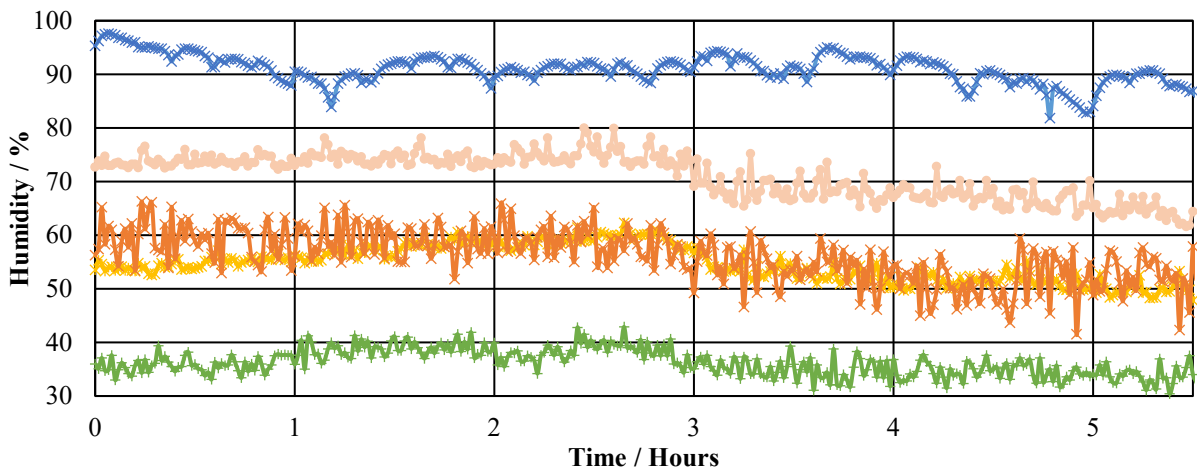
Figure 46 Humidity Profile for Top Floor Speed of 12 minutes

Using a k_{evap} as 0.1 s^{-1} resulted in Figure 48, the results are similar to the 5 minute and the 12 minute experimental data and for the 3 minute run resulted in slightly higher values. Therefore to fit the data to the results at 5 minutes a lower k_{evap} value would be better suited and for the 3 minute interval between floor movement a larger k_{evap} would be better suited, an example of which is a lower k_{evap} of 0.065 s^{-1} shown in Figure 47.
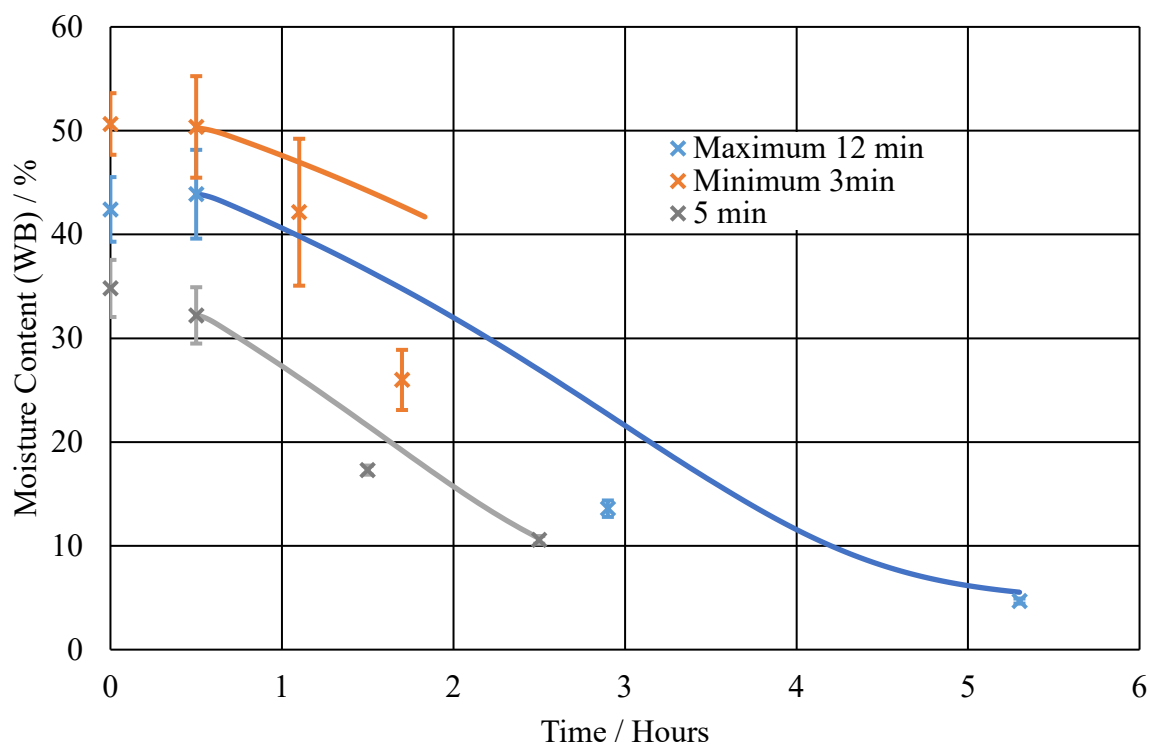
Figure 47 Measured and Simulated Results Different Drier Bed Speeds (k_{evap}=0.065 s^{-1})
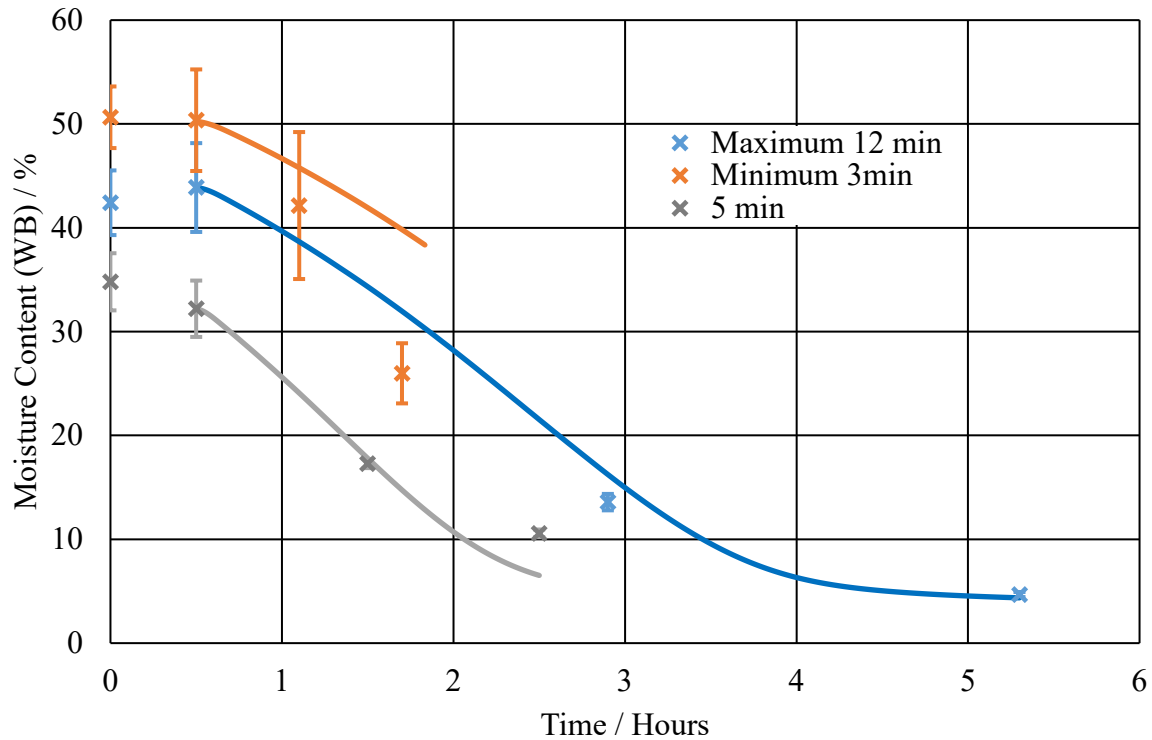
Figure 48 Measured and Simulated Results Different Drier Bed Speeds (k_{evap} = 0.1 s^{-1})

Figure 47 and Figure 48, show simulated and experimentally measure values of moisture content, with results pertaining to the drier bed speed, for the moisture content vs time and k_{evap} of 0.1 s^{-1} and 0.065 s $^{-1}$. The experimental measurements are presented by scatter plots and are based on results illustrated in Table 33. The results of the CFD simualtions are given by the line plots. The simulated results in Figure 48 and Figure 47 show that the rate of moisture loss starts to decrease as a moisture content of 10% on a wet basis is reached. In the case of the results from the drier bed however, the readings from the centre of the bed and for the fastest bed speed show that the rate of drying for moisture contents higher than 10% is in practice faster than predicted and the rate decreases earlier than this point. This difference in drying rate shows that the mixing induced by the moving bed improves the drying rate at higher moisture contents as the surface area in contact with the airflow changes with woodchip orientation. The simulation fits the 12 minute and 5 minute runs well showing that as moisture content decreases over time the mixing has less of an impact on the drying rate.

Temperature

Figure 49 to Figure 51 report the temperature readings above the drier bed for the 3 experiments surrounding moving bed floor speed. As with previously reported plots, transient profiles of temperature with time were plotted. It is noticeable that for the 12 minute interval test, the temperature of the bed is much higher than in the other two instances (Reference temperature is about the same in all cases). The slowest run (12 minute interval time Figure 51) had a more consistent temperature along the first four meters of the drier bed, the fastest and median runs had similar temperature distributions (Figure 50 and Figure 49) with the hotter temperature at the start of the drier bed and 2-4 °C lower at the centre of the drier bed. The airflow is hotter at the start of the open drier bed as hot air is passed through the metal grating before and after the sensor. At the start of the drier bed, to the heat source less heat is lost to the surroundings at this point. At the end of the bed the sensor is above the point at which the metal grating and hot air flow end, making it closer to an average value between the surrounding air temperature and the drier bed temperature. The centre of the bed is hotter for the 12 minute floor speed run due to the lower moisture content at this point, meaning less heat is taken from the surroundings to evaporate the water in the woodchip.
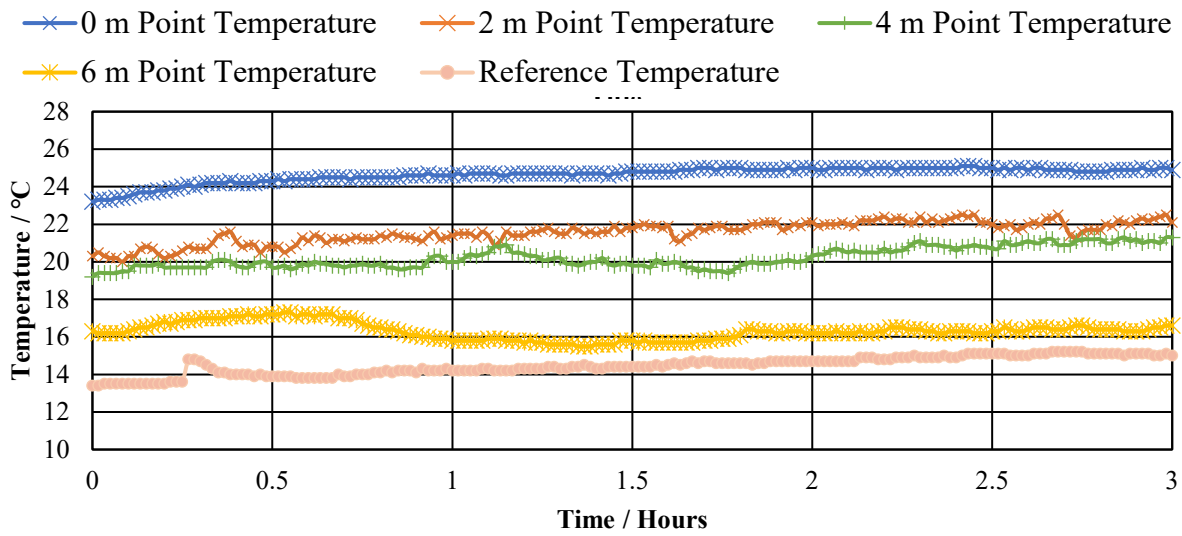
Figure 49 Temperature Profile for Top Floor Speed of 3 minutes
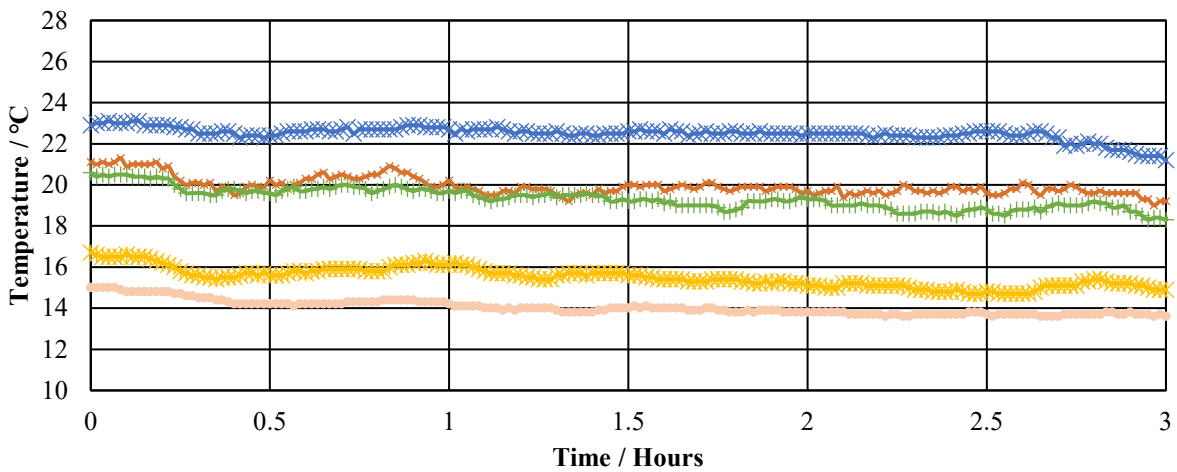
Figure 50 Temperature Profile for Top Floor Speed of 5 minutes
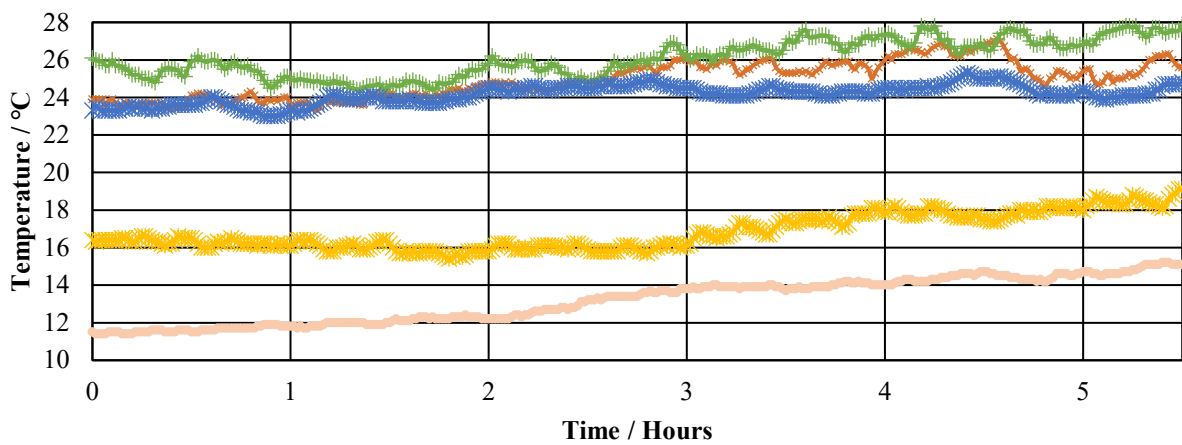
Figure 51 Temperature Profile for Top Floor Speed of 12 minutes

Taking temperature profile results from the model for across a 2D Cut line of the bed, in Figure 52 is used to show the temperature over time.
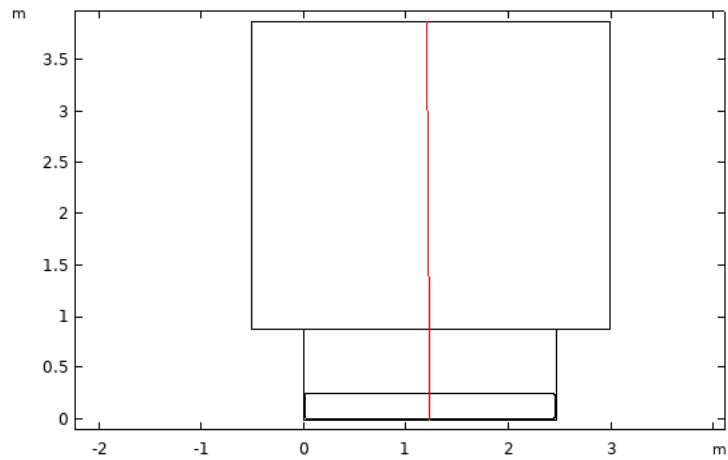
Figure 52 2D Cut Line of Woodchip Bed

Within Figure 53 to Figure 55 it can be see that the temperature at the bottom of the bed near the heat source is hotter than the air stream above at 0 m, 3 m and 6 m across the open drier bed, over the woodchip the temperature decreases and above the woodchip bed the temperature is constant. In real world conditions there is additional convection and airflow above the drier as well as heat loss through conduction through the metal drier walls so the temperature above the drier bed is colder.
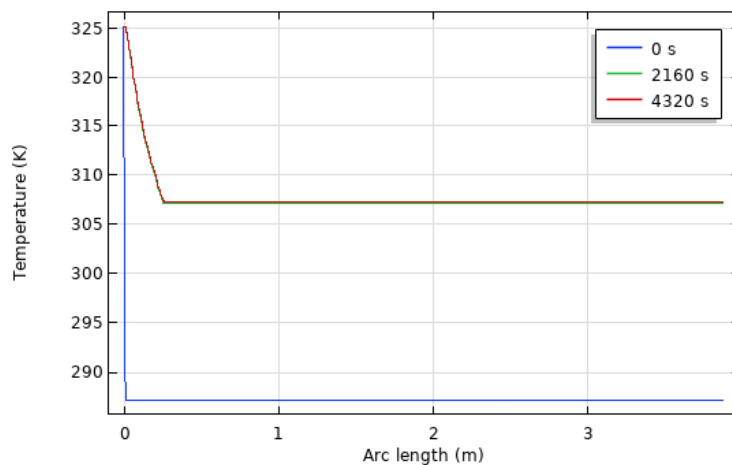
Figure 53 Temperature Profile Across the Woodchip Bed - Simulation 3 minute floor Speed

As you can see in Figure 53 at the middle and final (3 m and 6 m) readings the simulation shows a very similar temperature profile, in the simulation at these points the moisture content of the woodchip is more than 37 %(WB), the gradient of the moisture lost over time curve (Figure 48) is nearly constant. Characteristically over a constant rate drying period the moisture loss over time is constant and therefore within this model so is the heat loss of the carrier gas (air).
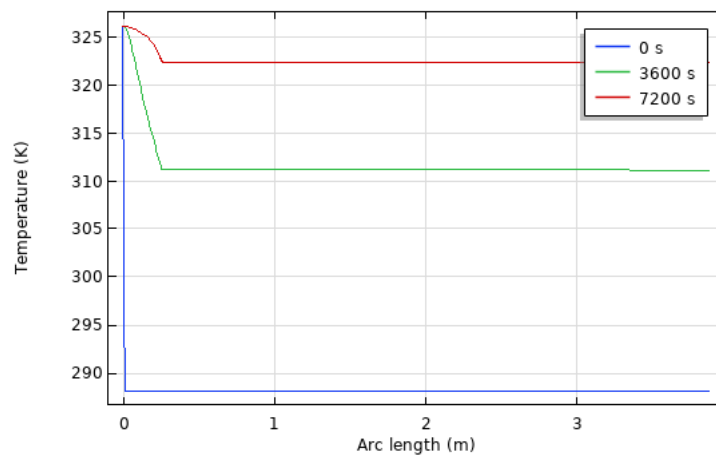
Figure 54 Temperature Profile Across the Woodchip Bed - Simulation 5 minute floor Speed

Within Figure 54 the temperature at 3 m and 6 m along the open drier bed significantly increases as the woodchip has a lower moisture content and less heat is required to evaporate a smaller quantity of water.
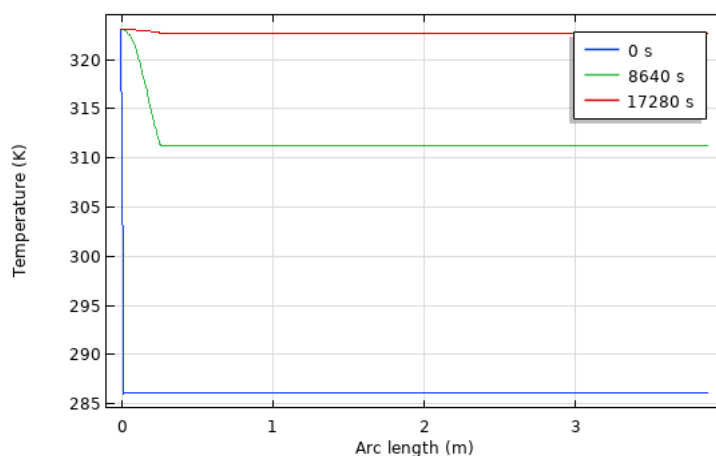
Figure 55 Temperature Profile Across the Woodchip Bed - Simulation 12 minute floor Speed

Figure 55 shows that over the open drier bed the temperature above the bed increases closer to the temperature of the inlet air, this is due to the moisture content being close to the equilibrium moisture content of the solid, when it is in equilibrium with the surroundings.

6.2.6 Investigating Covering the Drier

The drier was covered using a 2 mm thick felted fabric, in aim to withhold heat into the system and allow water vapour to escape. Similar to the bed depths and floor speed experiments the moisture content of woodchip, temperature and humidity were recorded over time.

Table 34 Parameters - Covering Drier Bed

	Uncovered	Covered
Temperature Air	SET-53 °C	SET-54 °C
Temperature Boiler	SET-86 °C	SET-87 °C
Velocity of Air	SET-0.14 m.s^{-1}	SET-0.14 m.s^{-1}
Top Floor Interval	5 min	5 min
Bed Depth	24.5 cm	24.5 cm
Cover	No	Yes
Average External Temperature	15 °C	18 °C

Table 35 Average Moisture Content Readings - Covering Drier Bed

	Uncovered		Covered	
	Start Mass	Moisture %	Start Mass	Moisture %
MC In	5.27±0.18	51.91±4.15	5.30±0.25	49.57±5.54
MC Start of Bed	5.32±0.11	48.61±5.16	5.42±0.14	48.34±11.48
MC Middle of Bed	5.44±0.26	46.81±4.96	5.25±0.26	45.26±5.65
MC End of Bed	5.31±0.18	34.78±6.06	5.19±0.11	19.57±0.94

The drier was covered after three hours of operation, which can be seen in both the humidity and temperature graphs with the temperature and humidity rising at the end and 4 m down the open bed section of the drier (Figure 56 and Figure 57 respectfully).
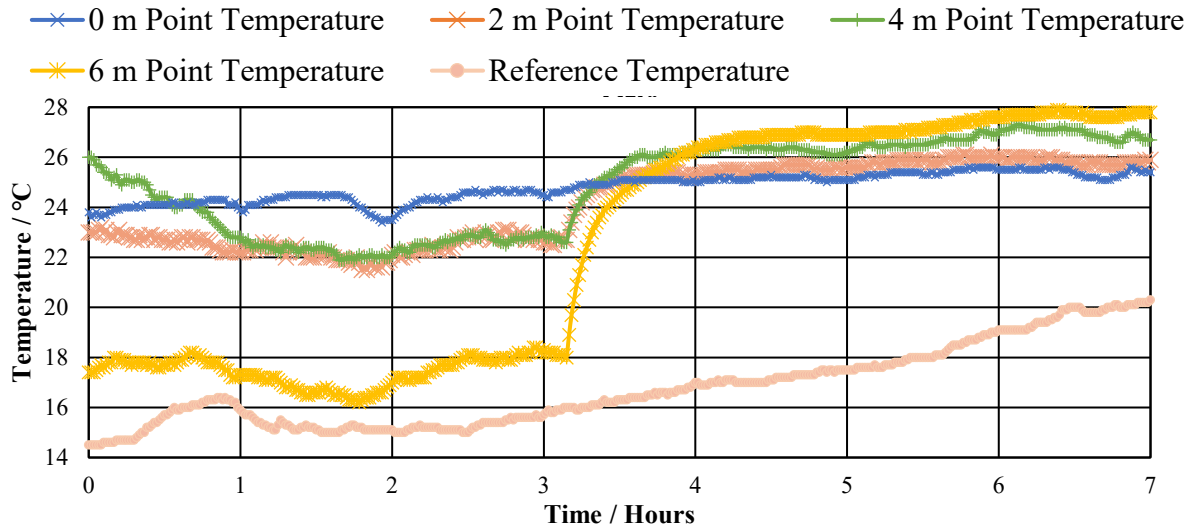
Figure 56 Temperature Profile for Uncovered (0-3 hrs) and Covered (3 hrs-7 hrs) Drier Bed

As seen in Figure 56 covering the drier increased the temperature at the end of the bed by over 8 °C which is over 40 % of the starting temperature. The temperature at the start of the bed is seemingly uneffected by covering the drier which is likely because the air is denser due to the high amount of water vapour that decreases the air flows velocity, the woodchip in this section has also come from the hopper which is heated meaning the woodchip also holds energy in the form of heat. Figure 56 shows that heat is conserved by covering the drier with a more uniform profile across the drier when it is covered, an area of concern however is the humidity once the cover is placed on the drier as if the air becomes saturated and the cover damp water can rehydrate reversing the effects of drying.
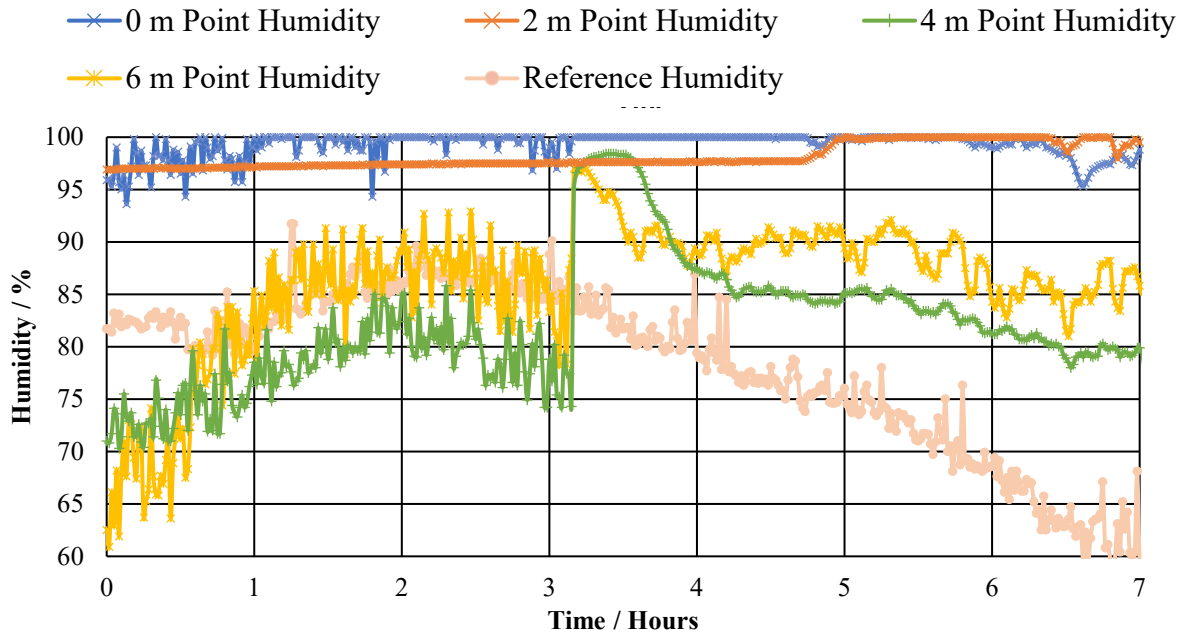
Figure 57 Humidity Profile for Uncovered (0 -3 hrs) and Covered (3 hrs-7 hrs) Drier Bed

From Figure 57 there is much less of an impact on the humidity at the start of the bed and 2 m down the open bed section. There is an increase however, in the humidity at 4 m and the end of the bed (6 m) where the air does not reach full saturation in this instance and does start to reduce back to a lower level. The reduction in humidity is likely due to an increase in moisture transport across the cover, as the cover acts as a porous medium as the fabric heats up any liquid water on the sheet can evaporate exiting atmosphere around the drier. The general trend in an open atmosphere is a higher temperature a lower humidity as water vapour rises to a higher point of lower pressure. With a cover this is not the case, the higher the temperature the more moisture is drawn from the woodchip into the atmosphere above, with the only means of escape through the fabric and the higher the temperature of the sheet above the greater the amount of moisture transport across the fabric.
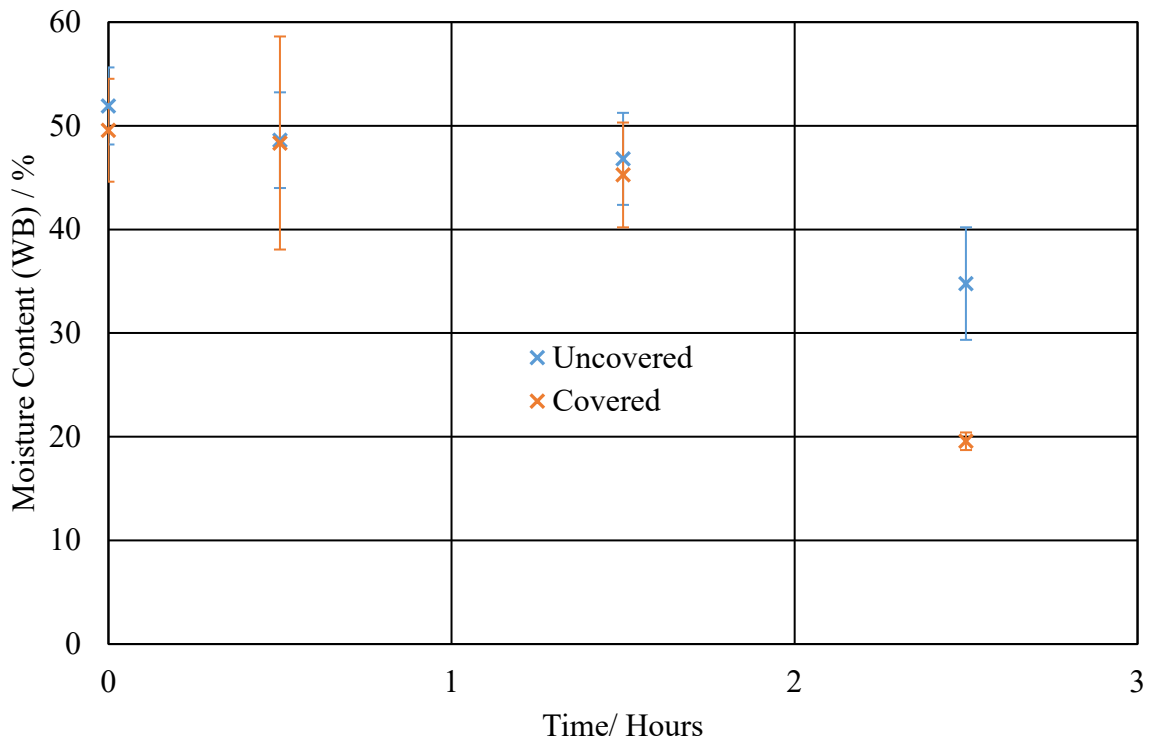
Figure 58 Moisture Content Results for the Covered and Uncovered Drier Tests

Figure 58 shows that closer to the end of the drier bed covering the drier has a greater impact, this may be due to the slight humidity build up over the first 4 m of the drier with water able to escape in the airflow at the end of the drier, rather than diffusively before this point. The moisture content at the end of the drier was ~15 % less when covered by comparison to covered. The data was taken with very similar starting moisture contents making these results easily comparable. The covered drier data was taken at maximum 4 hours after covering the drier, over which time diffusion through the cover may have a lower mass loss than the woodchip itself causing an increase in humidity over time, in addition to the initial increase in humidity because of covering the drier. Over larger lengths of time the moisture within the now covered drier may build up reducing drying, though preliminary results show covering the drier will aid the drying process.

6.2.7 Temperature Profiles
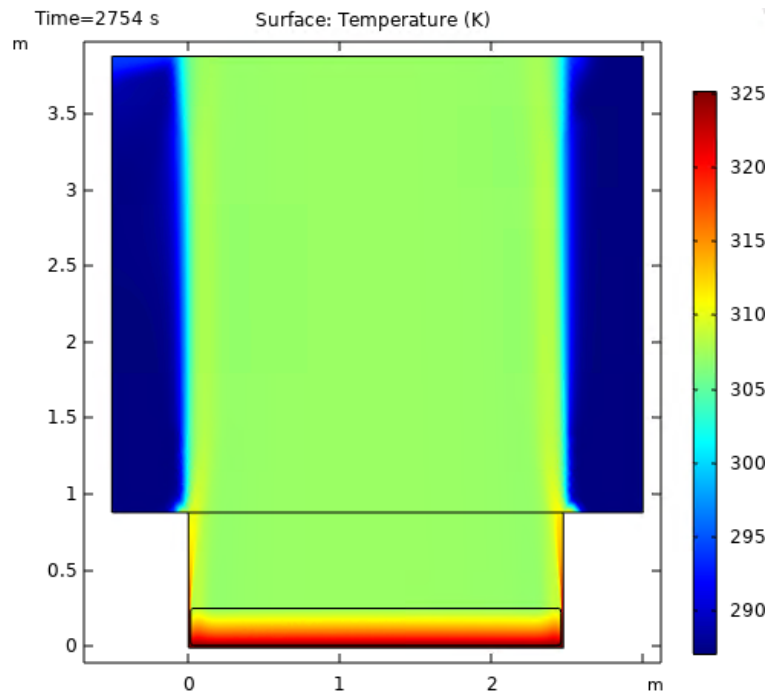
Figure 59 Temperature Profile Drier Bed for 3min Floor Speed Run

The temperature through the woodchip bed, shown in Figure 59, has a heat front moving upwards, away from the heat source, as the water within the woodchip and the woodchip itself takes heat from the air stream the temperature above the bed is approximately 20 °C less than the heat source. Figure 60 shows a similar effect for the single woodchip, with greater temperatures closer to the edge of the woodchip, which is in direct contact with the hot air flow.
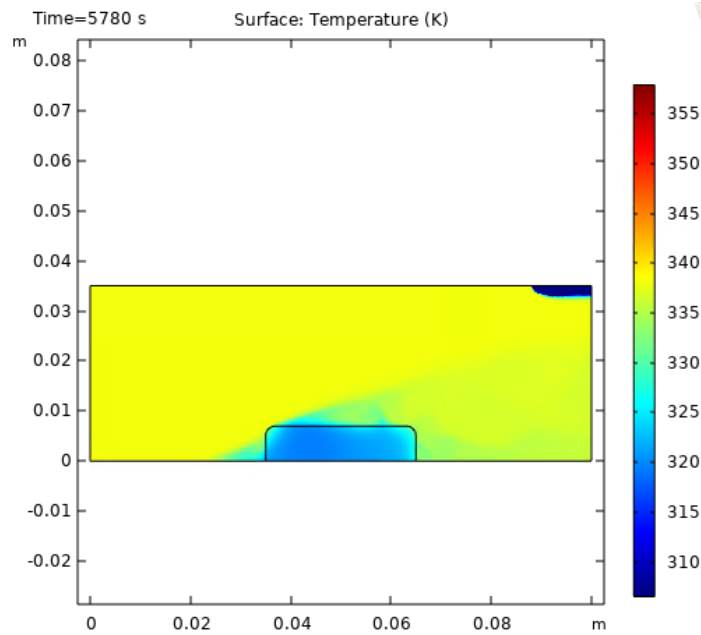
Figure 60 Temperature Profile Around the Woodchip with Velocity 2.3 m.s^{-1}

6.2.8 Velocity Profiles

Velocity profiles of the bed drier are consistent over time and due to the porosity of the porous

media, the velocity through the bed is similar to the inlet velocity as shown in Figure 61.
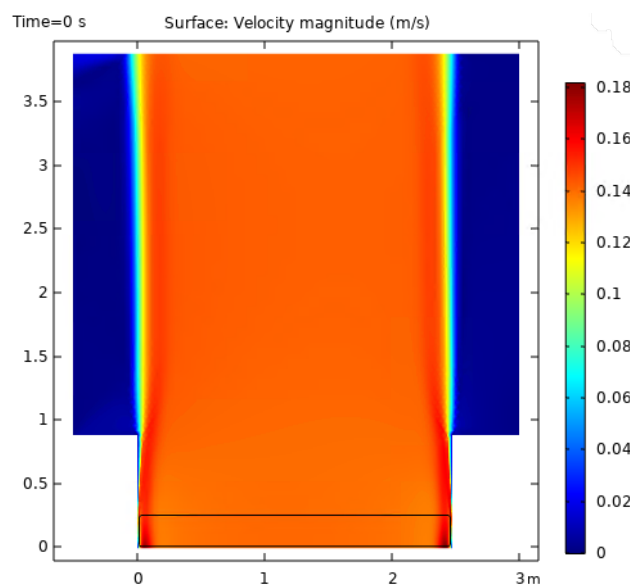
Figure 61 Velocity Profile Drier Bed for 3 min Floor Speed Run

For the single chip model, as the air flow over the chip is a factor of ten greater the airflow

around the woodchip as can be seen in Figure 62 (a) and (b). Next to the woodchip, there is a

region of unsteady airflow. As the flow separates over woodchip, causing recirculation of air occurs. This region is highly unstable and causes numerical convergence difficulties.
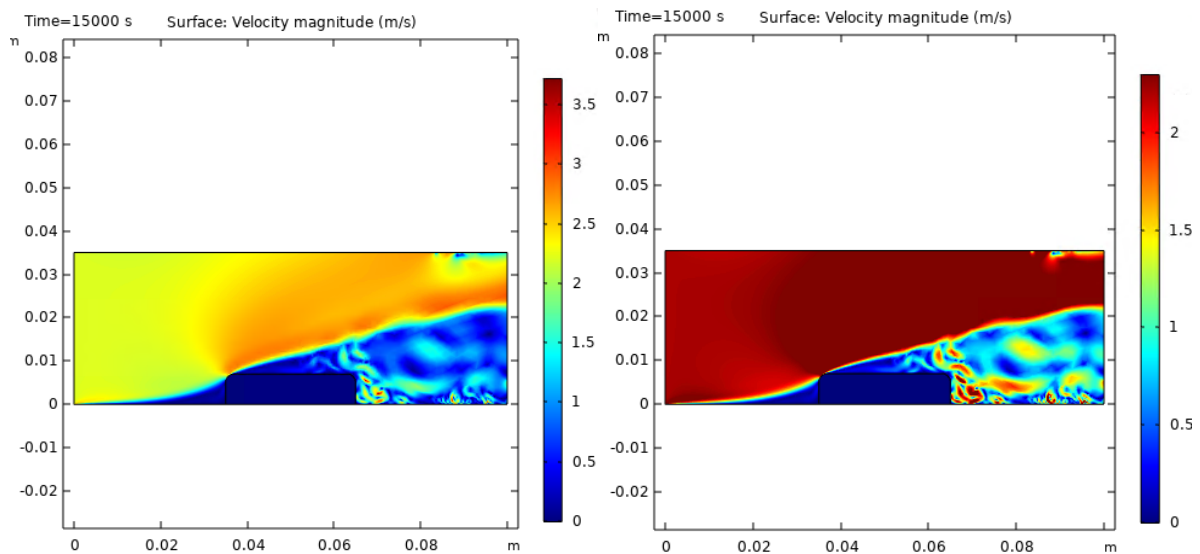
Figure 62 Velocity Profile Around the Woodchip with Velocity 2.3 m.s^{-1} (a) With the colour scale 0 – 3.5 m.s^{-1} (b) With the Colour scale 0- 2 m.s^{-1}

6.2.9 Moisture Content Profiles

Moisture content profiles of the drier bed show that water front moves from the bottom of the bed to the top, with the base temperature increasing and the water vapour diffusing upwards to the surface where it can escape. Close to the edges, the water front is slightly higher as shown in Figure 63.
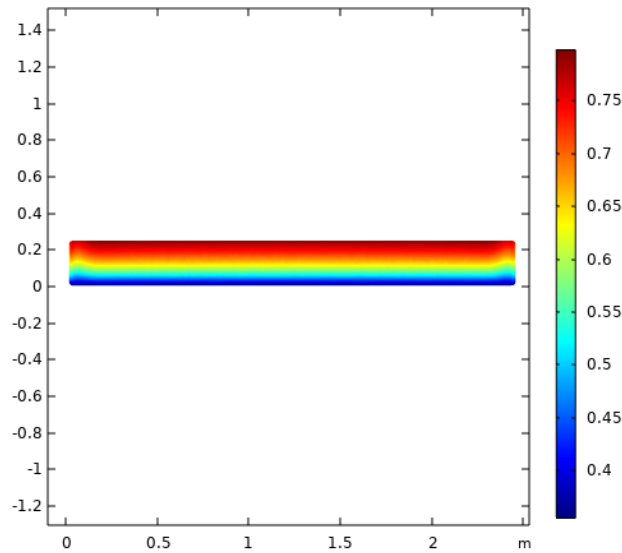
Figure 63 Moisture Content Profile of Woodchip Bed 3 minute Floor Speed

Figure 64 shows the moisture content within a woodchip with airflow over the chip, more moisture is lost on the side opposing the air flow, as the velocity is lower in this section heat transfer is more effective. As the moisture content becomes significantly less, the centre of the chip holds the most moisture as heat has to transfer through the woodchip to this region.
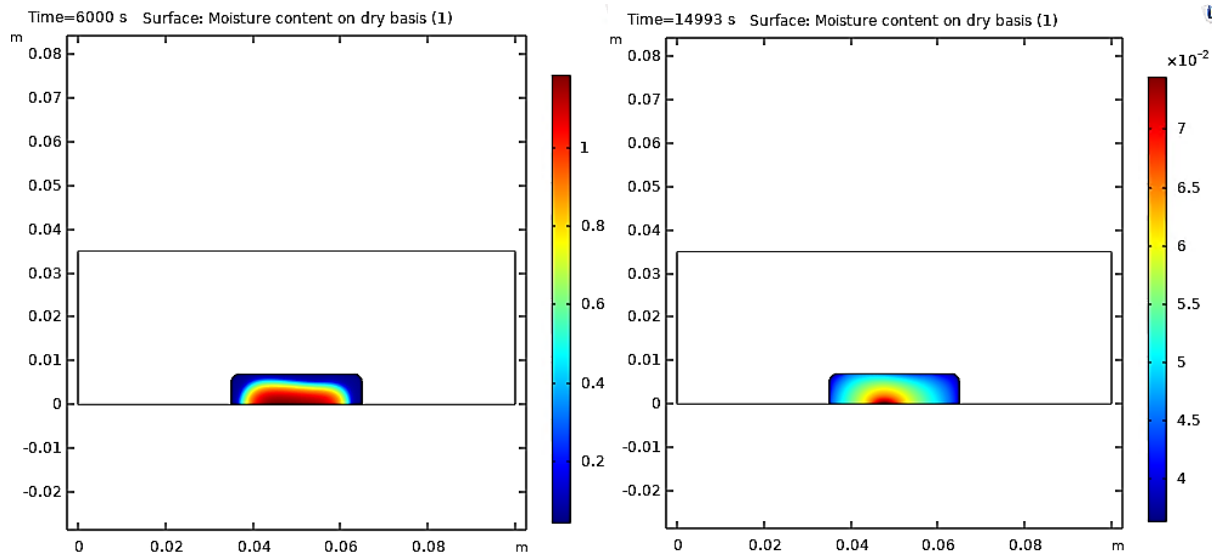
Figure 64 Moisture Content Profile of Woodchip Bed 2.3 m.s^{-1} Velocity (a) at 6000 seconds (b) at 14993 seconds

6.3 Chapter Summary

This chapter reviewed the simulation and experimental results. The effect of different situational parameters was assessed to measure the effect of moisture content in a packed bed and on a single wood chip. Showing moisture content data under specific conditions, in addition to temperature, velocity and moisture profiles. The ANSYS simulation shows the air flowrate decreases along the drier bed and the bottom corner has a stagnant area of air. This has highlighted that a better designed bed dryer can improve the flow through the packed bed. Example of this research can be found in (Phupaichitkun et al., 2013) and (Román et al, 2012). Both experimental analyses and the Comsol-based CFD simulations have shown that an increase in air temperature and flow rate independently decreased drying time. The simulations and experiments also showed good qualitative agreement and a discussion around and the reasoning for the differences between experiments and simulations was also included. Experiments also determined that IR drying was faster than convective drying at the same temperature. Increasing the bed depth, changing floor speed and covering the drier influenced moisture loss across the open section of the drier.

Chapter 7

Drying Conclusions and Recommendations

This section includes recommendations based on the drying results obtained in the previous chapters. These parameters and trends are also defined.

7.1 Effect of Temperature

An increase in temperature led to a faster rate of drying in both the simulated and measured results. Between 65 °C, 75 °C and 85 °C the increase in rate for the experimental results (steepness of the curve) is less than that for 55 °C to 65 °C, with the curves at these temperatures closer together. Increasing the temperature by 30 °C decreased the time taken to reach 0.2 % moisture content on a wet basis by approximately 30 minutes. On the drier, the increase in temperature would have a similar effect; however, this increase in temperature would mean changing equipment and infrastructure as well as increasing the risk of fire and burns. The throughput limited by storage, which reaches full capacity over the course of the year as supply and demand changes. It is recommended not to increase the temperature of the hot air flow over the drier bed as the benefits would not outweigh the costs.

7.2 Air Flow Rate

Increasing air flow rate decreased the drying time, however within the system at Bowland Bioenergy, an increased air flow will likely reduce the temperature of the air flow as less heat will be transferred per volume, assuming amount of heat energy transferred each second will stay constant. Doubling the airflow decreased the drying time by around 50% for 1.6 m.s^{-1} to 2.3 m.s^{-1}.

7.3 IR Drying

Infrared drying of woodchip was significantly faster than convective drying, for one woodchip the drying took less than half the time, with a lower final mass reached. This drying method

heated the base plate as well as the woodchip itself to higher temperatures than convective drying alone under the same temperature settings.

7.4 Bed Depth

Increasing the bed depth decreases the change in moisture content from the inlet to the final product. At 43 cm, the moisture content reduced by less than 8% from a starting MC of 55%. When the bed depth was at 34 cm, experimentally, the change in moisture content was found to be close to that of a 23 cm bed depth. The model however showed bed depth to have a greater impact at 34 cm compared to 23 cm than the experimental data. This difference in impact is likely due to the mixing of woodchip during the movement of the drier bed which allows for more moisture to be released. The movement also aids the heating process as the woodchip is churned so heat is more evenly distributed.

In the case of the 43 m bed depth, the height of the chip in comparison to the ladder height of the moving floor did not create enough mixing within the bed to move woodchip from the base of the bed to the top layer before the heat is lost. Insufficient mixing at this height was evident from the top layer of the drier bed, being cooler and damper than that at the other bed depths. In turn, the simulation represented the lowest and highest bed depths well but the mixing effect from the ladder floor impacts the 34 cm bed depth greater than the others measured. The decrease in moisture content from the top of the drier bin to the start of the drier bed also indicates that the 34 cm bed depth had less woodchip within the drier bin, altering the starting temperature of the woodchip, where by comparison the initial woodchip temperature in model was set to the external temperature measured.

7.5 Floor Speed

Decreasing the interval time between runs decreases the time the woodchip is dried for, reducing the change in moisture content from the inlet to the product stages. The impact however of this between 5 minutes and 3 minutes is minimal this is likely because the moisture

transport during the first two hours of drying is faster. The similarity between the 3 minute and 5 minute runs by locational comparison show that mixing during drying has an impact on drying rate and, as the mixing induced in both cases is indifferent, the moisture content change in both the 5 minute and 3 minute cases are very similar.

7.6 Covering the Drier

From experimental data covering the drier increased to moisture loss by ~15 %, showing that the moisture content at the end of the drier bed was lower than the uncovered bed, yet the moisture content at the centre of the drier bed is similar to the uncovered result. The humidity and temperature increased after covering the drier bed, allowing more heating of the woodchip and water, however the increase in humidity causes a smaller concentration gradient and reduces the driving force and rate. The end of the drier has an open section where the moist air can escape and this is likely why the moisture content reduction from covering the bed becomes greater at this point. Over longer periods of time the increase in humidity could significantly limit drying due to droplets forming and the water falling back onto the woodchip.

7.7 Recommendations

Industrial Recommendations

The laboratory experiments showed a maximum of 20 minutes saved in drying time between 55 °C and 85 °C, demonstrating that changing the equipment to achieve a higher temperature would not be beneficial to Bowland Bioenergy. The cost of equipment changes would outweigh the expenditure saved with time, higher temperatures would mean increased safety measures and more fuel and greater control would likely be required to achieve higher temperatures.

Relatively increasing the flow rate will increase demand on the heat exchanger to achieve the same temperature. This increase on heating and power requirements for the hot air would not be beneficial as the increased utility and equipment costs (if the pump does not have a variable speed drive) would have a small impact on the flow rate over the woodchip. Due to large

surface area, the effective change in air speed is minimal, with the current value at 4 m³.s⁻¹, an increase of 1 m³.s⁻¹ would achieve, with no frictional losses, an increase in air flow rate of 0.035 m.s⁻¹ over the drier bed.

To implement the maximum bed depth, the auger would need to have an increased capacity. In practice however, the maximum bed depth cooled the inlet air stream causing very little evaporation, the median bed depth produced similar results to the smallest bed depth and it is recommend that increasing the depth to this median bed depth (34 cm) when a higher throughput is needed and storage is available. This increase in bed depth would lead to having to top up the drier more frequently, as this would increase throughput by 39 %.

$$\text{Throughput(BD, FI)} = \left(\text{BDm} \times 2.24\text{m} \times \left(0.05\text{m. min}^{-1} \times \frac{5}{\text{FI min}}\right)\right) \text{m}^3\text{min}^{-1} \qquad (200)$$

Where FI is the top floor interval time, between 3 minutes and 12 minutes and BD is the bed depth between ~0.23 m and ~0.43 m.

The floor speed can be altered depending on the input and the output, for the 24.5 cm bed depth setting an estimation of the floor speed required can be calculated if the final moisture content is more than 0.05. When the interval between floor movements is 5 minutes the time taken to travel to the end of the bed is 2 hours, for 12 minutes the time taken is 4 hours 48 minutes and for three hours the time taken is 1 hour 12 minutes. Based off these times the relationship between the interval time and the time in the drier is shown in Equation 196 if the time required in the open bed drier is known the required floor speed can be calculated.

$$\text{FI} = \frac{\text{Time(hours)}}{0.4} \qquad (201)$$

Using MATLAB curve fitting to fit a two-term dependent equation to the data acquired Equations 202 and 203 were derived.

From Experimentation:

$$\text{Time}(X_{in(WB)}, X_{out(WB)}) = 4.058 + 0.118(X_{in(WB)} - X_{out(WB)}) - 0.2173X_{in(WB)} +$$

$$0.003658 \left(X_{in(WB)} - X_{out(WB)}\right)^2 - 0.003238 \left(X_{in(WB)} - X_{out(WB)}\right)X_{in(WB)} +$$

$$0.002826 \times 10^{-5} \left(X_{in(WB)}\right)^2 \qquad (202)$$

From Simulation:

$$\text{Time}(X_{in(WB)}, X_{out(WB)}) = 0.02462 + 0.02377(X_{in(WB)} - X_{out(WB)}) +$$

$$0.002084\, X_{in(WB)} + 0.001205\left(X_{in(WB)} - X_{out(WB)}\right)^2 + 0.001112\left(X_{in(WB)} - \right.$$

$$\left. X_{out(WB)}\right)X_{in(WB)} + 8.017 \times 10^{-5} \left(X_{in(WB)}\right)^2 \qquad (203)$$

Where FS is the floor speed, Time is the time in the open drier bed, $X_{in(WB)}$ is the input moisture content, $X_{out(WB)}$ is the desired output moisture content (≥ 0.05). If the floor speed is outside of the operating range of the drier blending of two different moisture contents will be required, however this is likely not the case for Bowland Bioenergy based on the moisture content of products offered.

Covering the drier improved the drying capabilities though this was on a dry and warm day where the external temperature also increased. The cover decreased the temperature change across the bed showing that heat was conserved by using the cover. However, humidity also increased, for long periods of time this could cause an issue though there is an outlet for the moisture at the end of the drier which may combat this. Over the four-hour period the outlet moisture content was lower than the uncovered operation and there was less dust released from the drier.

IR drying is only suitable for shallow depths of woodchip as IR can only penetrate through 0.3mm of wood (Dupleix et al., 2013). Introducing IR drying to the process may increase the efficiency however the design of the drier would need to be significantly altered, changing existing infrastructure with a large capital expenditure, the current setup allows for the product

to be utilised heating the airflow. If the drier does require replacing a combination of IR and convective drying has been proven as a more efficient drying method (Mujumdar, 2006).

Academic Recommendations

The evaporative rate constant was changed between the drier bed and the single chip models, with the value significantly reduced for the drier bed simulation. This reduction in mass evaporated per unit area could be because the temperature profile of the drier is less than the temperature used from the heat exchanger, as shown by Figure 2 the temperature of woodchip when the drier is on is closer to 30 °C. Though this image could have been taken shortly after the start-up of the drier, the model does not account for the initial heating of the air flow and the temperature used is measured before the air enters the drier and will be in practice lower than the temperature used.

The results in Section 6.2.5, investigating the top floor speed, for all cases simulated the moisture content centre of the drier bed in practice was less than the simulated value for the equivalent time. This suggests a higher diffusivity transport at this time and the value of D_{cap} could be further adjusted.

This study investigated the effect of air flow rate, bed depth, floor speed, covering the drier and IR drying on woodchip drying, in addition to this the effect of relative humidity, porosity and woodchip size could be investigated.

Further development of this model would be to extend the physics to a 3rd dimension, taking into consideration the radial, tangential, and longitudinal permeability of liquid water and water vapour through woodchip.

7.8 Chapter Summary

In this section shows the conclusions from the simulation and experimental data for the effect of temperature, air flow rate, top floor speed, covering the drier and IR drying. Temperatures

influence on drying time in the laboratory was not significant, with a 30 ℃ temperature increase leading to a 30 minute time saving, this time saving would not be beneficial on a energy consumption, cost and current capacity basis. Increasing air flow rate by ~40 % decreased the time taken by 50 %, this experiment however was over a single woodchip and the cost of keeping the same temperature on site whilst increasing flowrate would outweighs the benefits. Increasing the bed depth from 23 cm to 34 cm is recommended as the moisture loss was similar. It is recommended to adjust floor speed based on product required and inlet moisture content. Covering the drier showed promise with regards to conserving heat in the system, however further investigation of humidity increase over time is required.

Chapter 8

Dust Characterisation

Dust from woodchip production originates from the unit operations and poses a serious issue for Bowland Bioenergy, due to the health and safety implications of the presence of dust and the impact on human health. Health surveillance guidelines in addition to mitigation and exposure monitoring methods are therefore identified. This section also provides understanding around the chipping, drying process and characteristic mechanisms of the industry and the resulting dust generation. The chapter also characterises the dust, with respect to shape, size, density and surface area. This characterisation of the collected dust is then used in the design sections, which pertain to reducing dust in the workplace through employing various mitigation devices. In the first instance, dust prevention by optimising unit operations to produce less dust is idealised over dust mitigation. This however would likely have a greater effect on production of woodchip as opposed to installing a mitigation system which may not be possible to impose.

8.1 Introduction and Problem
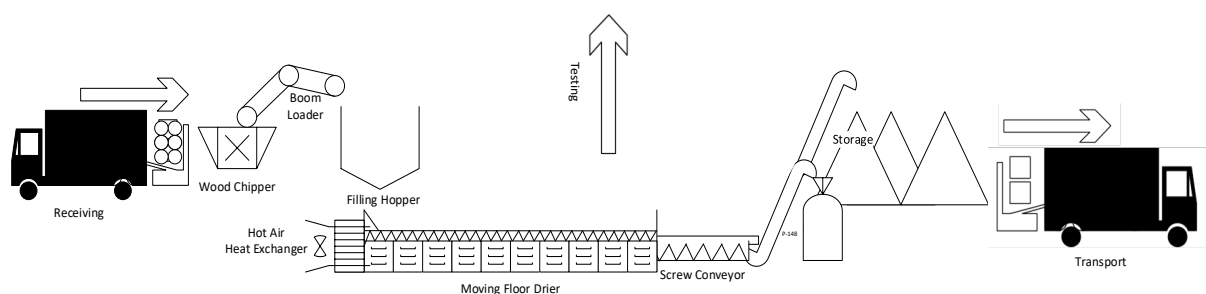
Figure 65 Process Overview

As wood is sent through a mechanical breakdown process dust is predominately generated from mechanical impact and abrasion (Kreith, 1998), shown in Figure 65 as the wood chipper. Aiming to understand measure and evaluate the production of dust from the manufacturing process, key questions involve:

1.   What are the possible impacts of wood dust?

2.   How does processing woodchip generate dust?

3.   Would operating parameters affect the production of dust?

4.   Is there any way of preventing dust production?

5.   What are the physical properties of the particulates produced, especially size and shape?

6.   What is the best method for collecting the produced particulates?

This section addresses these questions regarding the requirement for dust prevention and mitigation, focusing on dust mitigation through further investigation of questions 1.-5. in Chapter 7 and question 6. in Appendix D.

8.1.1 Impacts of Wood Dust

The risk of dust is not only to machinery, but also the hazards to health and risk of explosion have been widely categorised within the process industry. ATEX (Appareils destinés à être utilisés en ATmosphères Explosives) directives first published in 1994 and 1999 (Eckhoff, 2003) outline equipment usage in potentially explosive atmospheres and the protection of workers from a health and safety perspective from explosive atmospheres, providing standards for manufacturers and users or equipment. Later in 2002, Dangerous Substances and Explosive Atmospheres Regulations (DSEAR) were the first specific legal requirement to carry out a hazardous area study, resulting in a "zone" plan of workspaces.

In selecting process equipment, Ingress Protection, or IP, ratings provide details specifically of the degree of protection against dust and water ingress. Additional details added to the IP rating show more information related to the device protections. This rating does not only cover the protection of equipment against the ingress of solid foreign objects and water,

ingress protection also should consist as well of protection of users against access to hazardous parts.

Hazards to Machinery

Dust can clog and break machinery, affecting instrumentation and safety systems. On site at Bowland Bioenergy, the heat exchange unit for the drier requires daily filter changes due to the volume of dust produced from processing the woodchip. This causes further expenses in labour, disposal and material. It is therefore beneficial for machine operation to reduce the amount of dust present in the facility.

Hazards to Health

The majority of impacts on health that relate to dust are respiratory related. Other impacts on health include injury from fire or explosion, dermal conditions and injury due to mechanical implications caused by dust. The smaller the particle, the deeper the particle can potentially penetrate lung tissue and other areas of the body, which can create irreversible damage. It is even reported that wood dust can cause a rare type of nasal cancer (Executive, 2020c). The workplace exposure limit is 3 mg.m^3 for hardwood and 5 mg.m^3 for softwood (Executive, 2020b). The most common health risks are (Rylander and Jacobs, 1994):

- *Respiratory:* Prolonged exposure to wood dust can cause a variety of respiratory disorders, such as bronchitis, asthma and allergic rhinitis, which is inflammation of membranes in the nose and throat. The effect of dust is dependent on characteristics and person specifics. The majority of particles greater than 5μm get trapped in the upper respiratory system, whilst particles smaller than this are more hazardous as they slowly travel to the lower respiratory system (Baran et al., 2009). Here they diffuse through and sediment on surfaces within the body, where the removal rate means that they stay in the body for over a month.

- *Eyes:* Wood dust can cause irritation in the eyes and as with any abrasive material if rubbed the surface of the eye can become cut and damaged.

- *Dermal:* Skin contact with wood dust can cause rashes; the dust absorbs moisture drying out the skins surface. Repeat exposure can cause an allergic reaction, as a sensitizer some people can have an immediate allergic reaction with wood and for others it can take longer to take effect. For this reason, it is best to limit exposure to the skin as much as possible even if these symptoms are not present.

- *Biohazards:* In moist environments moss, fungi and bacteria can grow on wood dust. The decomposition of wood from fungi also leads to the release of toxins which can be hazardous.

Risk of Explosion

For an explosion to occur, in addition to the oxidant, an ignition source and fuel within a fire triangle a dispersion and confinement are also required, shown in Figure 66. Without confinement an explosion could become a flash fire or a jet fire. Mixture refers to the fuel and air - these need to be mixed to increase the combustion rate, which rapidly increases the size of a fire. An incident often referred to in demonstrating the severity of the risk of dust within process industries is the 2008 Imperial Sugar refinery explosion and fire. On the 7th of February 2008 14 workers were killed and 38 injured (Hiles, 2010). The presence of ignitable dust significantly increased the impact of an ignition that occurred in a conveyor in the sugar refinery. Surrounded enclosures were not equipped with dust removal systems or dust-explosion vents. The conveyor was under two 2300 tonne silos, which stored granulated sugar. From an unknown ignition source, the primary explosion dislodged dust that had accumulated around the factory over time, raising flammable particulates into the air propagating further explosions throughout the building. Each explosion added to the shock wave that cascaded through the refinery, lifting concrete floors 8 cm thick, moving wooden roofs and rupturing

water pipes. These pipes caused the sprinkler system to fail, with superheated air instantaneously causing burns. Workers had little time to escape in dark smoke-filled areas from the heat and projectiles.
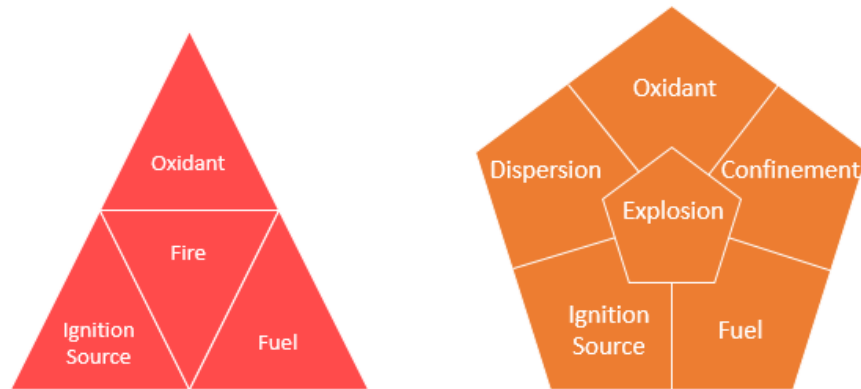
Figure 66 Fire Triangle and Explosion Pentagon

Described as diffusive combustion within fires, the fuel requires contact with oxygen in the air from diffusion. Refining solids to smaller sizes increases the exposed surface area, which in the case of dust if it is suspended in air - the exposed flammable surface area does not decrease over time, which is the case with solid flammable material. Ignition of new flammable material is therefore easier within dust clouds meaning the material will burn rapidly and energy is unable to dissipate quickly releasing heat and reaction products. How effectively energy dissipates is affected by the surface area exposed to an oxygen rich atmosphere. The more flammable the atmosphere or the greater the dust concentration the higher the chance of an explosion. For dust within air, the lower explosive limit is the minimum concentration at which dust is capable of exploding. As a rule of thumb, for wood flour HSE suggests 60 g/m^3 (Executive, 2020a).

For an explosion to occur, the dust needs to be combustible, dispersed in a cloud, at a density above the lower explosive limit and within an oxygenated environment. Particle size is particularly important in for dust explosion as covered in Chapter 7.

Hazards Which May Lead To Explosion

Open Flames

Policies and procedures are in place to control open flames. Smoking is not permitted on the Bowland Bioenergy site. Hot work is not performed on site, if this was the case hot-work-permit procedures should be followed, with safety personnel and combustible material control. Contractors to the site should follow their own procedures in addition to those on site. The biomass boiler on site is temperature controlled and situated away from the dust source.

Electric Spark Ignition

Were possible all equipment should be ATEX Zone 0 rated, for equipment such as the auger motor where this rating is not applicable IP6X rated enclosures should protect equipment and installed in flammable dust free environments.

Mechanical Generated (Friction) Spark

Moving parts in machinery itself can cause ignition, with bearings and motors generating heat, it is important for equipment to be lubricated and continuously maintained. Foreign objects within high speed equipment such as chippers and augers pose a spark risk (Mannan and Lees, 2005). To avoid small metal objects entering the process, magnetic separators could be installed in suitable locations, alternatively a metal detector which trips machinery may be more suitable. Electronic magnets should also have a trip system if the electric current supplying the magnet is affected. Further foreign bodies may be removed through pneumatic separation; however, the materials require a significant difference in density and separation is also affected by size, this would also be a costly option.

Hot Surface

In the case of drying, a hot surface is present by design, however the minimum ignition temperature of wood dust is around 370 °C with a particle size of 71 μm with the ignition temperature decreasing as particle size decreases (Osvaldova et al., 2020), which is much lower than the operating temperature of the equipment. Flammable dust should not accumulate near

the heater and air for combustion should be from a dust free zone away from where people are normally employed.

Particle Size

It is known that the finer the dust the easier it is to ignite, and it is also reported that dust coarser than 100~300 microns is not usually explosive (Eckhoff, 2003). Agglomerates are often formed by fine dusts, these are lumps which make it difficult to test particle size if the coagulation persists in the test solvent, in Section 8.2.3 agitation stopped this from occurring during tests. The degree of dispersion in air as well as the concentration of dusts determines the strength of an explosion. Further particle size analysis can be found within Section 8.2.3.

Primary and Secondary Explosions

As within the case of Imperial Sugar subsequent explosions can occur as primary explosions are ignited by an ignition source and this primary explosion ignites secondary explosions. Air flow from the initial explosion disturbs settled dust, as an increase in temperature causes gas expansion, the process of subsequent explosion is called deflagration.

8.1.2 Wood Dust Production

The dust produced from woodchip manufacturing is primarily from the chipping and drying unit operations. As logs are fed into a dedicated hopper, they are chipped mechanically using a toothed disk rotor. This chipping produces various sizes of woodchip and as wood characteristically has various knots and grains splitting by force produces much smaller particulates (Testing and Sciences, 1966). Alternative chippers include a drum chipper which has steel discs mounted on a common rotor shaft with knives placed between each pair of discs forming a continuous cut across the width of the chipper. Knives cut against a fixed anvil with chip being retained in the chipper drum until it can pass through a screen which control particle size. The logs are stored outdoors and loaded by hydraulic crane. The wood log feed is partially

air dried prior to this procedure, because of this the natural lignin and moisture within the bark prevents the dust suspension within the atmosphere. This process is also takes place outside so any particulate production is unable to accumulate.

Drying is the main contributor for dust within the environment at Bowland Bioenergy. The smaller particles, which are stuck to larger chips, dry and decouple from the bulk material as air flows through. In addition to this, mechanical aggregation of the drier free trapped dust (as well as moisture) from the woodchip into the air stream. The larger production of dust from this area is visually apparent, as there are larger dust deposits around the drier, noticeably more-so than any other location. Dust from downstream process such as extraction via augers, haulage, storage and loading is somewhat apparent. However, the woodchip from the drier sent to a vertical dispenser via augers contains significantly fewer light particulates than the feed and the processing stages.

8.1.3 Wood Dust and Operating Parameters

During drying dust becomes airborne as hot air passes over the woodchip. Further, as the dust attached to the woodchip dries it becomes less adhered to the surface of the chip as the surface tension and mass of the water holds it in place. Hotter airflow will dry the dust faster and a greater speed of airflow will provide a larger force to dislodge particulates, aggregation is vital to release trapped moisture and any reduction of these parameters will increase the drying time. Though these parameters affect the quantity of airborne dust at any given time they do not have an effect on overall dust present in the process as smaller particles have been produced prior to the drying stage, and the drying stage is where the particles are released. These particulates would become loose from the woodchip once the desired moisture content is reached regardless of the driers operating parameters.

As these operating parameters affect the drying process and the moisture released has a direct effect on the dust released hence the only operational method to reduce the wood dust is to reduce the abundance of smaller particulates produced within the process.

8.1.4 Prevention of Wood Dust Production

Reviewing the process at Bowland, as described in Figure 65, and an evaluation of operating parameters it has been determined that the source of the dust has been determined to be the wood chipper. To completely reduce the dust from this process, the wood would have to be splinter free with a straight wood grain flush lined directly with the chipper's blades. The nature of the wood that is chipped for woodchip usually has twisted grain, making it unsuitable for use in other industries and all wood is prone to splintering. Hence, reducing the dust through altering the chipper is significantly limited by the woodchip itself, therefore mitigative methods are investigated (in Appendix D) rather than preventative methods.

8.2 Wood Dust Characterisation

For designing filtration and ventilation systems it is first necessary to understand the material that needs to be removed from the environment. This section investigates the dust produced from the drier system at Bowland Bioenergy. The analysis techniques used include: Scanning Electron Microscopy (SEM), size distribution by laser refraction and Brunauer–Emmett–Teller (BET) surface area.

8.2.1 Characterisation Sampling

Three different dust samples were collected from around the drier, shown in Figure 67, to represent the dust produced during the operation. These were taken from the centre of the left-hand side of the drier, the end plate of the drier and underneath the drier. This dust had accumulated over time at Bowland Bioenergy which has the standard operating bed depth of

24.5 cm and a floor interval speed of between 5-7 minutes. Using appropriate PPE (mask and gloves), samples from the relevant surfaces were brushed using a soft tipped brush into plastic labelled containers. Each sample collected weighed approximately 20 g.

Figure 67 Dust Sample Locations – Left Side, Centre and Under the Drier

8.2.2 Characterisation Particle Shape

Imaging techniques were used to analyse particle shape imaging techniques. Several imaging techniques can be used and are based on the following: static or dynamic, 2D or 3D, and qualitative or quantitative. Quantitative methods, whereby the dust is analysed and classified on like-properties such as similar size or shape, these are not widely accepted due to varied interpretation of results, though a few standards (BS 812- -105.2 (Institute, 1990), BS EN 933-3 (Institute, 2012) and ASTM D5821 (Materials, 2017)) do exist regarding this method of analyses. For qualitative analysis, for example 3D imagery, this requires complex equipment to scan a surface containing the particles in question and replicate into a computer model using orthogonal imagery in three dimensions, in contrast 2D imagery is much simpler to perform as only one angle of the particle is required and in many cases software is easier to use.

Optical imagery has a lower resolution in general than scanning electron microscopy (SEM), which makes SEM more suitable to evaluate the morphology of dust particles. Due to the expected size variation of particles, as the dust is produced by irregular separation of wood, a static SEM is to be used.

As a detailed particle distribution is required for the design of the filter this qualitative method characterises the shape profile of the dust and a particle sizing technique is to be used for the quantitative size distribution (Section 8.2.3).

SEM

Scanning Electron Microscopy uses electrons to create an image. Due to the very short-wave lengths of electrons, this beam of electrons provides a better resolution than white light. Electrons are focused using electromagnetic lenses and apertures from an electron gun, this hits the sample surface and the electrons and reflected. The resulting emitted X-rays and scattered electrons are detected through multiple detectors. The focused beam scans the sample surface as it is controlled using deflecting coils, forming an image from the detectors.

Use of Analysis

The particles shape can have a direct effect on the efficacy of potential mitigation measures. For instance, in filtration, where the dust shape affects the shear, filter cake production and entrapment on surfaces (Wakeman, 2007). The more spherical the particle, the less air resistance for particles of the same diameter, affecting cyclone filtration. At the right alignment 'Rod' shaped particles can pass through filters which are finer than their overall length, reducing filter efficiency. Smaller particles with uneven shapes may lodge in cell tissue making them more harmful to the lungs (Golosinski and Yuguang, 1996). Therefore, this dust particle analysis is crucial to determine the dust characteristics. In addition, this analysis can also highlight any variation in the particles present in the sample, i.e. if there are any dust particles that vary widely in appearance, or if there may be other chemical elements or compounds present. The dust shape also needs to be determined for quantitative measuring and the size distribution, as spherical particles require different settings from uneven particles as they can affect the diffraction of light. SEM analysis provides an inexplicit idea of particle size, as

measurements can be taken of the still images of the particles, which can be compared to the particle size distribution results. SEM can also be used to assess particle microstructures, fractures in the sample, and surface conditions. This is useful for surface area analysis as, when using BET, micro and microporous structures have different adsorption characteristics due to pore volume affecting the surface area of particles.

Method

To perform SEM imaging the sample is first prepared. Dust is attached to a sample stage using double sided tape. Once the surface is covered dry air is blown over the surface to ensure all particulates that have not adhered are removed. An example provided in Figure 68, shows the dust sample prepared for the SEM analyses.

Figure 68 SEM Samples

A magnification of 400× to 2000× at 5 eV in backscatter compositional mode (BEC), was used to view the particles and the process repeated for the three dust samples. When using small nonconductive particles static charge can be an issue for SEM imaging, as charge affects the illumination of a particle in SEM images, making details less or more defined depending on the degree of electron activity. Therefore, a trade off may be required for contrast settings.

Results

It is clear from Figure 69 that the surface of some of the particles are irregular with pores and depressions in which fibrous particles have impregnated themselves or broken off. Visually there is an indication that the sample taken from below the drier is comprised of a larger proportion of smaller particles. The particle size distribution for this sample is expected

to have a lower average mean length. Figure 69 shows a tubular structure in some of the particles. Visual analysis also indicates that pores within the dust particle are commonplace, which can hold smaller particulates and harbour bacteria.
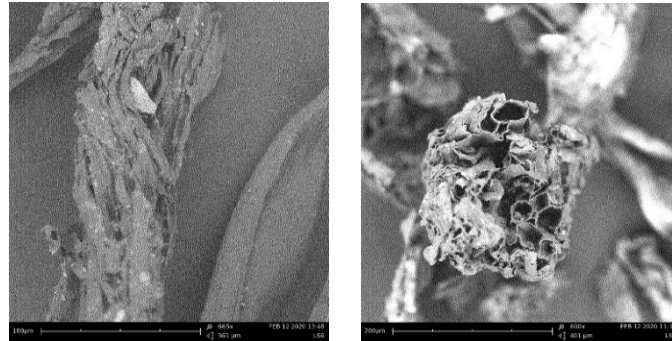
Figure 69 SEM Images Showing Pores and Depressions (Width 360 μm and 400 μm)

Figure 70 shows there is a variation in particle size with some particles having over twice the viewable sectional area than others, providing an indication of a size distribution ranging at least from 10 μm to 200 μm, this is further supported by quantitative-based analysis within Section 8.2.3. The shape as well as size variation can also be seen in Figure 70.
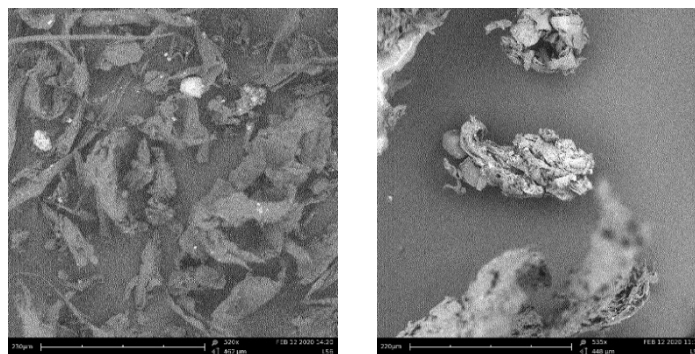
Figure 70 SEM Images Showing Variation in Particle Size (Width 460 μm and 440 μm)

As mentioned previously, long and thin particles may be able to pass through filters when an orientation such that the cross-sectional dimensions of the particle is less than that off the gap in the filter medium. Figure 71 shows that such particles are present in the sample so a filtration media alone may not be suitable to remove the particles.
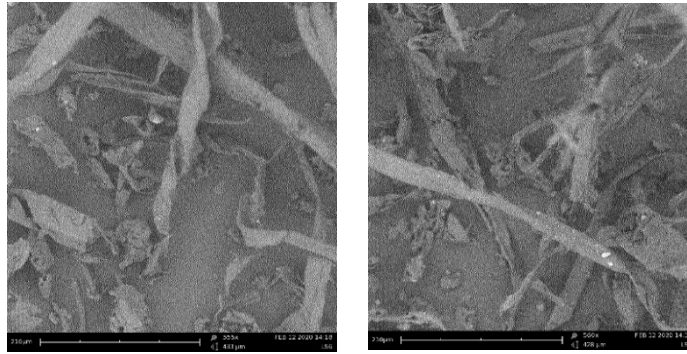
Figure 71 SEM Images Showing 'Rod' Shaped Particles (Width 420 µm and 460 µm)

Particles also vary from close to spherical to elongated, rough to smooth and charge varies between particles and surface deposits, shown in Figure 72.
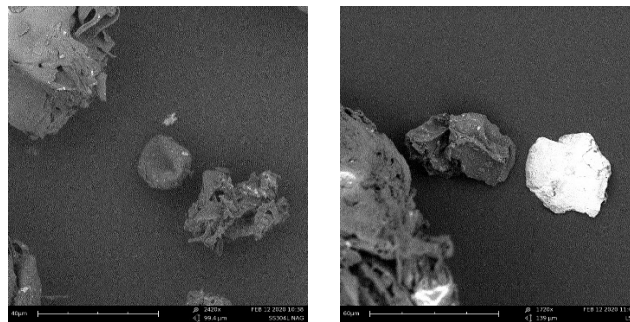
Figure 72 SEM Images Showing Spherical and Charged Particles (Width 80 µm and 120 µm)

Of the samples analysed it was clear that most of the particles conformed to the standard particle sizes and shapes discussed. Very few particles had different appearances from that in the main sample body. Figure 73 shows one such particle. Of those that were present, it was determined they were unlikely to be from wood and could be salt deposits, fly ash or mineral fragments from where the wood is stored prior to chipping.
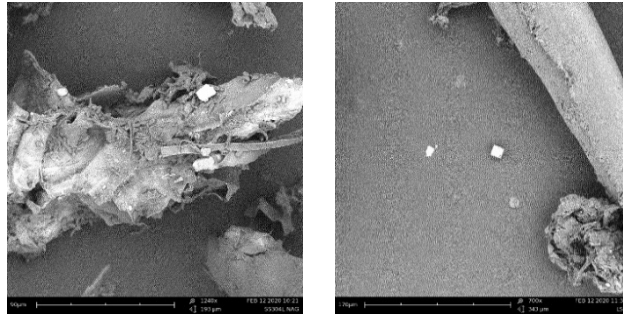
Figure 73 SEM Images Showing Foreign Particles (Width 180 µm and 240 µm)

The particles themselves proved difficult to analyse and use with the SEM, as although they are adhered to the sample surface and air was blown over the surface to prevent dust from entering the atmosphere within the microscope it was found that despite pre-treatment a degree of debonding was shown with particles moving whilst within the SEM.

Conclusion

The surface structure of the dust particles was analysed and found that many surface defects were visible from the images taken, with fragmentation and variation apparent. Overall, it was found that the particles were irregular in shape, size and differed in surface roughness. The particles measured ranged from 10 µm to 200 µm providing an indication of the range of particle sizes in the larger sample to be processed in Section 8.2.3.

Key Findings

- Fragmentation could be seen within the sample at a 400× magnification.

- Pores were visible on the majority of particles.

- The majority of particles were not spherical.

- Tubular structures were visible within the particles.

- Measured particles ranged from 10µm to 200 µm.

Highlights and limitations

Due to the high volume of particles in a sample of this nature it is difficult to identify small anomalies across the sample and characterise a shape, size or pore size distribution using this method. The images taken show clearly showed the range of shapes, sizes and surface characteristics of the sample.

Recommendations

A size distribution can be determined using a quantitative method and compared to the particles measured using SEM imaging. Samples of dust with differing levels of age could be compared, to observe possible fungal growth on samples left to the open atmosphere, or coagulation and dissociation of particles within a sample over time.

8.2.3 Characterisation Particle Sizing

Geometrically SEMs can be used to produce sizing results, however for a larger throughput microscopy is unsuitable as counting statistics must be accurate. To find the size distribution with SEM, many tens of thousands of particles under different levels of magnification would need to be measured for a suitable measure of statistical averages. Thus, a faster quantitative assessment was considered as more suitable. Here a single characteristic number describes the diameter or, for non-spherical particles, multiple length and width measurements can be made to characterise the dust shape. These descriptions are more accurate as they provide a greater overall complexity in results, especially over a large number of particles. Particle sizing techniques can be categorised into equivalent spherical diameter and aerodynamic diameter measurements.

Aerodynamic diameter measurements are based on measurements of an idealised spherical particle. As dust particles are irregular in shape and size, it would be extremely difficult to characterise them individually, therefore they are collectively expressed based on an idealised spherical particle(s). The aerodynamic diameter measurements can thus group

like-particles based on settling velocity for instance, where a tested particle is considered under the same temperature, pressure and humidity conditions (Smichowski and Gómez, 2015). The most common method for aerodynamic diameter measurement is to use cascade impactors, which collects particles as a gas stream passes over surfaces and those with greater mass fall (Allen, 2012).

Aerodynamic diameter methods include sedimentary, which measures the falling rate of particles through a viscous medium, this method is complex with particles of this size and density, in addition coagulation and flaking affects the drag. Aerodynamic sizing methods require adjustments based on a dynamic shape factor which covers a wide range of values for particle shapes and can be effected by coagulation and pores, this adjustment becomes less and less accurate for irregularity amongst particles in the same sample. Other methods which depend on aerodynamics gauge a size on the principles of drag with the distance from a jet outlet measured and particles with higher mass to drag ratios accelerate slower (Petavratzi, 2006).

Equivalent spherical diameter methods include; 1. sieving which tends to highlight the second smallest dimension due to orientation and the non-spherical shape factor (Merkus, 2009), and is easier to define on a mass basis rather than particle count, therefore this method is also unsuitable. 2. Dynamic light scattering for finding the equivalent spherical diameter, trace angular scatter and can produce equivalent spherical diameters as well as morphologically the diameter of equivalent volume or cross-sectional area (Reid et al., 2003). This is achieved through optical counters that measure the amount of light scattered from a beam. Detectors measure the refracted light, providing an equivalent diameter from the refractive index. Various types of optical detectors use different detection methods i.e. measure each wavelength of light or viewing ranges.

The method selected to measure the size distribution of the dust is the equivalent spherical diameter optical method of laser diffraction particle size analysis. The sample is suspended in water, irregular particle shape selected, and the refractive index of wood dust and water used.

Mastersizer

The Mastersizer 3000 uses the optical method of laser diffraction to record particle size analysis. As the laser is scattered from its original path by the dispersed particulate sample, this scatter can be used to determine the refractive index of the particles and the suspension solution. Laser diffraction is a form of geometric diameter measuring, where the geometric diameter, D_p, is the diameter of a circle with the same cross-sectional area as an image of the particle (Lundgren et al., 1974). This differs from the aerodynamic diameter, Da, defined as the diameter of a sphere having the same density and settling velocity as the irregularly shaped dust particle (Lundgren et al., 1974). The Mastersizer was used to measure particle size distribution within various samples taken from around the site, detailed in Section 8.2.1. The Mastersizer 3000 measures profiles of dry or wet dispersion, within a sizing range off 0.01-3283 μm.

Use of Particle Size Analysis

Separation of a particle population with a large size-distribution was achieved using particle diameter and mass. Producing a size distribution of particles can show the suitable types of separation or filtration required for removing the particulates from the air. For two such devices, the cyclone and filter; the flow conditions, particle size and particle matter concentration in the feed are required (Section 8.2.5). This provides details on capacity, style and size.

Consider the mass balance equation for a mesh filter or a single-entry separator for gas/solid separation. Both separators separate particles above a particular size from the rest of the mixture. In a single-entry separator, there are two product streams, denoted with subscripts 1 and 2 in Figure 74. Within a mesh filter, there is a product stream and an accumulation stream, which also can be described as 1 and 2. For a single entry separator the overflow stream 1 contains the majority of finer particles and the base stream 2 the larger particles. For a mesh filter, the discharge contains finer particles and the accumulation stream larger particles.
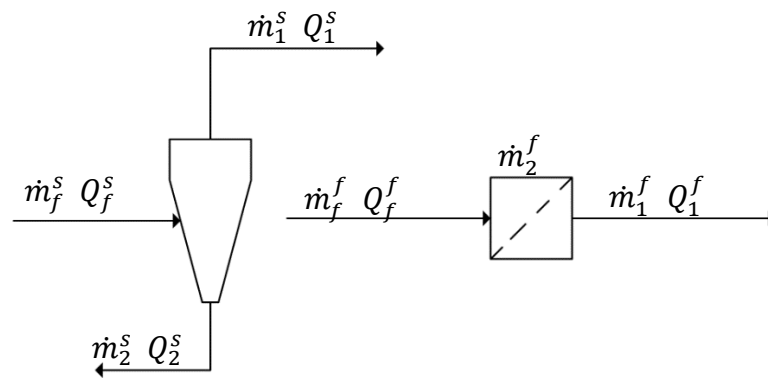
Figure 74 Schematic of Mass Balances for Cyclone and Mesh Filter

The overflow stream should have a higher flow rate of carrier fluid (in this case air) than the base stream, the design objective of a single-entry separator is to have the overflow stream as particle free as possible. Ideally, no particles would be present in the overflow stream but within real world situations, the higher the degree of separation, the greater the difficulty in achieving it, hence coarser and finer particles are likely to appear in both streams.

Method

The settings for the Mastersizer operation is provided in Table 36. The values for refractive and absorption index are pre-set within the program with the particle name and dispersant name selected.

Table 36 Mastersizer Sample Settings			
Property	Value	Property	Value
Sample Name	Wood Dust LS6	Analysis Model	General Purpose
Particle Name	Wood Flour	Particle Refractive Index	1.53
Dispersant Name	Water	Dispersant Refractive Index	1.33
Particle Absorption Index	0.1	Scattering Model	Mie
Weighted Residual	0.43%	Analysis Sensitivity	Normal

A small spatula of the dust sample is suspended within water and mixed using a pipette. The machine is turned on and the dispersant tank, which is used to wash the equipment and transport the sample is filled from a source of deionised water. An empty flushing's container is placed at the outlet of the equipment. The washing stage is initiated and once this is complete the sample is loaded into the sample dispersion unit. The sample dispersion unit is a wet unit, which requires a sample suspended in solution. Particles are encouraged to disperse through forced stirring. As the sample is added, the percentage laser obscuration is shown (nominally between 0 and 20 %). A pipette is used to introduce the suspended sample into this unit until this upper value is reached. This ensures the suspension of particles is dispersed at a suitable concentration and stable before entering the optical area.

Measurement is taken in the optical area, as the dispersed sample is passed through the path of the laser beam, illuminating the particles. A series of detectors measure the intensity of the light scattered through the sample. Placed over a range of angles, these measure the red and blue light refracted.

Results

In total, 15 Mastersizer tests were run, 5 repeats on three samples from the same origin, with dust samples collected from the left side, centre and under the drier, shown in Figure 67. Table 37 shows the mean, standard deviation and relative standard deviation of the percentage of particles below a certain particle size (10 μm, 50 μm and 90 μm). The relative standard

deviation (RSD) is below 10 for all particles showing that the samples had a good repeatability between samples from the same location. The largest variation within the samples was for the left side of the drier, this sample had the greatest mean particle size and the widest distribution, shown in Figure 75. The larger standard deviation in laser obscuration for this sample indicates that the samples used differed in overall particle quantity possibly due to particles sticking to the side of the dispersion vessel or those left in the pipette.

Table 37 Mastersizer Average Results

	Dx (10) (μm)	Dx (50) (μm)	Dx (90) (μm)	Laser Obscuration (%)
Left Side of the Drier				
Mean	114.36	376.1	1038	4.99
Standard Deviation	10.00	21.97	96.13	1.62
RSD (%)	8.75	5.84	9.26	32.4
Centre of the Drier				
Mean	43.7	146	509	8.20
Standard Deviation	2.65	6.34	16.5	0.14
RSD (%)	6.07	4.34	3.25	1.76
Under the Drier				
Mean	28.2	100	479	9.01
Standard Deviation	0.815	3.31	37.5	0.50
RSD (%)	2.89	3.3	7.81	5.52

The dust from under the drier has a lower average size of 100 μm, the smaller the size the smaller particles, the greater chance that they can cause damage by depositing within the gas exchanging regions of lungs (Mahowald et al., 2014). It is known that the finer the dust the easier it is to ignite and it is also reported that dust coarser than 100 μm is not usually explosive (Eckhoff, 2003). Therefore, it is important to reduce the quantity of dust smaller than this size within the building.
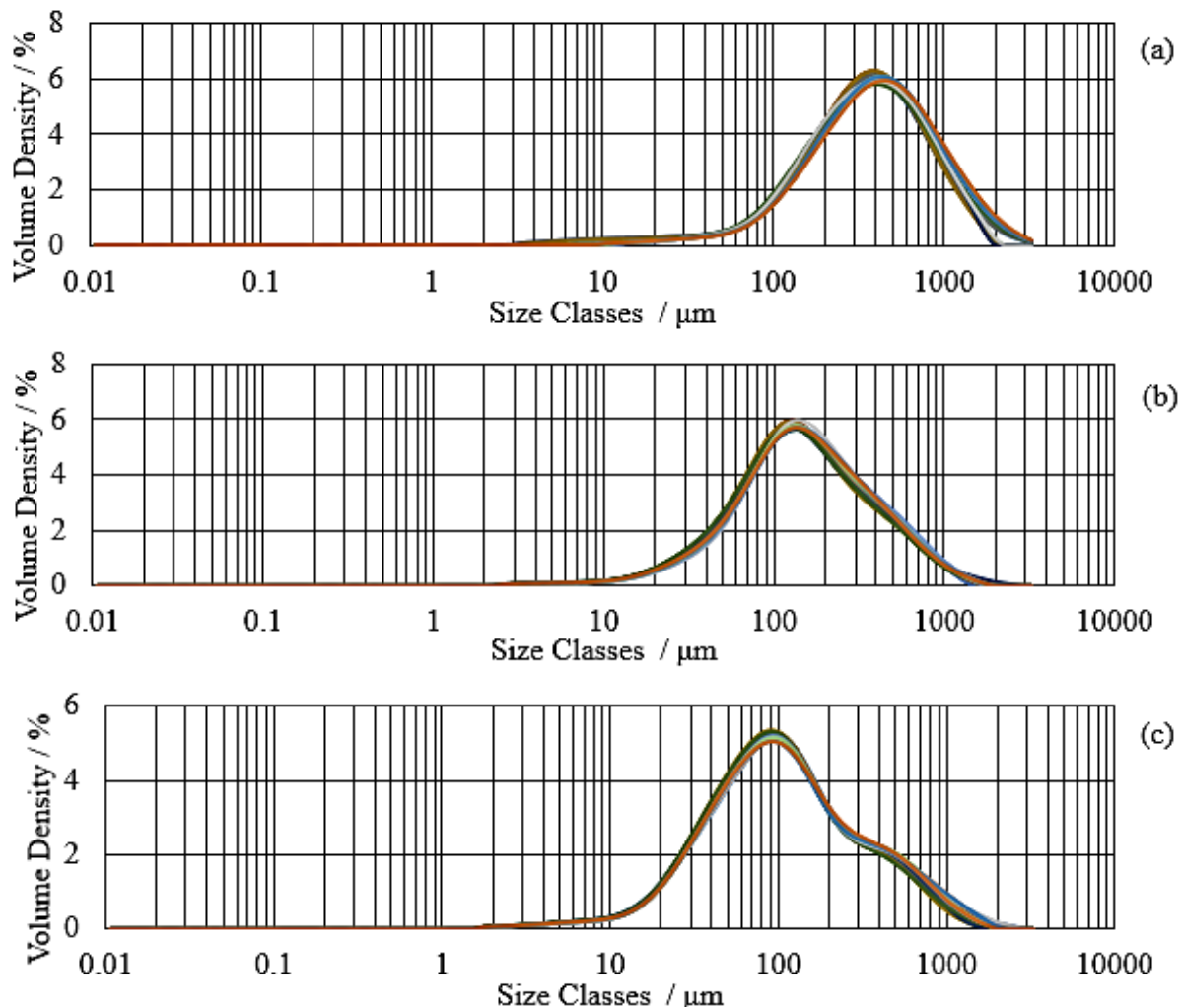
Figure 75 Mastersizer Distribution of Particle Size for samples from (a) The Left Hand Side of the Drier, (b) The Centre of the Drier, and (c) Under the Drier. Colours denote each of the 5 runs.

Conclusion

The dust samples from under the drier have the smallest size distribution, compared to the other samples. The particle size analyses also found that the dust from the left of the drier had larger particle sizes.

Key Findings

- The average particle size from the samples were 376 μm, 146 μm and 100 μm.

- The size distributions of the samples were shown by the bottom 10th percentile values of 114 μm, 43.1 μm and 28.2 μm respectively and top 10th percentile values of 1038 μm, 509 μm and 479 μm.

- Small standard deviations showed a good level of repeatability between samples.

- The particle size distribution curves were smooth showing that there are no random variations of size in the samples.

Highlights and Limitations

There were no clear anomalies within samples and between samples of the same origin as the repeatability was good. However, with impact that the particulates can also break apart or embed smaller pieces in other areas, as shown by the SEM images in Section 8.2.2, it may alter the size distribution and the effect of this from the origin of the dust is not measured.

Recommendations

Results can be compared between various methods of particle size analysis or using the same method with stationary particles or a different dispersant. The dependency of explosivity on particle size can be investigated requiring explosion test equipment which measures the pressure emitted from a sample of a specific concentration and average particle size (Liu et al., 2018).

8.2.4 Characterisation Surface Area Analysis (BET)

To measure the surface area of irregular shaped objects, imaging or physical chemistry can be used. Photographic measurements depend on the resolution of the software and hardware used and the span of views of the sample (Sabliov et al., 2002). The greater the pores on the samples surface, the greater the difficulty to get an accurate reading of surface area. Chemical and physical methods involve coating the sample in a layer of a compound and measuring the amount adsorbed.

Due to the irregularity and surface roughness of dust particles, adsorption methods provide greater detail regarding the surface area. The very small particle size means that a gas or nitrogen adsorption methods are suitable, as this highlights the overall surface area including deep apertures within the particle. The Brunauer, Emmett and Teller (BET) method is an

extension of the Langmuir isotherm. For the adsorbate, nitrogen is to be used. This is the most commonly used adsorbate as the size of nitrogen particles is well known and the physical and chemical adsorption of nitrogen has been widely studied.

BET Adsorption

The specific surface area of a powder can be determined by physical adsorption of gas. The amount of gas on the solid surface corresponding to a mono layer of molecules is calculated within the BET method. Physical adsorption is due to weak van der Waals forces between the molecules of the gas and the surface of the powder. The amount of gas adsorbed can be measured using volumetric or continuous flow measurement, using liquid nitrogen to reduce the test temperature. Measurements are taken of pressure and the volume of gas adsorbed, for BET 3 data points are required ideally in the range of P/P_0 as 0.05 to 0.5 to treat the results according to the BET equation (detailed in the results)

Use of Surface Area Analysis

Surface area directly correlates with reactivity, dissolution, catalysis and separation (Somasundaran, 2006). The greater the porous area, the greater volume of vapours particles can carry to the lower respiratory tract causing health problems (Rothenberg et al., 1989). Fungal spores can also reside in crevices and in the case of wood mould can grow on the porous surface (Klyosov, 2007). The surface area of particles affects interactions with surroundings. In the case of flammable dust, the greater the pore volume the greater the combustibility (Kollmann et al., 2012) and ability to cause harm to the lungs.

Method

There are two key stages to BET surface analysis: in situ de-gassing, which removes volatiles from the sample, and the second is sample measurement. Prior to starting the experiment, the

sample is weighed in custom vials - generally 2-3 g of particles is suitable. There are three ports so three tests can be run in parallel using the same procedure. These experiments were carried out using the Micromeritics 3Flex 3500 Multi-Port Gas Adsorption Analyser.

The first stage of the process is preparing the sample by degassing, which removes any gas or vapour that may be physically adsorbed onto the surface. The vials are then placed into thermal jackets and capped with a rod, which allows gas in and out of the vial. An insulating lid keeps the samples at temperature. The vials are each passed through the lid, which is lined up with the temperature probe, and placed into the analysis port using an o-ring, ferrule and frit which is hand tightened. Prior to heating the thermal insulating jacket is moved up the sample vial so it does not interact with the heating mantle. This stage in the process required a heating mantle, where the mantle is plugged in, held to cover the samples and support tray relocated to under the samples. The temperature of the mantle is set to 105 °C to drive off any moisture. The sample name and mass is inputted into the computer program and conditions set, as BET does not require the full pressure range a pressure range of P/P_0=0-0.5 is set. The process time depends on the sample size and volume of volatiles within the sample, this can take from 3-9 hours.

Once degassing is complete, the heating mantle and support can be removed, and the jackets moved down to the base of the vials. The heating mantle is unplugged and stored away and the temperature probe relocated to within the insulating lid. Nitrogen is then poured into the sample holder, in compliance with health and safety procedures, until the nitrogen is visible on the sample gauge. The nitrogen container is then placed on the base of the equipment under the sample vials. The protective screen is installed before this base lifts, covering the sample. The procedure is then continued by the computer program which submerges the sample and runs the adsorption.

Results

Data from the Micromeritics machine can be treated according to the BET isotherm equation:

$$\frac{1}{\left[Q_a\left(\frac{P_0}{P}-1\right)\right]} = \frac{C-1}{Q_m C}\frac{P}{P_0} + \frac{1}{Q_m C} \tag{204}$$

Where Q_a is the absorbed gas quantity (cm³.g⁻¹), P_0 is saturation pressure of adsorbate (mmHg), P is the equilibrium pressure of the adsorbate (mmHg), and C is the BET constant (dimensionless).

y = 4.242x + 1.203

y = 9.460x + 0.1078

y = 6.569x + 0.5244

Figure 76 BET Analysis Results
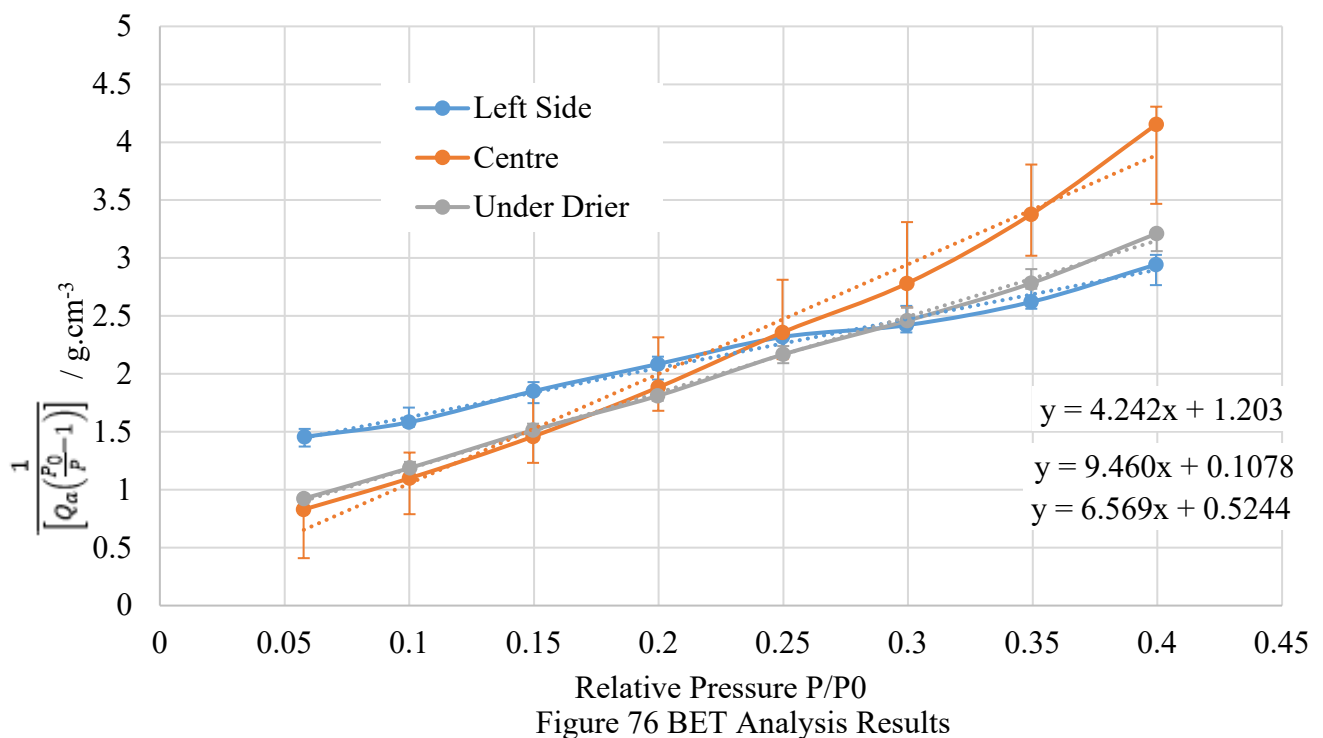
Shown in Figure 76, plotting $\frac{P}{P_0}$ on the horizontal axis and $\frac{1}{\left[Q_a\left(\frac{P_0}{P}-1\right)\right]}$ (g.cm⁻³) on the vertical axis, the slope and intercept of the graph in terms of a linear function can be described, with gradient $m_{BET} = \frac{C-1}{Q_m C}$ and intercept $c_{BET} = \frac{1}{Q_m C}$ respectively, using the minimum and maximum slopes which fit the data to form error bars.

For the sample from the left side of the drier:

$$m_{BET} = \frac{C-1}{Q_m C} = 4.242 \text{g.cm}^{-3} \text{ and } c_{BET} = \frac{1}{Q_m C} = 1.203 \text{g.cm}^{-3} \tag{205}$$

Where C is the BET constant (dimensionless):

$$C = e^{\frac{E_1 - E_L}{RT}} \tag{206}$$

Where E_1 is the heat of adsorption for the first layer and E_L the heat of vaporization in Kelvin.

Rearranging the equations for the gradient and intercept of the line:

$$Q_m = \frac{1}{m_{BET} + c_{BET}} = \frac{1}{4.242 g.cm^{-3} + 1.203 g.cm^{-3}} = 0.1837 cm^{-3}.g \tag{207}$$

$$C = 1 + \frac{m_{BET}}{c_{BET}} = 1 + \frac{4.242 g.cm^{-3}}{1.203 g.cm^{-3}} = 4.527 \tag{208}$$

The resulting monolayer adsorbed gas volume can then be used to determine the total specific surface are of the sample (Sadeghbeigi, 2012):

$$S_t = \frac{Q_m S_0 N_a}{V_{STP}} = \frac{0.1837 g.cm^{-3} \times 16.2 \times 10^{-20} m^2 \times 6.022 \times 10^{23}}{2.24 \times 10^4 cm^3.mol^{-1}} = 0.800 m^2.g^{-1} \tag{209}$$

Where N_a is Avogadro's number (6.022×10^{23}), S_0 is the cross sectional area of a nitrogen molecule at liquid state (16.2×10^{-20} m^2) and V_{STP} is the volume of a mole of N_2 at standard temperature and pressure (2.24×10^4 cm^3.mol^{-1}). For each of the sample locations the results are shown in Table 38.

Table 38 BET Surface Area Analysis Results

Location	Sample Specific Surface Area m^2.g^{-1}
Left Side	0.800$\pm$0.025
Centre	0.455$\pm$0.026
Under Drier	0.614$\pm$0.010

The expected trend is that the smaller the average dust size the greater the specific surface area, however Table 38 shows no clear correlation between average dust size, from the Mastersizer size distribution and the specific surface area determined. This could be due to smaller dust entering the sample vial, with the small sample used not having the same size distribution. The BET isotherm for the sample form the centre and from under the drier both have similar

characteristic values at relative pressures lower than 0.2, however the sample from the left side of the drier shows a visually different curve with a lower gradient and higher intercept.

For sawdust with an average particle size of 182.8 μm the average surface area has been found to be 0.3742 $m^2.g^{-1}$ (Mane and Vijay Babu, 2013), smaller than specific surface area values found in this case for wood dust with much smaller particle diameters. The specific surface area of 0.634 $m^2.g^{-1}$ to 0.890 $m^2.g^{-1}$ has been previously quoted for grain dust with a larger than 3 μm diameter (Martin, 1981) within the range of specific surface area values in Table 38.

Conclusion

Key Findings

- The surface areas found for the samples ranged from 0.4 -0.8 $m^2.g^{-1}$.

Highlights and Limitations

The BET equation was used to calculate surface areas from the three samples. The results were consistent with those for grain dust.

Recommendations

With further time, the Micromeritics equipment can be used to find data on pore volume, pore size and Langmuir Isotherm results. With results showing a decrease in surface area for samples of smaller average diameter, repeats of this experiment are also recommended.

8.2.5 Characterisation of Dust Load and Density

Dust load and dust density are required for cyclone separation design, as the denser the particles, the heavier they will be and the more likely they will be entailed in the base stream at the same spherical diameter. Density will affect the trajectory of particulates, efficiency of cyclone separation and pressure profile in the separator.

The dust load is especially important in filter design as the greater the dust load the faster filter cake production and decrease in efficiency of the filter. Once a filter is blocked, a build-up of dust will also effect the system to the filter. It is therefore important to know the dust load on the filter so that a capacity and time period of use can be calculated. This will notify the user when to replace or clean filters and the size filter required.

Method

To evaluate the dust load created by the drier clean sample boxes and containers were placed in 11 locations above and surrounding the drier for a week. The mass of the settled dust and the area covered can then be measured. This mass per area over time will provide an estimation for the dust load.

$$\text{Dust Load} = \frac{\text{Dust mass}}{\text{Air flow} \times \text{Time Accumulated} \times \text{Area}} \tag{210}$$

To calculate the density of the dust, a pycnometer with deionised water was used. The pycnometer is weighed empty, full of water, with the dust sample only and full of water with dust. The empty, clean, and dry pycnometer is placed on the scales, which has an accuracy of ±0.0005 g and the mass recorded. The pycnometer is then filled with deionised water until halfway up to the neck of the flask, the capillary stopper is inserted (liquid should fill the capillary), and the outside of the pycnometer dried. Once the pycnometer is dry and there are no air bubbles in the liquid, the mass can be recorded by placing the pycnometer onto the balance. Taking the pycnometer off the balance, empty and drying, the mass of the empty flask is measured and the dust added. Recording the current mass of the dust and pycnometer, deionised water is used to fill the pycnometer and the outside of the pycnometer dried before the final mass is recorded.

The dust volume is given by the following equation:

$$V_{dust} = \frac{W_{pycometer-water} - (W_{pycometer-dust-water} - W_{dust})}{\rho_{deionised-water}} \qquad (211)$$

The density of the dust is thus:

$$\rho_{dust} = \frac{W_{dust}}{V_{dust}} \qquad (212)$$

Results

The calculated dust loads can be seen in Appendix C Table 43 and Table 44. With an average dust load of approximately 2 $g.m^{-3}$ for all of the samples taken. Calculated densities can be seen in Appendix C Table 45 and Table 46, averaging 502 $kg.m^{-3}$.

Dusts from pine (softwood) and from light and heavy oak (hardwood) have previously been found to have the respective densities 560 $kg.m^{-3}$, 590 $kg.m^{-3}$, and 930 $kg.m^{-3}$ (Tian et al., 2007), teak wood dust 800 $kg.m^{-3}$ (Mohapatra et al., 2014). The majority of wood within the drier is softwood (recall the type of wood fed into the drier is not consistent), so a density around 560 $kg.m^{-3}$ is expected. However due to air entrainment in the porous structure between the wood dust particles the density measurement may be smaller than this which the average of the results from Table 45 and Table 46 is 494 $kg.m^{-3}$.

8.2.5 Conclusion

Dust settled in all of the sample locations over the period of a week. Using a pycnometer for all of the samples collected a density value was calculated. The density and dust load results are suitable to use in Appendix D.

Key Findings

- The average density from all of the dust samples was 502 $kg.m^3$.

- The average dust load found was 2 $g.m^{-3}$.

Highlights and Limitations

Though the density of the wood dust was measured with scales to three decimal places, in a pycnometer and using deionised water the dust is absorbent of water, has air trapped in pores and between dust particles. Any water absorbed or air trapped alters the resulting density.

Recommendations

To improve on these results for dust load the volume of dust in the air can be measured by forced airflow through a filtrate media, measuring the mass of the filter before and after exposure to the dusty environment, this will provide a measurement of airflow as well as reducing the handling required to collect the dust samples.

8.3 Chapter Summary

This section has detailed the shape, size, surface area and density of multiple dust samples taken from Bowland Bioenergy. Showing the potential impacts of wood dust on human health and the environment. Finding that mitigative rather than preventative methods are suitable to use for reducing wood dust on site.

Key Findings

- Wood dust poses a risk to equipment and human health.

- The majority of particles were not spherical with fragmentation, pores and some 'rod' shaped particles.

- The average particle size from the samples were 376 µm, 146 µm and 100 µm.

- The surface areas found for the samples ranged from 0.4-0.8 $m^2.g^{-1}$.

- The average density from all of the dust samples was 502 $kg.m^3$.

- The average dust load found was 2 $g.m^{-3}$.

Chapter 9

Thesis Conclusions

9.1 Industrial Conclusions

This research has shown that by increasing the considered woodchip drier bed depth from the current 24.5 cm to 34 cm the throughput can be increased by 39 %. In addition, the results highlighted that covering the drier will help in reducing the energy required to reduce the MC of the woodchip.

Mathematical models to predict the floor speed required for uncovered woodchip at 24.5 cm bed depth were found, these can be used to calculate floor speed based on the starting moisture content and the desired moisture content. For a higher initial moisture content to achieve a desired moisture content the floor speed can be changed. As the moisture content increases increasing the time interval between top floor movements increases the moisture loss, this is becasue the woodchip is dried for longer.

An assessment, in Appendix D, has shown that a cyclone filter with a baghouse would be most suitable to reduce the dust around the drier. A thorough analysis of the dust produced on site, the woodchip drying facility was conducted, with the dust characterised and particle size distributions based off diameters provided; this information can be taken to a supplier and a HVAC engineer to design ducting and provide a system for reducing the level of wood dust.

9.2 Academic

A two-dimensional CFD-based COMSOL Multiphysics simulation has been developed. This model describes the heat and mass transfer of drying considering a multicomponent system of a porous matrix, liquid water, water vapour and air. Parameters for this model were found both experimentally and through literature. The numerical simulations showed that air temperature and air speed have an impact on the drying time of woodchip.

The wood dust from the drier was characterised through laboratory experiments. It was found that the majority of particles were not spherical but fragmentation, pores and some 'rod' shaped particles. The average particle diameters from the samples were 376 μm, 146 μm and 100 μm. The surface areas found for the dust samples ranged from 0.429 to 0.825 $m^2.g^{-1}$. The size distributions of the samples were shown by the bottom 10th percentile values of 114 μm, 43.1 μm and 28.2 μm respectively and top 10th percentile values of 1038 μm, 509 μm and 479 μm.

The average density of all the dust samples was 502 $kg.m^3$ and the average dust load found was 2 $g.m^{-3}$.

9.3 Future Work

This work considered parameters surrounding drying as singularities, to establish a more thorough analyses of parameters on drying rate, altering multiple settings in parallel way, further showing dependency of the drying rate on these parameters should be carried out. In addition to the parameters considered, the effect of relative humidity, porosity and woodchip size could be investigated.

The multiscale nature of the COMSOL model meant that some approximations needed to be made. One of the approximations was the evaporation rate within the bed Equation 138, within which the vapour concentration and saturated vapour concentration primarily impacted the overall loss of water in the woodchip. The evaporation this could be altered to reflect the falling rate kinetics of the woodchip by using $R=k(X-X_{eq})$ where the equilibrium moisture content can be determined experimentally and corresponding to the relative humidity which is dependent on the isotherm within the woodchip.

This CFD-based studies could be extended to three dimensions, which will require greater computational time, computer power and complexity, but would account for the radial,

tangential and longitudinal permeability of liquid water and water vapour through woodchip. The physics of the study could be applied to different geometries to replicate other driers. The existing COMSOL simulation could also be adapted to better fit the data by altering the relationships used for evaporation rate. In addition to simulate covering the drier would require altering the geometry, removing the airflow over the woodchip bed and adding an upper region which would as a second porous membrane, in this case the properties would need to be altered for properties of felted material. To simulate IR drying a similar geometry to the single woodchip drying could be used with a radiation inlet from the upper boundary.

For the wood dust filtration a detailed plan of the facility would allow for more in depth analysis through designing of the ducting system and filter based on pressure drops and velocities, this could have been carried out using either analytical methods (Darcy equation) or CFD. As changes are planned to increase the capacity of the woodchip storage this would ideally be carried out using the new design.

References

ABABOU, R. (2019). Capillary Flows in Heterogeneous and Random Porous Media, Wiley.

ABACI, S., EDWARDS, J. & WHITTAKER, B. (1992). Relative permeability measurements for two phase flow in unconsolidated sands. Mine water and the environment, 11, 11-26.

AGUILAR, F. X. & PUBLICATIONS, U. N. (2019). Wood Energy in the ECE Region: Data, Trends and Outlook in Europe, the Commonwealth of Independent States and North America, UN.

AKTAE, M., SC6ZEN, A., AMINI, A. & KHANLARI, A. (2017). Experimental analysis and CFD simulation of infrared apricot dryer with heat recovery. Drying Technology, 35, 766-783.

ALAQQAD, M., C. P. J. BENNINGTON & MARTINEZ, D. M. (2012). The permeability of wood-chip beds: The effect of compressibility. The Canadian Journal of Chemical Engineering 90 (5) 1278-1288.

ALLEN, T. (2012). Particle Size Measurement, Springer Netherlands.

ANDERSON, J. D. & WENDT, J. 1995. Computational fluid dynamics, Springer.

ANDREASSEN, E., HINRICHSEN, E. L. & LARSEN, C. 1992. Computer Modelling of Polymer Processing, Pergamon Press.

ANSYS-INC. (2015). ANSYS Fluent in ANSYS Workbench User'sGuide.

ANSYS-INC. (2020). Technical Report release 18.2, . Fluent theory guide. .

ANTONY, J. AND SHYAMKUMAR, M.B., (2016). Study on sand particles drying in a fluidized bed dryer using CFD. International Journal of Engineering, 8(2), pp.129-145.

BABU, A. K, KUMARESAN, G, ANTONY AROUL RAJ, V, AND VELRAJ, R., (2020). CFD studies on different configurations of drying chamber for thin-layer drying of leaves. Energy sources. Part A, Recovery, utilization, and environmental effects, 42(18), pp.2227–2239.

BAJPAI, PRATIMA. (2018). Biermann's Handbook of Pulp and Paper. San Diego: Elsevier.

BARAN, S., SWIETLIK, K. & TEUL, I. (2009). Lung function: occupational exposure to wood dust. European journal of medical research, 14, 1-4.

BARTH, W. 1956. Berechnung und Auslegung von Zyklonabscheidern auf Grund neuer Untersuchungen. Brennst.-Warme-Kraft, 8, 1-9.

BEJAN, A., DINCER, I., LORENTE, S., MIGUEL, A. & REIS, H. (2013). Porous and Complex Flow Structures in Modern Technologies, Springer New York.

BELGACEM, MOHAMED NACEUR, & PIZZI, A. (2016). Lignocellulosic Fibers and Wood Handbook. Hoboken: John Wiley & Sons, Incorporated.

BISHT, D. & IQBAL, Z. (2018). Lyophilization - Process And Optimization For Pharmaceuticals. International Journal of Drug Regulatory Affairs, 3, 30-40.

BRUNNER, K. (1980). Investigation Of The Separation Efficient Of A Plate Separator.

CHAI, H., ZHAO, J. & CAI, Y. (2018). Development and Validation of a Simulation Model for the Temperature Field during High-Frequency Heating of Wood. Forests, 9, 327.

CHANDRA MOHAN, V.P, & Talukdar, Prabal. (2010). Three dimensional numerical modeling of simultaneous heat and moisture transfer in a moist object subjected to convective drying. International Journal of Heat and Mass Transfer, 53(21), 4638-4650.

CHEN, X. D. & PUTRANTO, A. (2013). Modelling Drying Processes: A Reaction Engineering Approach, Cambridge University Press.

CHILKA, AMARVIR G & RANADE, VIVEK V, (2019). CFD modelling of almond drying in a tray dryer. Canadian journal of chemical engineering, 97(2), pp.560–572.

CLAIR, B., ALTEYRAC, J. R. M., GRONVOLD, A., ESPEJO, J., CHANSON, B. & ALMC)RAS, T. (2013). Patterns of distribution of longitudinal and tangential maturation stresses in Eucalyptus nitens plantation trees. Annals of Forest Science, 68, 681-688.

COKER, A. K. (2011). Ludwig's Applied Process Design for Chemical and Petrochemical Plants, Elsevier Science.

COMSOL (1998–2017). COMSOL - Heat Transfer Application Library Manual 5.3a.

COMSOL (1998–2018). COMSOL - CFD Module Users Guide.

COMSOL (2007). COMSOL - Evaporation in Porous Media with Large Evaporation Rates.

COOPER, C. D. & ALLEY, F. C. (2010). Air Pollution Control: A Design Approach, Fourth Edition, Waveland Press.

DAÏAN, JEAN-FRANÇOIS, & DAIAN, JEAN-FRANCOIS. (2014). Equilibrium and transfer in porous media 1. Somerset: WILEY.

DATTA, A. (2007a.) Porous media approaches to studying simultaneous heat and mass transfer in food processes. I: Problem formulations. Journal of food engineering, 80, 80-95.

DATTA, A. (2007b). Porous media approaches to studying simultaneous heat and mass transfer in food processes. II: Property data and representative results. Journal of food engineering, 80, 96-110.

DENNY, M. & MEETING, A. S. O. Z. (1993). Air and Water: The Biology and Physics of Life's Media, Princeton University Press.

DIETL, C., GEORGE, O. & BANSAL, N. (1995). Modeling of diffusion in capillary porous materials during the drying process. Drying Technology, 13, 267-293.

DUPLEIX, A., DE SOUSA MENESES, D., HUGHES, M. & MARCHAL, R. C. M. (2013). Mid-infrared absorption properties of green wood. Wood Science and Technology, 47, 1231-1241.

DUROUDIER, J. P. (2016). Liquid-Gas and Solid-Gas Separators, Elsevier Science.

ECKHOFF, R. K. (2003). Dust Explosions in the Process Industries: Identification, Assessment and Control of Dust Hazards, Elsevier Science.

ELGAMAL, R., RONSSE, F. AND PIETERS, J., (2013). Modeling deep-bed grain drying using Comsol Multiphysics. In COMSOL Conference 2013.

ELMAN, HOWARD C, SILVESTER, DAVID J, & WATHEN, ANDREW J. (2005). Finite Elements and Fast Iterative Solvers. Oxford: Oxford University Press.

EL-MESERY, H. S. & MWITHIGA, G. (2015). Performance of a convective, infrared and combined infrared-convective heated conveyor-belt dryer. Journal of food science and technology, 52, 2721-2730.

EXECUTIVE, H. A. S. (2020a). Fire and explosion - What you need to know. In: EXECUTIVE, H. A. S. (ed.).

EXECUTIVE, H. A. S. (2020b). Wood dust - What you need to know. In: EXECUTIVE, H. A. S. (ed.).

EXECUTIVE, H. A. S. (2020c). Wood dust Controlling the risks. In: EXECUTIVE, H. A. S. (ed.) Woodworking Sheet No 23 (Revision 2).

FAULKNER, W. & SHAW, B. (2006). Efficiency and pressure drop of cyclones across a range of inlet velocities. Applied engineering in agriculture, 22, 155-161.

FERNANDO, H. J. 2012. Handbook of Environmental Fluid Dynamics, Two-Volume Set, CRC Press.

FIORENTINI, C., DEMARCHI, S.M., RUIZ, N.A.Q., IRIGOYEN, R.M.T. AND GINER, S.A., (2015). Arrhenius activation energy for water diffusion during drying of tomato leathers: The concept of characteristic product temperature. Biosystems Engineering, 132, pp.39-46.

FOLEY, C. (2003). Modeling the Effects of Knots in Structural Timber.

GAVHANE, K. (2014). Unit Operations-II, Nirali Prakashan.

GIANFRANCESCO, A., TURCHIULI, C., FLICK, D. & DUMOULIN, E. (2010). CFD modeling and simulation of maltodextrin solutions spray drying to control stickiness. Food and Bioprocess Technology, 3, 946-955.

GOLOSINSKI, T. S. & YUGUANG, G. (1996). Mining Science and Technology 1996, Taylor & Francis.

GOVERNMENT, U. (2020). Government takes action to cut pollution from household burning. In: DEPARTMENT FOR ENVIRONMENT, F. R. A. (ed.). https://www.gov.uk/government/news/government-takes-action-to-cut-pollution-from-household-burning: UK Government.

GREEN, D. W. & PERRY, R. H. (2007). Perry's Chemical Engineers' Handbook, Eighth Edition, McGraw-Hill Education.

HALDER, G. (2014). Introduction to CHEMICAL ENGINEERING THERMODYNAMICS, PHI Learning.

HEBBAR, H. U., VISHWANATHAN, K. & RAMESH, M. (2004). Development of combined infrared and hot air dryer for vegetables. Journal of food engineering, 65, 557-563.

HELDMAN, D. R. (2003). Encyclopedia of Agricultural, Food, and Biological Engineering (Print), CRC Press.

HENDERSON, S. (1974). Progress in developing the thin layer drying equation. Transactions of the ASAE, 17, 1167-1168.

HENDERSON, S. M. A. P., S. (1961) Grain Drying Theory: Temperature Effect on Drying Coefficient. Journal of Agricultural Engineering Research, 6, 169-174.

HERVÉ, R. (2010) Fluid Flow Simulations Using New CFD Module – Wood drying simulation. COMSOL Conference, Paris.

HETSRONI, G. (1982). Handbook of multiphase systems.

HILES, A. (2010). The Definitive Handbook of Business Continuity Management, Wiley.

HO, C. K. & WEBB, S. W. (2006). Gas Transport in Porous Media, Springer Netherlands.

HUA TAN, REZA MASOODI & PILLAI, K. M. (2011). PORE-FLOW© User's Manual. version 1.2.

HUTTEN, I. M. 2015. Handbook of Nonwoven Filter Media, Elsevier Science.

INCORPORATED, D. (2020). Duct Incorporated Sizing Information - [Online]. Available: http://www.ductincorporated.com/sizing-info.html [Accessed].

INGHAM, D. B. & POP, I. (2005). Transport Phenomena in Porous Media III, Elsevier Science.

INSTITUTE, B. S. (1990). Testing aggregates. Methods for determination of particle shape. Elongation index of coarse aggregate. BS 812-105.2:1990.

INSTITUTE, B. S. (2012). Tests for geometrical properties of aggregates. Determination of particle shape. Flakiness index. BS EN 933-3:2012.

INSTITUTE, B. S. (2014a). Solid biofuels. Fuel specifications and classes. General requirements. BS EN ISO 17225-4:2014.

INSTITUTE, B. S. (2014b). Solid biofuels. Fuel specifications and classes. General requirements. BS EN ISO 17225-1:2014.

INSTITUTE, B. S. (2017). Solid Biofuels. Sampling. BS EN ISO 18135:2017.

INSTITUTE, B. S. (2017b). Solid biofuels — Determination of moisture content — Oven dry method BS EN ISO 18134-2:2017

JUN, S. & IRUDAYARAJ, J. M. (2008). Food processing operations modeling: design and analysis, CRC press.

JUN, S. & IRUDAYARAJ, J. M. (2008). Food processing operations modeling: design and analysis, CRC press.

KARIM, A. & LAW, C. L. (2017). Intermittent and Nonstationary Drying Technologies: Principles and Applications, CRC Press.

KARNIADAKIS, G., BESKOK, A. & ALURU, N. (2006). Microflows and Nanoflows: Fundamentals and Simulation, Springer New York.

KASSEM, A. (1998).Comparative studies on thin layer drying models for wheat. 13th international congress on agricultural engineering, 2-6.

KLYOSOV, A. A. (2007). Wood-Plastic Composites, Wiley.

KOLLMANN, F. F. P., KOLLMANN, F. & COTE, W. A. J. (2012). Principles of Wood Science and Technology: I Solid Wood, Springer Berlin Heidelberg.

KREITH, F. (1998). The CRC Handbook of Mechanical Engineering, Second Edition, Taylor & Francis.

KUO, J. (2018). Air Pollution Control: Fundamentals and Applications, CRC Press.

KURJATKO, S. & KC:DELA, J. (1998). Wood Structure and Properties '98, Arbora Publishers.

KURNIA, J.C., SASMITO, A.P., TONG, W. AND MUJUMDAR, A.S., (2013). Energy-efficient thermal drying using impinging-jets with time-varying heat input–A computational study. Journal of food engineering, 114(2), pp.269-277.

LAPPLE, C. (1951). Processes use many collection types. Chem. Eng., 58, 144-151.

LEWIS, W. K. (1921). The Rate of Drying of Solid Materials. Journal of Industrial & Engineering Chemistry, 13, 427-432.

LI, Y. AND ZHU, Q., (2003). Simultaneous heat and moisture transfer with moisture sorption, condensation, and capillary liquid diffusion in porous textiles. Textile Research Journal, 73(6), pp.515-524.

LIU, S.-H., CHENG, Y.-F., MENG, X.-R., MA, H.-H., SONG, S.-X., LIU, W.-J. & SHEN, Z.-W. (2018). Influence of particle size polydispersity on coal dust explosibility. Journal of Loss Prevention in the Process Industries, 56, 444-450.

LJUNG, A.L., (2008). Drying of iron ore pellets: analysis with CFD (Doctoral dissertation, Luleå tekniska universitet).

LOMBARD, MATT. (2018). Introducing SolidWorks. In Mastering SolidWorks (pp. 3-24). Indianapolis, Indiana: John Wiley & Sons.

LU, H. 2006. Experimental and modeling investigations of biomass particle combustion.

LUNDGREN, D. A., MOSS, O. R. & KERTESZ-SARINGER, M. (1974). Airborne Pollutants: Characteristics & Detection, MSS Information Corporation.

LUNGULEASA, A., COSEREANU, C. & LICA, D. (2009) Method for determining the specific area of chips. Proceeding of the 1st International Conference on Manufacturing Engineering, Quality and Production Systems MEQAPSb, 2009.

MAHAPATRA, ARCHANA & TRIPATHY, PUNYADARSHINI PUNAM, (2018). Modeling and simulation of moisture transfer during solar drying of carrot slices. Journal of food process engineering, 41(8).

MAHOWALD, N., ALBANI, S., KOK, J. F., ENGELSTAEDER, S., SCANZA, R., WARD, D. S. & FLANNER, M. G. (2014). The size distribution of desert dust aerosols and its impact on the Earth system. Aeolian Research, 15, 53-71.

MANE, V. S. & VIJAY BABU, P. V. (2013). Kinetic and equilibrium studies on the removal of Congo red from aqueous solution using Eucalyptus wood (Eucalyptus globulus) saw dust. Journal of the Taiwan Institute of Chemical Engineers, 44, 81-88.

MANNAN, S. & LEES, F. 2005. Lees' Loss Prevention in the Process Industries: Hazard Identification, Assessment and Control, Elsevier Science.

MARTIN, C. (1981). Characterization of grain dust properties. Transactions of the ASAE, 24, 738-0742.

MASUDA, H., HIGASHITANI, K. & YOSHIDA, H. (2006). Powder Technology Handbook, CRC Press.

MATERIALS, A. S. F. T. A. (2017). Standard Test Method for Determining the Percentage of Fractured Particles in Coarse Aggregate. ASTM D5821 - 13(2017).

MCKENNA, J. D. & TURNER, J. H. (1989). Fabric Filter-- Baghouses I: Theory, Design, and Selection : (a Reference Text), ETS.

MEHRABIAN, R., ZAHIROVIC, S., SCHARLER, R., OBERNBERGER, I., KLEDITZSCH, S., WIRTZ, S., SCHERER, V., LU, H. & BAXTER, L. L. (2012). A CFD model for thermal conversion of thermally thick biomass particles. Fuel Processing Technology, 95, 96-108.

MERKUS, H. G. (2009). Particle Size Measurements: Fundamentals, Practice, Quality, Springer Netherlands.

MFG, S. (2015). Engineering Data -Spiral pipe and fittings.

MIKHAILOV, M.D., (1975). Exact solution of temperature and moisture distributions in a porous half-space with moving evaporation front. International Journal of Heat and Mass Transfer, 18(6), pp.797-804.

MINDSET, T. E. (2020). Properties of Air at atmospheric pressure [Online]. Available: https://theengineeringmindset.com/properties-of-air-at-atmospheric-pressure/ [Accessed].

MOHAPATRA, R. C., ANTARYAMI, M. & BIBHUTI, B. C. (2014). Experimental study on thermal conductivity of teak wood dust reinforced epoxy composite using Lee's apparatus method. Int J Mech Eng Appl 2 : 98-103.

MOHINDROO, K. K. (1997). Basic Principles of Physics, Pitambar Publishing.

MORRIS, ARTHUR E, FINE, H. ALAN, & GEIGER, GORDON. (2011). Handbook on Material and Energy Balance Calculations in Material Processing (3. Aufl. ed.). Hoboken: Wiley-TMS.

MUJUMDAR, A. S. (2006). Handbook of Industrial Drying, CRC Press.

MUSCHELKNAUTZ, E. (1972). Die berechnung von zyklonabscheidern fC<r gase. Chemie Ingenieur Technik, 44.

NORTON, T. S., TIWARI, B. & SUN, D.-W. (2013). Computational fluid dynamics in the design and analysis of thermal processes: a review of recent advances. Critical reviews in food science and nutrition, 53, 251-275.

NWIGBO, M. N. (2019). Design, Fabrication and Performance Evaluation of a Cyclone System for Saw Dust Emission Control International Journal of Engineering and Modern Technology 5.

ONWUDE, DANIEL I, HASHIM, NORHASHILA, CHEN, GUANGNAN, PUTRANTO, ADITYA, AND UDOENOH, NSIKAK R, (2019). Experimental studies and mathematical simulation of intermittent infrared and convective drying of sweet potato (Ipomoea batatas L.). Food and bioproducts processing, 114, pp.163–174.

OSVALDOVA, L. M., MARKERT, F. & ZELINKA, S. L. (2020). Wood & Fire Safety: Proceedings of the 9th International Conference on Wood & Fire Safety 2020, Springer International Publishing.

PALIN, M. A. & PETTY, J. (1983). Permeability to water of the wood cell wall and its variation with temperature. Wood Science and Technology, 17, 187-193.

PELEG, M. (1988). An empirical model for the description of moisture sorption curves. Journal of Food science, 53, 1216-1217.

PERRE, P. & KEEY, R. B. (2014). Drying of Wood: Principles and Practices. In Handbook of Industrial Drying.

PETAVRATZI, E. (2006). An assessment of dust generation from ores. PhD University of Nottingham.

PETERSON, C. M. & WHITBY, K. T. (1965). Fractional efficiency characteristics of unit type collectors. ASHRAE J, 7, 42-49.

PHUPAICHITKUN, S., PRUKWARUN, W., KHUMCHOO, W. & SEANCOTR, W. 2013. CFD Simulation of fixed bed dryer by using porous media concepts: Unpeeled longan case. International Journal of Agricultural and Biological Engineering, 6, 100-110.

PLAWSKY, JOEL L. (2014). Transport Phenomena Fundamentals (Vol. 138, Chemical industries). Bosa Roca: CRC Press LLC.

PLÖTZE, M. & NIEMZ, P. (2011). Porosity and pore size distribution of different wood types as determined by mercury intrusion porosimetry. European Journal of Wood and Wood Products, 69, 649-657.

PRAKASH, O. & KUMAR, A. (2017). Solar Drying Technology: Concept, Design, Testing, Modeling, Economics, and Environment, Springer Singapore.

PRYCE, M., CHENELER, D., MARTIN, A. & AIOUACHE, F. (2020). Mathematical Model Analysis for Mass and Rates of Woodchip IR Drying.

PURCHAS, D. & SUTHERLAND, K. (2002). Handbook of Filter Media, Elsevier Science.

RAMACHANDRAN, G., LEITH, D., DIRGO, J. & FELDMAN, H. 1991. Cyclone optimization based on a new empirical model for pressure drop. Aerosol Science and Technology, 15, 135-148.

REID, J. S., JONSSON, H. H., MARING, H. B., SMIRNOV, A., SAVOIE, D. L., CLIFF, S. S., REID, E. A., LIVINGSTON, J. M., MEIER, M. M. & DUBOVIK, O. (2003). Comparison of size and morphological measurements of coarse mode dust particles from Africa. Journal of Geophysical Research: Atmospheres, 108.

ROMÁN, FRANZ, STRAHL-SCHÄFER, VITUS, & HENSEL, OLIVER. (2012). Improvement of air distribution in a fixed-bed dryer using computational fluid dynamics. Biosystems Engineering, 112(4), 359-369.

ROTHENBERG, S. J., NAGY, P. A., PICKRELL, J. A. & HOBBS, C. H. (1989). Surface Area, Adsorption, and Desorption Studies on Indoor Dust Samples. American Industrial Hygiene Association Journal, 50, 15-23.

ROWELL, R. (2005). Handbook Of Wood Chemistry And Wood Composites.

ROWELL, R. M. (2012). Handbook of Wood Chemistry and Wood Composites, CRC Press.

RUYS, A. (2019). 12 - Alumina as a wear-resistant industrial ceramic. In: RUYS, A. (ed.) Alumina Ceramics. Woodhead Publishing.

RYLANDER, R. & JACOBS, R. R. (1994). Organic Dusts Exposure, Effects, and Prevention, Taylor & Francis.

SABLIOV, C. M., BOLDOR, D., KEENER, K. M. & FARKAS, B. E. (2002). Image Processing Method to Determine Surface Area and Volume of Axi-Symmetric Agricultural Products. International Journal of Food Properties, 5, 641-653.

SADEGHBEIGI, R. (2012). 11.4.5 Air and Spent Catalyst Distributor. Fluid Catalytic Cracking Handbook - An Expert Guide to the Practical Operation, Design, and Optimization of FCC Units (3rd Edition). Elsevier.

SANDBERG, D. & HOLMBERG, H. (1996). Radially sawn timber: Knots-number, type and size in star-sawn triangular profiles of pine (Pinus silvestris L) and spruce (Picea abies Karst). European Journal of Wood and Wood Products, 54, 369-376.

SAPTO, W., WONG, C., KAMARUL, A. & NURUL HIDAYAH, A. (2016). CFD SIMULATION FOR TRAY DRYER OPTIMIZATION.

SAUNDERS, PETER. (2007). Radiation Thermometry. Bellingham: SPIE.

SCHERER, G.W., (1990). Theory of drying. Journal of the American Ceramic Society, 73(1), pp.3-14.

SCHERER, V., MÖNNIGMANN, M., BERNER, M. O. & SUDBROCK, F. (2016). Coupled DEM–CFD simulation of drying wood chips in a rotary drum – Baffle design and model reduction. Fuel, 184, 896-904.

SCHLUNDER, E. U. (1983). Heat exchanger design handbook.

SELIMEFENDIGIL, FATIH, ÖZCAN ÇOBAN, SEDA & ÖZTOP, HAKAN F, (2020). Convective drying of a moist porous object under the effects of a rotating cylinder in a channel. Journal of thermal analysis and calorimetry, 141(5), pp.1569–1590.

SHAMEY, R. & ZHAO, X. (2014). Modelling, simulation and control of the dyeing process, Elsevier.

SHEPHERED, C. & LAPPLE, C. (1939). Flow pattern and pressure drop in cyclone dust collectors. Industrial & Engineering Chemistry, 31, 972-984.

SHOKRI, N., LEHMANN, P. AND OR, D., (2009). Critical evaluation of enhancement factors for vapor transport through unsaturated porous media. Water resources research, 45(10).

SILVA, W., SILVA, C., SOUSA, J. A. D. & FARIAS, V. S. O. (2013). Empirical and diffusion models to describe water transport into chickpea (Cicer arietinum L.). International Journal of Food Science and Technology, 48, 267-273.

SINGH, R.(2007). The saturated permeability of composite pulp fiber and filler mats, State University of New York College of Environmental Science and Forestry.

SINNOTT, R., COULSON, J. M. & RICHARDSON, J. F. (2005). Chemical Engineering Design: Chemical Engineering Volume 6, Elsevier.

SJÖSTRÖM, E. & RAIMO, A. (2013). Analytical methods in wood chemistry, pulping, and papermaking, Springer Science & Business Media.

SMICHOWSKI, P. & GÓMEZ, D. (2015). Chapter 8 - Spectroscopic and Chromatographic Techniques and Methodologies for the Determination of Metals, Metalloids and Ions in Atmospheric Aerosols. In: FORBES, P. B. C. (ed.) Comprehensive Analytical Chemistry. Elsevier.

SMITH, R. (2016). Chemical Process Design and Integration, Wiley.

SMITH, R. D. & MINES, U. S. B. O. (1987). Lead Reduction in Ambient Air: Technical Feasibility and Cost Analysis at Domestic Primary Lead Smelters and Refineries, U.S. Department of the Interior, Bureau of Mines.

SOMASUNDARAN, P. (2006). Encyclopedia of Surface and Colloid Science, Taylor & Francis.

SPECIALIST, O. A. I. A. H. (2015). Engineering Data. In: SPECIALIST, O. A. I. A. H. (ed.) Catalog ENG-409 Supersedes ENG-203.

STAIRMAND, C. J. (1951). The design and performance of cyclone separators. Trans. Instn. Chem. Engrs., 29, 356-383.

SWIFT, P. (1969). Dust control in Industry-2. Steam Heat. Engr., 38, 453-464.

SYSTEMS, A. H. (2015). Air Handling Design Guide.

TEMAM, R., & SOCIETY FOR INDUSTRIAL APPLIED MATHEMATICS. (1995). Navier-Stokes equations and nonlinear functional analysis (2nd ed., CBMS-NSF regional conference series in applied mathematics ; 66). Philadelphia, Pa.: Society for Industrial and Applied Mathematics (SIAM, 3600 Market Street, Floor 6, Philadelphia, PA 19104).

TERZI, A., FOUDHIL, W., HARMAND, S. AND JABRALLAH, S.B., (2016). Liquid film evaporation inside an inclined channel: Effect of the presence of a porous layer. International Journal of Thermal Sciences, 109, pp.136-147.

TESTING, A. S. F. & SCIENCES, M. D. O. M. (1966). Orientation Effects in the Mechanical Behavior of Anisotropic Structural Materials: A Symposium Presented at the Fifth Pacific Area National Meeting, American Society for Testing and Materials, Seattle, Wash., Oct. 31-Nov. 5, 1965, American Society for Testing and Materials.

THEODORE, LOUIS, & RICCI, FRANCESCO. (2010). Mass Transfer Operations for the Practicing Engineer (Essential engineering calculations series). Hoboken: John Wiley & Sons, Incorporated.

TIAN, Z. F., INTHAVONG, K. & TU, J. Y. 2007. Deposition of Inhaled Wood Dust in the Nasal Cavity. Inhalation Toxicology, 19, 1155-1165.

TOWLER, G. & SINNOTT, R. 2012. Chemical Engineering Design: Principles, Practice and Economics of Plant and Process Design, Elsevier Science.

TSILINGIRIS, P. 2008. Thermophysical and transport properties of humid air at temperature range between 0 and 100 C. Energy Conversion and Management, 49, 1098-1110.

TSOTSAS, EVANGELOS, & MUJUMDAR, ARUN S. (2014). Modern Drying Technology, Volume 5. Somerset: John Wiley & Sons, Incorporated.

TSOUMIS, G. T. 2000. Wood: Cellular Composition of Wood. Types of Cells Present in Hardwoods and Softwoods. Encylopaedia Britannica Inc.

TU, JIYUAN, YEOH, GUAN HENG, & LIU, CHAOQUN. (2012). Computational Fluid Dynamics. London: Elsevier Science & Technology.

TYAGI, V. 2009. Essential Chemistry Xii, Ratna Sagar.

VERMA, L. R., BUCKLIN, R., ENDAN, J. & WRATTEN, F. 1985. Effects of drying air parameters on rice drying models. Transactions of the ASAE, 28, 296-0301.

WAKEMAN, R. 2007. The Influence of Particle Properties on Filtration. Separation and Purification Technology, 58, 234-241.

WANG, G. & SINGH, R. 1978. Single layer drying equation for rough rice. ASAE Paper.

WANG, L. K. & PEREIRA, N. C. 2012. Air and Noise Pollution Control: Volume 1, Humana Press.

WANG, SHUANGQING, ZHANG, HUILE, CHEN, HUIMIN, ZHONG, YI, & YUE, XIAOLI. (2020). A numerical model of the open-width coupling drying process for cotton fabrics based on the theory of heat and mass transfer in porous media. Textile Research Journal, 90(13-14), 1639-1657.

WANG, YAJING & LU, SEN & REN, TUSHENG & BAOGUO, LI. (2011). Bound Water Content of Air-Dry Soils Measured by Thermal Analysis. Soil Science Society of America Journal. 75. 481-487. 10.2136/sssaj2010.0065.

WARHAFT, Z. 1997. An Introduction to Thermal-Fluid Engineering: The Engine and the Atmosphere, Cambridge University Press.

WERNECKE, ROLAND, & WERNECKE, JAN. (2014). Industrial Moisture and Humidity Measurement. Weinheim: John Wiley & Sons, Incorporated.

WIDDEN, M. 1996. Fluid Mechanics, Macmillan Education UK.

YIOTIS, A.G., TSIMPANOGIANNIS, I.N., STUBOS, A.K. AND YORTSOS, Y.C., (2006). Pore-network study of the characteristic periods in the drying of porous materials. Journal of colloid and interface science, 297(2), pp.738-748.

ZHOU, FAN, FU, ZONGYING, ZHOU, YONGDONG, ZHAO, JINGYAO, GAO, XIN, & JIANG, JINGHUI. (2020). Moisture transfer and stress development during high-temperature drying of Chinese fir. Drying Technology, 38(4), 545-554.

ZHU, B. (2018). The Finite Element Method: Fundamentals and Applications in Civil, Hydraulic, Mechanical and Aeronautical Engineering, Wiley.

ZIMMERMAN, W. B. J. (2006). Multiphysics Modeling With Finite Element Methods, World Scientific Publishing Company.

Appendix A
Carbon Report

A.1 Centre For Global Eco-Innovation CO₂e Calculator

Name: Marcia Pryce	
Project: LoCaL-i 107 Energy efficiency of wood chip biomass	
Industry Partner: Bowland Bioenergy	
Academic Supervisors: David Cheneler, Farid Aiouache	

Description of project:

This project investigates the drying of woodchip for production of woodchip fuel. The research concentrates on reducing heat losses to the environment, which should in turn increase the calorific value of the woodchip produced. It also investigates methods of increasing throughput through the drier. The aims are to: optimise the temperature, airflow and chip flow through the drier, by reviewing if improvements are possible on the boiler, hot water accumulator vessel and heat exchanger; and reduce wood chip dust volumes around the site.

Summary of GHG emission reduction:

The assessment of CO_2e emission reduction on this project is based on increased throughput of woodchip to be processed and converted to fuel. Although the CO_2e emissions from generating heat energy remains constant, the novel capability to produce the same quantity of product annually reduces equipment runtime and therefore CO_2e emissions per annum (as the emissions are reduced per unit of woodchip processed).

Bowland Bioenergy (BB) share a site with Wood Fuel Testing Ltd, using facilities on the same meter readings and the bills are split between the two companies, with Bowland Bioenergy using the majority of resources. All calculations with referenced values are quoted to 4 significant figures, except in the case of readings and measurements taken from Bowland Bioenergy. The CO_2e emissions were calculated for the proportion of CO_2e produced by the equipment this research focuses on.

On average during a weekend Bowland Bioenergy (BB) can dry 15.43 tonnes of woodchip fuel. Calculating the daily amount multiplied by number of working days per year ((15.43/2)*325)) shows that overall they produce and sell around 2,500 tonnes per annum. With the proposed modifications of increasing the drier bed depth by 9.5cm, 39% additional dried fuel can be processed per annum. This reduces CO_2e emissions from 22.1 to 13.5 tCO_2e per annum for the same production volume, as the run time required to produce the same volume over the year is reduced.

GHG emissions before support	Current GHG emissions	Total GHG reduction 8.63 tCO₂e	Percentage of reduction
22.13 tCO2e per annum	13.5 tCO2e per annum		39%

Section one – Baseline of CO₂e emissions relating to original process, service or product

Scope one – Direct emissions from company owned and controlled operations

CO₂e from **company facilities and the fuels used for operations (e.g. heating and cooling)**

Fuel for equipment

Wood chip

It is assumed 90% of the wood chip used heats the drier (i.e. relates to equipment this research project focused on) and 10% goes towards general heating on the site. From site fuel store records during 2018 212.7 tonnes of woodchip was burnt in the biomass boiler.

From Fuel Store Volumes:

- Biomass: UK Wood Chip = 59.03 kgCO2e per tonne [1].

Time Scale	Resource	Total Weight (tonnes)	Conversion Factor	kgCO2e	tCO2e	Equipment Usage (90%) kgCO2e	Equipment Usage (90%) tCO2e
1 Year	Wood Chip	212.7	59.03	12560	12.56	11298	**11.30**

Scope two – Indirect emissions purchased by company

CO₂e from **purchased energy for own use (electricity, steam, heating and cooling)**
Electricity
Based on the loads from Manufacturers Guides and conversion factors [1]:

- Purchased Electricity: UK Electricity Generated = 0.2556 kgCO₂e per kWh [1].

	W load/ rating	Annual Load kWh	Conversion Factor	kgCO₂e	tCO₂e
Schmid Biomass Boiler	500	4380	0.2556	1120	1.120
Heat Exchange Unit	1700	14892	0.2556	3806	3.806
Fliegel Chip Dryer Unit	2635	23083	0.2556	5900	5.900
Total					**10.83**

Scope three – Other indirect emissions from the supply chain owned and/or purchased by suppliers and consumers
Total baseline emissions figure
- Woodchip usage of Schmid Biomass Boiler for relevant equipment = 11.30 tCO_2e.   - Electricity for the Schmid Biomass Boiler, Heat Exchanger Unit and Feigl Chip Dryer Unit = 10.83 tCO_2e.   **Total =   22.13 tCO2e per annum.**
Section two – Reduction of CO₂e emissions relating to new process, service or product
Scope one – Direct emissions from company owned and controlled operations
CO_2e from **company facilities and the fuels used for operations (e.g. heating and cooling)** As the bed depth has increased from 24.5cm to 34cm the throughput has increased, therefore producing the same amount of woodchip per year reduces the run time required, as the process is semi batch it can be stopped and started based on the quantity of product. $$\text{Throughput}(BD, FI) = \left(BDm \times 2.24m \times \left(0.05m.\min^{-1} \times \frac{5}{FI \min} \right) \right) m^3 \min^{-1}$$ Where BD is bed depth in meters, FI is the interval time between bed movements, keeping FI the same i.e. at 12min gives a throughput change of $0.0114 m^3 \min^{-1}$ to $0.0158 m^3 \min^{-1}$ an increase of 39% throughput. Assuming the density is the same the same volume will be required over the year for the same annual production. $$2500 \text{tonne.year}^{-1} = 2.5 \times 10^6 \text{kg.year}^{-1} = \left(\frac{2.5 \times 10^6 \text{kg.year}^{-1}}{394 \text{kg.m}^{-3}} \right) m^3.\text{year}^{-1}$$ $$6,345 m^3.\text{year}^{-1}$$ $$\text{Runtime} = \frac{\text{Annual Production}}{\text{Throughput}}$$ Initial Runtime = 9,276 hours   Amended Runtime = 6,693 hours Reduction in runtime is 39%, assuming an even distribution of woodchip usage and electricity usage over the year a 39% reduction in runtime leads to a 39% savings in electricity usage, biomass usage and emissions as conversion factors are fixed.

From Fuel Store Volumes:

- Biomass: UK Wood Chip = 59.03 kgCO2e per tonne.

Time Scale	Resource	Total Weight (tonnes)	Conversion Factor	kgCO2e	tCO2e	Equipment Usage (90%) kgCO2e	Equipment Usage (90%) tCO2e	New Equipment Usage tCO2e
1 Year	Wood Chip	212.7	59.03	12560	12.56	11298	**11.30**	**6.89**

Scope two – Indirect emissions purchased by company

CO_2e from **purchased energy for own use (electricity, steam, heating and cooling)**

With an additional 39% throughput, emissions reductions will be by 39%

Based on the loads from Manufacturers Guides and conversion factors [1]:

With a 39% reduction in wood chip throughput:

- Purchased Electricity: UK Electricity Generated = 0.2556 $kgCO_2e$ per kWh [1].

	W load/ rating	Annual Load kWh	Conversion Factor	$kgCO_2e$	tCO_2e
Schmid Biomass Boiler	500	4380	0.2556	1120	1.120
Heat Exchange Unit	1700	14892	0.2556	3806	3.806
Fliegel Chip Dryer Unit	2635	23083	0.2556	5900	5.900
Total					**10.83**
New Total					**6.61**

Scope three – Other indirect emissions from the supply chain owned and/or purchased by suppliers and consumers

Total reduction emissions figure (savings)

Baseline
Equipment = 22.13 tCO2e per annum.
New emissions
Equipment = 6.89 + 6.61 = 13.5 tCO2e per annum.
Saving of 8.63 tCO_2e per annum (39%)

References

[1] UK Government (2019) 'GHG Conversion Factors for Company Reporting.'
"https://www.gov.uk/government/publications/greenhouse-gas-reporting-conversion-factors-2019" [Accessed 27/01/2020].

Appendix B

B.1 Density of Woodchip–Pycnometer

The pycnometer was weighed in 3 states: 1. Empty 2. full of water and 3. full of water with a wet woodchip. From this, the density of the woodchip can be found. First, to determine the mass of the woodchip, the chip was first dried at 105°C and weighed on its own. As woodchip was porous, and soaked up water, it was carefully placed in deionised water for 15 hours. After the chip has soaked, the empty and dry pycnometer were placed on the scales, which had an accuracy of ±0.0005g, and the mass was recorded. The pycnometer was then filled with deionised water until half way up to the neck of the flask, the capillary stopper was inserted such that liquid fills up the capillary. To ensure accuracy, the pycnometer was dried so only water within the flask was recorded with no air bubbles in the liquid. The final measurement was the chip within the pycnometer (filled with water). Figure 77 demonstrates the use of a pycnometer using wood dust.

Figure 77 Pycnometer – With wood dust, with wood dust and water, with wood dust and water showing sedimenting and buoyant wood dust

B.2 Initial Moisture Content

The moisture balance was set to stop when a change of 0.001g per 99 seconds with a temperature of 105℃. The samples were heated using the infrared moisture balance under these conditions once and the moisture content provided recorded.

B.3 Experimental Drying Data Collection

Sampling

To achieve a representative sample of the chip the sample was taken throughout the pile. For sampling the woodchip the same procedure as Bowland Bioenergy was used. This method uses a container of the same size to take five samples from a pile in the path of an "M" shape, these samples were then placed within one container, mixed through shaking, placed on the clean floor, divided into four and one of these quarters was the then distributed into the final container until this was full.

EN ISO 18135 (Institute, 2017) describes sampling tools though as plastic food container with lid was used and the sample randomised by sampling different points in the pile and mixing. An airtight bucket with lid was also the suggested storage method. Though this standard suggests that sampling was better from a moving stream there were health and safety factors as well as availability on site limiting this. The materials composition also changes over time and sampling closer to the time that the customer receives the woodchip was preferred to further ensure the correct stockpile was sampled. Hence the method for sampling from stockpiles during build up or reclaiming was used extracting increments from the working face.

The masses of the sample and container were recorded when the initial sample was taken. Moisture content of samples of the woodchip before entering the drier were going to be taken as well as those after to evaluate the average moisture content entering the drier can be determined and tested at Bowland Bioenergy to evaluate the drying curves in relation to the

drier. This will be using the ML-50 and oven drying method, the same method used by on site for samples exiting the drier in moisture content test certificate reports.

Labelling

Every sample was to be labelled with the following;

Sample No.	
Owner	
Supervisor	
Date	
Time	
Location Collected	
Disposal Review	
Disposal Method	

Transporting

Samples were transported from Bowland Bioenergy in the sample containers, effectively sealed, by car. Dates for transporting the woodchip from site were determined in advance and agreed with staff at Bowland Bioenergy.

Weighing

In the first instance the scales used can only manually log mass. This was recorded on a sheet with the sample number and time to the decimal places shown on the scales, but only once the initial value has settled, as the mass will be changing due to evaporation this value was recorded when the scales initially show the "g" symbol for this case.

The time was recorded to the nearest minute at which the mass was taken. For further improvements to these timed measurements, there was scope to log the time and mass electronically by linking the existing scales up to a computer

Recording Data

The readings were inputted into an Excel document with the full label recorded with the experiment date on the cover sheet. Files saved to record data were named after the sample number and the date recorded.

Disposal

The material must be returned to Bowland Bioenergy or burnt for disposal off as currently wood infected with *Phytophthora ramorum* is within stockpiles at Bowland Bioenergy.

Initial Method Convective Drying

Though the recommended mass was 300 g of woodchip for a moisture content reading, 30 g samples were used to produce moisture content change over time curves, due to the size limitation of the oven used, the maximum mass for the scales and that larger masses take a longer time to dry.

Measurements of the mass and temperature were taken every 5 minutes until the system reached steady state at a constant mass. For the initial method the oven was set to 105 $^{\circ}$C, a ceramic dish was filled with 30 g of woodchip, the dish was transported to the scales and weighed every 5 minutes recording the mass and temperature of the oven at that instance. Initially, the oven was closed during the 5 minute intervals then for the second instance the oven was open for the duration of the experiment to assess the effect on temperature fluctuation. After the initial experiment suggestions, were made such as keeping the oven open to reduce temperature fluctuation and wiping the container before weighing to remove any silica transferred from the oven.

Equipment Requirements

Oven

The oven used can be set to 105 $^{\circ}$C and the door opened so a reading can be taken every 5 minutes. The temperature of the oven was also measured for the duration of the experiment. The inner dimensions of the oven were 40.5x15x18.5 cm^3.

Scales

The scales measure to the closest 0.001 g, however the value will fluctuate as mass was still lost during the measurements.

Sample Containers

The containers have dimensions of 16x10.5x6 cm^3 with a sealable lid for transport.

Oven Safe Container

A circular ceramic bowl was used with a diameter of 7 cm and depth of 5 cm

Base Method Results and discussion
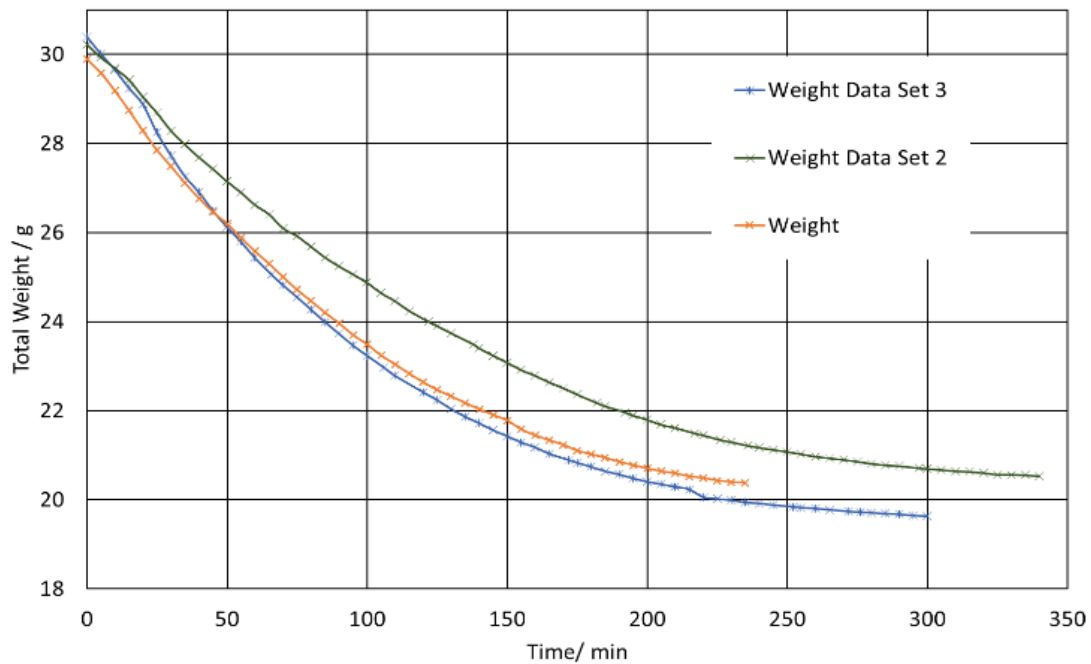
Figure 78 Weight vs Time Graphs

Three sets of results were recorded over periods of 4 and 5 hours for a sample taken before the drying process straight from the chipper. These measurements were taken on different dates over the span of two weeks and the samples stored in plastic sealed food containers.

The mass results produced smooth curves with little noise, therefore a 5 minute sampling period was appropriate. The third data set shows a jump in mass and has a ridge within the first 5 minutes, this was likely due to the transfer of silica from the base of the oven to the dish and the loss of volatile dust, for this set of data the scales were calibrated after every reading which they were not for the other two data sets.
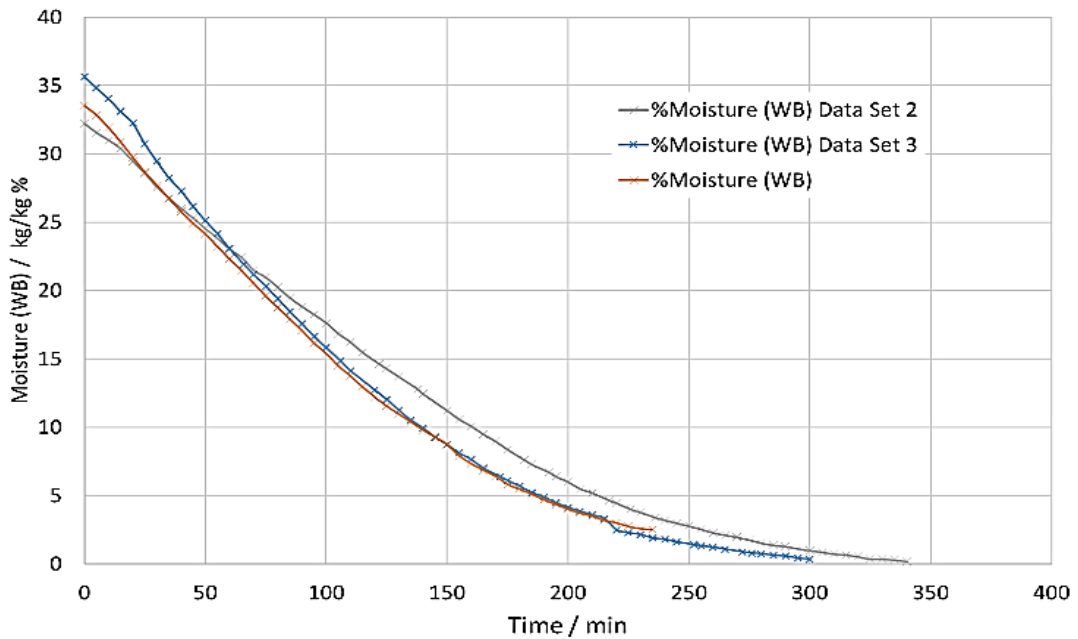
Figure 79 Moisture vs Time Graphs for Sample

During the drying process the temperature of the oven also varied, especially within the first 50minutes, this may be due to the ramp rate set on the oven heating it past the 105 °C set point. Ideally the oven should be at the desired temperature from the start, reducing the fluctuation in temperature during the experiment.
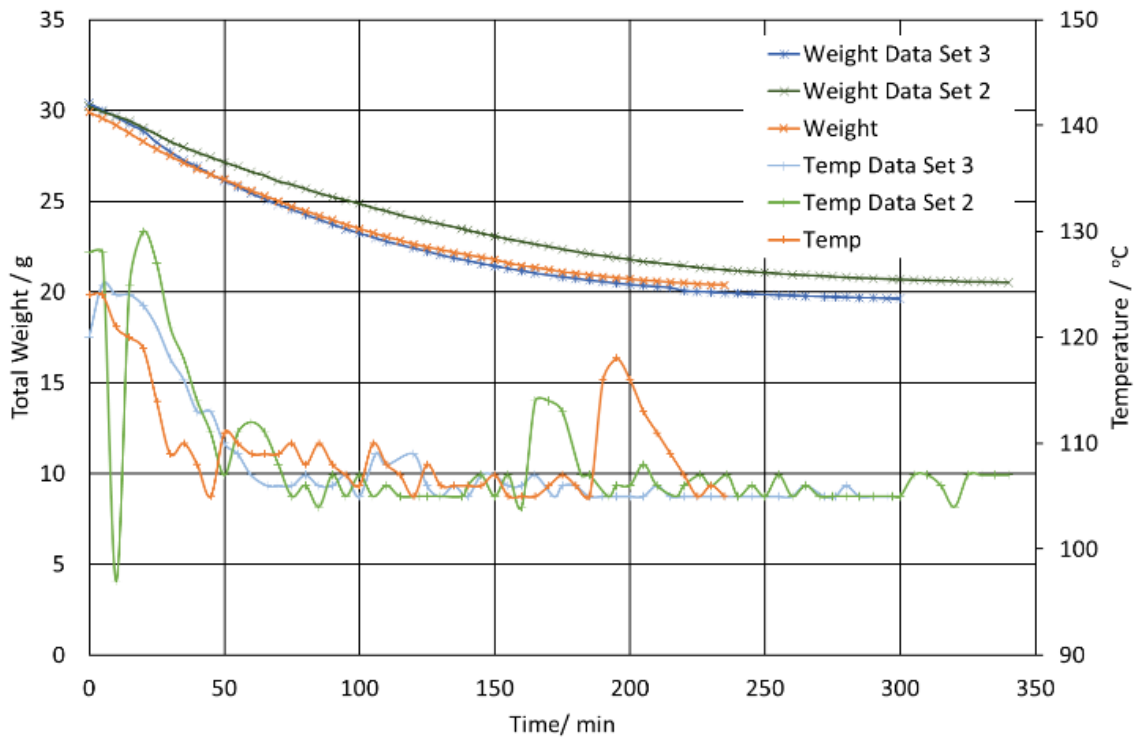
Figure 80 Convective Experiment Results Initial Method

All of the drying curves produced showed falling rate drying as the gradient reduces over time. The drying rates however seemed to change between the samples, with samples starting at a higher moisture content drying having a steeper curve.

Appendix C

Raw Experimental Data

C.1 Section 4.2.5

Table 39 Density Readings

Sample	$\rho_{woodchip}$ / g.cm^{-3}	$\rho_{woodchip-pores\,removed}$ / g.cm^{-3}	Sample	$\rho_{woodchip}$ / g.cm^{-3}	$\rho_{woodchip-pores\,removed}$ g.cm^{-3}
1	0.263	0.680	6	0.434	0.917
2	0.351	0.657	7	0.427	1.018
3	0.343	0.782	8	0.413	0.994
4	0.368	0.816	9	0.396	1.119
5	0.415	1.023	10	0.526	0.936
		Average		0.394	0.894

C.2 Section 6.2.4

Table 40 Moisture Content Readings - Variable Bed Depth

	43 cm		34c m		24.5 cm	
	Start Mass	Moisture %	Start Mass	Moisture %	Start Mass	Moisture %
MC In 1	5.65	44.39	5.124	42.4	5.460	31.90
MC In 2	5.672	56.6	5.401	60.06	5.620	39.00
MC In 3	5.815	58.41	5.127	54.64	5.340	35.70
MC In 4	5.55	49.04	5.21	56.58	5.370	31.80
MC In 5	5.138	45.6	5.524	54.28	5.290	35.60
MC Start of Bed 1	5.181	49.07	5.169	44.27	5.523	29.05
MC Start of Bed 2	5.907	58.71	5.124	41.89	5.043	32.20
MC Start of Bed 3	5.575	62.41	5.704	51.05	5.164	35.03
MC Start of Bed 4	5.559	55.93	5.513	51.1	5.073	29.31
MC Start of Bed 5	5.66	52.25	5.252	45.65	5.042	35.43
MC Middle of Bed 1	5.698	59.76	5.154	22.84	5.315	17.49
MC Middle of Bed 2	5.187	56.24	5.069	27.33	5.244	18.02
MC Middle of Bed 3	5.175	49.45	5.225	25.97	5.369	17.04
MC Middle of Bed 4	5.4	54.2	5.091	30.69	5.170	16.75
MC Middle of Bed 5	5.528	56.49	5.107	28.26	5.578	17.18
MC End of Bed 1	5.7	50.72	5.12	15.76	5.006	11.01
MC End of Bed 2	5.355	44.72	5.425	13.53	4.990	10.11
MC End of Bed 3	5.23	43.93	5.409	14.44	5.005	10.25
MC End of Bed 4	5.104	48.51	5.197	14.26	5.023	10.53
MC End of Bed 5	5.026	48.07	5.08	14.84	5.087	10.97

C.3 Section 6.2.5

Table 41 Moisture Content Readings - Variable Top Floor Speed

	5 min		Maximum 12 min		Minimum 3min	
	Start Mass	Moisture %	Start Mass	Moisture %	Start Mass	Moisture %
MC In 1	5.460	31.9	5.307	39.18	5.020	46.18
MC In 2	5.620	39.0	5.733	47.52	5.814	48.40
MC In 3	5.340	35.7	5.290	39.25	5.591	51.40
MC In 4	5.375	31.8	5.330	42.37	5.764	54.16
MC In 5	5.290	35.6	5.225	43.75	5.534	53.09
MC Start of Bed 1	5.523	29.05	5.465	46.11	5.270	41.05
MC Start of Bed 2	5.043	32.20	5.170	47.14	5.530	51.91
MC Start of Bed 3	5.164	35.03	5.653	35.59	5.778	54.57
MC Start of Bed 4	5.073	29.31	5.182	46.51	5.468	50.37
MC Start of Bed 5	5.042	35.43	5.653	44.04	5.291	53.91
MC Middle of Bed 1	5.315	17.49	5.445	12.9	5.308	41.43
MC Middle of Bed 2	5.244	18.02	5.315	13.5	5.416	35.51
MC Middle of Bed 3	5.369	17.04	5.290	13.4	5.216	33.56
MC Middle of Bed 4	5.170	16.75	5.605	15.0	5.533	51.69
MC Middle of Bed 5	5.578	17.18	5.670	13.1	5.650	48.53
MC End of Bed 1	5.006	11.01	5.365	4.9	5.131	23.88
MC End of Bed 2	4.990	10.11	5.270	4.4	5.035	25.68
MC End of Bed 3	5.005	10.25	5.205	4.8	5.450	23.17
MC End of Bed 4	5.023	10.53	5.095	4.8	5.218	25.80
MC End of Bed 5	5.087	10.97	5.260	4.5	5.035	31.40

C.5 Section 6.2.6

Table 42 Moisture Content Readings - Covering Drier Bed

	Uncovered		Covered	
	Start Mass	Moisture %	Start Mass	Moisture %
MC In 1	5.454	51.38	5.291	46.16
MC In 2	5.095	45.06	5.078	50.02
MC In 3	5.143	53.35	5.590	56.71
MC In 4	5.170	53.92	5.050	52.55
MC In 5	5.465	55.86	5.513	42.41
MC Start of Bed 1	5.355	53.43	5.278	45.36
MC Start of Bed 2	5.439	44.24	5.424	35.58
MC Start of Bed 3	5.163	44.88	5.623	59.52
MC Start of Bed 4	5.250	45.53	5.476	61.12
MC Start of Bed 5	5.375	54.98	5.315	40.12
MC Middle of Bed 1	5.103	42.90	5.160	36.8
MC Middle of Bed 2	5.516	54.24	5.027	48.2
MC Middle of Bed 3	5.757	43.62	5.014	51.38
MC Middle of Bed 4	5.576	49.61	5.59	47.16
MC Middle of Bed 5	5.234	43.68	5.438	42.75
MC End of Bed 1	5.301	41.95	5.215	20.46
MC End of Bed 2	5.173	40.6	5.048	19.77
MC End of Bed 3	5.201	29.17	5.360	18.06
MC End of Bed 4	5.616	32.32	5.183	19.34
MC End of Bed 5	5.237	29.85	5.145	20.2

C.6 Section 8.2.5

Table 43 Dust Load from Smaller Containers

Sample Box	Mass of Box + Dust / g	Mass of Box / g	Mass of Dust / g	Area / m^2	Time Accumulated/ minutes	Air Flow Rate / $m.s^{-1}$ *	Dust Load / $g.m^{-3}$
1	170.737	165.305	5.432	0.01815	10800	0.0001	4.619
2	156.798	155.589	1.209	0.01815	10800	0.0001	1.028
3	160.248	159.19	1.058	0.01815	10800	0.0001	0.900
4	158.404	157.363	1.041	0.01815	10800	0.0001	0.885
5	155.461	154.811	0.65	0.01815	10800	0.0001	0.553
6	159.638	157.863	1.775	0.01815	10800	0.0001	1.509
7	160.587	155.557	5.03	0.01815	10800	0.0001	4.277
8	170.085	158.149	11.936	0.01815	10800	0.0001	10.15
9	160.507	159.433	1.074	0.01815	10800	0.0001	0.913
10	160.186	159.433	0.753	0.01815	10800	0.0001	0.640
11	158.564	157.341	1.223	0.01815	10800	0.0001	1.040
*Approximate						Mean	2.4

Table 44 Dust Load from Larger Containers

Sample Location	Mass of Bag + Dust / g	Mass of Bag / g	Mass of Dust / g	Area / m^2	Time Accumulated/ minutes	Air Flow Rate / m.s^{-1} *	Dust Load / g.m^{-3}
1	6.953	1.232	5.721	0.04564	10800	0.0001	1.934
2	10.395	1.232	9.163	0.12705	10800	0.0001	1.113
3	11.378	1.232	10.146	0.17815	10800	0.0001	0.8789
4	15.469	1.232	14.237	0.13395	10800	0.0001	1.640
9	7.618	1.232	6.386	0.05978	10800	0.0001	1.649
10	23.469	1.232	22.237	0.10135	10800	0.0001	3.386
*Approximate						Mean	1.8

Table 45 Densities from Dust in Smaller Containers

Sample Box	Mass of Dust/ g	Mass of flask/ g	Mass of flask + Deionised water/ g	Mass of flask + Dust + Deionised Water/ g	Mass of Water Displaced/ g	Volume of Dust/ m^3	Density/ kg.m^{-3}
1	0.551		141.304	140.038	1.817	1.822	302
2	0.319		141.304	140.388	1.235	1.239	258
3	0.634		141.304	140.887	1.051	1.054	601
4	0.430		141.304	140.970	0.764	0.766	561
5	0.151		141.304	141.059	0.396	0.397	380
6	0.940		141.304	141.170	1.074	1.077	873
7	1.709		141.304	140.818	2.195	2.202	776
8	2.575		141.304	139.781	4.098	4.110	626
9	0.556		141.304	138.770	3.090	3.099	179
10	0.292		141.304	141.162	0.434	0.435	671
11	0.950		141.304	140.546	1.708	1.713	555
						Mean	526

Table 46 Densities from Dust in Larger Containers

Sample Location	Mass of Dust/ g	Mass of flask/ g	Mass of flask + Deionised water/ g	Mass of flask + Dust + Deionised Water/ g	Mass of Water Displaced/ g	Volume of Dust/ cm^3	Density/ kg.m^{-3}
1	2.381	46.239	141.304	139.235	4.450	4.463	533
2	0.538	46.240	141.304	140.289	1.553	1.558	345
3	1.136	46.245	141.304	139.460	2.980	2.989	380
4	1.625	46.239	141.304	139.086	3.843	3.855	422
9	1.757	46.239	141.304	138.809	4.252	4.265	412
10	0.602	46.240	141.304	140.991	0.915	0.918	656
						Mean	458

Appendix D

Dust Removal Design
As mentioned in Chapter 8, the most suitable method of reducing exposure to dust on site is through mitigation rather than prevention. Mitigation methods include reducing footfall in the area, cleaning areas with significant quantities and on-line dust collection systems. As the footfall in the area is already limited and the area is regularly cleaned a more robust method for mitigation such as an air filtration system is required. This section discusses collection systems, which can be put in place to reduce employee's exposure to dust.

D.1 Dust Removal Style Selection
There are a few existing dust removal systems, each graded for different size dust particles. The dust size distribution determined in Section 8.2.3 will be the basis of the dust removal system design. The majority of the dust was found to be above $10\,\mu\text{m}$ and below $1000\,\mu\text{m}$ in size. From Figure 81 a cyclone filter was selected on this basis.

Alternatives include electrical precipitators and ultrasonic filters, which are expensive, settling chambers which require larger particle sizes and densities and liquid scrubbers require additional chemicals. Centrifugal separators, including cyclone filters, have the best coverage of the particle diameter range. In addition, fractional efficiency can be improved by adding a bag filter in series; this filter will remove very small particulates (<5 μm) that the centrifuge cannot. This is also supported by a summary of dry dust separators in the wood working industry cyclones are frequently used with occasional use of high efficiency centrifuges, wet collectors are rarer and fabric arresters are frequently used (Coker, 2011).
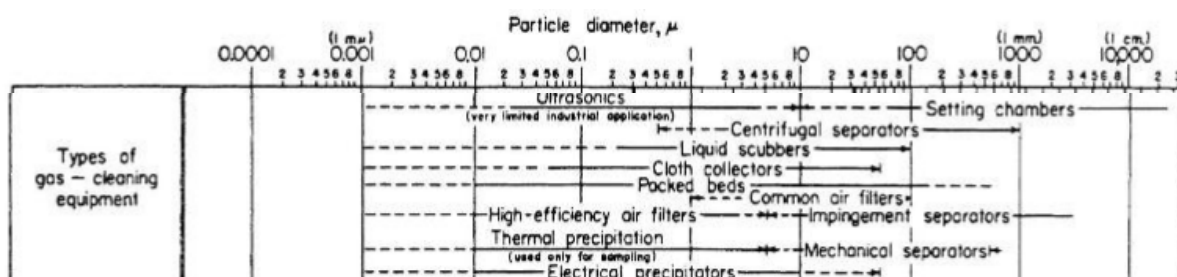
Figure 81 Cleaning Equipment for Gas Streams (Green and Perry, 2007)

D.2 Cyclone

Cyclones separate particles using centrifugal force to push particles heavier than the carrier fluid to the outer edges and drop down to the base. The carrier fluid, in this case air, enters through a tangential inlet into a cylindrical barrel, and converges into a helical motion which causes a centrifugal force. The dimensions of cyclones separators affect separation efficiency, as the shape of the separator alters characteristics of the internal and external vortex of carrier fluid, it is therefore important to define these dimensions for a specified purpose. Air is the carrier fluid used to collect wood dust, the air density, air velocity, inlet diameter and length of ducting to the inlet of the cyclone play an important role in collection efficiency and collected volume.

In the following calculations all examples shown use 'Lapple standard dimensions', as Lapple's work determined in what manner dimensions of cyclones affect performance and has become industry standard (Lapple, 1951). The Lapple standard ensures all dimensions listed (e.g. inlet height) are normalized to the cyclone's body diameter, and are thus given as ratios. For cyclone diameter of 0.5 m and a target cut off diameter of less than 10 μm, it is found that an inlet gas flow rate of at least 15 m.s^{-1} is required. This provides the closest cut off diameter to 10 μm within the range of 15 m.s^{-1}-25 m.s^{-1} (Duroudier, 2016),calculated using Excel Solver's Generalized Reduced Gradient (GRG) Nonlinear algorithm, defining the flow rate as the variable to change with limits between 15 m.s^{-1}-25 m.s^{-1} and a target of 10 μm for the applicable cell. Pre-determined factors include dust load of 2 g.m^{-3} (from Section 8.2.5), gas viscosity of 1.83×10^{-5} Pa.s, gas density of 1.184 kg.m^{-3} and solid density of 500 kg.m^{-3} (from Section 8.2.5), which are shown in calculations where relevant.

D.2.1 Dimensions

Cyclone dimension ratios can vary significantly between sources (Ramachandran et al., 1991), however, over time repetitive investigative work on 'optimal' dimensions determined by

Shepherd and Lapple (1939) (Shephered and Lapple, 1939) has led to 'standard' cyclone dimensions, as defined by many research papers displayed in Table 47. The same calculations can be carried out for all these ratios of dimensions and used to optimise cyclone design. For the purpose of this research, the Shepherd and Lapple model was selected due to the commonality of these dimensions and for all designs additional gas flow will be required which can be altered to optimise collection efficiency based on particle size.

For classical cyclone design, knowledge of flow conditions, particulate concentrations and size distributions in addition to the type of cyclone design are required. The particulate size distribution can be found within Section 8.2.3, Figure 75. Flow conditions can be altered using an impeller to force air through the system. Particulate load has been measured on site Section 8.2.5 and a style of design and diameter to height ratio of the cylindrical barrel selected.

Table 47 Standard Geometry Ratios for tangential inlet cyclones (relating to Figure 82)

Dimensions	High Throughput		Standard			High efficiency	
	(Stairmand, 1951)	(Swift, 1969)	(Lapple, 1951)	(Swift, 1969)	(Peterson and Whitby, 1965)	(Stairmand, 1951)	(Swift, 1969)
$H_c/D_c = K_H$	0.75	0.8	0.5	0.5	0.583	0.5	0.44
$B_c/D_c = K_B$	0.375	0.35	0.25	0.25	0.208	0.2	0.21
$S_c/D_c = K_S$	0.875	0.85	0.625	0.6	0.583	0.5	0.5
$D_i/D_c = K_i$	0.75	0.75	0.5	0.5	0.5	0.5	0.4
$L_c/D_c = K_L$	1.5	1.7	2	1.75	1.333	1.5	1.4
$Z_c/D_c = K_Z$	2.5	2.0	2	2	1.84	2.5	2.5
$D_S/D_c = K_D$	0.375	0.4	0.25	0.4	0.5	0.375	0.4

A trusted manufacturer is required for final Cyclone design and construction to ensure that it conforms to regulations, guidelines, is certified safe for use and ensure viable yield and operation. Figure 82 shows the dimensions required for design and manufacturing, the results of the following calculations for and based off these dimensions should be used as guidelines only.

For this purpose, the inlet of the cyclone is a rectangular parallelepiped and the other components are cylindrical.
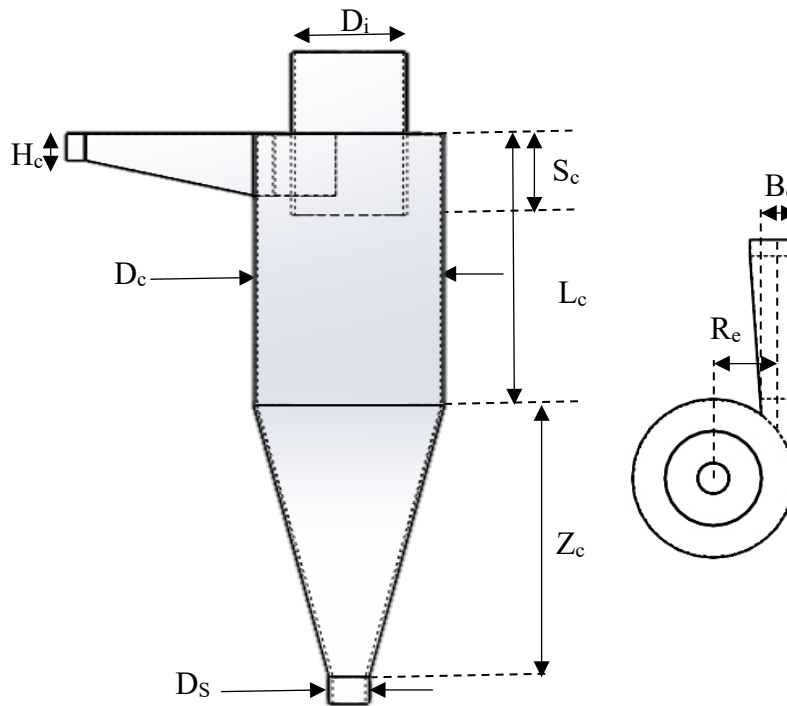
Figure 82 Cyclone Filter Dimensions

D.2.2 Resulting Dimensions

The desired result is to increase the overall separation efficiency. In order to calculate this, the particle size and density are required. The mass flow rate in the collected base stream is increased as the separation efficiency due to particle size increases, therefore the dimensions were derived from solving for the maximum value the separation efficiency due to particle size at each of the standard dimension ratios.

A second variable factor in particle collection is the gas flow rate through the cyclone, due to the low flow rate of air from the drier on site an additional impeller will be required to collect the small particle size desired. From setting D_c to 0.5m and using the Lappel model from Table 47 are described in the sections above which result in the Table 48.

Table 48 Cyclone Dimensions

	Dc	Hc	Bc	Sc	Di	Lc	Zc	Ds
Size (m)	0.5	0.25	0.125	0.3125	0.25	1	1	0.125

D.2.3 Defined Terms

Prior to starting the cyclone design, the physical properties of the dust stream to separate as well as some dimensional factors are required. Chapter 8 established the physical properties of the dust stream required experimentally, and the viscosity and density of air were taken from literature (Wang and Pereira, 2012). The results yielded are shown in Table 49.

Table 49 Set Properties Cyclone Design			
Dust load		2	g.m^{-3}
Gas viscosty	μ_g	1.83×10^{-5}	Pa.s
Gas density	ρ_g	1.184	kg.m^{-3}
Solid density	ρ_p	500	kg.m^{-3}

As the flow rate of air from the drier is less than the required 15 m.s^{-1} (Duroudier, 2016), the cut off diameter is defined from the dust analysis and the diameter set. The cut off diameter required from Section 8.2.3 was under 100 μm and the lowest measured particle size was just over 1 μm, anywhere within this range in theory should collect over 25 % of the dust present.

The diameter selected for the cyclone design is 0.5 m and the standard geometry selected is the Lapple dimension ratios in Table 47, due to the commonality of use of these standards (Nwigbo, 2019).

D.2.4 Number of Effective Turns N$_e$

The number of effective turns for a single-entry cyclone is the number of revolutions that the gas flow makes whilst traveling to the base of the separator in an external vortex. The more turns in this external vortex, the greater the degree of separation and collection. The Lapple Model defines the numerical value for Number of Effective Turns, N_e, as:

$$N_e = \frac{1}{H_c}\left[L_c + \frac{Z_c}{2}\right] = \frac{1}{0.3m}\left[1.0m + \frac{1.0m}{2}\right] = 5 \tag{213}$$

Equation 208 contains the inlet length, H_c, the cylinder length, L_c, and the length of the conical section, Z_c, Figure 82 further describes these dimensions.

D.2.5 Efficiency from Particle Size

The diameter of the particles collected with 50 % efficiency is the cut point diameter. This provides an indication of the range of particle sizes which the filter can collect. Increasing cut point diameter reduces the efficiency if the cut point diameter is within the range of desired collected particle size. This value should be as close as practicable to the smallest particle size measured with the Mastersizer or lower. The size distribution measured by the Mastersizer is in equivalent sphere diameter, using spherical diameters the cut point diameter is described by:

$$d_{50} = \left[\frac{9\mu_g H_C}{2\pi N_e v_{in}(\rho_p - \rho_g)}\right]^{0.5} = \left[\frac{9 \times 1.83 \times 10^{-5} \text{Pa.s} \times 0.25\text{m}}{2\pi \times 5 \times 15\text{m/s} \times (500\text{kg/m}^3 - 1.184\text{kg/m}^3)}\right]^{0.5} = 8 \ \mu\text{m} \tag{214}$$

Where the cut off diameter is d_{50} (μm), gas viscosity is μ_g (Pa. s), inlet width is H_c(m), the number of effective turns N_e is from the previous Section D.2.3, v_{in} is the inlet gas velocity (m.s⁻¹), ρ_p and ρ_g are the density of the particulates (kg.m⁻³) and gas respectively.

A general curve developed by Lapple (Lapple, 1951) shows the predicted collection efficiency for any particle size, an example of which is shown in Figure 83.
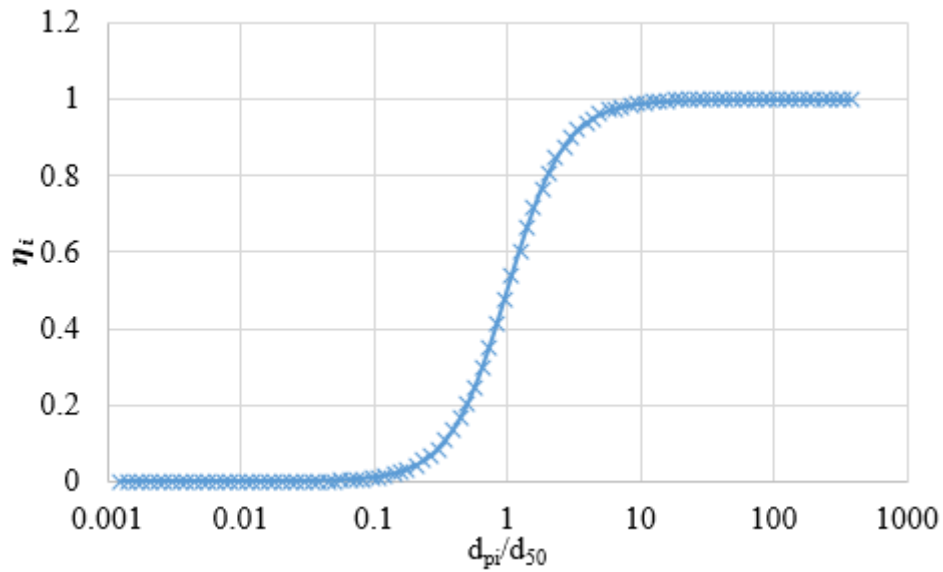
Figure 83 Predicted Cyclone Efficiency Depending from Diameter – Under the drier

The curve was produced from the known size distributions from Section 8.2.3, using an equation fitted to the original curve by Thedore and DePaola (1980) (Cooper and Alley, 2010). For this, each particle size d_{pi}, is based on the cut point diameter d_{50}, a prediction of collection efficiency $\mathbf{\eta_i}$ can be made, for example at 5µm:

$$\mathbf{\eta_i} = \frac{1}{1+\left(\frac{d_{50}}{d_{pi}}\right)^2} = \frac{1}{1+\left(\frac{8\mu m}{5\mu m}\right)^2} = 0.2809 \tag{215}$$

The weighted average of the collection efficiencies of particle sizes within the range.

$$\mathbf{\eta} = \sum \eta_i m_i \tag{216}$$

Where η_i is the collection efficiency for particle diameter i, and m_i is the mass fraction of particles with diameter i, (assuming mass fraction is equal to volume fraction). Note the particle size distribution entering the cyclone is not taken into account in the above efficiency equations, which is believed to have an impact on the collection efficiency as collisions between particulates effects particle trajectory.

For an estimation of performance efficiency, the three particle size distribution curves from Section 8.2.3 were collated to show the mass fraction in ranges of particle size and the individual particle size measurements in the range were multiplied with their respective mass fractions for the performance contribution, shown in Table 50.

Table 50 Particle Size Distribution Contributing to Performance

Particle size range μm	Mass Fraction %	Performance Contribution %	Mass Fraction %	Performance Contribution %	Mass Fraction %	Performance Contribution %
	Left Side		Centre		Under Drier	
$0 < d_{pi} \leq 2$	0.00	0	0	0	0.07	0.003672
$2 < d_{pi} \leq 4$	0.06	0.01041	0.29	0.03623	0.51	0.05945
$4 < d_{pi} \leq 6$	0.19	0.05442	0.4	0.1118	0.67	0.1890
$6 < d_{pi} \leq 10$	0.43	0.2071	0.56	0.2902	1.01	0.5247
$10 < d_{pi} \leq 18$	0.80	0.5933	1.28	0.9648	2.47	1.865
$18 < d_{pi} \leq 30$	0.96	0.8679	3.21	2.864	6.59	5.882
$30 < d_{pi} \leq 50$	1.44	1.386	6.97	6.678	12.51	11.97
$50 < d_{pi} \leq 100$	4.51	4.457	25.22	24.91	28.82	28.44
$100 < d_{pi} \leq 200$	17.90	17.85	27.88	27.79	21.18	21.11
$200 < d_{pi} \leq 500$	39.40	39.38	24.74	24.72	16.52	16.51
$500 < d_{pi} \leq 1000$	23.35	23.34	8.93	8.929	7.92	7.919
$1000 < d_{pi} \leq 2000$	10.22	10.22	0.52	0.5200	1.74	1.740
$2000 < d_{pi} \leq 3500$	0.73	0.7311	0	0	0	0
	Overall	99.1%	Overall	97.8%	Overall	96.2%

From these efficiencies, the lowest is for under the drier, as the sample from this location had the smallest average particle size and a smaller size distribution.

D.2.6 Gas Residence Time and Characteristic Velocities

To entrain particles into the base stream of a separator, the particles are forced to the walls of the cyclone. The increase in centrifugal force accelerated the particle in the horizontal direction. Residence time Δt (s), in terms of inlet velocity v_{in} (m.s^{-1}), cylindrical section diameter D_c (m) and number of effective turns N_e within the outer vortex can be described as:

$$\Delta t = \frac{\text{path length}}{\text{speed}} = \frac{\pi D_c N_e}{v_{in}} = \frac{\pi \times 0.5\text{m} \times 5}{15\text{m.s}^{-1}} = 0.5236 \text{ s} \tag{217}$$

The inlet velocity can be determined using the inlet gas volumetric flow Q_g (m^3.s^{-1}), the inlet height H_c (m) and inlet width B_c (m).

$$v_{in} = \frac{Q_g}{H_C B_C} = \frac{1687.5 \text{m}^3.\text{h}}{0.25 \times 0.125} = 15 \text{ m.s}^{-1} \qquad (218)$$

Similarly, the outlet velocity v_{out} m.s^{-1} can be determined using the inlet gas volumetric flow Q_g (kg.s^{-1}) and the diameter of the outlet D_i (m).

$$v_{out} = \frac{4Q_g}{D_i^2 \pi} = \frac{4 \times 1687.5 \text{m}^3.\text{h}^{-1}}{0.25 \text{m}^2 \times \pi} = 34380 \text{m.h}^{-1} = 9.549 \text{ m.s}^{-1} \qquad (219)$$

Terminal velocity in the radial direction v_{tr} (m.s^{-1}) is a function of the width of the cyclone inlet and the gas residence time:

$$v_{tr} = \frac{H_C}{\Delta t} = \frac{0.25 \text{m}}{0.5236 \text{s}} = 0.4775 \text{ m.s}^{-1} \qquad (220)$$

A second method for calculating the radial velocity is using the aspect ratios of the cyclone in the Section D.2.1:

$$v_{ri} = \frac{Q_g}{\pi D_c^2 K_i (K_L + K_Z - K_S)} = \frac{1687.5 \text{m}^3.\text{h}}{\pi \times 0.5^2 \times 0.5 \times (2+2-0.625)} = 0.3539 \text{ m.s}^{-1} \qquad (221)$$

Assuming that the drag force on each of the particles is according to stokes law, $F_{drag} = 3\pi d_p V_{td}$ (kg.m.s^{-2}) and the particle has a centrifugal force of $F_{cent} = \frac{mv^2}{r}$ (kg.m.s^{-2}). Where m is the mass of the particle minus the mass of the air displaced, the velocity is equal to the inlet flow and as the radius is half of the diameter results in:

$$V_{td} = \frac{(\rho_p - \rho_g) d_p^2 V_i^2}{9 \mu_g D_c} = \frac{(500 \text{kg/m}^3 - 1.184 \text{kg/m}^3) \times (5 \times 10^{-6})^2 \times (15 \text{m.s}^{-1})^2}{9 \times 1.83 \times 10^{-5} \text{Pa.s} \times 0.5 \text{m}} = 0.03407 \text{ m.s}^{-1} \qquad (222)$$

D.2.7 Pressure Drop (ΔP)

Pressure drop is due to the dissipation of energy due to friction, which causes a loss of kinematic energy, and due to the work done against the centrifugal forces, which occurs when the mixture returns to the mouth of the outlet pipe (Barth, 1956, Muschelknautz, 1972, Brunner, 1980).

Using Geometry Ratios

Inlet and outlet velocities

$$v_{in} = \frac{Q_g}{K_B K_H D_c^2} = \frac{1687.5 \text{m}^3.\text{h}}{0.25 \times 0.5 \times 0.5^2} = 15 \text{ m. s}^{-1} \tag{223}$$

$$v_{out} = \frac{4Q_g}{K_i^2 \pi D_c^2} = \frac{4 \times 1687.5 \text{m}^3.\text{h}}{0.5^2 \times \pi \times 0.5^2} = 9.554 \text{ m. s}^{-1} \tag{224}$$

Friction Coefficients

$$C_e = 1 - \left(0.680 - 0.151 \frac{K_i^2}{K_B K_H}\right) K_B^{\frac{1}{3}} = 1 - \left(0.680 - 0.151 \times \frac{0.5^2}{0.25 \times 0.5}\right) 0.25^{\frac{1}{3}} = 0.7619 \tag{225}$$

$$\frac{v_{walls}}{v_{in}} = (0.889 - 0.408 K_B)^{-1} = (0.889 - 0.408 \times 0.25)^{-1} = 1.271 \tag{226}$$

$$v_{walls} = \frac{v_{walls}}{v_{in}} \times v_{in} = 1.3 \times 15 \text{m. s}^{-1} = 19.06 \text{ m. s}^{-1} \tag{227}$$

$$Re_g = \frac{\rho_g v_{walls} D_c}{\mu_g} = \frac{1.184 \text{kg/m}^3 \times 19.06 \text{m.s}^{-1} \times 0.5}{1.83 \times 10^{-5} \text{Pa.s}} = 616600 \tag{228}$$

$$C_f = 2.5 \times 10^{-3} + \frac{144}{Re_g} = 2.5 \times 10^{-3} + \frac{144}{Re_g} = 0.002734 \tag{229}$$

Characteristic ratios and velocities:

$$\frac{R_i}{r_e} = \frac{K_i}{1 - K_B} = \frac{0.5}{1 - 0.25} = \frac{2}{3} \tag{230}$$

$$\frac{A_e}{A_i} \frac{R_i}{r_e} = \frac{4}{\pi} \frac{K_H}{K_i} \frac{K_B}{1 - K_B} = \frac{4}{\pi} \times \frac{0.5}{2} \times \frac{0.25}{1 - 0.25} = 0.4246 \tag{231}$$

$$\frac{A_f}{A_i} = \frac{4K_S}{K_i} + \frac{1}{K_i^2}[1 + 4K_L + 2K_Z(1 + K_S)] - 1 \tag{232}$$

$$= 4 \times \frac{0.625}{2} + \frac{1}{2^2}[1 + 4 \times 2 + 2 \times 2(1 + 0.625)] - 1 = 66 \tag{233}$$

$$\frac{v_{c\theta i}}{v_{out}} = \left[C_e \frac{A_e}{A_i} \frac{R_i}{r_e} + C_f \frac{A_f}{A_i} \sqrt{\frac{R_i}{r_e}}\right]^{-1} = \left[0.7619 \times 0.4246 + 0.002734 \times 66 \times \sqrt{\frac{2}{3}}\right]^{-1} = 2.124 \tag{234}$$

$$v_{c\theta i} = \frac{v_{c\theta i}}{v_{out}} \times v_{out} = 2.124 \times 9.554 \text{m. s}^{-1} = 20.29 \text{ m. s}^{-1} \tag{235}$$

For the coefficients within the pressure drop term:

$$\frac{A_f}{\pi R_i \sqrt{R_c R_i}} = \frac{1}{K_i^{\frac{3}{2}}} [1 - K_i^2 + 4(K_i K_s + K_L) + 2K_z(1 + K_s)] \tag{236}$$

$$= \frac{1}{2^2} [1 - 2^2 + 4(2 \times 0.625 + 2) + 2 \times 2(1 + 0.625)] = 46.67 \tag{237}$$

This value is required for ξ_{ce} (the pressure drop coefficient of the inlet and inside of the cyclone), which along with ξ_{ci} (the pressure drop coefficient for the outlet of the cyclone) is part of the overall pressure drop coefficient of the cyclone, ξ_c.

$$\xi_{ce} = \frac{D_i}{D_C} \left[\left(1 - C_f \frac{A_f}{\pi R_i \sqrt{R_c R_i}} \frac{v_{c\theta i}}{v_{out}}\right)^{-2} - 1 \right] \left(\frac{v_{c\theta i}}{v_{out}}\right)^2 \tag{238}$$

$$= \frac{0.25m}{0.5m} [(1 - 0.002734 \times 46.67 \times 2.124)^{-2} - 1](2.124)^2 = 1.989 \tag{239}$$

$$\xi_{ci} = 0.75 \left[2 + 3\left(\frac{v_{c\theta i}}{v_{out}}\right)^{\frac{4}{3}} + \left(\frac{v_{c\theta i}}{v_{out}}\right)^2\right] = 0.75 \left[2 + 3(2.124)^{\frac{4}{3}} + (2.124)^2\right] = 11.03 \tag{240}$$

$$\xi_c = \xi_{ce} + \xi_{ci} = 1.989 + 11.03 = 13.02 \tag{241}$$

The resulting pressure drop ΔP_c (Pa):

$$\Delta P_c = \xi_c \frac{1}{2} \rho_g v_{out}^2 = 13.02 \times \frac{1}{2} \times 1.184 \text{kg.m}^{-3} \times (9.554)^2 = 703 \text{ Pa} \tag{242}$$

This value is within the <2000 Pa suggested (Masuda et al., 2006).

Alternative Methods

The pressure drop in number of inlet velocity heads provides an estimation for the pressure drop over the system, though this does not account for the height of the cyclone as it is based on the inlet dimensions H_c the height of the inlet and W the width of the inlet. From the inlet velocity and the gas density, the static pressure can be calculated:

$$H_V = K \frac{H_c W}{D_e^2} \tag{243}$$

$$\Delta P = \frac{1}{2} \rho_g v_{in}^2 H_V \tag{244}$$

Alternate approaches for pressure require knowledge of the total inlet and outlet velocity pressures, P_{Vin} and P_{Vout}:

$$\Delta P = K(P_{Vin} + P_{Vout}) \tag{245}$$

A second alternative is to calculate component pressure drops, which collectively describe the overall pressure drop of the system.

D.2.8 Overall Separation Efficiency

Within process industries overall efficiency is often concentrated on as a vital consideration to processes, in practice this can be determined from performing a mass balance over the system with feed $\dot{m}_f^s$, overflow $\dot{m}_1^s$ and base stream $\dot{m}_2^s$ mass flow rates (kg.s^{-1}), as described in Figure 74:

$$\dot{m}_f^s = \dot{m}_1^s + \dot{m}_2^s \tag{246}$$

Overall, the separation efficiency can be calculated from the ratio of successfully collected mass flow to the feed mass flow. This is a suitable alternative to using overall cyclone collection efficiency if the aim of the cyclone is to collect all particulates within the feed:

$$\eta = \frac{\dot{m}_2^s}{\dot{m}_f^s} = \frac{\dot{m}_2^s}{\dot{m}_2^s + \dot{m}_1^s} = 1 - \frac{\dot{m}_1^s}{\dot{m}_f^s} \tag{247}$$

D.2.9 Simulation

From the recommended dimensions calculated in Section D.2.1 and D.2.2, Table 48, and the particle size distribution in Section 8.2.3 plotted a simulation in the commercial CFD Finite Volume based ANSYS Fluent 19.3 can be used to predict the pressure exerted on the cyclone walls. This wall pressure is required for the design load and stresses. Using the dimensions from Table 48, a 3D model of a cyclone separator shown in Figure 84, was created using

SolidWorks, version 19. Importing into CFD software allowed the simulation of how dust flows through the cyclone filter.

The realizable k-ε model was chosen to account for turbulence and was selected as it commonly used in cyclone design. This is preferred over other modelling techniques, as it contains a function that includes the effects of mean strain, rotation rates and the angular velocity of the system rotation, when predicting swirling flows and strong streamline curvature, such as that experienced in the cyclone (Ansys-Inc., 2020). Standard wall functions were implemented to account for the boundary layer.
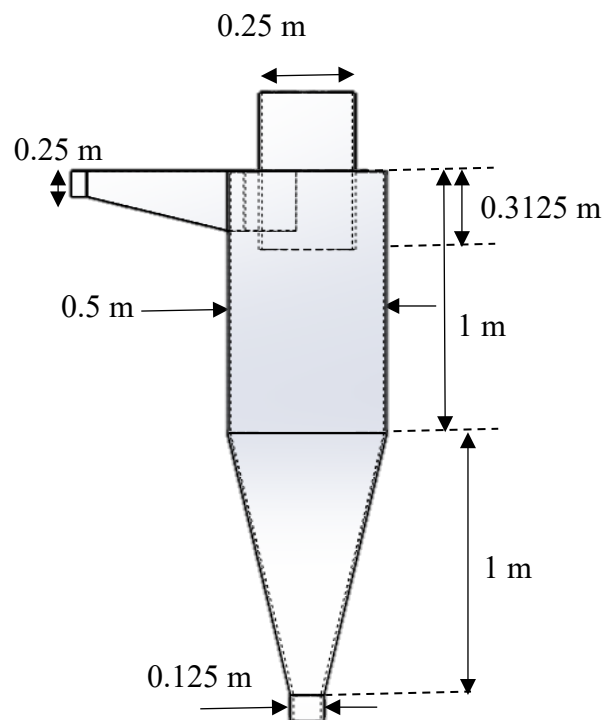
Figure 84 3D Model of Cyclone Separator

Design Loads

A design pressure of 5-10% above the working pressure is recommended by Coulson and Richardson (Sinnott et al., 2005). The centripetal force from air velocity and particle and negative pressure from the impeller will have an impact on the forces acting on the separator. To check this result ANSYSFluent was used to model the cyclone to the defined dimensions,

a particle diameter of 15 μm, dust load of 0.001 g.s^{-1} and air flow rate 25 m.s^{-1}. Figure 85 shows that the resulting pressure on the walls of the cyclone was 281 Pa hence a design pressure of 310.2 Pa is to be used to define shell thickness.
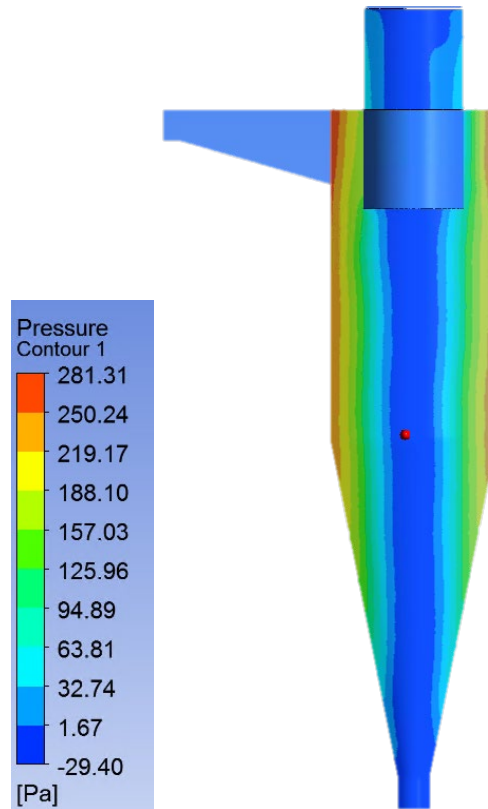
Figure 85 Pressure Contours Cyclone

D.2.10 Construction

Within this section the material of construction was selected and a material thickness calculated.

D.2.11 Material Selection

The material selected for construction can have a high durability or an additional thickness to account for corrosion allowance can be applied. Ceramics, glass or enamel are widely used for this purpose, specific polymer-based materials can be used to coat surfaces exposed to

corrosive materials. The inlet stream (particle dust flow) processed contains no erosive or corrosive components.

To reduce costs, plastics, such as polystyrene (PS), polyvinylchloride (PVC) and polyvinylidenefluoride (PVDF), are commonly used to construct cyclone separators. However as plastic is not conductive of charge; a build-up of static within the separator can become a potential hazard and because of the small particles in the processed stream reduce cyclone efficiency. A more durable and conductive solution is to use metal or metal alloy such as stainless steel, aluminium, nickel. As the material does not need to be significantly corrosive resistant the material can be selected based on the most widely available and cheapest material (Sadeghbeigi, 2012). Alumina is the most common lining material for cyclones, which is one third of the price of silicon carbide (Ruys, 2019).

Stainless steel is the selected material due to its rigidity, ability to be formed, welded, resistant to corrosion and strength, plastic would be a cheaper alternative however due to localised static build-up there is a possible spark risk involved in using this material. Specific suppliers may have specialised designs to overcome static from using plastic. However, this is outside of the scope of this work as discharging discrete localised static can prove difficult. An austenitic grade is required for formability, machinability and mild corrosive resistance. Grade 304 is the most widely used grade and is suitable for this purpose (Smith, 2016).

Thickness

In addition to the dimensions of the separator outlined in Section D.2.2, the wall thickness of the cyclone is required. To calculate the wall thickness the principles of pressure vessels were used to calculate the wall thickness at various sections and the largest of these thicknesses was used to determine the required overall thickness.

For every thickness calculated, the design stress of the material is required. The material selected, SS304, is austenitic with 45% elongation after fracture, therefore from EN 13445-3 the design stress f_d (MPa) is;

$$f_d = \max\left[\frac{R_{p1.0/T}}{1.5}; \min\left(\frac{R_{p1.0/T}}{1.2} : \frac{R_{m/T}}{3}\right)\right] \tag{248}$$

In BS EN 10088-2:2014 for 1.4301 (SS304) hot rolled the 1% proof strength and tensile strength defined as;

$$R_{p1.0/T} = 240\text{MPa}; R_{m/T} = 520\text{MPa} \tag{249}$$

$$f_d = \max\left[\frac{240}{1.5}; \min\left(\frac{240}{1.2} : \frac{520}{3}\right)\right] = 173\text{MPa} \tag{250}$$

A joint coefficient z increases the thickness to allow for minor joint flaws, though it may be possible that the parts would be formed by pressing and radiography can determine if a joint coefficient of 1 is suitable, a value of 0.85 to allow for some flaws. Using Stainless Steel means that the design is over engineered due to the low pressure inside, however, this material will be resistant to some impact from fork lift trucks.

Flat Top Shell Thickness

For a flat ended vessel the design thickness e (mm) is shown by Equation 246.

$$e = C_p D_c \sqrt{\frac{P_i}{f_d z}} = 0.55 \times 0.5\text{m} \times \sqrt{\frac{310.2\text{Pa}}{173\text{MPa} \times 0.85 \times 10^6}} = 0.399\text{mm} \tag{251}$$

Where the design constant C_p ranges from 0.55 to 0.4 dependent on the construction of the vessel, hence the value of 0.55 was used for the largest thickness value.

Cylindrical Body Shell Thickness

$$e = \frac{P_i D_c}{2 f_d z - P_i} = \frac{310.2 \times 10^{-6}\text{MPa} \times 0.5\text{m}}{2 \times 173\text{MPa} \times 0.85 - 310.2 \times 10^{-6}\text{MPa}} = 0.527\mu\text{m} \tag{252}$$

Conical Base Shell Thickness

$$e = \frac{P_i D_s}{2f_d z - P_i} \frac{1}{\cos(\alpha)} = \frac{310.2 \times 10^{-6} \text{MPa} \times 0.5\text{m}}{2 \times 173\text{MPa} \times 0.85 - 310.2 \times 10^{-6} \text{MPa} \times \cos(11.31)} = 1.70\mu\text{m} \quad (253)$$

Corrosion Allowance

To allow for a corrosion an additional 2 mm is usually added (Sinnott et al., 2005), however, as the selected material is resistant to corrosion from both the atmosphere and the material flowing through the separator, and thus the extra thickness is not necessitated.

Overall

The resulting shell thicknesses from the above calculations are all below 0.4mm which is thin for a cyclone of this size as the vessel needs to withstand its own mass. This thickness would not be able to withstand external pressure from possible forklift incidents, human interaction or the hoop stress of the construction, a more commercially available thickness of sheet metal and stronger for this environment is 1 mm thick.

The design stresses for the above are only to be used if the hoop, σ_{hoop} (MPa) and longitudinal, $\sigma_{\text{longitudinal}}$ (MPa), stresses for the thickness calculated are less than the design stress, with the new 1 mm thickness the hoop and longitudinal stresses are:

$$\sigma_{\text{hoop}} = \frac{P_{\max}D}{2e} = \frac{310.2 \times 10^{-6} \text{MPa} \times 0.5\text{m}}{2 \times 1 \times 10^{-3}\text{m}} = 77.6\text{MPa} \quad (254)$$

$$\sigma_{\text{longitudinal}} = \frac{P_{\max}D}{4e} = \frac{310.2 \times 10^{-6} \text{MPa} \times 0.5\text{m}}{4 \times 1 \times 10^{-3}\text{m}} = 38.8\text{MPa} \quad (255)$$

Both of which are below f_d (173MPa).

D.2.12 Specification Sheet

Table 51 Cyclone Specification Sheet

Gas Flow - Air				Dust - Wood				
Gas flowrate	Vc	1687.5	$m^3.h$	Section D.2	Solid density	500	$kg.m^{-3}$	Section 8.2.5
Gas viscosty	μc	1.83×10^{-5}	Pa.s	(Mindset, 2020)	Dust load	2	$g.m^{-3}$	Section 8.2.5
Gas density		1.184	$kg.m^{-3}$	(Mindset, 2020)	Other Characteristics		Coagulates when damp, Absorbent, Accumulates Charge	

Cyclone		
Operating Pressure	1	atm
Maximum Allowable Pressure Drop	2	kPa (Faulkner and Shaw, 2006)
Construction Materials	Stainless Steel	1 mm thick
ASME Code Construction	ASME VIII Div 1; ASME B31.3, B31.4; B31.8	

Auxiliaries	
Cyclone Stand	Fixed
Clean Air Outlet	Fitted to Bag House Filter
Dust Hopper	2kg Capacity for emptying every week
Dust Discharge Valve	Yes
Other	Bag House Filter Connected To air Outlet
Desired Collection Efficiency	>90%

Table 52 Particle Size Distribution - Using Mastersizer 3000

	Dx (10) (μm)	Dx (50) (μm)	Dx (90) (μm)	Laser Obscuration (%)
Left Side of the Drier				
Mean	114.36	376.0667	1037.6	4.994667
Standard Deviation	10.00434	21.96903	96.12849	1.616499
RSD (%)	8.748113	5.84179	9.264503	32.36451
Centre of the Drier				
Mean	43.7	146	509	8.2
Standard Deviation	2.65	6.34	16.5	0.14
RSD (%)	6.07	4.34	3.25	1.76
Under The Drier				
Mean	28.2	100	479	9.01
Standard Deviation	0.815	3.31	37.5	0.5
RSD (%)	2.89	3.3	7.81	5.52

D.2.13 Conclusion

Key Findings

- In an ideal situation, the proposed cyclone design has a theoretical collection efficiency of over 96%.

- Simulations of the cyclone show increased pressure at the sides of the vessel due to the centrifugal force from the particles and due to airflow hitting the walls.

- The advised material of construction is stainless steel 1 mm thick.

Highlights and Limitations

The ANSYS Fluent simulation of the cyclone only takes into account one size of particle so does not contain the distribution results, which would produce a prediction for the fractional efficiency curve (FEC) of the cyclone filter. The predicted collection efficiency curve does not take into account the reduction of efficiency as particle size increases, particles will not be carried by the carrier gas into the separator if they are too heavy to be lifted by the inlet air stream.

Recommendations

A comparison of results for cyclones of the standard dimension ratios from Table 47 using the same method would provide details of the impact of aspect ratios on collection efficiencies, pressure drops across the cyclone and velocity profiles. To test the materials integrity finite element analysis could be used on a model of the cyclone.

D.3 Baghouse Filter

As in this case, apparent particulates which are extremely fine and low density, cyclone separation is not entirely effective, and the gas-solid stream can be vented through a fabric filter further refining the stream. Bag type fabric filters, commonly known as baghouse filters, are made of fabric as a filter medium. Entering the bag house by suction or positive pressure the substrate stream is directed to the baghouse filter. Heavier particles fall whilst lighter particles are held in the air stream through to the filter bag. Depending on the design, air is drawn through the bags and accumulates on one side of the filtrate material. Dust, which accumulates on the filtrate forms a cake, increasing resistance to gas flow and therefore decreasing efficiency.

To improve efficiency the filter, bags need to be cleaned once a sufficient pressure drop occurs. There are filters which need to be on-line and some which can be off-line during

cleaning which is inherent of the design. Similar to a cyclone, if the inlet stream is at an angle of incident the air flow can cause a vortex improving separation.

Baghouse filters can collect particles with sizes between 0.001 μm and 50 μm (Figure 81) and have efficiencies reportedly in the region of 99.5 % for particles <5 μm (Smith and Mines, 1987). As a layer of dust settles on the fabric, filtration increases as the dust forms an additional layer for particulates to get through.

D.3.1 Collection Mechanisms

By design filters separate by particle size, as dust is larger than gas, the gas molecules can pass through the filter whereas the particulates cannot. With the particulates accumulating on the fabric these filters use mechanisms such as straining, impact, direct interception and diffusion. Straining removes particles larger than the gaps between fabric fibres, like a sieve, removing larger particles. Impacting removes large particles as they hit fibres directly and cannot free themselves due to the gas stream. Direct interception is where molecules go round the fibres and end up coming to a stop halfway round them. Due to Brownian diffusion, some molecules are removed from the gas stream due to random motion as the particle deflects within the gas stream. In addition to these mechanisms entrapping particles in the fabric (depth filtration) particles also get trapped within the filter cake (cake filtration).

D.3.2 Depth Filtration

Particles can get caught on fibres within the fabric. Due to Van der Waal's forces, the particles adhere to the fibres as they stray from the airflows convoluted trajectory. Through nonwoven fabric this filtration method means that dust cake forms slower as flow is more uniform than in woven fabric, where there are areas of concentrated flow. In high humidity situations, especially with wood dust as it absorbs moisture and can stick to the surface, as clogging can occur.

Cake Filtration

Woven fabrics act more like sieves as they allow particles of a certain size through the mesh of the fabric. As particles deposit on this surface filtration improves due to the new flow paths created effectively reducing the size of the mesh. However, there is an optimum layering of filter cake as increased thickness increases the pressure drop in turn decreasing operation. Hence, cleaning is required to maintain operation.

Operating without a layer of dust reduces efficiency so it is recommended that an initial cake construction period takes place with lower air flow which gradually increased to prevent clogging. In both methods, dust acts as a filtration media so an understanding of the fabric and dust properties are important to complement these methods.

D.3.2 Pressure Drop

The difference in pressure between the clean air and contaminated air side of the filtrate is the differential pressure. This is caused by the resistance to flow as the air passes through the filter and filter cake, and thus the pressure drop is an important consideration in design. A high-pressure drop means higher energy cost as air is pushed or pulled through the filter by fans. Differential pressure gauges are the best way of indicating operating status, however these have to be maintained, as over time they can become clogged or damaged. Sudden drops indicate a leak and sudden spikes indicate that the filter has become blocked by particulates.

D.3.3 Materials

Generally made of woven or unwoven fabric the properties of the selected material are important. However, the temperature in this case does not surpass 50 °C and the material is not acidic or alkaline, making more materials suitable than if this were the case. The materials and

method of manufacturing effect the characteristics of the filter are listed in Table 53 and Table 54.

Table 53 Baghouse Filter Material Characteristics

Material	Characteristics (Purchas and Sutherland, 2002) (McKenna and Turner, 1989)				
	Maximum Operating Temperature °C	Abrasion	Alkalis	Acids	Relative Cost
PP-Polypropylene	120°C	Good	Excellent	Excellent	0.5
Nylon-6 Polyamide	105-120°C	Excellent	Excellent	Fair	0.6
PET-Polyester	150°C	Excellent	Poor	Good	0.5
LDPE-Low Density Polyethylene	65-74°C	Good	Excellent	Excellent	-
HDPE-High Density Polyethylene	93-110°C	Good	Excellent	Excellent	-
Nomex®-Polyamarid	205-230°C	Excellent	Fair	Good	2.0
Cotton	93°C	Fair	Poor	Good	0.4
Fiberglass	280°C	Poor	Poor	Poor	1.0
Teflon®	260°C	Fair	Excellent	Excellent	6.7

Table 54 Baghouse Filter Material Details

Material	Details (Purchas and Sutherland, 2002) (Hutten, 2015)
PP-Polypropylene	Tough, rigid thermoplastic commonly used for gases and non-aqueous fluids. Resistant to static build up. High temperature resistance and flow rates. Up to 7 g/ denier tenacity.
Nylon-6 Polyamide	Hydrophobic with high tensile strength. Suitable for high flow rates and long life. Used in wet filtration and absorbs water. Tenacity of 10g/denier.
PET-Polyester	Very widely used. High flow rates. Low differential pressures and low extractables. Low tenacity up to 9 g/ denier.
LDPE-Low Density Polyethylene	Hydrophobic, low tenacity of up to 6 g/ denier, but dependent on processing.
HDPE-High Density Polyethylene	Higher melting point than LDPE, low tenacity of up to 6 g/ denier
Nomex®-Polyamarid	Flame resistant but combustible dusts impregnating fibres can combust and damage the fabric.
Cotton	Absorbent and inexpensive, but can allow fungal growth
Fiberglass	Does not adsorb water. High flow rates. Good wet strength and high holding capacity. Can be woven or felted, but very brittle.
Teflon	Very chemical resistant. High cost, poor abrasion resistance. High cost. Low tenancy of up to 5 g/ denier.

As high temperatures, acid resistance and alkaline resistance are not required in this system from Table 53 polymer-based material has the cheapest cost and abrasive resistance. In addition

to the base material, finishes, which improve material properties, are available. Polyester and Polypropylene are most suited to this situation from criteria in Table 53 and Table 54.

Specified also for baghouse filter design is an indication of thickness in the form of 'weight per unit area'. Permeability depends upon if the fabric is woven or unwoven, space between weaves and the thickness. Woven fabric is more suited in this case as, discussed in Section D.3.1, clogging can occur in nonwoven fabrics.

D.3.4 Durability and Fabric Testing

Durability of baghouse filters can be affected by temperature (thermal durability), abrasion and chemical attack. If the operating temperature is higher than the design temperature the filter will be prone to failure. In this case the temperature is below 50 °C so the design temperature is not significantly high. In addition, highly corrosive chemicals are not used and the majority of the filter stream will contain moist air. Abrasion however is of concern and is a common issue due to the cleaning methods used, often whereby motion is used to dislodge particles and, in the process, could also cause damage.

To ensure the fabric is suitable for purpose British Standard and ASTM tests such as BS 5636:1978, BS EN 29073-3:1992, ASTM D3885 - 07a (2019), and ASTM D2176-69 can be performed. These tests include permeability, flexibly and strength testing. If the fabric does fail, these tests can also be used to analyse the mode of failure.

D.3.5 Mechanical Designs

As mentioned earlier in Section D.3 baghouse filters can have different designs with different flow directions and methods of dust removal. In all the designs, solids are collected in the base utilising gravity. These include the mechanical shaker design, reverse airflow and pulse jet, with each having a unique design feature for dust collection.

Mechanical Shaker

As the name suggests mechanical shaker baghouse filters use mechanical motion to move the filtrate fabric and as dust accumulates it reaches a threshold where it has a large enough mass to dislodge itself and subsequently falls to the collected solids. Fine dust is collected from the contaminated stream and the cleaning mechanism imposes this motion. The filter bag is flexible and motion creates waves along the fabric.

The efficiency of these filters is affected by the material used, the tension in the material and the nature of the mechanical motion. Frequency and amplitude of the motion are typically 4 Hz and 2-3 inches (Hetsroni, 1982). Fabric tension depends on how taught the bags are pulled when installed.

The airflow must be diverted during cleaning as the positive pressure stops dust from falling off the filter fabric. To avoid a batch operation this can be diverted through a second baghouse filter compartment. These filters have a large space requirement and the fabric used has to be durable due to the mechanical movement involved. This means there is limited downtime for operation allowing for a continuous process of filtration.

Reverse Airflow

Due to the fragility of fiberglass and fabric derivatives, a new method of cleaning was sought, which brought about a less intensive method of bag cleaning. This method involves removing dust from the bags through the reverse air cleaning process. With stationary tube filters a system of valves and piping the air flow is reversed through the filters causing the solids to dislodge from the filter bag and collect into a compartment. The contaminated flow is accumulated through the centre of the bags, with dust collecting on the inside of the fabric.

As before to operate in continues mode more compartments are required. The airflow is reversed in one compartment with filtration stopped, the slow introduction of reversed air

collapses the fabric, dislodging the dust and cleaning the bag. Woven fabrics are more suited to this design as dust is less penetrative in woven compared to felted fabrics. As the fabric collapses on reverse airflow stiff rings are installed in the fabric in intervals to prevent the bag closing. Again, tension on the filter bags plays a role in the efficiency of the filter.

Pulse Jet

Pulse jet bag filters use compressed air in high pressure pulses from the top of each bag to clean off the dust. With or without a venture at the top of the filter, the filter is more ridged than the previous designs and is cleaned quickly with a pulse of air. A caging supports the filter material preventing collapsing. Once a layer has accumulated onto the filter material valves are opened which releases pressured air through the filters dislodging the dust and cleaning the filter. Separated dust then moves through a valve or lock which helps prevent air from entering the hopper through the outlet.

These filters have a short cleaning period so can be operated with very little down time during cleaning. With short, fast bursts of airflow the fabric can be effectively cleaned. Felted fabrics are better suited to this type of filter as filter cake is dislodged during the cleaning process.

As pulse jet filters require dry compressed air and are not suited to wetter streams this filter type is not suited to the wood dust produced from drying as the air has a higher moisture content than the natural airflow. Mechanical shaker and reverse airflow baghouse filters are better suited to the situation.

Air to Cloth Ratio

The gas-to-cloth ratio largely depends on the fabric (woven or non-woven), the dust characteristics, and the mechanical design of the filter. In case the gas-to-cloth ratio is

significantly higher than required, the efficiency is then lowered, and reducing the life of the fabric. The cost will then be higher than required.

For wood dust, the recommended gas-to-cloth ratio is 3.5 ft^3min^{-1} for woven fabric and 12 ft^3min^{-1} for nonwoven fabric. Alternate methods for calculating gas-to-cloth ratios include using manufacturers factors which are dependent on the baghouse style. The larger this gas-to-cloth ratio, the grater the interference with the gas stream. This ratio is then multiplied via a guide that follows an overall cloth area.

Table 55 Cloth Area - Woven and Non-Woven Fabrics

Net Cloth Area / ft^2	Woven Gross Cloth area / ft^2	Nonwoven Gross Cloth area / ft^2
$1 < \leq 4000$	7.000	24.000
$4000 < \leq 12000$	5.250	18.000
$12000 < \leq 24000$	4.375	15.000
$24000 < \leq 36000$	4.095	14.040
$36000 < \leq 48000$	3.938	13.500
$48000 < \leq 60000$	3.885	13.320
$60000 < \leq 72000$	3.850	13.200
$72000 < \leq 84000$	3.815	13.080
$84000 < \leq 96000$	3.780	12.960
$96000 < \leq 108000$	3.745	12.840
$108000 < \leq 132000$	3.710	12.720
$132000 < \leq 180000$	3.675	12.600
$180000 <$	3.640	12.480

Conveying Velocity

The conveying velocity is dependent on the material and describes the minimum velocity required to carry the material. For wood, dust an estimation of the desired conveying velocity is 4000 ft/min (Systems, 2015). The airflow in the system is dependent on head height, the ductwork system size and bends, and the filters.

D.4 Duct System

The network of piping to the filter is called the duct system, and this carries the contaminated airflow to the filter. Through this ducting, a minimum conveying velocity is required which

will stop dust from building up, causing blockages and effecting air flow. If the air flow is too great, it will erode the ducting through abrasion. To carry dust air must also flow above or at minimum speed equal to the conveying velocity. In this case, the dust is also flammable so care must be taken to avoid build-up. In the main ducting 4000 ft/min is required, and within the branches a velocity of 4500 ft/min is more suitable (Systems, 2015). Due to the small particle diameter and the woodchip fines collected this velocity may be lower in practice.

The primary source is above the drier bed, in addition secondary sources, that can be implemented around the building if desired.

Table 56 Air Volume in Circular Ducting (Incorporated, 2020)

Diameter	4000ft/min	4500ft/min
3 "	195 ft^3 /min	220 ft^3 /min
4 "	350 ft^3 /min	395 ft^3 /min
5 "	545 ft^3 /min	615 ft^3 /min
6 "	785 ft^3 /min	885 ft^3 /min
7 "	1070 ft^3 /min	1205 ft^3 /min
8 "	1395 ft^3 /min	1570 ft^3 /min
9 "	1765 ft^3 /min	1990 ft^3 /min
10 "	2180 ft^3 /min	2455 ft^3 /min

Joining branches means that the airflow required after the joining branches is the sum of the ft^3.min^{-1} of each branch; for example a 3 " and a 5 " are 195 ft^3 /min and 545 ft^3 /min from Table 56 therefore 740 ft^3 /min is needed to travel down the main pipe. From Table 56 It can be seen that the ducting will need to be ~6 " in diameter.

Considering the drier as the only primary source, a concave 'fume hood' which covers the drier with a single ducting towards the filter with a secondary smaller duct into the room with the heat exchanger should be an adequate for the removal of dust. Additional areas of ducting may be for the boiler room or storage, however the volume of dust in these areas was found to be significantly lower. In addition, using a fume hood over the bed in this instance will also reduce the level of dust in other areas.

Elbows within the ducting should be less than 90°, as greater angles cause more airflow resistance and back pressure. The resistance to flow is described by coefficients shown in Section D.4.1. This reduces the chance of blockages and improves the quality of airflow.

The sizing of the selected ducting will be dependent on the ducting supports, height and location of the filter and should be carried out by a qualified duct piping system design engineer. The example system in Figure 86 shows how branches can link and will be used to calculate the system pressures in Section D.4.1.
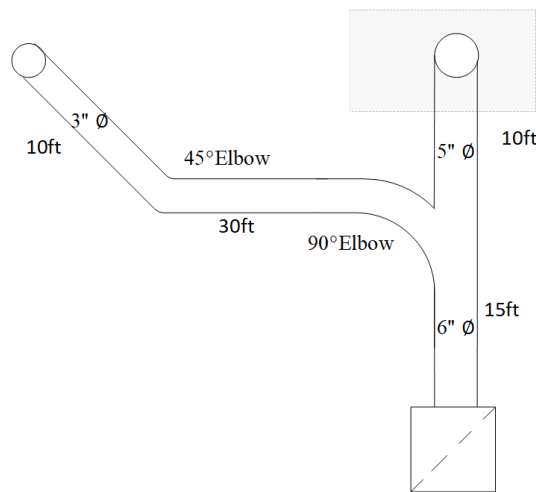

Figure 86 Example Ducting System from Drier and Heat Exchanger Room to Filter

D.4.1 Pressure

Within filter design, the vacuum pressure and static pressure play a significant role. These describe the suction and resistance to suction. Fans must be able to pull the dust from above the drier to the filter system and through the filter media, thereby overcoming the static pressure created by the ducting system. These are measured in inches of water gauge, iwg.

Table 57 Frictional Loss (Static Pressure) iwg per 100ft of duct (Specialist, 2015)
(*extrapolated from graph)

Diameter	4000ft/min	4500ft/min
3 "	9.5*	12*
4 "	7.03	8.80
5 "	5.36	6.70

6 "	4.29	5.36
7 "	3.55	4.44
8 "	3.02	3.78
9 "	2.75*	3.5*
10 "	2.3	2.88

Table 58 Percentage Coefficient for Equivalent Resistance of Straight Duct for Elbows (1.5CLR) (MFG, 2015)

Diameter	90°	60°	45°	30°
3 "	5	3	3	2
4 "	6	4	3	2
5 "	9	6	5	3
6 "	12	8	6	4
8 "	13	9	7	4
10 "	15	10	8	5

Table 59 Percentage Coefficient for Equivalent Resistance of Straight Duct for Branch Entry (MFG, 2015)

Diameter	45°	30°
3 "	4	3
4 "	6	4
5 "	7	5
6 "	9	6
7 "	10	6
8 "	11	7
9 "	13	8
10 "	14	9

For the example in Figure 86 there is 10 ft of 3 " diameter pipe, 30 ft of 3 " diameter pipe,10 ft of 5 " pipe and 15 ft of 6 " pipe at 4000 ft/min.

$$9.5 \times \frac{10}{100} + 9.5 \times \frac{30}{100} + 5.36 \times \frac{10}{100} + 4.26 \times \frac{15}{100} = 4.975 \; iwg \; \text{SP} = 1240 \; \text{Pa} \qquad (256)$$

In addition, there is a 3 " 45 ° elbow and a 3 " 90 ° elbow.

$$9.5 \times \frac{3}{100} + 9.5 \times \frac{5}{100} = 0.76 iwg \; \text{SP} = 189 \; \text{Pa} \qquad (257)$$

As the 90 ° elbow is a 45 ° branch entry.

$$9.5 \times \frac{4}{100} = 0.38 iwg \; \text{SP} = 94.65 \; \text{Pa} \qquad (258)$$

For the baghouse filter the operating pressure is usually designed at 3 iwg-5 iwg, as an overestimate 6iwg is used.

Overall static pressure can be calculated.

$$4.975 + 0.76 + 0.38 + 6 = 12.097 iwg \text{ SP} = 3010 \text{ Pa} \qquad (259)$$

When multiple branches are in place the branch with the highest static pressure and the main trunk are added to the baghouse operating differential pressure to calculate the total system static pressure.

D.4.2 Additional Options

Airflow will change if the ducting is altered so a variable speed drive fan would provide system control when the load changes, i.e. when the air flow in the drier is stopped, potentially saving energy when loads change. Recirculating airflow will conserve heat, if the airflow is not returned, the open side building design will produce enough airflow to balance out the air removed. The dust discharge, usually a manually operated door, can be automated. The manual option is suited if the load is light, however if the hopper is not kept clean there can be damage to the filter and operational issues. A rotary airlock can be installed however this will likely cost upwards of £2000. Traps can be installed which allow for cleaning along the ducting. An additional capacity can be installed which is less costly if an expansion is factored into the original design.

To reduce the risk of explosion or fire spark arresters, explosion vents, inert gas injection or sprinklers are preventative and protective measures that can be installed.

D.4.3 Cleaning

The parameters within each cleaning device are summarised in
Table 60.

Table 60 Cleaning Mechanism Parameters

Cleaning Parameter	Mechanical Shaker	Reverse Airflow	Pulse Jet
Regularity	Frequent- Adjustable at several cycles a second.	Continuous - Cleaned compartmentally, can be continuous or initiated by a set pressure.	Very frequent- A row of bags in sequence.
Movement	Mechanical – ripple motion of the filter .	Slow collapse and inflation of the filter bag.	Air shock wave
Amplitude		N/A	N/A
Online/Offline	Offline-Compartmentally	Offline-Compartmentally	Online
Duration	Dependent on number of cycles can be 30seconds to 5 minutes.	1 to 2 minutes for operation and dust to settle	Pulse duration 0.1 seconds
Tension	Variable during cleaning	50 to 120lbs	N/A

Though the duration of cleaning is longer reverse airflow is more suited to this purpose as the change in direction of airflow can be achieved with equipment which is present in both the mechanical shaker and the reverse airflow. Due to the mechanical shakers having additional parts which will required additional steps in maintenance the reverse airflow design is selected.

D.4.4 Safety

When working with filters make sure the appropriate PPE is worn, i.e. gloves, safety glasses and dust masks. Follow guidelines on equipment regarding maintenance or cleaning of moving parts and electrical components.

D.4.5 Conclusions

From Sections D.2 to D.4 the design criteria in Table 61 were determined.

Table 61 Design Criterial Baghouse Filter

Baghouse Type	Reverse Airflow
Static Pressure	Example Design- 12iwg
Minimum Conveying Velocity	Main 4000ft/min Branches 4500ft/min
Air to Cloth Ratio	3.5ft^{3}min^{-1}
Material	Polypropylene
Woven/Nonwoven	Woven
Size	Large enough for 10% (90% of dust collected in cyclone) of 2kg (200g) for cleaning once a week.

D.5 Appendix D Summary

This appendix section has highlighted the design of baghouse filters, ducting and cyclone filters. Though specifications are concluded consulting a local exhaust ventilation engineer is advised who can deem if it is necessary to install a filtration system or if the air from the building can be released without filtration. This will be deemed by local factors and Health and Safety Executive (HSE) standards.